

**Aerosol Technologies for Fabrication, Collection, and  
Deposition of Engineered Nanoparticles**

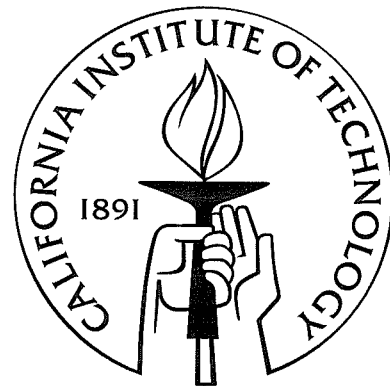
Thesis by

Dean M. Holunga

In Partial Fulfillment of the Requirements

for the Degree of

Doctor of Philosophy



California Institute of Technology

Pasadena, California

2006

(Defended January 20, 2006)

© 2006

Dean M. Holunga

All Rights Reserved

# Acknowledgements

Many, many thanks to my wife of seventeen years, Virginia, who supported me through many years of night classes, full-time day classes, internships and graduate school. Starting, as we did, ten years later than the typical student, meant sacrifices including not buying a home or not starting a family for what often seemed an unreasonable amount of time. But, during this time, she finished her degree and built a successful career.

Many thanks, though he is too young to understand why, to my young son, Marcu. For me, being a father began to heal the loss I still felt from my father's untimely death thirty-eight years ago.

I am very grateful to my fellow graduate students for all the help along the way. I hope the friendships we forged last a lifetime. Best wishes to my golfing buddies, Adam Olsen, Mohan Sankaran, Robb Walters, Tim Van Reken, and Brian Mader. The stolen moments on the links will not be forgotten. The concept of random walk (chasing golf balls) and statistically invariant outcomes – two golf balls lying close to each other – became much clearer after eighteen holes and a couple of pints. Or was it eighteen pints and a couple of holes...

Thanks to the Seinfeld lab whose generous help made labwork much easier. Tracey, Tomtor, Sally, and Roya always gave their time generously and donated innumerable scavenged or new Swagelok<sup>TM</sup> pieces to many projects that went awry.

Thanks to the Atwater lab students who also contributed time and expertise. Julie B., Domenico, Pieter and others.

Thanks to the newer students, Nick, Harmony, Armin, Jay, and Shane who also shared relevant questions and interpretations.

Last, I wish to thank my advisors, Rick Flagan and Harry Atwater, whose breadth of knowledge and attention to detail continually reinforced a pursuit of comprehensive understanding and the creative application of that knowledge to new endeavors. Early in my graduate studies, I often wondered how Rick and Harry could share their ideas with potential competitors so freely. Later on, I understood that those with a multitude of ideas do not fear the loss of one or two. Thanks for the patient direction throughout.

# Abstract

We demonstrate a turbulent mixing reactor capable of producing highly monodisperse,  $\sigma_G \approx 1.1$ , heterogeneous oxide-coated silicon nanoparticles from pyrolytic decomposition of silane. Particle concentrations approach  $10^9 \text{ cm}^{-3}$  as measured with a radial differential mobility analyzer and fA resolution electrometer. Turbulent mixing power, induced by locally high-momentum jets that actually remain below turbulent Reynolds numbers, induce mechanical mixing within a pathlength comparable to the diameter of the major flow channel. Timescales for transport are enhanced orders of magnitude above laminar processes, enabling nanoparticle evolutionary processes such as densification and crystallization to complete in the absence of significant agglomeration. Use of multiple jets in series may well enable the homogeneous introduction of additional reagents to facilitate additional heterogenous particle development.

Particles formed in the Inconel reactor were further studied using both transmission electron microscopy and photoluminescence measurements. Spherical particle morphology with faceted and unfaceted crystalline cores were observed, and thermal oxides appeared uniform. Particle purity and a high quality passivation of the particles were demonstrated by photoluminescence, although particles occasionally required additional processing to complete  $\text{O}_2$  passivation. Photoluminescence measurements are in good agreement with models of quantum-confined exciton recombination, both in emitted wavelength and photolumines-

cence decay. Particle contamination studies using Electron Energy Loss Spectroscopy and Energy Dispersive X-Ray Spectroscopy found no evidence of metal contamination within particles studied for both native oxide and thermal oxide-coated particles. A phenomenological comparison of size information from the radial differential mobility analyzer and photoluminescence spectra demonstrated that thermally grown oxide shells and native oxide shell have initially opposite trends in the variation of thickness with particle size, although over time, native oxide shells thicken considerably.

A thermophoretic deposition chamber was designed for uniform deposition on wafers ranging in size from 100 mm–300 mm and over a range of flowrates from 500 sccm to 15000 sccm. A power-law hyperbolic inlet nozzle was shown theoretically to minimize separation. A uniform axial temperature gradient is developed using programmable temperature-controlled heaters along with active cooling. Characterization by atomic force microscopy studies on 150 mm wafers demonstrated uniform coverage both radially and in the azimuth, in good agreement with model results. Deposition uniformity is predicted on larger wafers, up to 300 mm.

Pyrolysis reactions in small diameter tubular reactors foul the reactors' walls continuously, with deposition morphology ranging from thin-films to dendritic, filter-like structures. The particle number concentration decays linearly with time. Hybridization of the turbulent mixing reactor with high energy seed reactors, such as a microplasma discharge, shows promise that may significantly reduce fouling, maintain or increase particle number concentration, maintain or increase particle monodispersity, expand chemistries available, and retain the ability to produce heterogeneous particles.

Laminar flow reactors are well suited to the production of monodisperse,  $\sigma_G \approx 1.1$ , aerosols. The rate of pyrolytic decomposition of silane precursor is kept relatively slow

during a gentle thermal ramp wherein the low temperature favors vapor deposition growth over additional nucleation. The resulting reduction in silane inhibits further nucleation as the temperature is increased. Slow flowrates, wherein diffusional losses of precursor assists the inhibition of additional nucleation, also contributed to maintaining lower nucleation rates, but are not necessary to achieve monodispersity or higher yield.<sup>7</sup>

# Contents

<b>Acknowledgements</b>	<b>iii</b>
<b>Abstract</b>	<b>v</b>
<b>1 Introduction</b>	<b>1</b>
<b>2 Development of a Scalable Turbulent Mixing Aerosol Reactor</b>	<b>6</b>
2.1 Introduction . . . . .	7
2.2 Reactor Design . . . . .	10
2.3 Impinging Jet Turbulent Flow Reactor . . . . .	14
2.4 Experimental Methods . . . . .	18
2.5 Results . . . . .	20
2.6 Discussion . . . . .	31
2.7 Conclusions . . . . .	35
2.8 Acknowledgments . . . . .	36
<b>3 A Tool for Uniform Coating of 300 mm Wafers with Nanoparticles</b>	<b>37</b>
3.1 Introduction . . . . .	37
3.2 Design . . . . .	41
3.3 Experimental Apparatus & Methods . . . . .	51

3.4	Results . . . . .	55
3.5	Conclusions . . . . .	66
<b>4</b>	<b>Photoluminescence From Oxide-Coated Silicon Aerosol Nanocrystals</b>	<b>67</b>
4.1	Introduction . . . . .	68
4.2	Experimental Apparatus & Methods . . . . .	70
4.3	Results and Discussion . . . . .	76
4.4	Conclusions . . . . .	95
<b>5</b>	<b>Reactor Fouling And Seeding</b>	<b>96</b>
5.1	Introduction . . . . .	96
5.2	Experimental Methods & Design . . . . .	100
5.2.1	Reverse Flow Shell & Tube Assembly . . . . .	100
5.2.2	Shell & Tube Nucleation/Growth with Subsequent Mixing Jet . . . . .	102
5.2.3	Laminar Flow Nucleation, Turbulent Mixing Jets Reactor . . . . .	102
5.2.4	Microplasma-Seeded Turbulent Mixing Jets Reactor . . . . .	103
5.3	Results . . . . .	104
5.3.1	Fouling in Reverse Flow Shell & Tube Assembly . . . . .	104
5.3.2	Fouling in Shell & Tube Nucleation/Growth With Subsequent Mixing Jet . . . . .	106
5.3.3	Fouling in Laminar Flow Nucleation, Turbulent Mixing Jets Reactor	106
5.3.4	Microplasma-Seeded Turbulent Mixing Reactor . . . . .	111
5.4	Conclusions . . . . .	115
<b>6</b>	<b>Experimental Evidence of an Inherent Monodisperse Particle Production Regime of Sinclair-LaMer Aerosol Reactors</b>	<b>116</b>

	x	
6.1	Introduction . . . . .	117
6.2	Experimental Methods & Design . . . . .	120
6.2.1	Reactor Configurations . . . . .	121
6.2.2	Nanoparticle Characterization . . . . .	123
6.3	Results . . . . .	124
6.3.1	Measurement Validation . . . . .	124
6.3.2	Product Particle Characterization . . . . .	128
6.3.2.1	RD1: Laminar Flow Single Tube Reactors And Particle Characterization . . . . .	128
6.3.2.2	RD2: Reverse Flow Shell & Tube Assembly . . . . .	130
6.3.2.3	RD3: Shell and Tube Nucleation/Growth With Laminar Quench . . . . .	133
6.3.2.4	RD4: Laminar Flow Nucleation, Turbulent Mixing Quench	134
6.4	Modeling . . . . .	139
6.5	Conclusions . . . . .	146
<b>7</b>	<b>Particle Collection</b>	<b>147</b>
7.1	Introduction . . . . .	147
7.2	Design . . . . .	148
7.2.1	Turbulent Mixing Virtual Impaction Aerosol Collector . . . . .	148
7.2.2	Electrostatic Precipitator . . . . .	159
7.2.3	Thermophoretic Depositor in ESP Housing . . . . .	163
7.2.4	Thermophoretic Liquid Trap . . . . .	166
<b>8</b>	<b>Appearance of Bipolarly Charged Particles</b>	<b>176</b>

8.1	Introduction . . . . .	176
8.2	Design . . . . .	177
8.3	Results . . . . .	177
8.4	Conclusions . . . . .	182
<b>9</b>	<b>Conclusions</b>	<b>183</b>
<b>A</b>	<b>Additional Information</b>	<b>185</b>
A.1	Reactor Design–First Order Analysis . . . . .	185
A.2	Inconel Turbulent Mixing Reactor Fluent Modeling . . . . .	189
A.3	Particle Charging From Neutralizer . . . . .	195
A.4	Coagulation & Densification . . . . .	197
A.5	Particle Distributions . . . . .	199
A.5.0.1	RD2: Reverse Flow Shell & Tube Assembly . . . . .	199
A.5.0.2	RD3: Shell and Tube Nucleation/Growth with Subsequent Mixing Jet . . . . .	200
A.5.0.3	RD4: Laminar Flow Nucleation With Subsequent Mixing Jet	201
<b>B</b>	<b>CAD Drawings And Software Code</b>	<b>204</b>
B.1	300 mm Thermophoretic Deposition Chamber Drawings . . . . .	204
B.2	300 mm Quartz Sleeved Forks . . . . .	227
B.3	Software Code . . . . .	229
B.4	Scanning Algorithm In Labview . . . . .	238
B.5	VB Code For MS Access Data Handling . . . . .	239

# List of Tables

4.1	Summary of particle size and calculated core diameter/shell thicknesses for median particles and applicable photoluminesce data. . . . .	88
6.1	Configurations of laminar flow nucleation reactors used. . . . .	120

# List of Figures

1.1	Representative images from the first four chapters. . . . .	5
2.1	Schematic of laminar flow turbulent mixing reactor. . . . .	15
2.2	Effect of varying flow ratios and number of jets on relative jet diameter to maintain jet powered mixing. . . . .	17
2.3	Asymptotic particle distribution measured, assuming steady state charge distribution on particles, with various ratios of ion rich gas well mixed with particles. . . . .	20
2.4	TEM images from brightfield, darkfield, HRTEM, and SAD of silicon nanoparticles from the mixing reactor. . . . .	24
2.5	HRTEM image of 8–12 nm oxide-coated silicon particles collected at reduced concentration. . . . .	25
2.6	TEM Image of 10–12 nm particles collected by electrostatic precipitation on holey carbon grid. Note uniformity of size and occasional grouping of particles in close-packed structures. Inset SAD diffraction pattern from randomly oriented nanocrystalline silicon. . . . .	26

2.7	Effect on measured particle distribution of varying quenching flow ratio on particle distribution for 150 ppm SiH <sub>4</sub> in 270 sccm N <sub>2</sub> . Normalized trace on right shows relative effect of quenchrate/dilution on the particle distribution normalized by the peak concentration. The 10:1 and 7:1 traces overlay each other. . . . .	27
2.8	Curve fitted to left mode of a particle distribution with geometric standard deviation of 1.1. Decreasing precursor concentration removes the right mode. . . . .	28
2.9	Shift in size distributions of particles characterized by radial DMA as precursor concentration is varied. The second mode in the 100 ppm trace is likely the rise of doublet particles. At 150 ppm, agglomeration of particles is overwhelming the monodispersity of the distribution. . . . .	29
2.10	Decrease in size and numbers of silicon particles as reactor fouls. . . . .	30
2.11	Calculated particle production rates (g/hr) for reactor using current $\tau_m \approx 1.5\text{ms}$ . . . . .	35
3.1	Isotherms of deposition chamber modeled in Fluent <sup>TM</sup> . Components of chamber: 1. Inner ring heater. 2. Outer ring heater. 3. Band heater and mount. 4. Top MDC SS Flange. 5. Bottom MDC SS Flange. 6. Water cooling chamber. 7. Aerosol inlet. 8. Gas outlet. 9. Viton Gasket. Modeled average current supplied to the heaters (with listed power capacity) as follows: 1. Inner ring heater, 0.4 A/1000 W, middle ring heater, 2. 0.6 A/1500 W, 3. Outer band heater 7.5 A/1500 W. . . . .	46
3.2	Modeled temperature rise for a constant 1800 W heater on the outer band and top of a water-cooled chamber with 30 lpm flowrate. . . . .	47
3.3	Velocity contour plots for flowrates without separation as modeled in Fluent <sup>TM</sup> . . . . .	48
3.4	Velocity contour plots for flowrates with separation as modeled in Fluent <sup>TM</sup> . . . . .	49

3.5	Temperature contour plots modeled in Fluent <sup>TM</sup> . . . . .	53
3.6	Streamfunction plots modeled in Fluent <sup>TM</sup> for flowrates of 1500 sccm. . . . .	54
3.7	Particle deposition and concentration at 1600 sccm modeled in Femlab <sup>TM</sup> . Arrows indicate particle fluxrate at the wafer surface. . . . .	56
3.8	Particle deposition and concentration at 2400 sccm modeled in Femlab <sup>TM</sup> . Arrows indicate particle fluxrate at the wafer surface. . . . .	57
3.9	Particle deposition and concentration at 3000 sccm modeled in Femlab <sup>TM</sup> . Arrows indicate particle fluxrate at the wafer surface. . . . .	58
3.10	Particle deposition and concentration at 3600 sccm modeled in Femlab <sup>TM</sup> . Arrows indicate particle fluxrate at the wafer surface. . . . .	59
3.11	Model predictions for particle deposition on 300 mm silicon wafer at various flowrates. . . . .	60
3.12	PSD and particle coverage on 150 mm silicon wafer. AFM images are seen in Fig. 3.13. . . . .	61
3.13	AFM images of particle deposition on 150 mm wafer. . . . .	62
3.14	Model predicts a reversed temperature gradient when aerosol is not preheated. .	63
3.15	Model predicts the lack of deposition at the wafer center if the aerosol is not preheated. The arrows are proportional to the magnitude of thermophoretic particle flux. . . . .	64
3.16	Modeling in Femlab <sup>TM</sup> corroborates the predicted reversed temperature gra- dient when aerosol is not preheated. . . . .	65
4.1	HRTEM images and corresponding particle size distributions from RDMA of silicon nanoparticles from the mixing reactor. . . . .	78

4.2	PL, PL decay, and particle size distribution from native oxide-coated silicon nanocrystals. . . . .	79
4.3	PL, PL decay, and particle size distribution from HTO-coated silicon nanocrystals. . . . .	81
4.4	PL, PL decay, and particle size distributions from similarly sized oxide-coated silicon nanocrystals. Native oxide-coated particles are exposed to O <sub>2</sub> after characterization with the RDMA. . . . .	82
4.5	Data matched PL Intensity to RDMA particle size characterization for native oxide-coated particles. . . . .	84
4.6	HRTEM images of native oxide-coated particles. . . . .	85
4.7	Data matched PL Intensity to RDMA particle size characterization for HTO-coated particles. . . . .	86
4.8	HRTEM images of HTO-coated particles showing greater uniformity of shell thickness than observed on native-oxide coated particles. . . . .	87
4.9	TEM images of various morphologies of HTO-oxide coated nanoparticles. . .	89
4.10	Particle size distributions of particles used in EELS study. . . . .	90
4.11	EELS, HRTEM, and HAADF from contamination studies on particles made in Inconel reactor. . . . .	92
4.12	EELS, Z-Contrast, and HAADF from contamination studies on particles made in Inconel reactor. . . . .	93
4.13	EELS and conventional TEM images from contamination studies on particles made in Inconel reactor. . . . .	94
5.1	Isotherms of Laminar Shell & Tube Reversing Flow Aerosol Reactor modeled in Fluent <sup>TM</sup> . . . . .	101

5.2	Microplasma Discharge Assembly Above Turbulent Mixing furnace. . . . .	103
5.3	From right to left: far right: Thermophoretic deposition of cooling nanoparticles leaves light brown coating on inside of exit tubing; middle: Silicon film deposits, likely from CVD; far left: fouling on the outer side of the inner tubing. Tube outer diameter is 6.35 mm. . . . .	104
5.4	Effect of fouling on particle distribution over time. . . . .	105
5.5	Images from reverse flow, shell-in-tube reactor of fouling deposits that lead to tube constriction, performance degradation, and reactor failure. . . . .	107
5.6	Effect of fouling on particle distribution with time observed from the shell and tube nucleation/growth with subsequent mixing jet reactor. . . . .	108
5.7	Effect of fouling on particle distribution with time observed from the laminar flow nucleation, turbulent mixing reactor. . . . .	110
5.8	Effect of fouling on particle distribution with time observed from the laminar flow nucleation, turbulent mixing reactor. . . . .	110
5.9	Densification of silicon particles from a microplasma discharge in Argon seeding a turbulent mixing reactor. . . . .	112
5.10	Densification of coagulated silicon nanoparticles from a microplasma discharge in Argon seeding a turbulent mixing reactor. . . . .	113
6.1	Two configurations of quartz laminar flow reactors. (a) RD1: Single tube reactors. (b) RD2: Reversed flow shell and tube reactor. . . . .	121
6.2	Two configurations of laminar flow nucleation reactors made from Inconel. .	123
6.3	Typical particle size distributions from RD1 with 17 mm diameter. . . . .	125
6.4	particle size distributions from RD1 type reactors. . . . .	126

6.5	Dilution of aerosol with ion-rich gas in ratios greater than 2:1 significantly reduce the agglomeration bias seen in particle size distributions. Traces are corrected for dilution. . . . .	127
6.6	Particle size distributions from 15 cm hotzone at 1023 K single 7.525 mm I.D. fused quartz tube laminar flow aerosol pyrolysis reactor with 50 ppm reactant silane. . . . .	129
6.7	Particle distributions observed from RD2 for variations silane concentration at 1273 K for low nucleation flowrate. . . . .	131
6.8	Particle distributions observed in RD2 for variations in silane concentration at 1273 K for large comparative difference in bottom to top flow. . . . .	132
6.9	Particle distributions observed for nucleation in RD3, an inconel shell & tube with turbulent mixer reactor. . . . .	134
6.10	Initial monodisperse peak observed from RD4 for a variety of inlet concentrations. . . . .	135
6.11	Particle size distributions recorded from RD4 from nucleating silicon nanoparticles in a 1.75 mm ID SS tube. . . . .	137
6.12	Mode-sized particle of monodisperse particles from reactors RD1-RD4 increase with reactor diameter. . . . .	138
6.13	Predicted size of nanoparticles from modeling in Femlab <sup>TM</sup> . . . . .	142
6.14	Particle concentrations from modeling. The effect of thermophoretic transport is clearly seen in the image. . . . .	143
6.15	Particle flux at reactor exit in [cm <sup>-3</sup> ]. . . . .	144
7.1	Exit gap adjustments for 3 mm diameter nozzle. . . . .	154
7.2	Exit gap adjustments for 1 mm diameter nozzle. . . . .	156

7.3	15° tapered nozzle with a venturi downstream in 1 mm exit gap. Impaction flow still penetrates the collection chamber. . . . .	157
7.4	Velocity profile using a straight jet modeled in Femlab. . . . .	157
7.5	Exit gap adjustments for 3 mm diameter nozzle. . . . .	158
7.6	Deposition modeling on 3 mm TEM Grid with a 2000 V electric field across a 1 mm gap and 2000 sccm flow through nozzle. . . . .	161
7.7	Deposition modeling of 5 nm particles on 3 mm TEM Grid with a 2000 V electric field across a 1 mm gap with varied flowrates. . . . .	162
7.8	Modeling of deposition of 5 nm particles onto a 3 mm TEM Grid with various electric field strengths across a 1 mm gap and using 5000 sccm flowrate. . . .	163
7.9	Modeling of thermophoretic flux of particles. In (a), the numbers correspond to: 1. Aerosol inlet. 2. Brass heater tape housing. 3. Aerosol outlet. 4. Styrofoam insulator. 5. Brass cold finger dipped into liquid N <sub>2</sub> . 6. Aluminum housing. 7. Teflon insulator. 8. Wafer fragment housing/deposition area. . .	165
7.10	Darkfield image of silicon core particle and oxide shell after exposure to frost. .	166
7.11	Collection efficiencies less than 50% are predicted for a chamber 10 cm x 5 cm x 1 cm. . . . .	169
7.12	Collection efficiency improves using a liquid nitrogen cooled surface, but remains unsuitably low. . . . .	170
7.13	Low flowrates with a water-cooled system, still yields low collection efficiency. .	171
7.14	Longer collection length yields greater collection of particles. . . . .	172
7.15	Comparison of H <sub>2</sub> O and liquid N <sub>2</sub> cooled 20 cm x 3 cm x 0.5 cm collectors. .	174
7.16	Thermophoretic flux arrows are most uniform for this design in this configuration with 2000 sccm, 400 K inlet, H <sub>2</sub> O cooled. . . . .	175

8.1	Current in fA measured with an electrometer from charged particles immediately exiting Inconel Reactor. . . . .	178
8.2	Current measured at electrometer from charged particles exiting reactor with various ratios of ion-rich N <sub>2</sub> from <sup>85</sup> Kr neutralizer. . . . .	180
8.3	Current measured at electrometer from charged particles exiting reactor with various ratios of ion-rich N <sub>2</sub> from <sup>85</sup> Kr neutralizer. . . . .	181
A.1	Meshed grid from Gambit for CFD modeling in Fluent <sup>TM</sup> . . . . .	190
A.2	Temperature and pressure contour plots of reactor with flowrates of 180 sccm Nucleation zone, 1800 sccm first jets, 400 sccm second jets. . . . .	191
A.3	Velocity contour plots of reactor with flowrates of 180 sccm Nucleation zone, 1800 sccm first jets, 400 sccm second jets. . . . .	192
A.4	Temperature contour when increasing nucleation and first mixing jet flow rates by 5x over those shown in Figs. A.2–A.3. . . . .	193
A.5	Contour plots of reactor with 1800 sccm nucleation and 180 sccm first mixing jet flowrates. . . . .	194
A.6	Asymptotic particle distribution measured, assuming steady state charge distribution on particles, with various ratios of ion rich gas well mixed with particles. . . . .	196
A.7	Particle distributions observed for variations in silane concentration at 1273 K for large comparative difference in bottom to top flow. . . . .	199
A.8	Particle distributions observed for nucleation in RD3, an inconel shell and tube with turbulent mixer reactor. . . . .	202
A.9	Particle size distributions from RD3 at relatively lower concentration of SiH <sub>4</sub> . .	203
A.10	Image of mixing reactor, RD4, described in ???. . . . .	203

B.1	Full Assembly. . . . .	205
B.2	Full Assembly. . . . .	206
B.3	Full assembly exploded. . . . .	207
B.4	Full assembly exploded. . . . .	208
B.5	Ring Heater Clamp. . . . .	209
B.6	Ring Heater Clamp. . . . .	210
B.7	Ring Heaters. . . . .	211
B.8	Ring Heaters. . . . .	212
B.9	Ring Heater Clamps. . . . .	213
B.10	Ring Heater Clamps. . . . .	214
B.11	Band Heater Mount. . . . .	215
B.12	Band Heater Mount. . . . .	216
B.13	Mounts for PID controller thermal sensors. . . . .	217
B.14	Mounts for PID controller thermal sensors. . . . .	218
B.15	Top Flange MDC. . . . .	219
B.16	Top Flange MDC. . . . .	220
B.17	Bottom Flange MDC. . . . .	221
B.18	Bottom Flange MDC. . . . .	222
B.19	Water cover plate, inlet jet and nozzle, and outlet port. . . . .	223
B.20	Water cover plate, inlet jet and nozzle, and outlet port. . . . .	224
B.21	Legs for supporting Top Flange and Assembly. . . . .	225
B.22	Legs that mount to bottom flange, water plate, and jackstand. . . . .	226
B.23	Quartz Tine to cover SS Forks for 300 mm wafer handling. . . . .	227
B.24	Forks for 300 mm wafer handling. . . . .	228

B.25	Page 1 of 8 C <sup>++</sup> code.	230
B.26	Page 2 of 8 C <sup>++</sup> code.	231
B.27	Page 3 of 8 C <sup>++</sup> code.	232
B.28	Page 4 of 8 C <sup>++</sup> code.	233
B.29	Page 5 of 8 C <sup>++</sup> code.	234
B.30	Page 6 of 8 C <sup>++</sup> code.	235
B.31	Page 7 of 8 C <sup>++</sup> code.	236
B.32	Page 8 of 8 C <sup>++</sup> code.	237
B.33	Labview code for RDMA scanning-mode data inversion algorithm of Collins et al. <sup>28</sup>	238

# Chapter 1

## Introduction

This thesis is focused on using aerosol technology to create engineered nanoparticles suitable for use within the microelectronic, biological, and academic communities. It is motivated, in part, from a challenge to coat a 300 mm wafer with a monolayer of optically active silicon nanoparticles within a few hours.

In Chapter 2, a new class of small volume aerosol reactor utilizing turbulent mixing is presented. At flowrates less than the Reynolds number, flows may be well mixed in a pathlength on the order of the reactor diameter using the mechanical power introduced through high velocity jets.<sup>30</sup> This reactor is capable of producing highly monodisperse,  $\sigma_G \approx 1.1$ , thermally oxide coated 10 nm silicon nanoparticles in particle concentrations approaching  $10^9 \text{ cm}^{-3}$ . This represents a two order of magnitude increase in particle number production, Fig. 1.1(a), over the previously used laminar flow reactor. The cost of using a small volume reactor, however, is that high mobility products formed during early particle development may deposit on the tubewall, diminishing reactor performance with time.

Chapter 3 introduces an aerosol deposition tool capable of uniform deposition on wafers from 100 mm–300 mm. A uniform axial temperature gradient combined with non-separable radially symmetric outward flow provides a constant driving thermophoretic force that enables uniform deposition. Atomic force microscopy confirms the predictions observed

from computational fluid dynamic modeling that the flow profile is non-separated, the temperature gradient uniform, and the deposition profile, Fig. 1.1(b), uniform. Modeling was also used to identify a working range for the tool and criteria that would lead to non-uniform deposition. Modeling of relatively slow flows indicate that, while deposition is no longer completely uniform due to the expected depletion of the aerosol, significant coverage extends beyond the range expected due to simple Brownian diffusion. Hence, the optimum deposition profile needs to be governed by thermophoresis alone. This deposition tool may be applied to studies that require nanoparticles to be located in a precise spatial position or it may be applied to address questions of particle behavior on an unencapsulated surface. While deposition studies were limited to 150 mm diameter, wafers, deposition uniformity on a 300 mm wafer is inferred using the results from modeling.

Chapter 4 presents evidence of photoluminescence spectra from the nanoparticles grown in the turbulent mixing reactor. Using particle size data from the radial differential mobility analyzer and comparing it to photoluminescence spectral (size) data, a phenomenological comparison, Fig. 1.1(c), illustrates that growth of the oxide for native oxide-coated particles shows an early trend of decreasing thickness with particle size. Over time, the oxide thickens. The thermally grown oxide layer is initially characterized as increasing with particle size. Using a high temperature Inconel reactor to produce “clean” nanoparticles, i.e., contaminant-free and defect-free, is investigated in this chapter. Studies using Electron Energy Loss Spectroscopy found no detectable contaminants in the particles, and the observation of photoluminescence spectra suggested that particles could be made with a minimum of defects. Occasionally, post reactor annealing was needed to observe photoluminescence.

Chapter 5 summarizes the fouling seen in the different configurations of the reactors. Since each reactor employed a Sinclair-LaMer type nucleation zone, the fouling mechanism

and decay pattern, Fig. 1.1(d), is also similar. A laminar sheath flow around nucleating particles shows some potential to reduce fouling, but using an alternate-source seed generator, such as a microplasma discharge reactor, appears to both maintain particle production numbers and particle size. Seeding the turbulent mixing reactor provides a means to densify particles and grow additional layers on nanoparticles within timescales where agglomeration remains insignificant. This project was a collaborative effort, with the microplasma technology coming from the collaborators.

In Chapter 6, we present experimental evidence that a monodisperse particle production regime,  $\sigma_G \approx 1.1$ , exists in Sinclair-LaMer type aerosol reactors for silane pyrolysis. The size of the nanoparticle can be changed by changing the dimension of the reactor. Narrower reactors are used for making smaller particles. Within this regime, vapor deposition on particles is the dominant growth mechanism. Within limits, small perturbations in feed concentration changes the number of particles that are characterized, not the size. Growth of large particles occurs when either the nucleation rate exceeds the vapor deposition rate, or, for large numbers of particles, when Brownian diffusion brings particles into frequent contact, causing agglomeration. Successful particle characterization of this monodisperse size production regime is hindered by the relatively slow diffusion-charging process in a so-called neutralizer.

Chapters 7 contains initial modeling of a design idea for a compact-sized high efficiency condensational growth-virtual impactor particle collector. Nanoparticles of  $\sim O(10 \text{ nm})$  are smaller than can be efficiently collected in high concentrations in using bubblers in liquids. Fouling also reduced the collection period. Relatively high flowrates evaporated volatile liquids before collection results were discernable. The numbers of particles from the turbulent mixing reactor are also too numerous to growth to micron sizes for collection with

a simple impactor. However, growth of a sizeable percentage to this size using turbulent mixing jets to supply condensable vapor and then remixing the large and small particle streams together can harness the increased coagulation efficiency of the large particles to collect the small particles. Particles might be collected into an inert environment by passing across a virtual impact plane. The modeling of a few nozzle geometries at flowrates up 0.3 Mach are presented, and one geometry incorporating a beveled entrance to the virtual impactor is presented, representing a potential solution to the design problem. An efficient particle-in-liquid collection device is needed for collaborative work involving aerosol grown nanoparticles to biological projects. Additionally, other labscale devices, such as the electrostatic precipitator and a thermophoretic depositor, were modeled to determine collection efficiencies within parameters that governed experiments.

Chapter 8 is a summary of an observation of bipolar particle charging, detected by the electrometer, in a proportion similar, but at fractions less than that experienced at steady-state within a neutralizer.

Appendix A contains first order mathematical modeling used in reactor design, unpublished modeling of the turbulent mixing reactor, (Chapter 2) some introductory material from peer journals and texts on coagulation, and an explanation of the method used to impart a charge distribution on nanoparticles while avoiding the relatively long residence time in a neutralizer.

Appendix B contains CAD drawings of the thermophoretic deposition tool, software written to extract data from RDMA discrete mode characterization, SQL Queries used to port data from RDMA scanning mode characterization into databases, and the GUI code of the scanning mode algorithm (Collins, et al.) used in Labview to collect RDMA data.

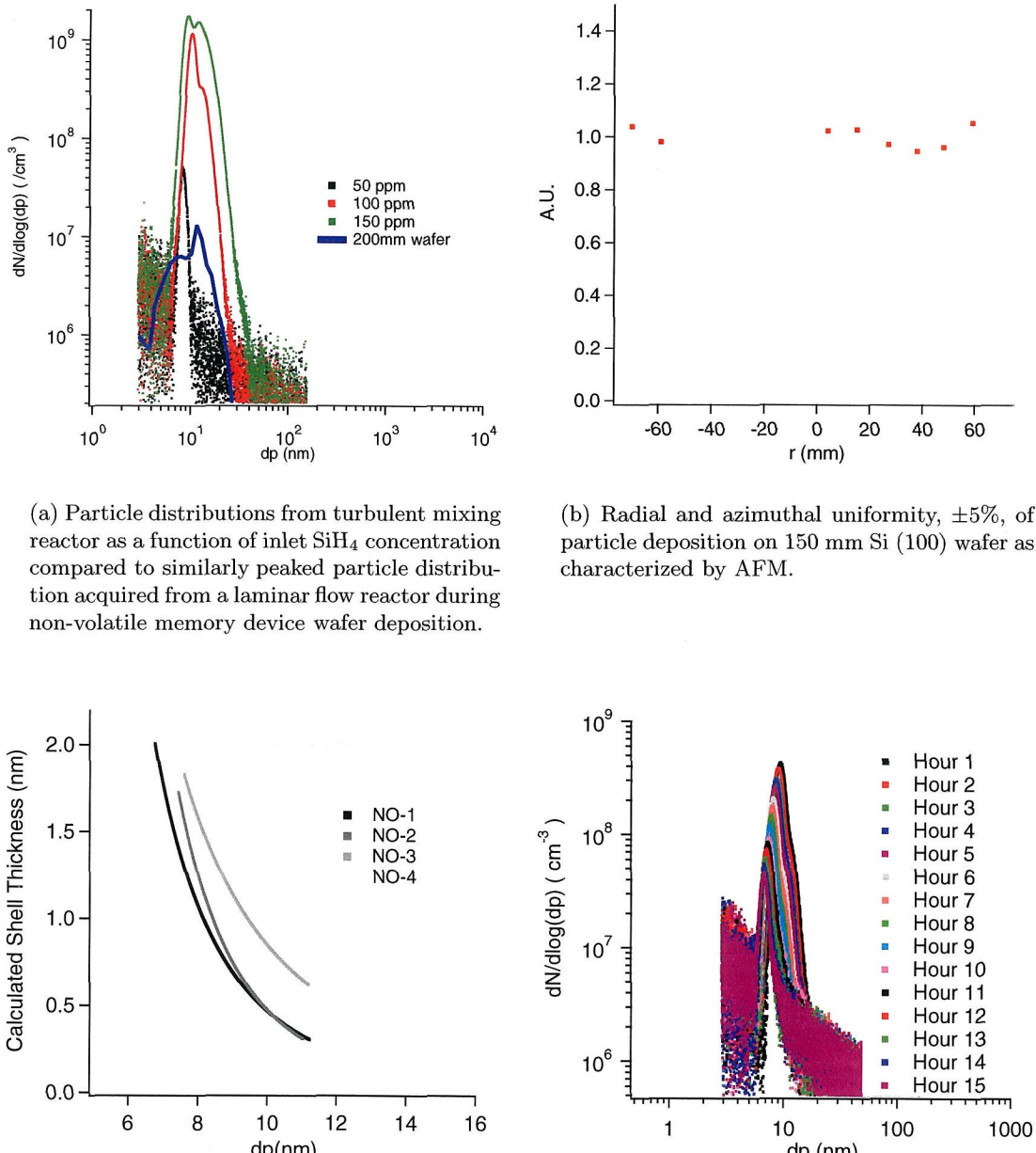


Figure 1.1: Representative images from the first four chapters.

## Chapter 2

# Development of a Scalable Turbulent Mixing Aerosol Reactor

### Abstract

<sup>1</sup> A new, turbulent flow aerosol reactor is described that enables synthesis of uniformly sized aerosol nanoparticles during a residence time of a few milliseconds. The short residence time allows processing of high number concentration aerosols, in excess of  $10^9\text{cm}^{-3}$ , to be processed with minimal coagulation, leading to an aerosol throughput approaching  $10^{11}\text{particles cm}^{-3}\text{s}^{-1}$ . Turbulent mixing speeds thermal and chemical transport beyond diffusional limits inherent in laminar flow reactors, providing the thermal energy to drive chemical reactions, coalescence, densification, and crystallization of particles. With enhanced transport, residence time in the reactor can be reduced, thus limiting coagulate particle growth while maintaining a high throughput of non-layered or multilayered aerosol particles. The turbulence that enables rapid mixing is generated by dissipation of kinetic energy supplied to the reactor by high velocity gas jets. The apparatus described here increased the throughput by a factor of 100 above previous laminar flow reactors, and the

---

<sup>1</sup>Reproduced with permission from D. Holunga, R. Flagan, and H. Atwater. A Scalable Turbulent Mixing Aerosol Reactor for Oxide-Coated Silicon Nanoparticles. *Ind. Eng. Chem. Res.*, 2005. Copyright 2005 American Chemical Society.

induced fast mixing enables scale-up to much higher throughput. Characterization of particles by Differential Mobility Analysis and Transmission Electron Microscopy confirmed uniformity in size and composition.

## 2.1 Introduction

Aerosol synthesis of nanoparticles has been the subject of numerous investigations employing the evaporation/condensation method,<sup>23,38,51</sup> externally heated laminar flow reactors,<sup>101</sup> and laser heating,<sup>52</sup> among other methods.<sup>70,133,135,149</sup> Control of particle size, crystallinity, and/or extent of agglomeration has been the focus of many of these investigations. For many applications, however, more complex particles are needed. Ostraat<sup>102</sup> synthesized nonagglomerated nanoparticles comprised of 5-10 nm diameter single crystal silicon cores encased in silica shells. These composite nanoparticles were synthesized under clean conditions, deposited on 200 mm diameter silicon wafers, and processed through an industrial semiconductor fabrication plant to produce novel nonvolatile memory devices in which the nanoparticles served as a discontinuous floating-gate, rendering the charge retention of the memory more robust than conventional devices with a continuous floating gate. Although the performance of the devices synthesized by this route was very promising, a number of challenges remain to be overcome before aerosol technology is routinely integrated into microelectronics processing. Foremost is reluctance to introduce particles into the manufacturing process after decades of work aimed at removing particles from the cleanroom and process tools. Skepticism about the use of aerosols in device fabrication will only fade after additional demonstrations of the unique capabilities of aerosol synthesis and further demonstrations that aerosol routes can be advantageously employed without risk to the expensive tools and processes involved in microelectronics fabrication.

Other challenges must be addressed as well. In particular, the laminar flow reactors that have been the focus of much of the work to date are not well suited to the production environment. Due to the long residence times in most laminar flow reactors, particle number concentrations must be kept low to prevent runaway agglomeration.<sup>38</sup> The low flow rates through laminar flow reactors, combined with the low number concentrations, lead to long deposition times. Successful incorporation of aerosol nanoparticle deposition into device fabrication will require that deposition times be competitive with conventional process steps. Higher throughput processes that maintain control over nanoparticle properties while minimizing contamination are, therefore, needed. Other nanoparticle technologies may relax the constraints on particle composition, while greatly increasing the quantities of material that must be synthesized to be technologically significant. Flagan and Lunden<sup>38</sup> showed that increases in aerosol nanoparticle production rates are best achieved by reducing the residence time in the reactor when particles are grown by coagulation.

Laminar flow reactors in which particles grow primarily by vapor deposition produce much narrower size distributions than do reactors in which coagulation is the primary growth mechanism. Indeed, a classical method for production of “monodisperse” aerosols is the so-called Sinclair-LaMer generator in which seed particles are grown by condensation, usually a low vapor pressure organic.<sup>122</sup> Similar control has been demonstrated in single-stage, laminar-flow aerosol reactors in which the seed particles are produced by homogeneous nucleation in a cool region of the reactor, where the reaction rate is relatively slow, and where the seeds are grown to size by gradually accelerating the reaction kinetics, usually accomplished by increasing the reaction temperature along the length of the reactor.<sup>99,146</sup> If the rate of production of condensable product is kept low enough that the growing particles adequately scavenge those products, homogeneous nucleation can be suppressed, and with

product aerosols narrow particle size distribution can be synthesized. This requires precise scheduling of the reaction rate as the gases flow through the reactor to prevent runaway nucleation from producing large numbers of particles that would then grow by coagulation, forming agglomerates and broadening the particle size distribution.<sup>38,145</sup> Combined with the low seed particle number concentrations required to suppress coagulation during growth of the seeds, this has, to date, severely limited the throughput of laminar flow reactors.

Higher number concentrations could be tolerated if reaction control were achieved much more rapidly, most likely by means other than controlling the wall temperature of a laminar tube flow, thereby facilitating higher particle production rate per unit of active reactor volume, here denoted as the volumetric production rate. Laser heating or photochemical reaction initiation, thermal plasmas, and flames can all achieve efficient precursor conversion in the short residence times needed to increase the reactor throughput, but methods that produce compound, precisely coated nanoparticles and other complex structures have not been demonstrated. Moreover, most high throughput aerosol reactors involve growth by coagulation, leading to a relatively broad particle size distribution known as the self-preserving size distribution.<sup>81</sup>

This paper describes an alternate approach to synthesis of narrow size distribution nanoparticles that enables higher volumetric throughput while maintaining control over particle properties, including the ability to synthesize compound nanoparticles for special applications. A two-stage version of this reactor is demonstrated in the synthesis of core-shell silicon nanoparticles with structures similar to those fabricated in Ostraat's laminar flow reactor.<sup>101</sup> In the initial application of this new reactor, silicon nanoparticles are first synthesized by silane pyrolysis. An oxide shell is then produced by thermal oxidation of the outer region of the particles. The rapid heating required to carry out these reactions

in a residence time as little as 25 ms for nucleation/initial growth and 10 ms for further development is achieved by turbulent mixing of a preheated carrier gas with cold precursors. The new reactor not only increases throughput above that of laminar flow reactors producing similar particles, it also enhances control over the particle size distribution. The present reactor was optimized to enable deposition of a uniform layer of nanoparticles on a 300 mm wafer, although the concept is broadly applicable to nanoparticle synthesis.

## 2.2 Reactor Design

In the discussion that follows, we consider the synthesis of nanoparticles by pyrolytic decomposition of a gaseous precursor, specifically silicon nanoparticle production by silane pyrolysis. This system has been extensively studied in previous experimental and theoretical investigations. In this system, the rate of reaction to form condensable products increases with increasing temperature. In the laminar flow reactor, the reactant gases are heated by convection from the hot wall of the reactor tube. The highest temperatures, and hence, highest reaction rates, occur at the tube wall while the core of the tube flow is slowly heated by thermal diffusion. The characteristic time for thermal diffusion

$$\tau_{td} \approx \frac{d_t^2}{\alpha} \quad (2.1)$$

where  $d_t$  is the internal diameter of the tube, and  $\alpha$  is the thermal diffusivity of the gas, thus places a lower bound on the residence time required for efficient precursor conversion to nanoparticles.

As the residence time in the reactor increases beyond the characteristic time for particle-particle collisions at the prevailing particle number concentration,  $N_p$ , coagulation becomes

the dominant growth mechanism. To first order, that time can be estimated as

$$\tau_c = \frac{2}{KN_p}. \quad (2.2)$$

These nanoparticles are much smaller than the mean-free-path of the gas molecules, so the collision frequency function is that for free-molecular particles, which can be expressed as

$$K = 4 \left( \frac{6k_B T}{\rho_p} \right)^{\frac{1}{2}} d_p^{\frac{1}{2}} \quad (2.3)$$

for particles of equal diameter,  $d_p$ , and  $k_B$  and  $T$  are the Boltzmann constant and temperature, respectively. In the size regime of these nanoparticles,  $K$  is only a weak function of particle size and temperature, so the characteristic time for coagulation is determined by the particle number concentration.

If coagulation contributes significantly to particle growth, undesirable agglomerate particles will form unless the particles coalesce completely between collision events.<sup>38</sup> The time required for complete coalescence,  $\tau_f$ , of the silicon nanoparticles synthesized in this study is determined by surface diffusion,<sup>96,147</sup> for which

$$\tau_f \approx \frac{2k_B T n}{64\pi\sigma_s D_{eff}} \quad (2.4)$$

where  $k_B$  is the Boltzmann constant,  $n$  is the number of silicon atoms comprising the coalescing particle,  $\sigma_s$  is the surface free energy of solid, bulk silicon, and  $D_{eff}$  is related to the solid state grain boundary diffusion coefficient,  $D_{GB}$ , and the thickness,  $\delta$ , of the grain boundary region where

$$D_{eff} = D_{GB} \frac{\delta}{d_p}. \quad (2.5)$$

At the temperatures of interest, sintering times for two 8 nm particles to coalesce into a dense 10 nm particle is  $\sim O(\mu s)$ , so dense particle growth can be anticipated for exit number concentrations less than  $10^{14} \text{ cm}^{-3}$ . For 10 nm product particles, this corresponds to a volumetric production rate of up to  $10^{-1} \frac{\text{g}}{\text{cm}^3 \text{s}}$ , provided residence times can be kept short enough.

Efforts to increase the throughput of the laminar flow reactor have been stymied by the increasing time required for gas heating with increasing reactor size, and the resulting decrease in the tolerable number concentration. The regime in which laminar flow can be maintained is constrained by the critical value of the Reynolds number,

$$Re = \frac{\rho U d_t}{\mu} < 2200 \quad (2.6)$$

at which tube flow becomes turbulent. Here,  $\rho$ ,  $\mu$ , and  $U$  are the gas density, viscosity, and mean velocity, respectively. Beyond the turbulent transition, turbulent mixing will enhance the rate of heat transfer, although the entrance length that is required to achieve fully developed turbulent flow is long.

Due to the long entrance length and the slow decay of temperature and composition fluctuations, turbulent pipe flow does not afford the degree of control over the synthesis process that is needed in aerosol nanoparticle synthesis. However, turbulence that is sufficiently intense to induce rapid mixing and, thereby, to allow the needed control can be created by introduction of sufficient fluid kinetic energy into a confined volume to overcome viscous dissipation.<sup>30</sup> In the discussion that follows, we present a turbulent flow reactor that enables efficient conversion of a volatile precursor into aerosol nanoparticles to be achieved within a small tubular reactor even when the tube flow Reynolds number is well below that

required for turbulent pipe flow.

Multilayered particle production in laminar flow reactors has also been subject to significant particle losses between stages. Typically, multiple furnace/tube assemblies are employed separated by convectively cooled sections. Reagents added at each stage require time to fully diffuse to the particles. Particle deposition by thermophoretic drift to the cold wall downstream from the exits to each furnace can easily account for losses of the majority of particles originally produced.

A compact design that incorporates multiple reactor stages into a single assembly can reduce the residence time by employing turbulence to ensure that reactants mix on a time scale that is short compared to the inherent kinetic times of the nanoparticle synthesis process, i.e.; nucleation and growth ( $\sim O(0.1 \text{ s})$ ), densification/crystallization ( $\sim O(\mu\text{s})$ ) /  $\sim O(< \text{ms})$ ), or additional layer growth ( $\sim O(\mu\text{s})$ ). These processes must be completed in a time that is short compared to  $\tau_c$ , so increasing the number concentration to increase throughput requires a corresponding decrease in the reactor space time,

$$\tau_{R,i} = \frac{V}{Q_i} \quad (2.7)$$

where  $V$  is the reactor volume and  $Q_i$  is the total volumetric flow rate through the  $i$ th stage of the reactor.  $\tau_{R,i}$  may not exceed  $\tau_{c,i}$  for a single stage, nor the sum of  $\tau_{R,i}$  exceed  $\tau_c$  for the entire reactor. The discussion that follows presents a simple multistage reactor that meets this requirement.

### 2.3 Impinging Jet Turbulent Flow Reactor

Flow from a narrow diameter jet into a large quiescent volume remains laminar only for  $Re < 30$ .<sup>115,132</sup> The resulting turbulence can be used to force rapid mixing into a flow that would otherwise be laminar. A jet impinging into a confined laminar flow introduces kinetic energy that will fully mix with the axial flow within a path length on the order of the mixing channel diameter.<sup>30</sup> Thermal and concentration fluctuations within this mixing volume reactor dissipate much more rapidly than they would without the added kinetic energy. Corrsin<sup>30</sup> showed that concentration fluctuations in mixing fluids can decay within the same length scale as the dissipation of turbulence. For isotropic or nearly isotropic flow, he described a characteristic time for mixing as,

$$\tau_m = 3.3 \left( \frac{ML^2}{P} \right)^{\frac{1}{3}} \quad (2.8)$$

where  $M$  is the mass of fluid in the dissipation region,  $P$  is the mechanical power introduced into that volume, and  $L$  is the integral dimension.

The present reactor, which is illustrated in Fig. 2.1, consists of a tubular region in which impinging jets introduce the kinetic energy required to induce rapid turbulent mixing, so the characteristic length of the reactor is its diameter, i.e.,  $L = d_t$ , and the power,  $P$ , is supplied by the kinetic energy of the incoming fluid jets,

$$P = \sum \rho v_i^2 Q_i \quad (2.9)$$

where  $Q_i$  and  $v_i$  are the volumetric flowrate and velocity of the fluid entering through the  $i$ th jet. Turbulent dissipation of that kinetic energy rapidly mixes the gas flows. A simi-

lar geometry has recently been used to create a simple, fast-mixing condensation particle counter in which a cold aerosol flow is mixed with a hot vapor-laden stream.<sup>74,139</sup> In that device, the resulting supersaturation leads to condensational growth of small particles to sufficiently large sizes that enable optical detection on a millisecond time scale. In spite of the intense turbulence, losses of the small particles to the mixing region wall were small, enabling an instrument with high nanoparticle detection efficiency to be developed, suggesting that the same approach may lead to an efficient nanoparticle synthesis reactor.

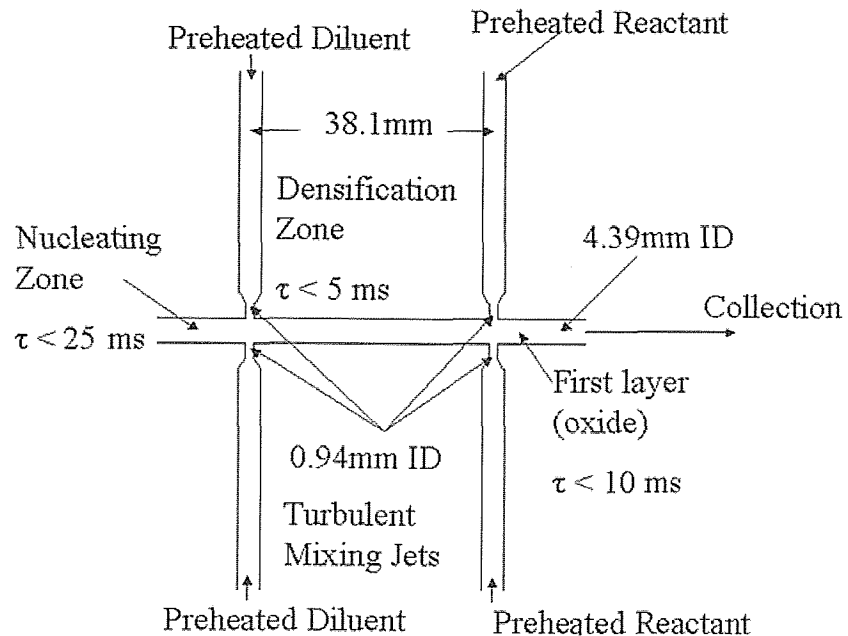


Figure 2.1: Schematic of laminar flow turbulent mixing reactor.

In the present aerosol reactor implementation, a dilute cold reactant stream containing SiH<sub>4</sub> in N<sub>2</sub> is preheated by convection from the inlet tube wall as the tubing passes through the insulated wall of a box furnace. The rapid heating that results induces pyrolytic decomposition of the silane, leading to particle formation by homogeneous nucleation of the

reactant products, and growth of the product particles by a combination of vapor deposition and coagulation, although preheating of the silane in the precursor introduction tube may initiate a reaction before the gases enter the turbulent mixing zone. Farther downstream, preheated  $N_2$  is mixed with the developing particles, raising the temperature sufficiently high to ensure that particles fully coalesce and anneal to produce dense, crystalline nanoparticles. In order to produce multilayered particles, such as a particle consisting of a shell of silica on a core of silicon, a second impinging jet reactor installed downstream of the first jets mixes pure  $O_2$  with the particle stream. The resulting oxidation of silicon produces a shell of silica on the particles.

In this reactor, a precursor flow of volumetric flowrate  $Q_o$  is mixed by a total jet flow rate,  $Q_j$ , that is injected equally through  $\phi$  impinging jets of diameter  $d_j$ . The characteristic mixing time thus becomes,

$$\tau_m = 3.3 \left( \frac{\frac{1}{32}\pi^2 d_t^2 L^3}{\frac{Q_j^3}{d_t^4} + \frac{Q_j^3 \phi^2}{d_j^4}} \right)^{\frac{1}{3}}. \quad (2.10)$$

When most of the turbulent mixing power is supplied through the jets, e.g.,  $Q_j \gg Q_o$ ,  $\tau_m$  varies as,

$$\tau_m \approx \tau_{R,m} \left( 2 \left( \frac{d_j}{d_t} \right)^4 \left( \frac{1}{\phi^2} \right) \right)^{\frac{1}{3}} \quad (2.11)$$

where  $\tau_{R,m}$  is the average residence time of the fluids in the mixing region. When  $\tau_m \ll \tau_d$ , turbulent mixing induced by the impinging jets quickly dissipates concentration and thermal fluctuations.

Figure 2.2 shows the effect on  $\frac{d_j}{d_t}$  for varying reactor/mixing flowratios  $\frac{Q_j}{Q_o}$  and number of jets  $N_j$ . Two trends are observed. First, as the ratio of  $\frac{Q_j}{Q_o}$  decreases, as inevitably must happen with subsequent downstream mixers in multilayer particle production,  $\frac{d_j}{d_t}$  must decrease to provide sufficient mixing power. Second, if the number of jets,  $N_j$ , is increased,

so also must  $d_j$  decrease, but it is not linear with  $N_j$ .

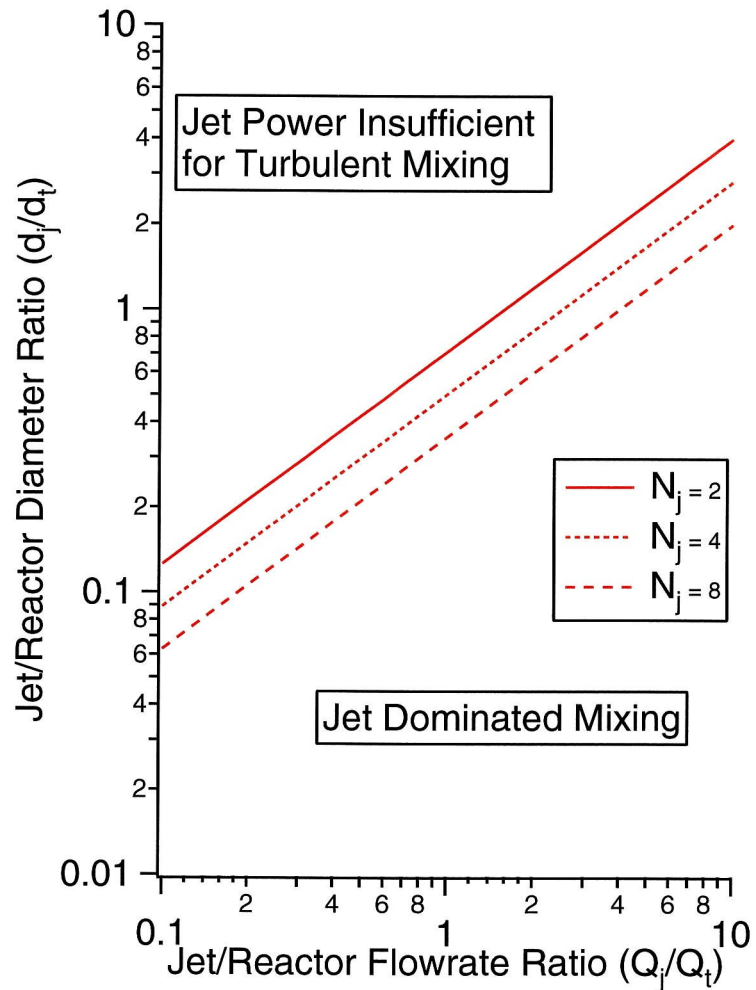


Figure 2.2: Effect of varying flow ratios and number of jets on relative jet diameter to maintain jet powered mixing.

## 2.4 Experimental Methods

Dilute  $\text{SiH}_4$  in  $\text{N}_2$ , ( $\sim O(ppm)$ ), is introduced via a 6.35 mm OD Inconel 600 tube. The precursor is heated by the tubewall within the insulated wall of a box furnace internally maintained at 1273 K. Thermal decomposition of the silane initiates silicon nucleation before the reactant enters the turbulent mixing zone. One of two growth mechanisms may dominate further particle evolution. If nucleated particle concentration is sufficiently low, then growth may proceed by vapor deposition leading to a narrow size distribution. If, however, nucleation produces too many particles, growth by agglomeration dominates leading to a relatively broad self-preserving size distribution.

Downstream from the nucleation zone, the reacting gases and particles enter the first turbulent mixing zone of the reactor where preheated  $\text{N}_2$  at 1273 K enters through two opposing radial positions at high velocities via small diameter tubing. The resulting high temperature, ( $\sim 1273$  K), ensures complete decomposition of the silane and provides the thermal energy for coalescence and densification, while the sudden dilution quenches coagulation within a length that is of the order of the diameter of the reactor.

To enable long term charge storage within the nanocrystal in the memory device application, a silicon oxide layer is grown on the outer surface. A flow of pure oxygen that has been preheated to 1273 K is introduced through a second pair of opposed mixing jets in a second turbulent mixing zone. Oxygen diffuses to and through the surface, oxidizing the silicon and shrinking the silicon core of the nanoparticle while creating the oxide shell. For a low defect, well-passivated oxide, the resulting concentration of  $\text{O}_2$  in the reactor is kept above 15%.<sup>102</sup>

The particle stream exits the furnace and is cooled by convection to room tempera-

ture. Particle size distributions were measured using a radial differential mobility analyzer (RDMA).<sup>23</sup> The RDMA classifies charged particles according to their electrophoretic migration velocities and measures the transmitted particles using a Faraday-cage filter system with an electrometer with a detection limit of 1 fA ( $10^{-15} A$ ). The RDMA was operated in scanning mode<sup>140</sup> and analyzed by the method of Collins, et al.<sup>28</sup> Central to the RDMA analysis is charging the particles in a known way. This is normally achieved by passing the aerosol through a so-called neutralizer in which the particles are exposed to an electrically neutral ambipolar ion cloud produced by an ionizing radiation source, e.g., a sealed capsule of  $^{85}\text{Kr}$ .<sup>40, 142</sup> Initial experiments revealed that the high particle concentrations in the stream exiting the present reactor led to unacceptable coagulation within the large volume of the neutralizer. Instead of passing the aerosol through the neutralizer, a portion of the aerosol was mixed with particle-free  $\text{N}_2$  that had been processed through the neutralizer.

Experiments were performed at a range of ratios of the ion-rich  $\text{N}_2$  diluent to aerosol to ensure that this new charging system results in an asymptotic charge distribution as predicted by the Fuchs charging model, although detailed characterization of this approach is beyond the scope of the present study. Figure 2.3 shows the total number concentrations measured using the RDMA (Radial Differential Mobility Analyzer) and corrected for dilution as a function of the dilution ratio. The Fuchs steady-state charge distribution was assumed in this evaluation, so the concentration estimates can be considered quantitative only at dilution ratios greater than 3:1 ( $\text{N}_2$  from neutralizer to aerosol from reactor) where the concentration approaches an asymptotic value. The observation that the inferred concentration does not change with increased dilution beyond this value strongly suggests that the desired steady-state charge distribution has been achieved. All observations reported below were made with a neutralizer dilution ratio of 7:1.

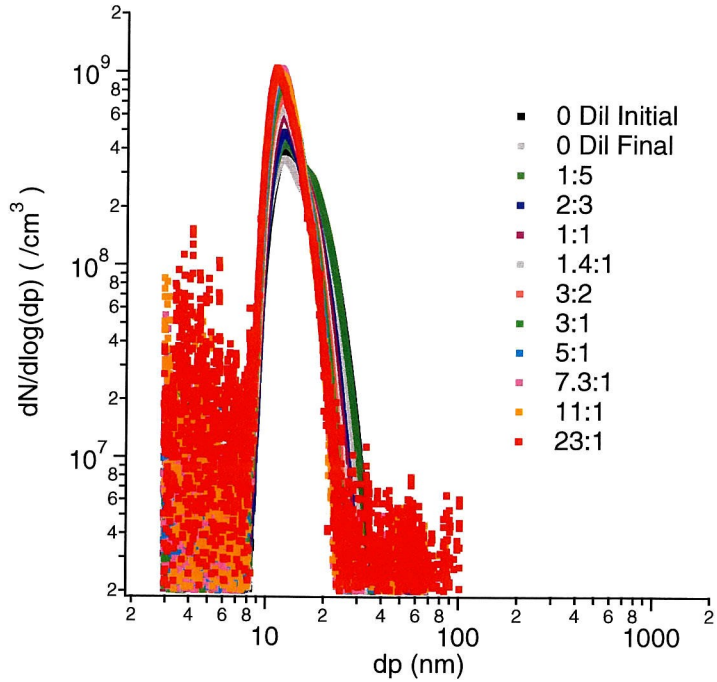


Figure 2.3: Asymptotic particle distribution measured, assuming steady state charge distribution on particles, with various ratios of ion rich gas well mixed with particles.

Particles from the remaining aerosol were deposited, by electrostatic precipitation (ESP) or thermophoretic deposition, on pieces of Si or Ge wafers, or on transmission electron microscope (TEM) grids for subsequent analysis and study. A Philips 430 Transmission Electron Microscope was used to probe particle structure and crystallinity.

## 2.5 Results

Particle concentrations as high as  $10^9 \text{ cm}^{-3}$  were recorded with a mean size of 10–12 nm and a geometric standard deviation,  $\sigma_G$ , of 1.25. Greater monodispersity ( $\sigma_G$  of 1.1) is seen at concentrations as high as  $5 \times 10^8 \text{ cm}^{-3}$ . TEM analysis of particles grown with a thermally oxidized shell shows that particles are spherical, have crystalline silicon cores of 4–6 nm and have an amorphous oxide layer of thickness 2–3 nm. Particles imaged by TEM demonstrate a diffraction pattern characteristic of silicon and show strong contrast

under darkfield illumination. High resolution TEM (HRTEM) images of particles show characteristic lattice fringes in the core region, further evidence for crystallinity and core size.

TEM images of oxide-coated silicon particles are shown in Figs. 2.5–2.5. These particles are highly agglomerated during passage through an aerosol neutralizer ( $\sim 10$  s) and collection time in the ESP ( $\sim 10$  min). In Fig. 2.4(a), particles collected by electrostatic precipitation on a holey carbon TEM grid are shown. These corresponding brightfield and darkfield images were taken at a magnification of 200 K. The intensity of the darkfield image, resulting from diffraction of the electron beam off crystal planes, reveals that particles are similar in their morphology. The narrow size distribution measured with the DMA is qualitatively confirmed in these images. In Fig. 2.4(b), HRTEM images at 550 K magnification shows several cold-agglomerated particles with a crystalline core of 4–6 nm and a non-crystalline shell of 2–3 nm. The thickness of the shell is consistent with a thermally grown oxide layer, rather than a native oxide, which typically yields a 1–2 nm thick layer, dependent upon time of exposure to ambient air. With HRTEM, particles must be in a correct orientation (e.g., near the [111] plane for silicon) for lattice fringes from crystals to be seen, so only a small fraction of the randomly oriented particles show lattice fringes but the diffraction intensity seen in the darkfield image, Fig. 2.4(a), reveals that most, if not all, particles possess a crystalline core. Figure 2.4(c) shows a diffraction pattern of these particles using a selected area diffraction (SAD) aperture of  $20\mu\text{m}$ . The multiple spot pattern seen in a ring attests that the few particles within the field of the aperture view are both crystalline and randomly oriented on the grid surface. Figure 2.5 shows an HRTEM image of particles collected at a much lower number density where the lattice fringes are more clearly visible.

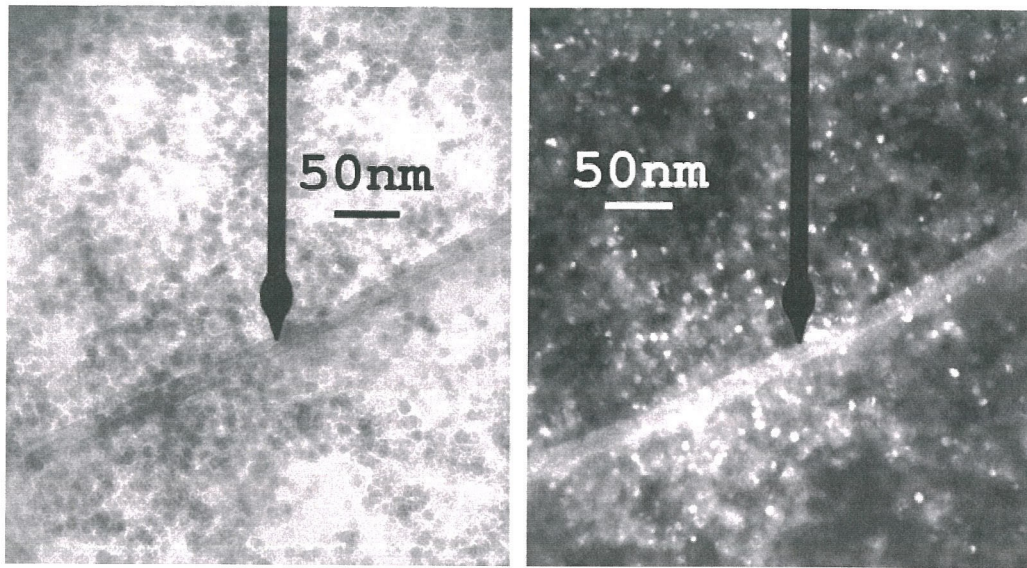
Figure 2.6 shows particles that were not sent through a neutralizer before being collected by electrostatic precipitation on a TEM grid. These particles, nearly 10 nm in size, are highly monodisperse, spherical, crystalline, and generally deposited as single particles rather than non-coalesced doublets, triplets, or fractal agglomerates. Avoiding the relatively long residence time in a neutralizer prevents significant cold agglomeration. The particles also appear to show a tendency to collect in a hexagonal monolayer array. An inset of the diffraction pattern is included to illustrate particle crystallinity.

The size distributions measured using the RDMA are extremely narrow, as shown in Fig. 2.7(a). Some agglomeration is apparent in the size distributions. Since the particles have already been shown to be dense, it appears likely that the second (larger diameter) peak results from coagulation of the smaller particles. For a constant inlet flowrate and silane concentration (150 ppm), the number concentration in the second peak is larger, relative to that of the smaller particles, for a quenching flow ratio of 5 : 1 than when larger quenching flow ratios are employed, but little difference is seen between the results at 7 : 1 and 10 : 1 quenching flow ratios. Since the number concentration measured is affected by the total flowrate, Fig. 2.7(b) shows the distributions normalized by the peak concentration to more clearly illustrate the effect of increased agglomeration. Particle size tended to increase and the distribution broadened when flow rates were decreased. Fitting the first peak, Fig. 2.8, to a log-normal size distribution reveals a value of  $\sigma_G$  of 1.1, much smaller than that of the self-preserving distribution produced by free-molecular coagulation ( $\sigma_G \approx 1.45$ ).

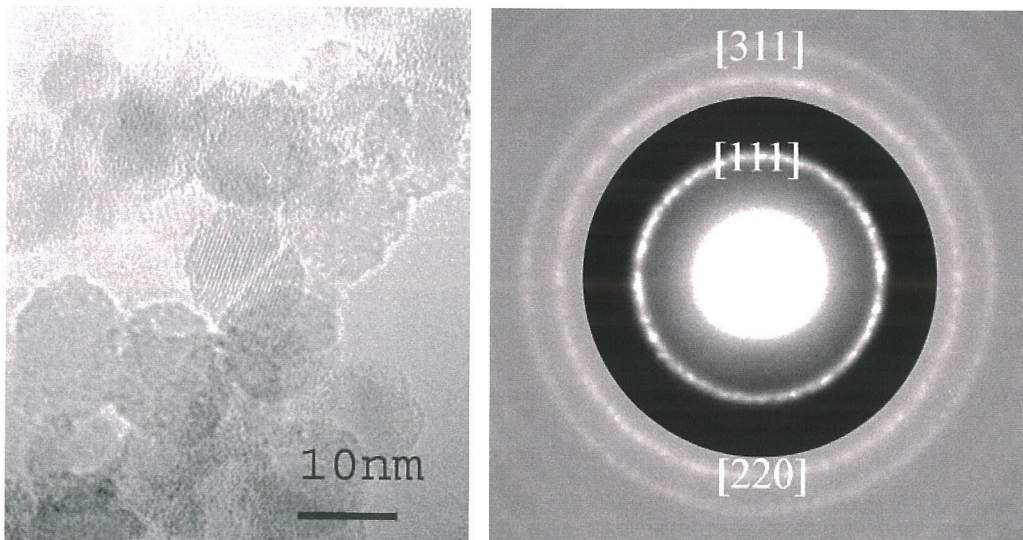
Increasing the precursor concentration to the point that nucleation produced particle concentrations beyond the agglomeration limits of the nucleation or sintering zones leads to broader size distributions as is shown in Fig. 2.9. Large excesses of precursor yields a self-preserving particle size distribution. At intermediate concentrations, the particle dis-

tribution is bimodal, with a second peak arising due to doublet particle formation. This second peak dominates as precursor concentration is increased. Non-densified doublet formation likely occurs near the end of the densification zone where the introduction of oxygen turns off surface diffusion or exit cooling slows surface diffusion. The resulting doublets have lower electrophoretic mobilities, producing a discrete shift from the original distribution.

With the present small reactor, the number of particles produced declines over time, as illustrated in Fig. 2.10. Both  $\text{SiH}_4$  and small Si clusters diffuse to the reactor walls and are lost, especially in the nucleation region. As dendritic structures form and build the tubing becomes choked and the particle-containing flow through the deposition area increases in velocity. Nucleation is pushed farther into the reactor towards the quenching jet, reducing particle numbers and decreasing particle size. Eventually, the reactor walls are completely fouled and all flow is impeded. With a reactor constructed from Inconel, performance is restored by mechanically cleaning the internal walls of the reactant feed tube using a drill bit.



(a) Brightfield and Darkfield TEM Images of 10–12 nm oxide-coated silicon nanoparticles. Crystallinity of the majority of particles is confirmed by darkfield image.



(b) HRTEM Image of 10–12 nm oxide-coated silicon particles similar to those from Fig. 2.4(a). These agglomerated, fractal-like whiskers were subject to charging and charge induced movement in the electron beam. Lattice fringes are evident in the core of a correctly oriented and focused particle.

(c) Selected Area Diffraction pattern of 10–12 nm particles such as the ones seen in Figs. 2.4(a)–2.4(b). Center spot and first diffraction ring, (111)-plane, are contrast-adjusted darker and inset within contrast-adjusted lighter outer rings. A discontinuity of contrast appears at the edge of the inset.

Figure 2.4: TEM images from brightfield, darkfield, HRTEM, and SAD of silicon nanoparticles from the mixing reactor.

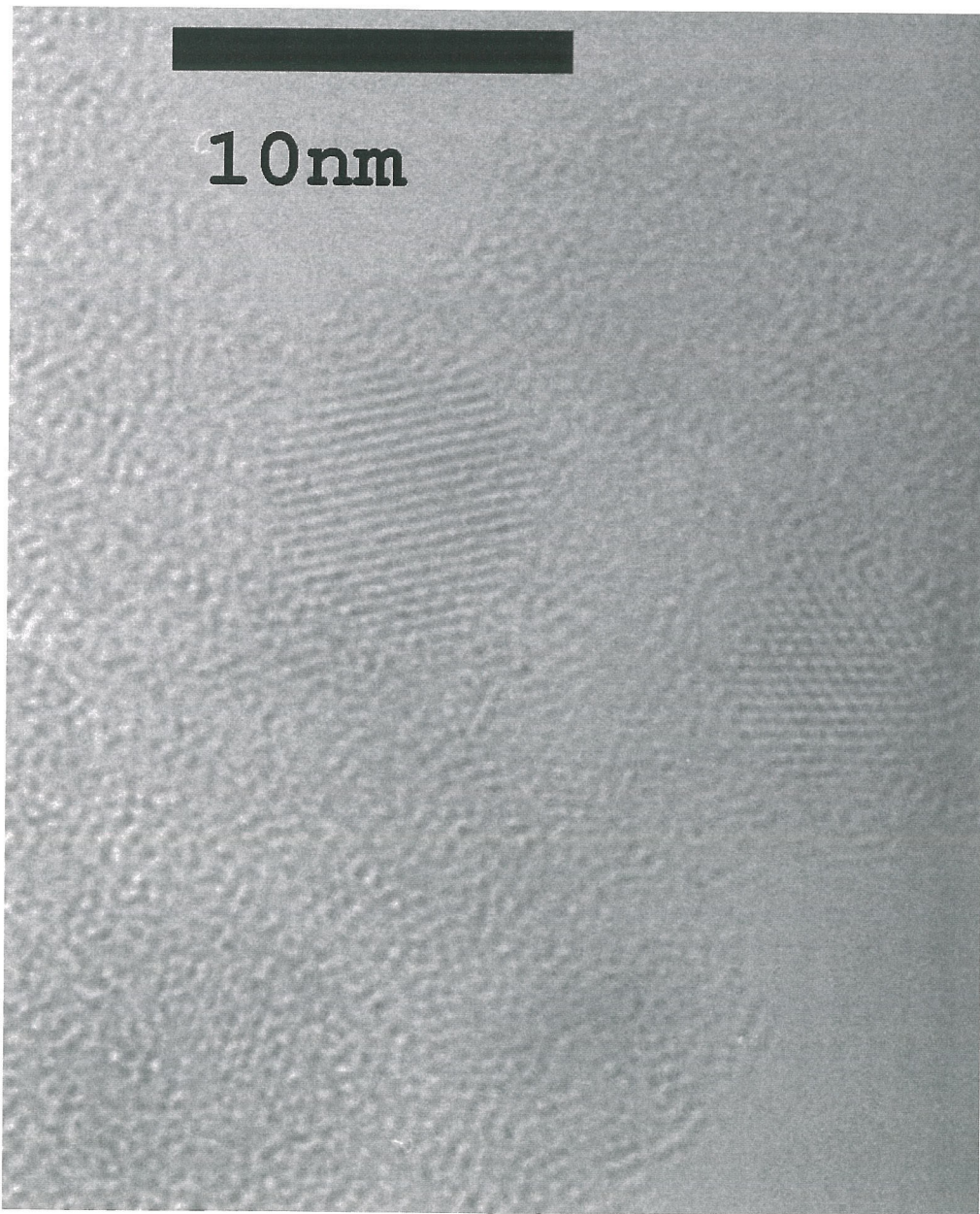


Figure 2.5: HRTEM image of 8–12 nm oxide-coated silicon particles collected at reduced concentration.

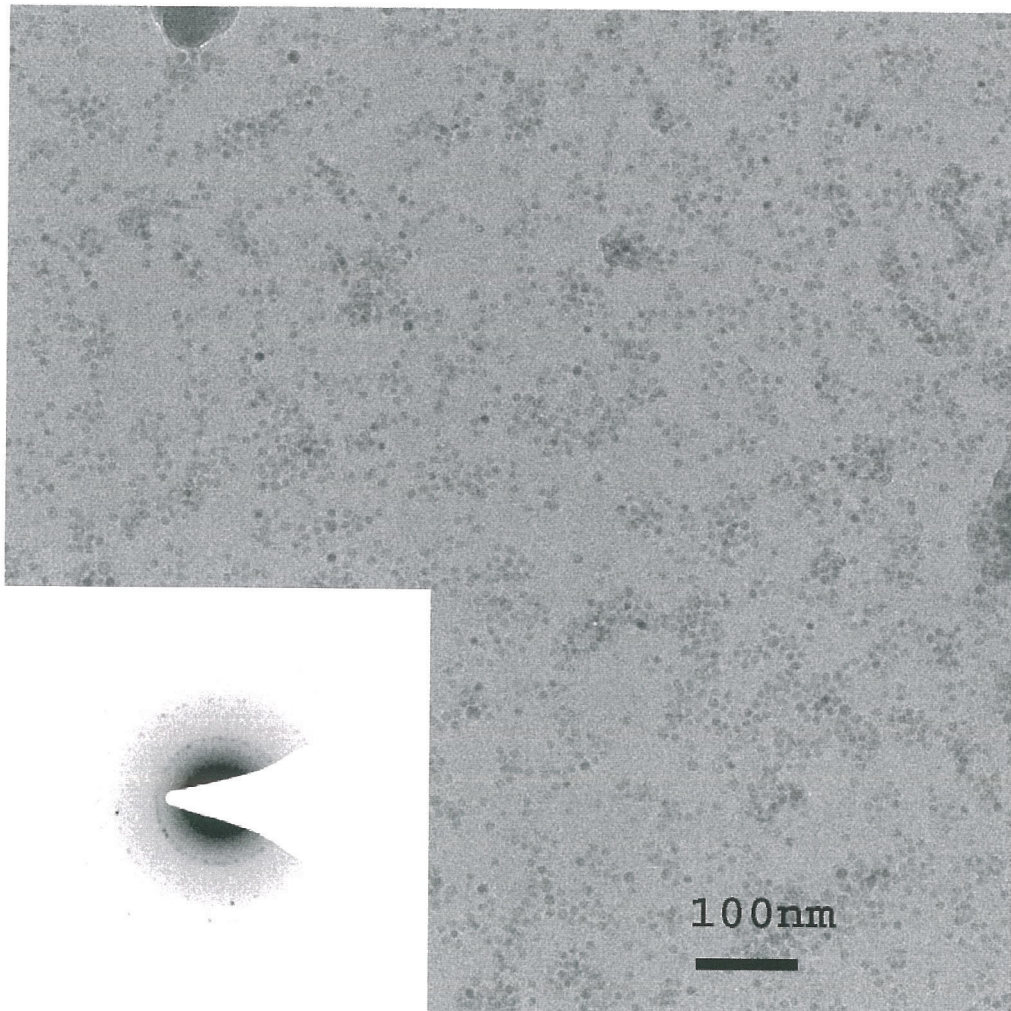
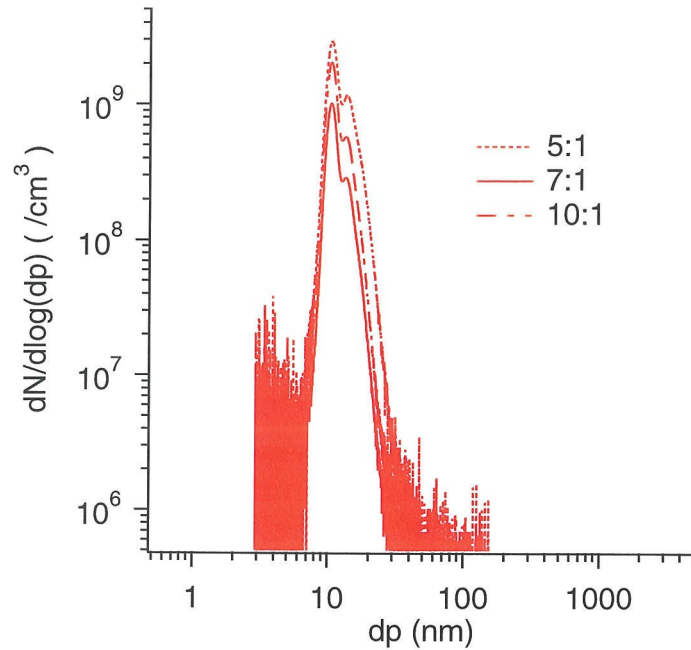
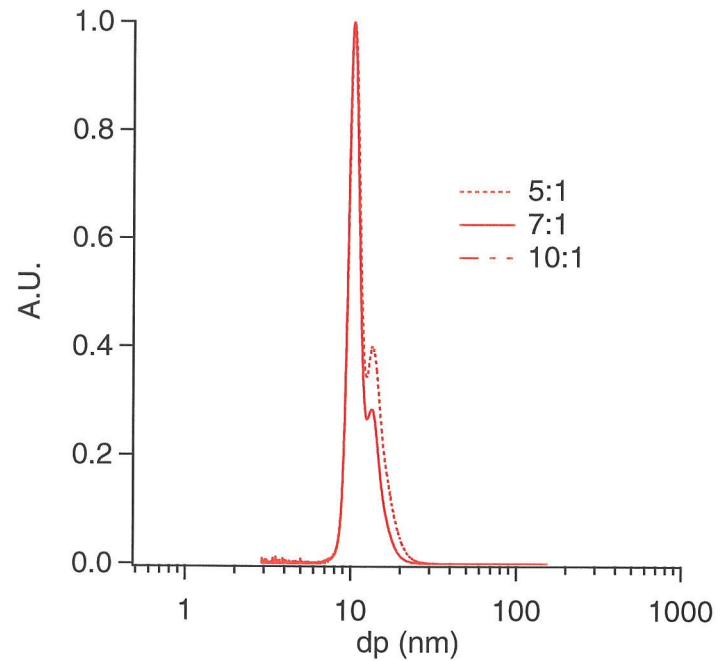


Figure 2.6: TEM Image of 10–12 nm particles collected by electrostatic precipitation on holey carbon grid. Note uniformity of size and occasional grouping of particles in close-packed structures. Inset SAD diffraction pattern from randomly oriented nanocrystalline silicon.



(a) Effect of  $N_2$  dilution at first mixing jet on particle distribution



(b) Normalized particle distributions seen in 2.7(a)

Figure 2.7: Effect on measured particle distribution of varying quenching flow ratio on particle distribution for 150 ppm SiH<sub>4</sub> in 270 sccm N<sub>2</sub>. Normalized trace on right shows relative effect of quenchrate/dilution on the particle distribution normalized by the peak concentration. The 10:1 and 7:1 traces overlay each other.

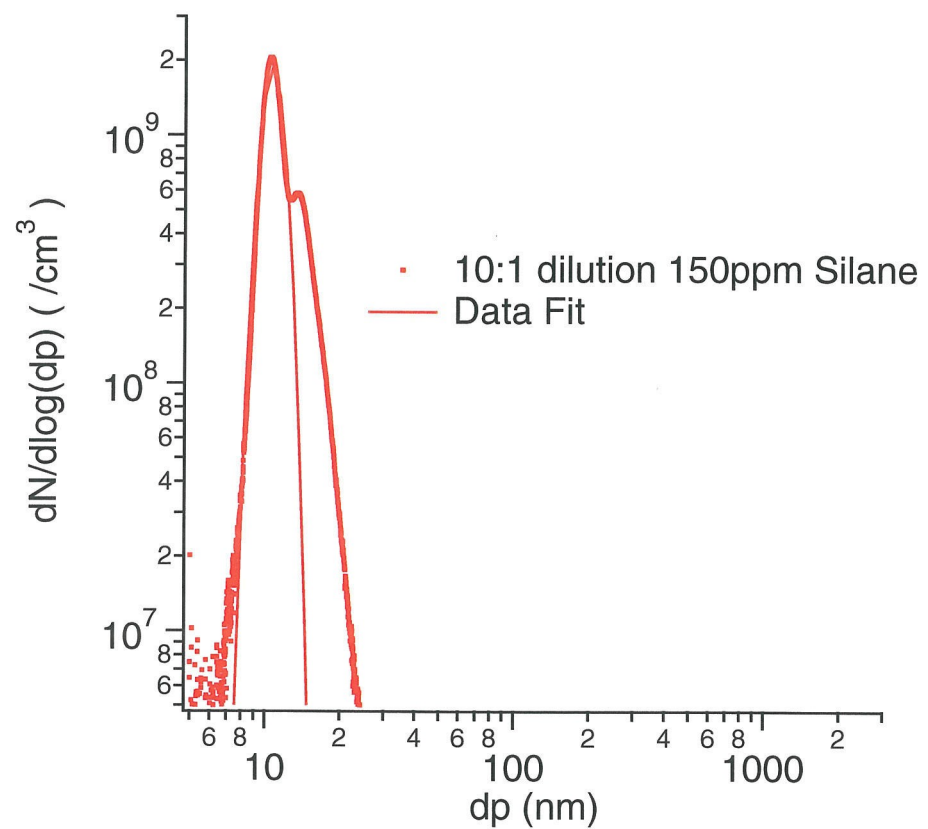


Figure 2.8: Curve fitted to left mode of a particle distribution with geometric standard deviation of 1.1. Decreasing precursor concentration removes the right mode.

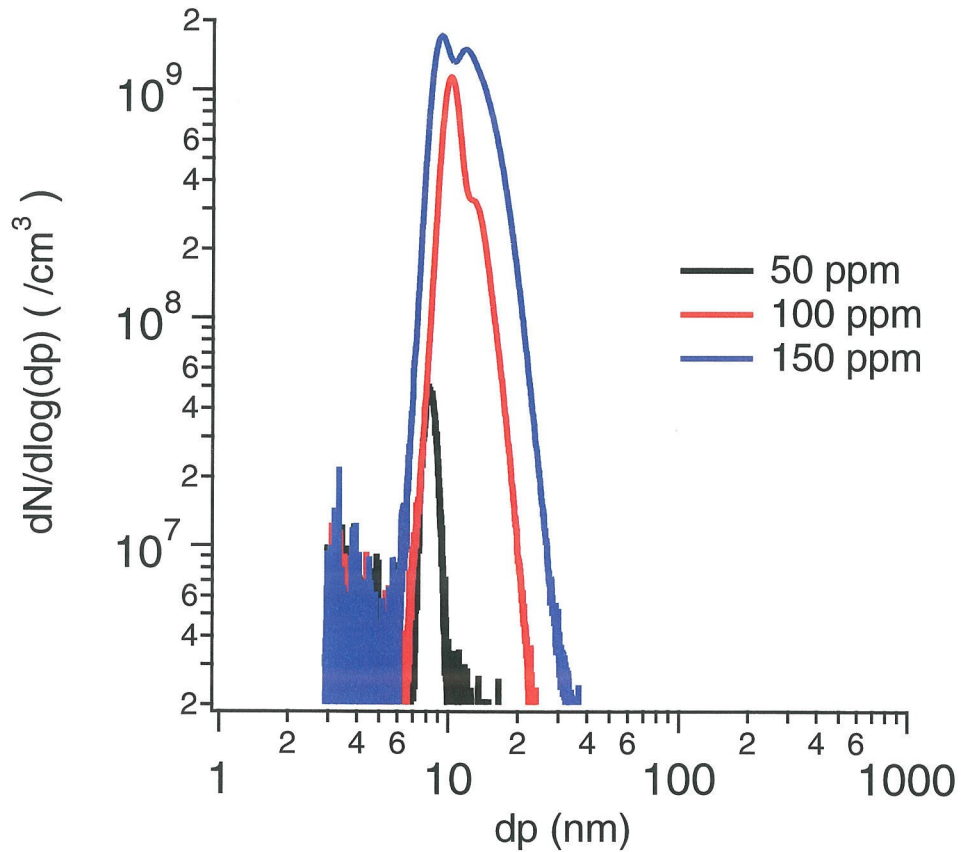


Figure 2.9: Shift in size distributions of particles characterized by radial DMA as precursor concentration is varied. The second mode in the 100 ppm trace is likely the rise of doublet particles. At 150 ppm, agglomeration of particles is overwhelming the monodispersity of the distribution.

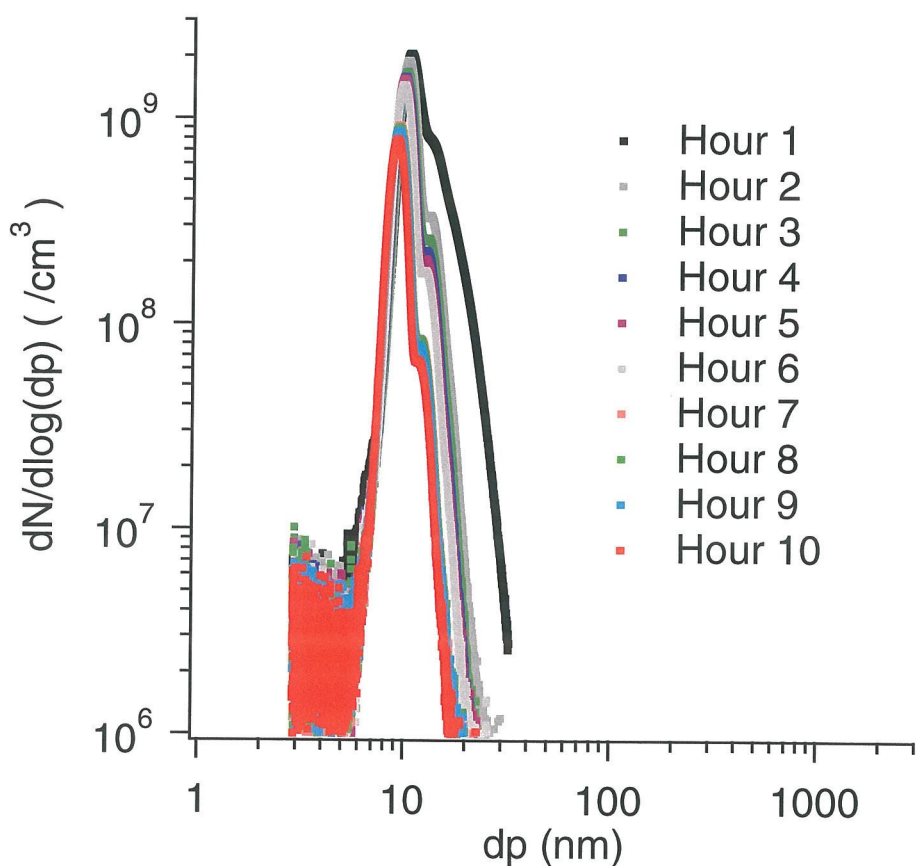


Figure 2.10: Decrease in size and numbers of silicon particles as reactor fouls.

## 2.6 Discussion

The experiments described above demonstrate the potential of this new reactor to produce nanoparticles with very narrow size distributions and carefully tailored structures, but much remains to be done. The reactor demonstrated in this initial implementation suffers serious losses that cause the product particle properties to vary over time and, ultimately, to foul the reactor. This fouling is an artifact of the construction of this small prototype reactor; active cooling of the feed gas could prevent reaction in the feed tube upstream of the larger mixing zone of the reactor. Maintaining reactor walls above the mixed gas temperature could further inhibit fouling by inducing thermophoretic diffusion radially inward, away from the reactor wall.

While preheating the silane led to undesirable deposition and fouling in this present experiment it also suggests a possible reason for the narrow size distribution observed with this reactor. Turbulent mixing of unreacted silane, nuclei produced as a result of a reaction in the feed tube, and preheated carrier gas rapidly produced a homogeneous gas containing nuclei at a concentration that is low enough to inhibit coagulation, but large enough to inhibit additional nucleation. These nuclei then served as seeds for particle growth by vapor deposition, a mechanism that produces size distributions that are much narrower than those resulting from growth by Brownian coagulation.

The kinetics of silane decomposition accelerate dramatically when the temperature exceeds about 1000 K, leading to homogeneous nucleation that produces number concentrations high enough for coagulation. Quenching nucleation before significant coagulation occurs leaves seed particles subject to further growth by vapor deposition and may lead to retained narrowing of the size distribution. This effect has previously been observed in

laminar flow particle synthesis reactors.<sup>146</sup> Here we show evidence that such narrowing is possible in turbulently mixed reactors.

A second fouling mechanism occurs in the nucleation zone. In the small reactor described here, thermal conduction from the primary reaction zone heats the precursor inlet tube. Some of the precursor vapors react on the tube walls; more react in the gas phase, producing particles by homogeneous nucleation in the laminar tube flow. Some of the resulting particles can deposit on the walls of the small feed tube by Brownian diffusion. Moreover, since the reactor wall is hotter than the core of the flow, the temperature gradient might be expected to be favorable for thermophoretic diffusion of particles toward the reactor center. Instead, latent heat release from silicon condensation as particles form and condense can adversely affect the actual local gradient,<sup>108</sup> although the low concentrations used in the present experiments are likely to minimize this effect. Preliminary experiments were performed using a quartz reactor that enabled direct observation of the dendritic structures that formed over time. As these structures form, they filter particles from the flow, enhancing deposition. The deposits could not be observed directly within the welded Inconel reactor, but the degraded reactor performance after extended operation could be returned to its initial state by mechanical cleaning.

In the present apparatus, the average residence time,  $\tau_{R,nucl}$ , from onset of silane decomposition at ( $\sim 1000$  K) to dilution at the first mixing jet is approximately  $\sim 25$  ms. First order estimates of particle coagulation suggest that the number concentration should decrease to  $5 \times 10^{10} \text{ cm}^{-3}$  in this time. The maximum number concentration measured, after a total dilution of 12:1 by the two pairs of mixing jets, was  $2 \times 10^9 \text{ cm}^{-3}$ , consistent with this estimated maximum.

Thus, the conduction-induced preheat zone appears to have served as a seed generation

reactor that facilitated production of very monodisperse particles by enabling growth by vapor deposition while suppressing coagulation. Obviously, the present reactor is far from perfect. Design of a reactor that separates the seed nucleation zone from the turbulent-mixing primary reaction zone and that suppresses reaction by cooling precursors prior to injection into that mixing zone could facilitate greater control while suppressing fouling as has previously been shown in laminar flow reactors designed to grow large particles.<sup>5</sup>

Hence, efforts to control particle size and/or increase particle concentration need to focus on optimizing the efficiency of mass transfer through the nucleation zone. One scheme, the addition of a radially inward flow through a micro-porous media would effectively reduce the nucleation zone volume and might alleviate fouling losses, thus maintaining or increasing particle numbers and decreasing particle size. Another scheme is to produce seed particles in a first, fast reaction stage, such as a microdischarge plasma,<sup>113</sup> and then inject them into the hot zone for annealing and further growth by vapor deposition.

Particle deposition at the outlet of the silane introduction tube limited the time that the present reactor could be run continuously. As we have noted above, heat conduction caused silane decomposition to begin within this tube. Resulting homogeneous nucleation produced the seed particles that enabled the growth by vapor deposition within the jet-mixed reaction zone that leads to the very narrow size distributions that we report here, but also fouls the reactor. Thus, the generation of seed particles upstream of the reactor is desirable, but the reactor design must be modified to where the primary precursor (silane) flow is injected into the jet-mixed reaction zone unreacted. Active cooling of the feed tube carrying the precursor can prevent early reaction initiation, although this will be easier to accomplish in a large reactor than the small prototype reactor that we have presented here. If inadvertent early reaction is eliminated, however, a separate source will be needed

to provide the seed particles. Alam and Flagan<sup>7</sup> have previously demonstrated nucleation suppression in seeded aerosol reactors. To synthesize nanoparticles in useful quantities, the seed particles must be much smaller, and the seed concentrations must be much larger than employed in that early work however. This requires fast reaction and short residence time in the seed generation system. We could employ a very small version of the present reactor, one that is designed to eliminate the precursor preheating, but several alternate methods seem promising.

A recently demonstrated microplasma reactor has the potential to produce high number concentrations of very small (1–5 nm) nanoparticles.<sup>113</sup> Laser ablation or laser-induced reaction can also produce rapid reaction within a very small volume. Hybridization of a low-loss seed generator with the jet-mixed reactor described here has the potential to increase the numbers of particles produced and preserve the narrow size distributions demonstrated with the present reactor.

The key feature of the present reactor is the control of the time scale for mixing through the kinetic energy injected into the mixing zone of the reactor. The jet-mixed reactor volume can be increased dramatically above that of the small prototype described here to increase throughput while maintaining the reaction environment of the present system and, at the same time, minimizing the potential for reactor fouling. Previous work with 17 mm diameter quartz tube laminar flow reactors showed visible deposits on the reactor walls but little effect on performance even after hundreds of hours of operation.

Considering the mixing time,  $\tau_m$ , as the critical feature in scale-up for this reactor, Fig. 2.11 shows potential particle production rates in g/hr for a reactor at current production rate  $\sim 10^9 \text{ cm}^{-3}$  of 10 nm particles using the current  $\tau_m \approx 1.5 \text{ ms}$ . Further constraints are limiting  $d_j$  and  $d_t$  to a range from 1 mm–1 m and maximum flow velocity less than Mach

1 at 1000 K. With suitable engineering of the nucleation zone, appreciable quantities of nanoparticles may be expected.

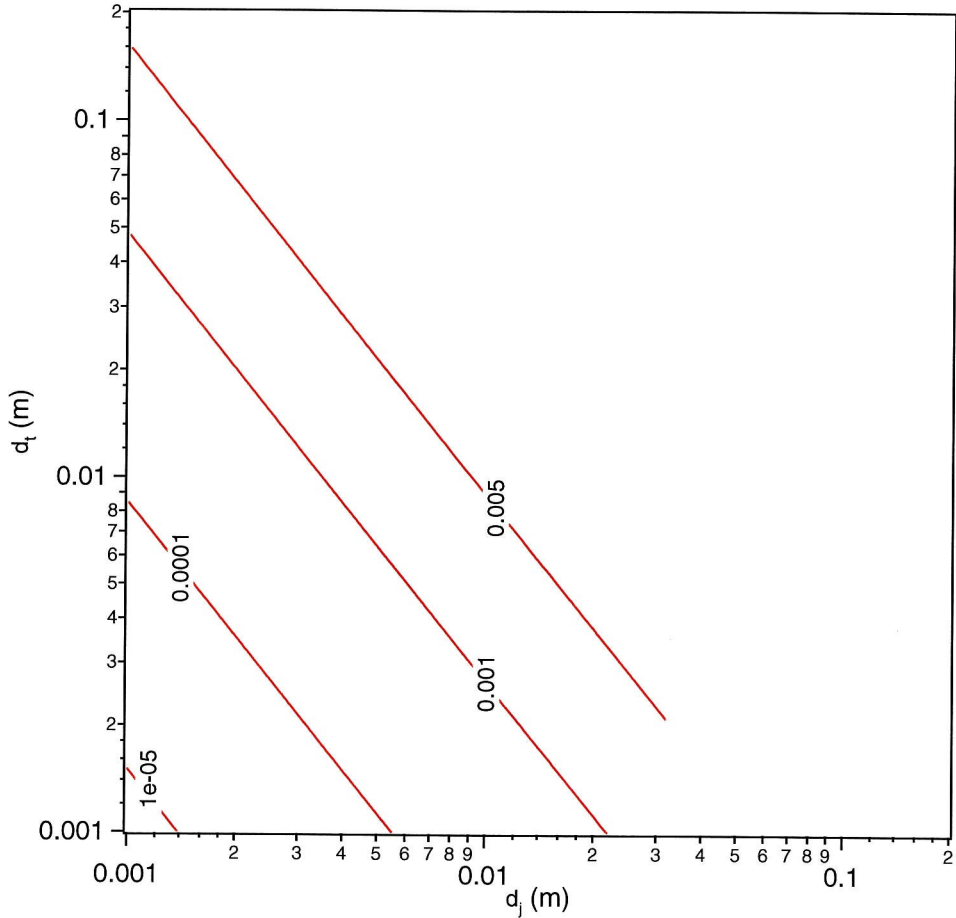


Figure 2.11: Calculated particle production rates (g/hr) for reactor using current  $\tau_m \approx 1.5\text{ms}$ .

## 2.7 Conclusions

An aerosol reactor incorporating turbulent mixing zones has been demonstrated that achieves high number throughput, highly monodisperse crystalline silicon or oxide-coated silicon nanoparticles. This reactor is capable, with suitable precursors and additional mixing zones, of producing onion-skin multilayered particles in quantities approaching the needs of ultra

large scale integration (ULSI) manufacturing. Turbulent mixers within the reactor enhance transport without increasing agglomeration. The product particles are highly monodisperse and consistent in morphology. Particle size is determined by a combination of nucleation rate and residence time within a nucleation zone. Further work to reduce fouling of reactors is needed as transport to the walls of developing nanoparticles is likely enhanced by local thermal gradients. Further investigation into the stability of particle adhesion on surfaces in the face of mechanical, electric, and other stresses is needed to ensure cleanliness of manufacturing facilities.

## 2.8 Acknowledgments

This work was supported by the NSF, grant number ECS-0103543. Special thanks to Carol Garland for assistance in High Resolution Transmission Electron Microscopy.

## Chapter 3

# A Tool for Uniform Coating of 300 mm Wafers with Nanoparticles

### Abstract

We report a laminar flow thermophoretic aerosol deposition tool suitable for depositing aerosol nanoparticles on a flat substrate such as silicon wafers up to 300 mm in diameter. Recirculation is prevented using a power-law hyperbolic-type nozzle that maintains dynamical pressure through the nozzle and remains robust with flowrate approaching 15 slpm. Aerosol coagulation is largely prevented with non-separating flow and high flowrate. Particle deposition is nearly uniform in both radial and azimuthal directions, with less than  $\pm 5.5\%$  variation on a 150 mm wafer. Modeling of the deposition onto a 300 mm wafer predicts similar coverage. Particle coverage is characterized using non-contact AFM imaging.

### 3.1 Introduction

Semiconductor nanoparticles have attracted interest for a wide range of applications that take advantage of the special features that these materials acquire when fabricated into nanoscale structures. At sizes from sub-nanometer to a few tens of nanometers, quantum mechanical effects alter the optical and electronic properties of the semiconductor, produc-

ing quantized energy levels that make them behave as “artificial atoms”<sup>12</sup> or quantum dots whose properties can be tailored by tuning the nanocrystal size. Semiconductor nanocrystals have been used as fluorescent probes in biological imaging and analysis.<sup>20,53,71</sup> Metal and metal oxide nanoparticles have properties to exploit as catalysts<sup>45,46,47,48,62,66,93</sup> and photocatalysts.<sup>11,65,129</sup> Other proposed applications that take advantage of those special properties of semiconductor nanocrystals include light emitting diodes,<sup>27,29,42,137</sup> optical amplifiers<sup>69</sup> and lasers,<sup>86</sup> optically addressed memory,<sup>138</sup> and single-electron transistors.<sup>72</sup>

While applications of nanocrystals that take advantage of quantum size effects have received considerable attention, device fabrication remains a significant challenge due to difficulties of controlling nanocrystal size and placement, particularly with materials that are compatible with today’s device fabrication infrastructure. Preventing process and tool contamination remains a major challenge when exotic materials or colloidal synthesis is considered, even though colloidal nanoparticles have been synthesized with precise control of size and optical properties for a wide range of materials, including silicon.<sup>34,59,104,120</sup>

Nevertheless, nanoparticle-based microelectronic devices have been fabricated without adverse effects on processing tools, albeit for less exotic applications. Tiwari and coworkers<sup>130</sup> proposed a silicon nanocrystal-based memory to overcome the charge leakage that plagues conventional floating gate devices as they are scaled into the sub-100 nm size regime. Both devices are metal oxide semiconductor field effect transistor (MOSFET) structures that incorporate a floating gate to store charge. In the conventional device, the floating gate is a continuous semiconductor layer that is separated from the silicon substrate by a thin barrier tunnel oxide. To store or erase information, charge is induced to tunnel through an oxide layer into the floating gate. Unfortunately, any leakage path between the floating gate and the underlying channel will eventually dissipate all the stored charge.

Tiwari's floating gate of isolated nanocrystals reduces the probability of complete information (charge) loss by separating the floating gate into a number of isolated storage elements within each transistor. The devices were fabricated by spontaneous decomposition during chemical vapor deposition. Feng<sup>35</sup> et al. have produced nanocrystals in the floating gate by thermal annealing after ion implantation. Neither method affords direct control over the particle size distribution. Moreover, at least in the case of ion implantation, in-situ nucleation leads to a distribution of nanocrystals through the depth of the gate oxide.<sup>18</sup> The resulting variability in the nanocrystal-to-channel spacing leads to a distribution in leakage current over the area of the transistor. Ion implantation leads to a distribution of nanoparticle sizes at different depths,<sup>18</sup> presenting a challenge in obtaining a uniform tunneling distance between the gate and the nanocrystal.

Ostraat<sup>101</sup> demonstrated an alternate approach to creating a nanocrystal floating gate MOSFET. Silicon nanoparticles were produced as an aerosol by gas-phase thermal decomposition of silane. The silicon nanoparticles were then oxide passivated while still suspended in the carrier gas. The oxide layer was created on the aerosol nanoparticles in two ways: (*i*) by chemical vapor deposition of tetraethylorthosilicate (TEOS), or (*ii*) by high temperature oxidation (HTO) of the surface of the aerosol silicon nanoparticles. After oxide passivation, the core/shell nanoparticles were deposited by thermophoretic diffusion onto a previously prepared tunnel-barrier oxide on 200 mm diameter silicon wafers. The HTO-passivated nanoparticles met the stringent contaminant limits and were processed to produce high performance devices through an industrial fabrication facility.<sup>102</sup>

Although the devices produced by Ostraat et al. showed excellent performance characteristics and demonstrated that aerosol-synthesized silicon nanocrystals can safely be taken through conventional device lithography and etching processes, many aspects of the

synthesis require further development before such processes see commercial applications. Foremost is discomfort of tool owners with taking particle laden wafers into the fabrication facilities, a problem that will require addressing a number of real and imagined hazards to the process equipment. Questions about the entrainment of nanoparticles from wafer surfaces<sup>105,111,112,123,124</sup> and, especially, about the existence of agglomerates that might more easily detach can only be addressed once suitable nanoparticle-coated wafer samples can routinely be processed for testing.

The original nanoparticle synthesis employed a low-throughput, multistage laminar flow aerosol reactor that enabled precise control of the size and structures of the product nanoparticles, but that produced relatively low number concentrations,  $1 \times 10^6 - 3 \times 10^6 \text{ cm}^{-3}$ , in 1500 sccm carrier gas flowrates. Nanoparticle coverage of a 200 mm wafer, dense at the center and sparse near the edge, required from 4–12 hours for each wafer, far too long for a production process. Extension to similar coverage of the 300 mm wafers would, at a minimum, double this deposition time.

Numerous groups have demonstrated much higher nanoparticle synthesis rates than that of Ostraat. Flame synthesis<sup>95,106,125,133</sup> reactors produce hundreds of grams per hour in the laboratory, and kilograms or more in industrial reactors, but are not suitable for the materials of interest here. Laser-induced decomposition<sup>17,25,26</sup> and plasma synthesis<sup>75,109</sup> can produce large quantities of silicon or other non-oxide nanoparticles, but the precise control of the state of agglomeration achieved by Ostraat et al. remains a challenge. Recently, Holunga<sup>60</sup> et al. demonstrated a higher throughput multistage reactor that employs turbulent mixing and short residence times to improve on the particle properties achieved in the laminar flow aerosol reactor. The short residence time allows number concentrations as high as  $10^9 \text{ cm}^{-3}$  to be processed with minimal agglomeration. The resulting

heterogeneous core/shell Si-SiO<sub>2</sub> aerosol nanoparticles provide an enabling technology for accelerated nanoparticle device processing.

While the deposition chamber used in early aerosol nanoparticle device synthesis demonstrated the potential of the approach, the areal density of deposited nanoparticles varied significantly over the surface of the wafers. While this proved useful in initial studies of device properties by enabling a range of devices to be produced in a single experiment, production tools will have to produce deposits that are uniform over the entire surface of larger (300 mm) production wafers.

The present paper focuses on the latter challenge. The discussion that follows reports on the design and characterization of a nanoparticle deposition tool for coating of 300 mm silicon wafers with aerosol-synthesized core/shell nanoparticles produced using the multistage turbulent mixing aerosol reactor.

### 3.2 Design

The deposition chamber, illustrated schematically in Fig. 3.1, consists of two radially mounted parallel plate heating and cooling surfaces. The aerosol is introduced and removed orthogonally through  $\frac{1}{2}$ " OD SS tubing at the center of the wafer. Three concentric heat sources provide a nearly uniform heat flux to the top plate. The bottom plate is cooled using a heat transfer fluid.

For radially outward, isothermal flow of a Newtonian fluid between flat plates, and in the creeping flow limit, the velocity profile as a function of  $z$  (height) and  $r$  (radius) is,<sup>13</sup>

$$v_r(r, z) = \frac{3Q}{4\pi r Z} \left(1 - \left(\frac{z}{Z}\right)^2\right) \quad (3.1)$$

where  $Q$  is the volumetric flowrate,  $z$  is the normal distance from the midplane between the plates, and  $Z$  is half the distance between the plates. This profile remains only approximately valid if a small temperature gradient exists between surfaces; however, for a small  $\Delta T$  at relatively large absolute  $T$ , the important characteristic remains that the velocity in the radial direction decreases as  $\frac{1}{r}$ .

The thermophoretic velocity for ultrafine particles,  $v_{th}$ , can be described as,<sup>38</sup>

$$v_{th} = -Th \frac{\mu}{\rho T} \frac{\partial T}{\partial z} \quad (3.2)$$

where  $\rho$  is the density,  $\mu$  is the viscosity of the effluent gas,  $T$  is the absolute temperature, and  $z$  is the coordinate of directional movement. The dimensionless number,  $Th$ , has been experimentally determined to be about 0.5.<sup>39</sup> If the absolute temperature is relatively high enough and the temperature gradient remains similar between the plates at all radial positions, then the  $z$ -axis thermophoretic velocity is nearly constant throughout the chamber.

The surface area being covered increases as the flow expands radially outward from the center of the wafer.

$$\frac{\partial A}{\partial r} = 2\pi r = C(r) \quad (3.3)$$

Since the deposition rate needed is proportional to both  $v_{avg}(r)$  and  $C(r)$ , while the velocity of the feed particles is decreasing with  $\frac{1}{r}$ , any  $r$  dependency in deposition can be eliminated using radial geometry. Ignoring Brownian diffusion, a constant deposition velocity from the  $Z$  direction should yield a homogeneous deposition flux at all locations on the wafer. With a robust design allowing flexibility in adjusting flowrates and temperature gradient, a suitable operating condition can be reached that would yield uniform deposition.

The critical feature for this deposition chamber is ensuring non-separating laminar flow through the nozzle and preventing recirculating flow. Aerosol in recirculation zones may agglomerate and either deposit on the chamber walls or re-enter the deposition flow and be driven to the collection surface in a non-desired size and configuration.

The nozzle shape was determined using a potential flow argument, in rectilinear coordinates, for stagnation flow around a corner. This approximation is locally valid as the nozzle begins to bend since the boundary layer is developing through the radius of the bend and also outward from the stagnation point above the wafer, approximating open channel non-viscous flow. In physical terms, the combination of a larger diameter inlet tubing, a small power-law hyperbolic nozzle (small change in  $r$ ) and a narrow gap allowed the flowfield to be approximated in rectilinear coordinates. The classical fluid flow field for an open channel incompressible laminar flow field around an L-shaped corner can be described by the vector equation,

$$\hat{v} = Ax\hat{i} - Ay\hat{j} \quad (3.4)$$

where  $x$  and  $z$  are the coordinates and  $A$  is an arbitrary constant dependent on the volumetric flowrate within the dimensions of the structure. The flow field solution is a hyperbolic family of streamlines,  $\psi = xy$ , wherein the channel width  $w$  (from the  $y$ -axis) is identical to channel height  $h$  from the  $x$ -axis. By symmetry, a point on a curve at  $\psi(a, b)$  is also on the same streamline at  $\psi(b, a)$ . Each streamline acts as a "pressure" wall to the fluid on either side of the streamline. A physical wall could be inserted without altering the streamfunction. The streamfunction for nonequal channels,  $w \neq h$ , is such that a fluid element entering at  $(wx_o, hy_o)$  might be constrained to find the point  $(wy_o, hx_o)$  on the way out. If

so, the vector flowfield above is transformed,

$$\hat{v} = Awx\hat{i} - Ahy\hat{j}. \quad (3.5)$$

Using the streamfunction approach with,

$$-\frac{\partial\psi}{\partial x} = v_y = -Aw y \quad (3.6)$$

$$\frac{\partial\psi}{\partial y} = v_x = -Ah x \quad (3.7)$$

yields the separable differential equation,

$$\frac{\partial y}{\partial x} = \frac{w}{h} \frac{y}{x} \quad (3.8)$$

and a solution of the form,

$$xy^{-\frac{h}{w}} = Constant \quad (3.9)$$

which describes a family of power law hyperbolic-type streamlines. A properly chosen streamline can be used to form the equation for the nozzle curve, with the nozzle shape described as,

$$\psi = \psi_o = (x - x_o)(y - y_o)^{-\frac{h}{w}} \quad (3.10)$$

provided that dynamical pressure inequalities do not lead to flow separation. This stipulation simply requires that the maximum flow velocity be essentially unchanged through the bend as the fluid leaves the nozzle and begins to traverse the deposition surface.

In 2D axisymmetric flow, i.e., cylindrical coordinates, the streamfunction solution to stagnation flow<sup>39</sup> from a jet is  $Constant = r^2 z$ . In the chamber, the actual ratio of  $\frac{w}{h}$  is

2.65. Applying the offset,  $(x_o, y_o)$  to the rectilinear solution, effectively chose a streamline very close to the axes (small  $r$ ) in which the error in the exponent became negligible.

This curve chosen should also smoothly join with the inlet tubing wall and the top plate of the chamber and be symmetric in the azimuthal. When the maximum flow velocity through the nozzle is similar to the maximum flow velocity of the gas in the inlet tubing, the dynamical pressure varies little, and streamlines remain intact. Acceleration or deceleration of gas through this region would give rise to pressure boundaries beyond which recirculation zones could appear. Particles trapped in recirculation pockets will agglomerate and eventually settle out, preventing homogenous coverage of a surface with particles of equivalent size.

The heater/chamber was modeled in Fluent<sup>TM</sup> using a laminar flow 2-D axisymmetric solver. The dimensions of an actual MDC flange were used in creating the model chamber. Incoming aerosol flow, 1500 sccm, was provided an entrance length sufficient to develop a parabolic velocity profile. The top flange was heated with ring-heaters that were assumed to be able to provide a constant heat flux, Fig. 3.1, or constant temperature, and the water coolant (which would have turbulent flow) was assumed to have heat removal capacity such that the metal in contact with the coolant was only 5–10 K above the incoming water temperature. A 3D  $\kappa - \epsilon$  turbulent model for the cooling water limits was also modeled, Fig. 3.2, wherein 30 lpm of water at 300 K is diverted into two opposing tangentially outward jets to cool 1800 W of energy transferred to the outer surface. The heat transfer coefficient for the top surface included conduction through a zone corresponding to the stainless steel MDC flanges as well as convection into a laminar flow gas. The modeled temperature rise of the coolant is less than 10 K.

With a working nozzle geometry determined, the Fluent<sup>TM</sup> model was run using a

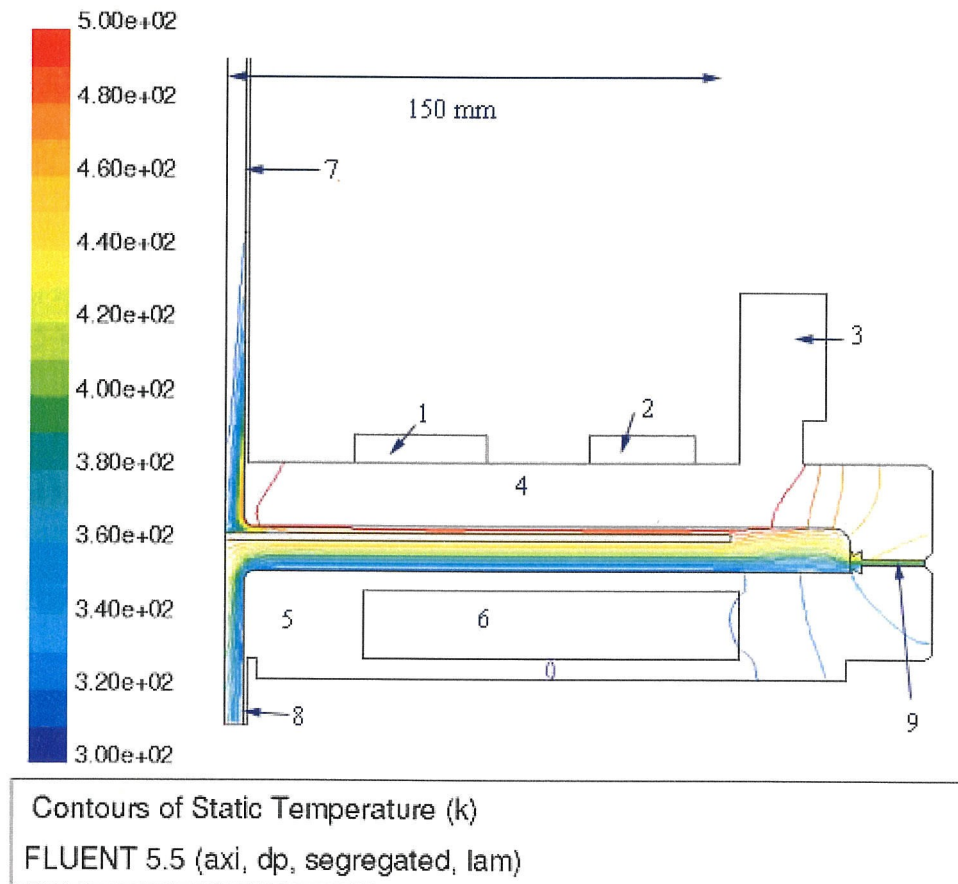


Figure 3.1: Isotherms of deposition chamber modeled in Fluent<sup>TM</sup>. Components of chamber:  
 1. Inner ring heater. 2. Outer ring heater. 3. Band heater and mount. 4. Top MDC SS Flange. 5. Bottom MDC SS Flange. 6. Water cooling chamber. 7. Aerosol inlet. 8. Gas outlet. 9. Viton Gasket. Modeled average current supplied to the heaters (with listed power capacity) as follows: 1. Inner ring heater, 0.4 A/1000 W, middle ring heater, 2. 0.6 A/1500 W, 3. Outer band heater 7.5 A/1500 W.

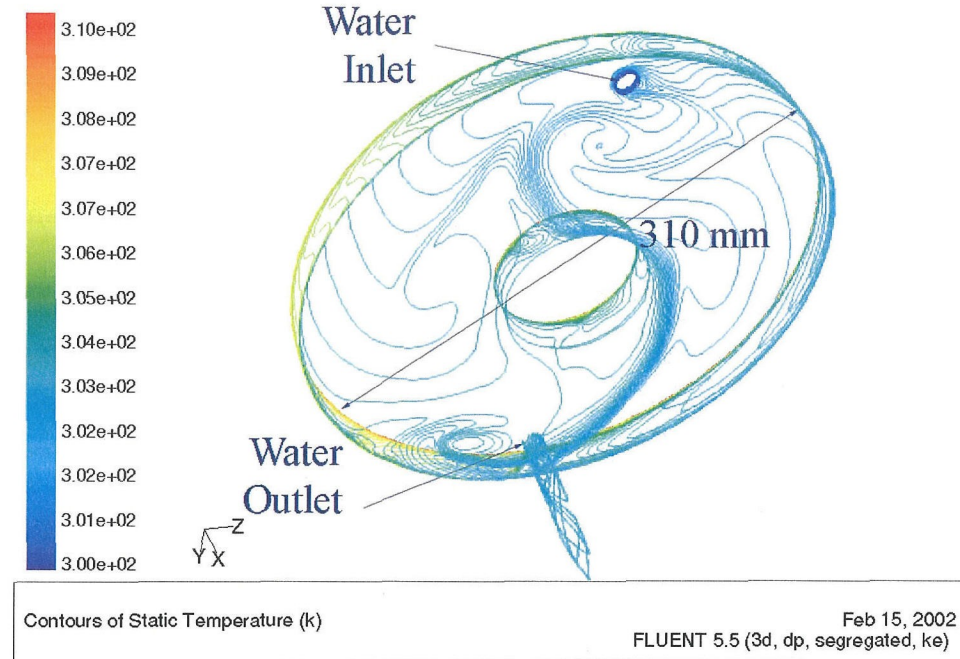
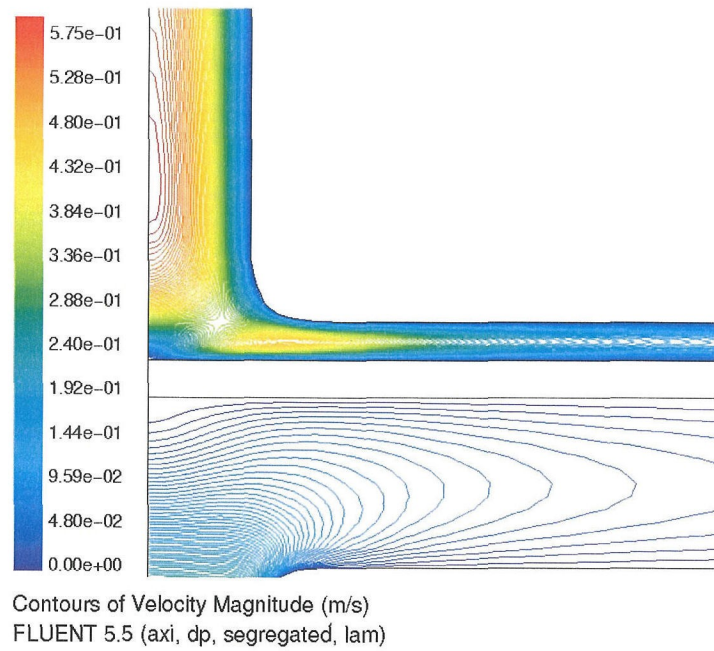


Figure 3.2: Modeled temperature rise for a constant 1800 W heater on the outer band and top of a water-cooled chamber with 30 lpm flowrate.

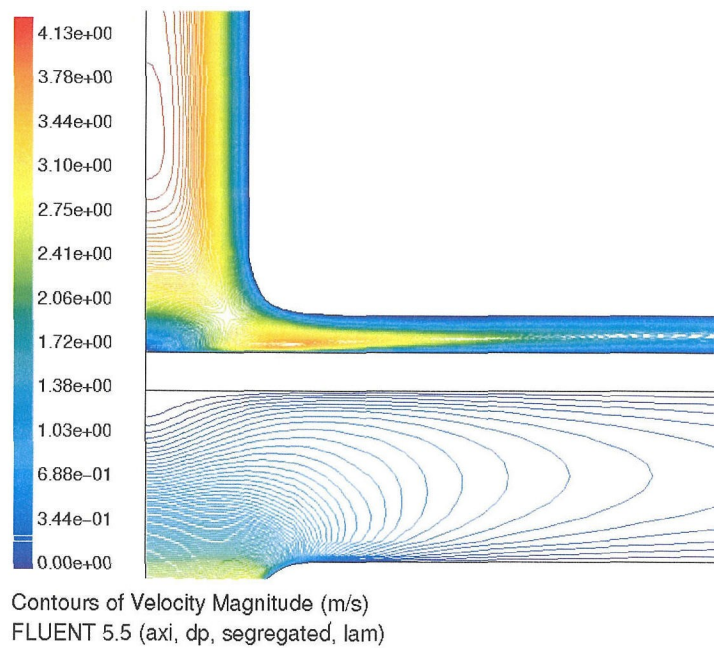
constant flux (power) source for the heaters rather than a constant temperature boundary condition. The necessary conditions of nearly uniform temperature gradient and adequate heat removal were also met in this scenario.

At a concentration of  $10^9 \text{ cm}^{-3}$  monodisperse 10 nm aerosol nanoparticles have a characteristic agglomeration time constant of  $\tau_a \sim 1 \text{ s}$ . The chamber operation must be robust enough to allow for higher flowrates of diluted nanoparticles should agglomeration need to be suppressed during the deposition process. Figures 3.3–3.4 shows modeled velocity profiles of 1500 sccm, 15000 sccm, 30000 sccm, and 60000 sccm. The modeling indicates that flowrates up to 15000 sccm are possible when employing a 2 mm gap between the wafer and heated top plate.

Wafer curvature is commonly seen in large wafers exposed to thermal gradients such as those found in plasma etch processes. The potential of having wafer curvature arising

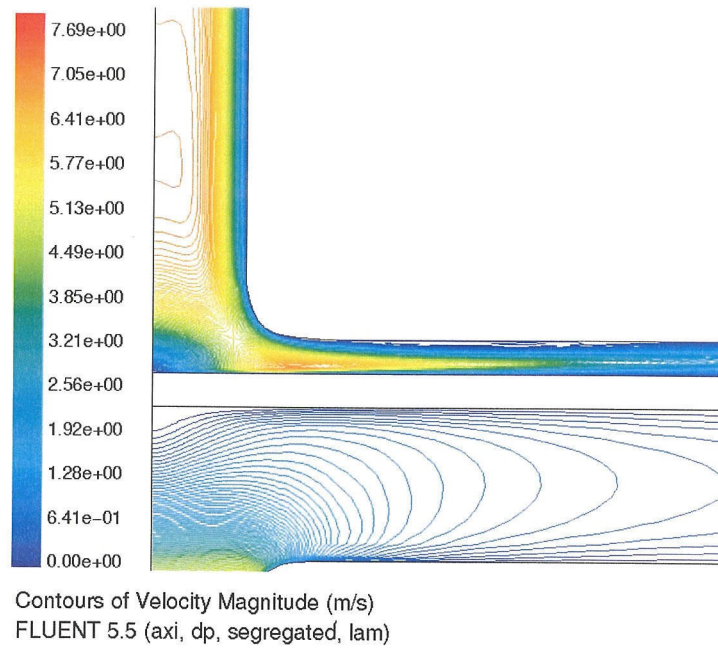


(a) 1500 sccm.

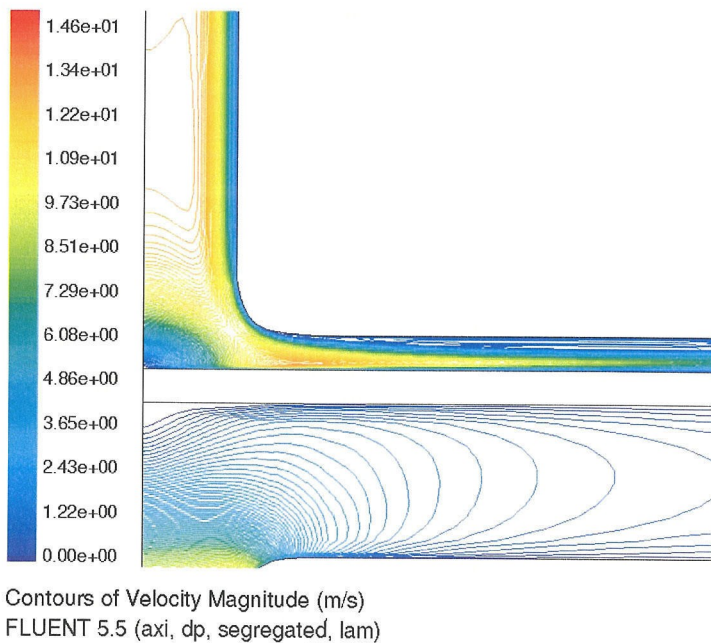


(b) 15000 sccm.

Figure 3.3: Velocity contour plots for flowrates without separation as modeled in Fluent<sup>TM</sup>.



(a) 35000 sccm.



(b) 60000 sccm.

Figure 3.4: Velocity contour plots for flowrates with separation as modeled in Fluent<sup>TM</sup>.

from the axial variation in thermal expansion was briefly investigated. Assuming isotropic expansion, a constant thermal expansion coefficient of  $\sim 4 \times 10^{-6} \text{ K}^{-1}$ , an axial temperature change of 1 K (about 5x larger than modeled predictions) through a 50  $\mu\text{m}$  wafer, the predicted radius of curvature of in a 300 mm wafer is  $\sim 125 \text{ m}$ . The predicted variation in height from center to edge is less than 0.1 mm. Although the curvature is minimal in this apparatus, the variation in height scales linearly with the temperature drop. Thus, wafer curvature may have a significant effect on deposition patterns at larger temperature gradients. Greater deposition nearer the edges would be expected as the flow slows at a rate greater than  $\frac{1}{r}$ .

### 3.3 Experimental Apparatus & Methods

Oxide-coated silicon nanocrystals are produced in a turbulent mixing aerosol reactor described previously.<sup>30,60</sup> A fraction of the stream is monitored continuously by a radial differential mobility analyzer<sup>22,28,37,150,151</sup> (RDMA) and a fA-resolution electrometer. The remainder of the 8–12 nm particle stream, with a concentration of  $\sim 10^8 \text{ cm}^{-3}$  and  $\sigma_G \approx 1.1$ , is sent via  $\frac{1}{4}$ " SS tubing to the deposition chamber inlet.

The deposition chamber consists of two modified MDC 18" SS vacuum flanges that serve as radially-mounted parallel plate heating and cooling surfaces. The aerosol is introduced orthogonally through  $\frac{1}{2}$ " OD SS tubing above the top plate at the wafer center and removed orthogonally at the wafer center from below through the bottom plate. Two concentric ring heaters and a third side-mounted band heater with a concentric ring-connected mount provide a nearly uniform heat flux to the top plate. A hollowed annulus in the bottom plate allows for heat transfer through the flange to a cooling fluid. Recirculated cooled water at 293 K at a flowrate of 30 lpm cools the bottom flange. The coolant is sealed using a SS covering plate with a Viton o-ring gasket. A small bi-directional nozzle is employed to provide equal coolant fluid flow around either perimeter of the water jacket. A single drain is located radially opposite the coolant source. A flat viton gasket separates the two flanges, serving as a thermal resistor to provide a more uniform temperature profile between the flanges.

The top plate is supported by three SS legs. The bottom plate rests on a SS jack that is manually raised and lowered during loading/unloading operations. All SS surfaces are electropolished.

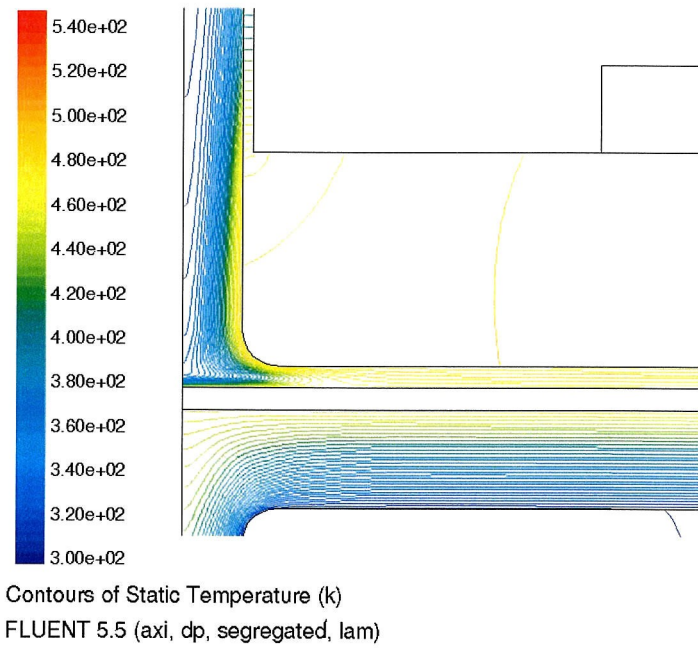
To maintain a uniform top plate temperature, each heating element is powered through

a Eurotherm 7100A thyristor monitored with thermocouples and PID controllers. The temperature profile and streamlines from a 2D axisymmetric solver in Fluent<sup>TM</sup> are shown in Figs. 3.5–3.6. A flowrate of 1500 sccm was used. The temperature drop from top plate to the wafer remains relatively uniform across the entire deposition region from the center, Fig. 3.5(a), to the edge of the wafer, Fig. 3.5(b). However, to avoid a region of sparse deposition from a reverse temperature gradient, observed in the modeling, when the aerosol is introduced relatively cold, a heating tape, thermocouple, and PID assembly are used to preheat the inlet aerosol.

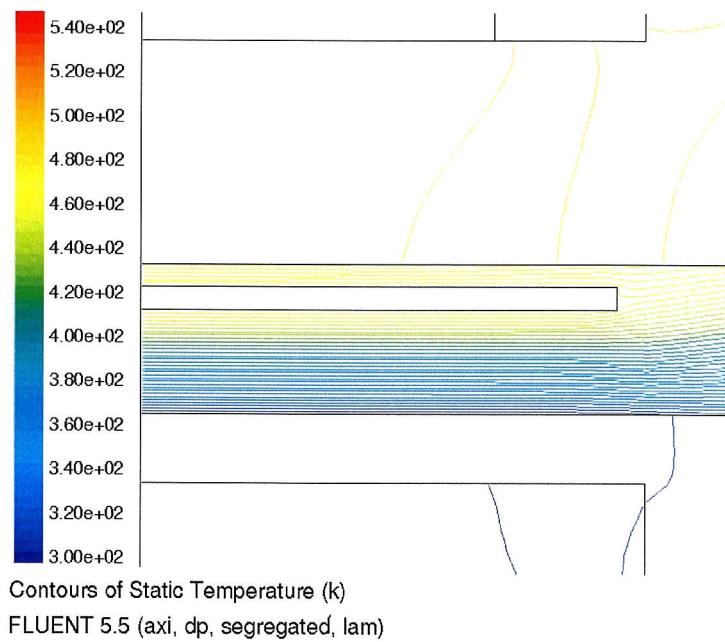
Figure 3.6 shows the corresponding streamlines for 1500 sccm flow to the modeled temperature profiles shown previously. Streamlines are parallel through the nozzle bend, Fig. 3.6(a), and over the wafer surface. Beyond the edge of the wafer, from the geometry imposed using this particular size of MDC flanges, Fig. 3.6(b), a recirculation pocket exists. However, this should have no effect on particle deposition over the wafer substrate.

Wafers are loaded using quartz-sleeved SS forks and rest upon three quartz or Teflon pegs in the chamber, providing a uniform wafer to plate distance and preventing contact with metal surfaces. The wafer is physically situated 2 mm below the heated top plate. With the absolute temperature relatively high, and the temperature gradient relatively large and uniform, small radial variations in temperature have little effect on thermophoretic transport. The quartz/Teflon pegs sit in machined depressions and the pegs are removable and replaceable. The adjustable height of the wafer adds another degree of freedom in determining thermophoretic velocity.

AFM samples were drawn from a center strip of a 150 mm [100] Si wafer that was tiled into 14 squares sized 1 cm x 1 cm using a wafer saw or cut into similar sized pieces using a diamond-tipped scribe. Before deposition, the tiled pieces were cleaned by sonication

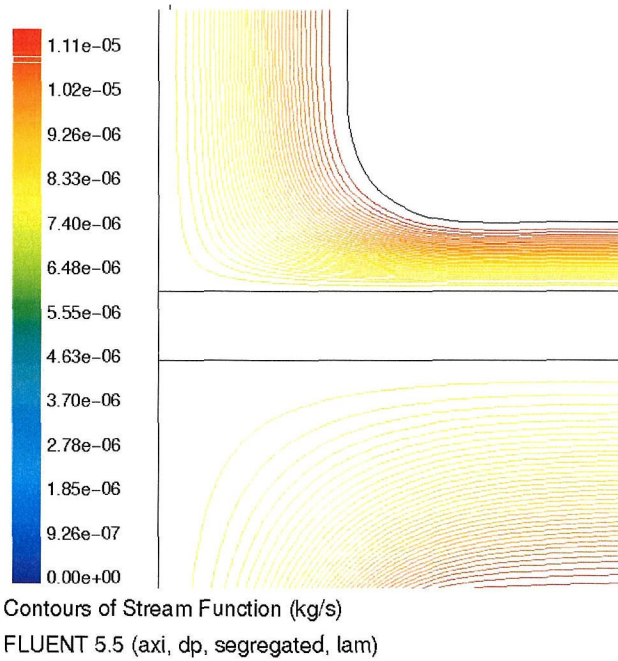


(a) Modeled temperature profile at the inlet and outlet region.

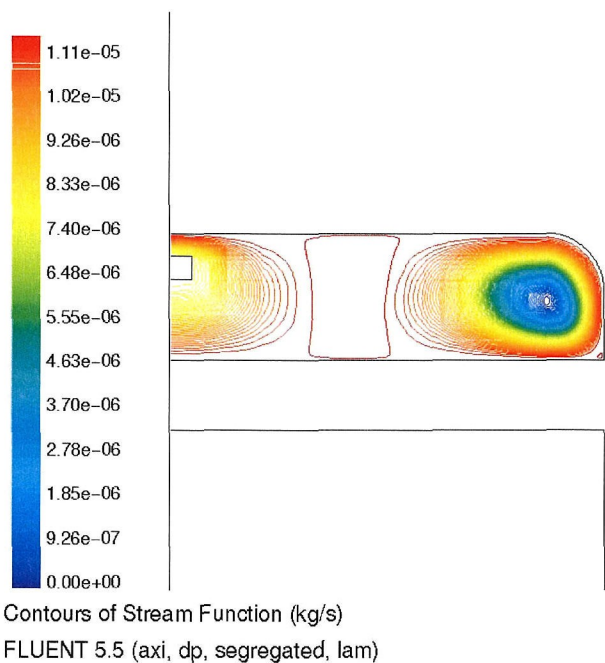


(b) Modeled temperature profile at the edge of wafer region.

Figure 3.5: Temperature contour plots modeled in Fluent<sup>TM</sup>.



(a) Modeled streamlines at the inlet and outlet region.



(b) Modeled streamlines at the edge of wafer region.

Figure 3.6: Streamfunction plots modeled in Fluent<sup>TM</sup> for flowrates of 1500 sccm.

in methanol, rinsed in deionized water, and dried using a jet flow of nitrogen. The tiled wafer was reconstructed on an intact wafer in the chamber, with the two “halfmoon” pieces secured using SS clips.

All SS surfaces were electropolished and cleaned with methanol prior to use within the cleanroom environment.

Non-contact AFM images were acquired over 512 x 512 resolution from a 5  $\mu m$  X 5  $\mu m$  grid. The AFM tip was estimated to be  $\sim 30 nm$  in diameter. Particle counts over the entire grid to determine coverage are reported in Fig. 3.12(b) and represent  $\sim 2000$  particles per image.

### 3.4 Results

Additional modeling of particle transport was conducted using Femlab<sup>TM</sup>. The results are shown in Figs. 3.7–3.10. The model used was a laminar flow, 2D axisymmetric representation of the deposition chamber. Temperature boundary conditions were imposed based on the results obtained earlier using Fluent<sup>TM</sup>, creating a temperature drop of  $\sim 30 K$  between the heated chamber top and the wafer. For simplicity, the particles are treated as a continuum species with uniform inlet concentration and temperature. The particles are subject to convection and thermophoresis as they travel through the chamber. Brownian diffusion is imposed for a single mode particle size, 10 nm, but particle loss to walls other than the wafer surface is neglected.

Figure 3.7 shows the particle distribution in the chamber with uniform top and bottom temperature,  $\Delta T = 165 K$ , and the incoming aerosol-laden N<sub>2</sub> 15 K cooler than the chamber top. Figures 3.8–3.10 show results for increasing flow ratios. A flowrate of 1600 sccm leads to insufficient deposition on the outer edge of a 300 mm wafer, but would be suffi-

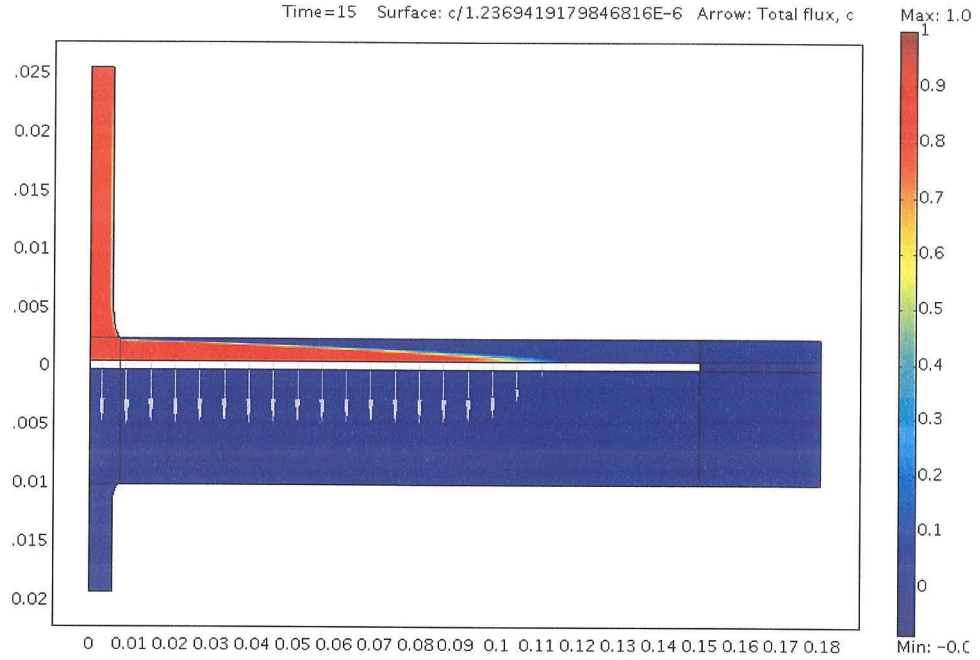


Figure 3.7: Particle deposition and concentration at 1600 sccm modeled in Femlab<sup>TM</sup>. Arrows indicate particle fluxrate at the wafer surface.

cient for a 150 mm wafer. The arrows in the figures indicate thermophoretic flux,  $v_{th}c$ , and that uniform deposition is predicted over the central portion of the wafer. Increasing the flowrate to 3600 sccm results in uniform deposition on a 300 mm wafer, Fig. 3.10, but is only achieved when some particles bypass deposition. At intermediate flowrates, uniform deposition coverage extends outward with increasing flowrate, while deposition rate decreases for similar aerosol inlet concentration. Figure 3.11 summarizes these model observations. Near  $r = 1$  mm, each trace predicts some inconsistency in the deposition uniformity. This perturbation could be reduced in the model, similar to that observed in the 3600 sccm trace, by adjusting the inlet temperature a few degrees lower, depending on the flowrate.

To examine the deposition uniformity attained by the deposition tool, silicon nanoparticles were deposited on a 150 mm wafer for 80 min with an aerosol flowrate of 1600 sccm and

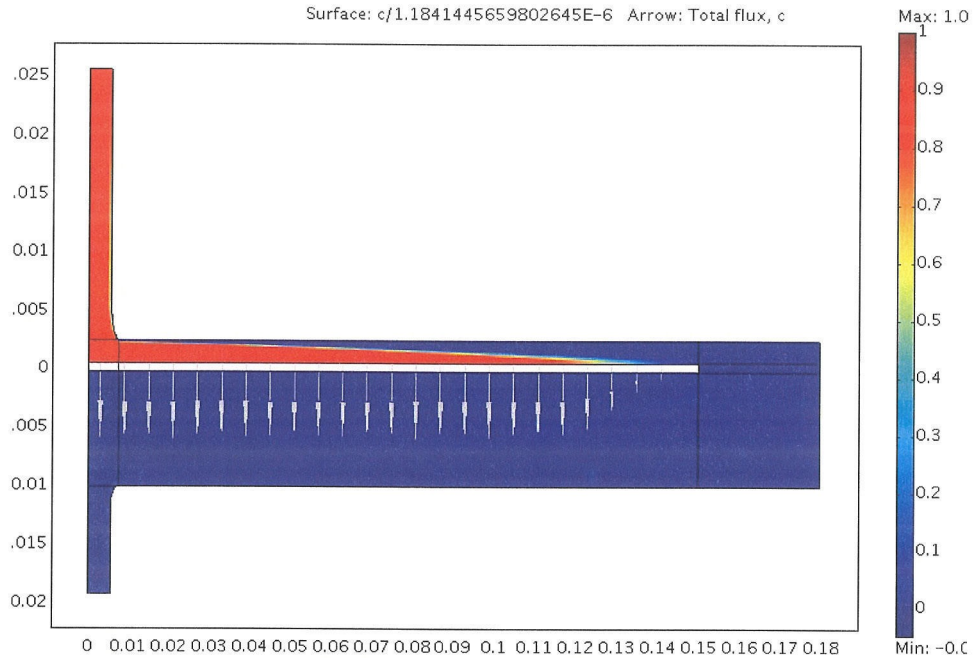


Figure 3.8: Particle deposition and concentration at 2400 sccm modeled in Femlab<sup>TM</sup>. Arrows indicate particle fluxrate at the wafer surface.

an aerosol concentration of  $2 \times 10^8 \text{ cm}^{-3}$ . As seen in the images in Fig. 3.13, the coverage was kept well below the monolayer than would be sought in device fabrication to facilitate quantitative areal density measurements. The particle size distribution of this test aerosol is shown in Fig. 3.12(a). The major mode in the distribution was 8.5 nm. The minor second mode at  $\sim 11$  nm reveals that limited ( $\sim 10\%$ ) aggregation occurred between the outlet of the synthesis reactor and the RDMA. The areal density of the deposited particles, shown in Fig. 3.12(b), is quite uniform, varying less than  $\pm 5.5\%$  over the radial and azimuthal by distributed samples probed.

Modeling in Fluent<sup>TM</sup> indicated that the particle stream needed to be preheated to a temperature within  $\sim 20 \text{ K}$  of the hot plate temperature to achieve deposition uniformity at the wafer center. A temperature too high produced a correspondingly larger thermal

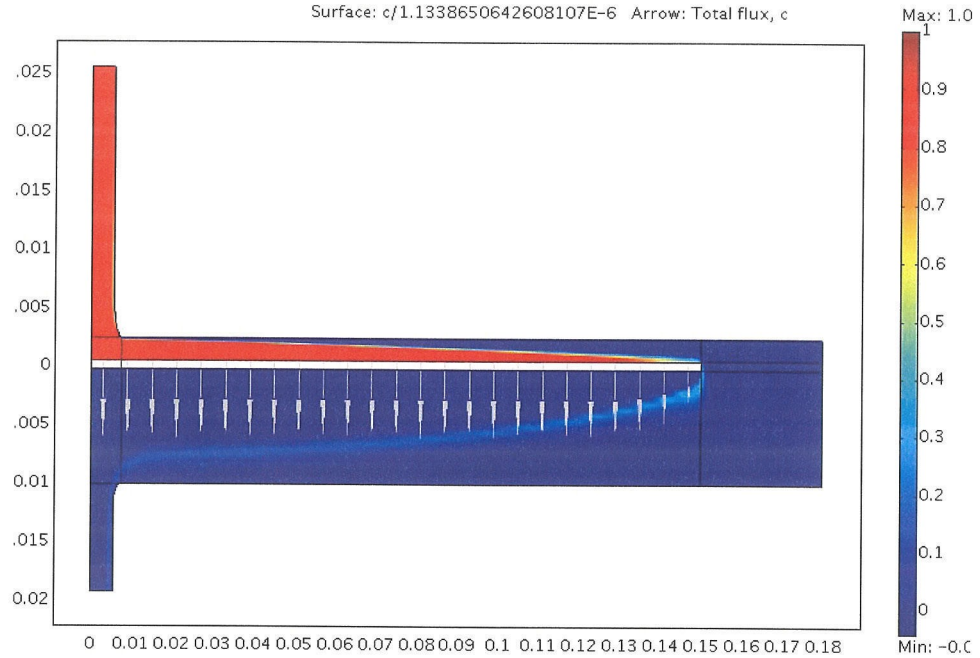


Figure 3.9: Particle deposition and concentration at 3000 sccm modeled in Femlab<sup>TM</sup>. Arrows indicate particle fluxrate at the wafer surface.

gradient near the center and the modeled deposition rate exceeded that of the outer surface.

If too cool, Fig. 3.14, then the model predicts insufficient or no deposition at the center.

Heat transfer within the silicon wafer is faster than through the aerosol-containing N<sub>2</sub>, raising the temperature of the wafer center above that of the heated inlet stream, and driving particles away from the wafer.

The reversed temperature gradient was also predicted with modeling in Femlab<sup>TM</sup>, as seen in Figs. 3.15–3.16. The magnitude of the thermophoretic flux away from the wafer is several times that of the flux toward the surface, indicating that the reversed temperature gradient is much greater.

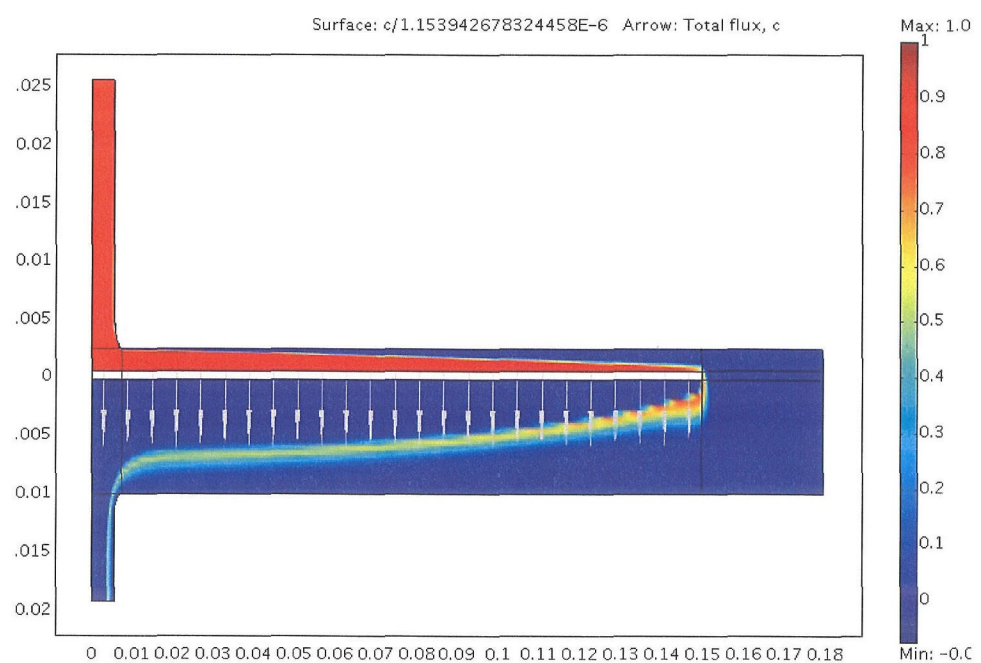


Figure 3.10: Particle deposition and concentration at 3600 sccm modeled in Femlab<sup>TM</sup>. Arrows indicate particle fluxrate at the wafer surface.

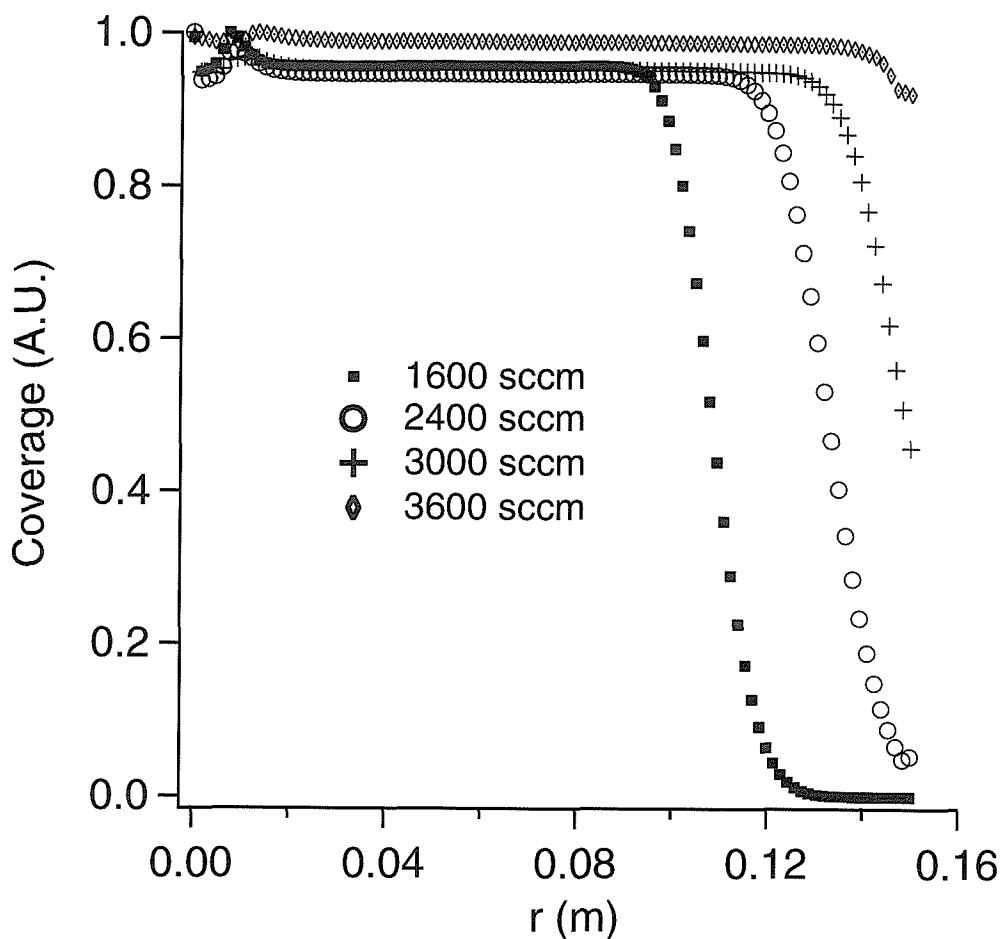


Figure 3.11: Model predictions for particle deposition on 300 mm silicon wafer at various flowrates.

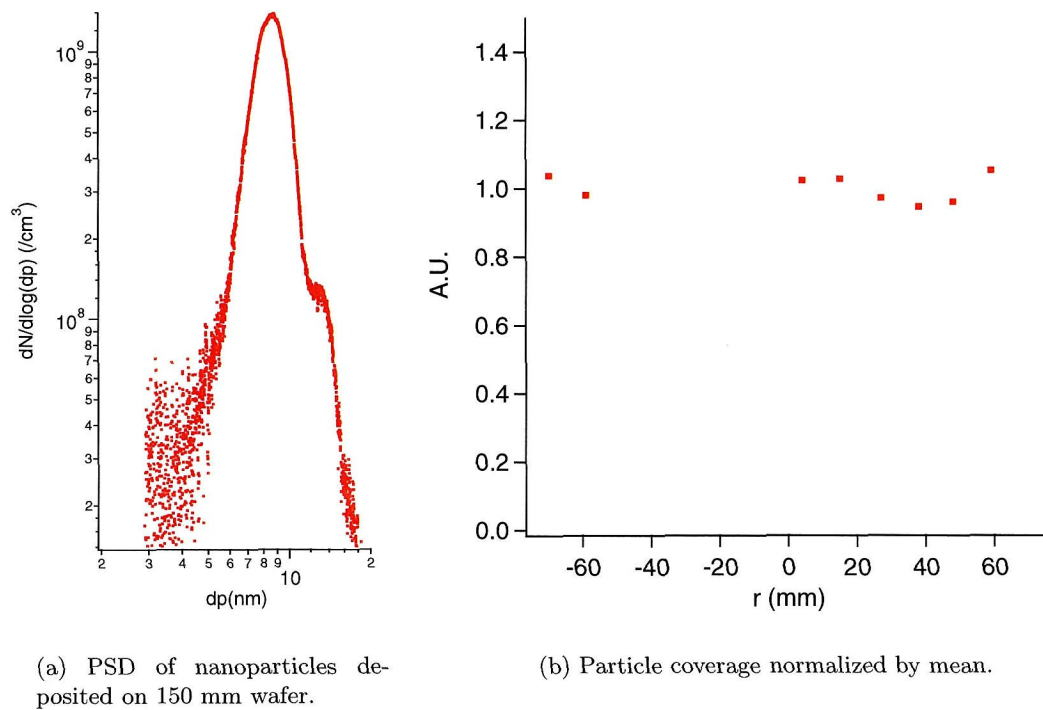


Figure 3.12: PSD and particle coverage on 150 mm silicon wafer. AFM images are seen in Fig. 3.13.

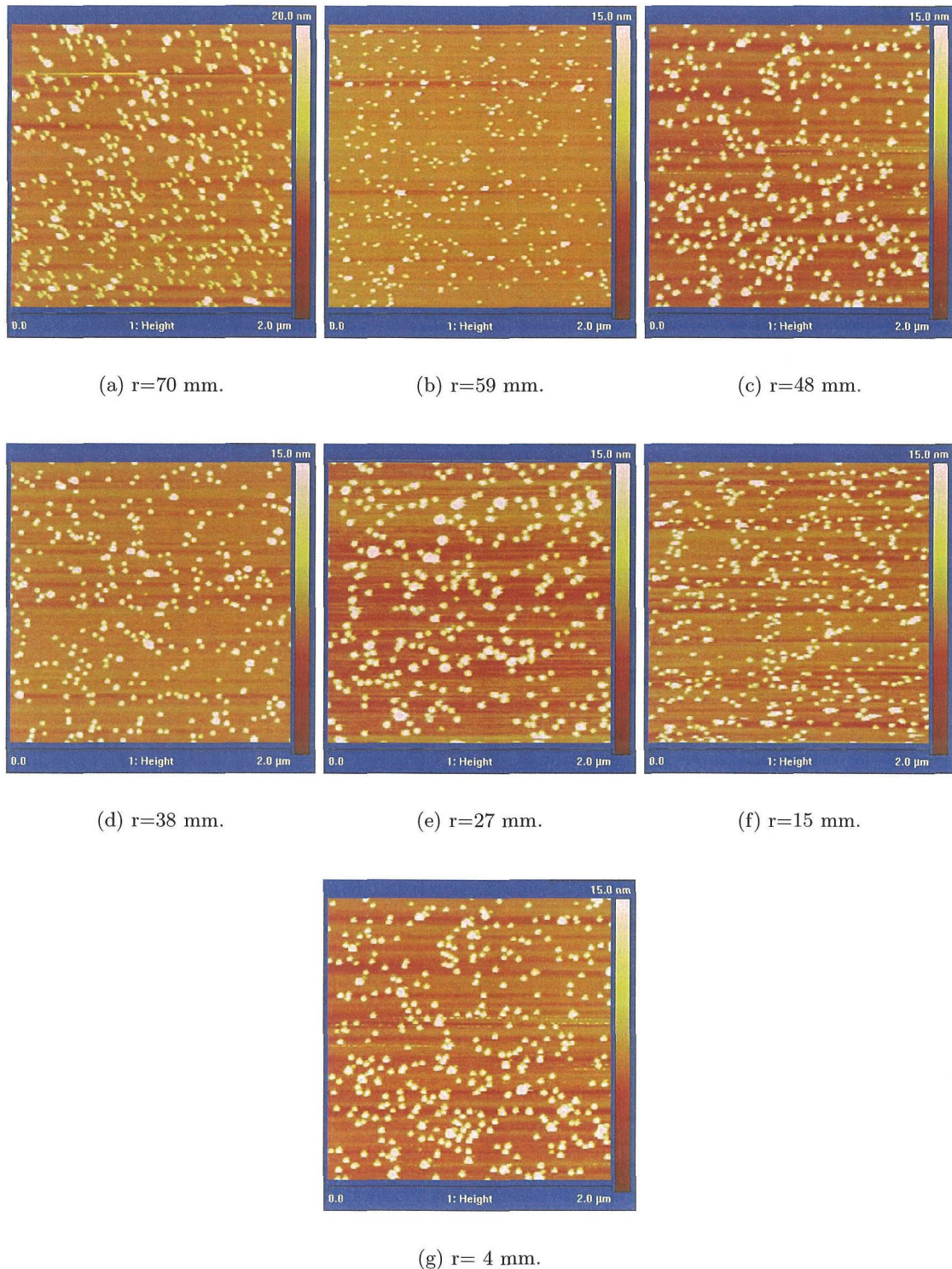


Figure 3.13: AFM images of particle deposition on 150 mm wafer.

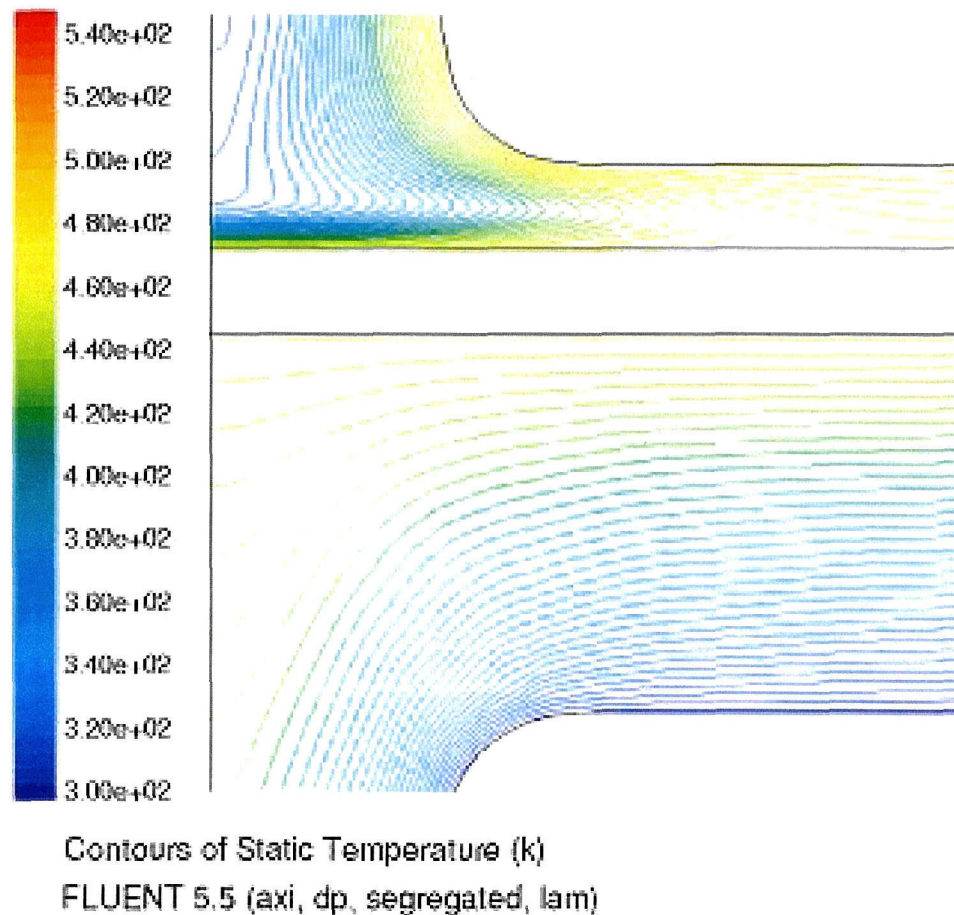


Figure 3.14: Model predicts a reversed temperature gradient when aerosol is not preheated.

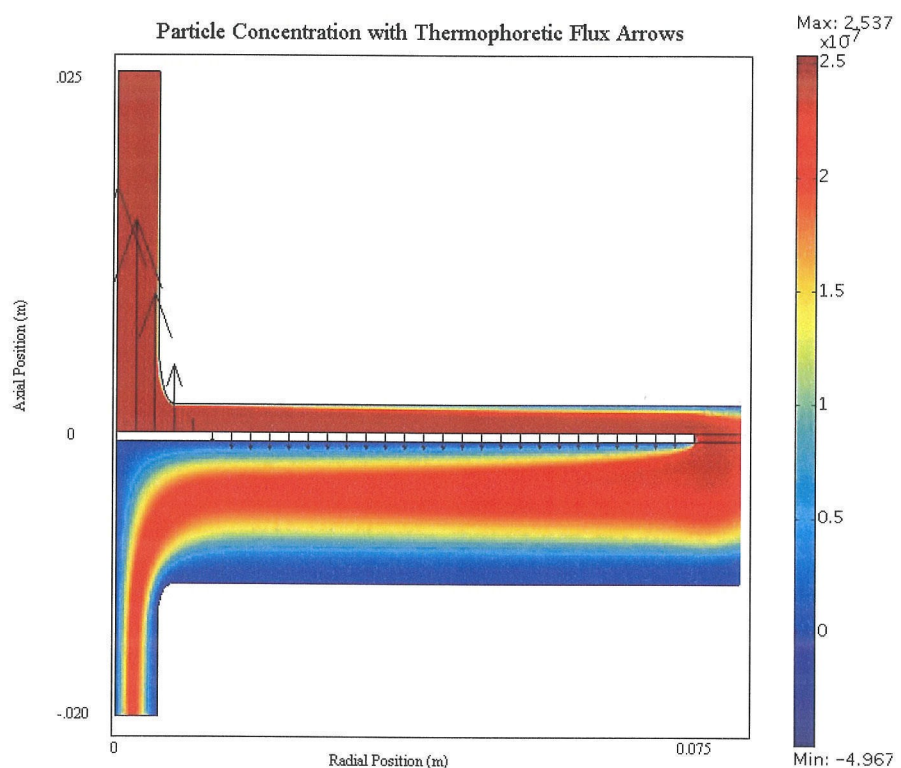


Figure 3.15: Model predicts the lack of deposition at the wafer center if the aerosol is not preheated. The arrows are proportional to the magnitude of thermophoretic particle flux.

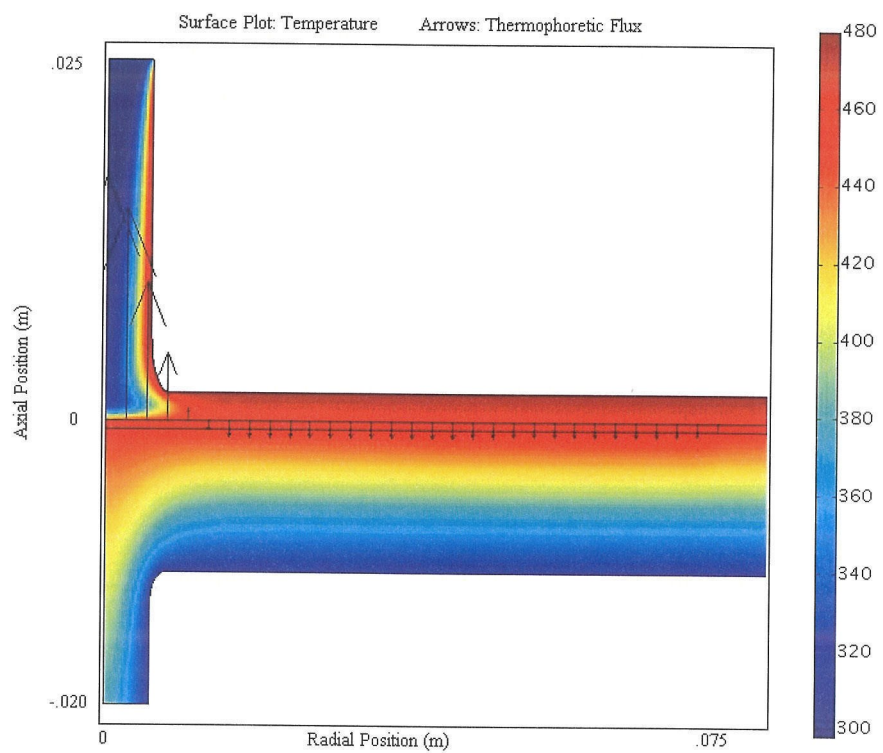


Figure 3.16: Modeling in Femlab<sup>TM</sup> corroborates the predicted reversed temperature gradient when aerosol is not preheated.

### 3.5 Conclusions

A 300 mm capable laminar flow thermophoretic deposition device demonstrates near uniform coverage of nanoparticles on a 150 mm wafer. Modeling suggests device operation is robust over a wide range of flowrates. A sparse array of particles randomly oriented over the surface was stably attached and remained adhered over a two-month period in which characterization by AFM was performed. Longer deposition times are expected to maintain deposition uniformity and yield coverages approaching monolayer. Deposition of nearly monodisperse nanoparticles may also self-assemble into close-packed structures, provided that agglomeration in the aerosol phase is avoided. Device fabrication with aerosol nanoparticles deposited using thermophoresis remains a potential new process for meeting narrower bandwidth requirements or producing new devices in which the nanoparticles' spatial positioning must meet tight tolerances.

## Chapter 4

# Photoluminescence From Oxide-Coated Silicon Aerosol Nanocrystals

### Abstract

Silicon nanocrystals and oxide-coated silicon nanocrystals fabricated by pyrolytic decomposition of silane and passivated by thermal oxidation or with low temperature native oxide layers in a multistage high temperature, atmospheric pressure aerosol reactor may photoluminesce without further processing. The observed photoluminescence decay is characteristic of exciton recombination in silicon nanoparticles, and the PL intensity is similar to that of silicon nanocrystals grown by ion implantation. The impinging jet, turbulent mixing flow reactor<sup>60</sup> used in this study produced nanoparticles with very narrow size distributions as measured using a radial differential mobility analyzer. Spherical heterogeneous core-shell nanoparticle morphology and size is confirmed by transmission electron microscope analysis. Particle contamination studies were conducted using Electron Energy Loss Spectrometry. Photoluminescence spectral measurements were used to determine the sizes of the photoluminescent core while mobility data determined the physical size. The difference between these two sizes provides an estimated oxide shell thickness. The variation of the oxide thick-

ness with the size of thermally oxidized nanoparticles differed from that observed in native oxide-coated nanoparticles. Native oxidation appears to consume small particles quickly with the oxide thickness decreasing as particle size increases. Over time, the native oxide thickened considerably, producing a blue shift in the photoluminescence spectrum. Further oxidation proceeds slowly for larger particles. By contrast, thermal oxidation provides a more uniform oxide layer wherein oxide thickness increases with particle size and remains stable over time. Core sizes below 4 nm were not observed in quantity.

#### 4.1 Introduction

The observation of photoluminescent silicon nanocrystals<sup>24</sup> has spurred much interest in developing silicon-based products including nanocrystal memory,<sup>130</sup> LEDs, optical amplifiers, lasers, etc. Recent consideration is being lent to applications outside of microelectronics such as tracers in biological systems.<sup>8,9,10</sup> Considerable effort has been focused on the production of high purity, monodisperse particles that may be positioned with precise spatial positioning in a device. While many *in situ* fabrication methods are showing maturity with respect to purity and particle size control, spatial positioning is still a challenge remaining to be met. In some methods, the thermal budget also remains large for successful nucleation, size control, or annealing of particles. Moreover, high energy growth methods, such as ion implantation, can leave damage in the surrounding matrix that can affect device performance.<sup>136</sup>

Production of nanoparticles via an aerosol route allows for real-time particle size and number characterization and subsequent non-damaging deposition control. Newer reactors are addressing the issues of low aerosol particle yield,<sup>78,106</sup> producing narrow size distributions,<sup>60</sup> with proven device quality cleanliness.<sup>101,102</sup> Newer fabrication methods, such

as the microplasma discharge reactor, access broader chemistries in novel particle production.<sup>113,114</sup>

Comprehension of the complete mechanism describing photoluminescence (PL) from silicon nanocrystals is maturing,<sup>54</sup> and it is well understood that radiative exciton recombination<sup>107</sup> may be channeled to a non-radiative pathway in the presence of defect states<sup>92,134</sup> in the nanocrystal arising from poorly passivated oxides or coatings, or impurities. Spectroscopic measurements demonstrate that the amount of oxygen at the particle's surface increases as non-luminescent nanocrystals become luminescent<sup>83</sup> and that the presence of O<sub>2</sub>, while not necessary for observation of PL, has an effect on the luminescent wavelength.<sup>16</sup> Relationships between particle size, oxide thickness, the variation of the oxide thickness over time, and their effects on PL are difficult to determine and are often inferred from limited subsets of particles viewed using transmission electron microscopy (TEM). In contrast, size characterization of particles fabricated by the aerosol route, which provides size data on a much larger ensemble of particles, offers an opportunity to compare a much larger dataset to PL spectral measurements, and thus offers insight into the growth of the oxide.

This present chapter examines the relationship between the PL spectral emission from oxide-coated silicon nanocrystals and the particle size distributions determined using on-line aerosol instrumentation for both Si nanoparticles in which a native oxide is allowed to develop or that are passivated with a thermal oxide. The variation of the thickness of the oxide shell with particles size and the stability of those shells over time are also examined. Dramatic differences will be shown for the two types of oxide coatings. We determine that native oxide layer growth is initially catastrophic for small particles,  $\sim 5$  nm, and the layer thickness thins as particle size increases. Over time, the oxide layer thickens relative to particle size and approaches the trends observed for thermally oxidized particles. We

infer that photoluminescence quenching results from energy interaction between small and bulk-sized particles and/or through poor passivation by the oxide layer.

## 4.2 Experimental Apparatus & Methods

Nanoparticles for this study are produced in an Inconel turbulent mixing reactor reported earlier.<sup>60</sup> Dilute  $\sim$  O(ppm) silane in nitrogen is introduced axially at atmospheric pressure into a small diameter Inconel reactor within a furnace maintained at  $\sim$  1000°C. The silane is heated as it enters the furnace and decomposes, nucleating to form small silicon clusters that grow, when silane concentration is relatively low, by vapor deposition into larger nanoparticles. Preheated nitrogen is introduced radially from two small diameter jets to dilute the reactants and quench nucleation. The hot dilution gas raises the temperature, driving reaction to completion, and quenching nucleation. Intense mixing produced by the high kinetic energy impinging jets rapidly homogenizes the gas, so particle evolution proceeds in a hot, homogeneous environment<sup>30</sup> wherein particles coalesce, densify, and crystallize. In a second reaction stage located downstream of the primary reaction zone, pure oxygen may be added through a second pair of jets to facilitate the growth of a high temperature oxide (HTO) layer. Two variants of the reactor were used, one that was optimized to produce 10–12 nm particles and one to produce 7–9 nm particles.

Particles leaving the reactor were collected by either electrostatic (ESP) or thermophoretic deposition. For the present experiments, particles were collected on holey carbon TEM grids by both deposition methods, on silicon wafer fragments by ESP, and on Germanium wafer fragments by thermophoresis. The particle concentration and size distribution were measured on-line by imparting a known charge distribution using a  $^{85}\text{Kr}$  “neutralizer”<sup>40,61</sup> and were then size classified using a radial differential mobility analyzer<sup>23</sup> (RDMA) and de-

tected with a fA ( $10^{-15}$  A) resolution electrometer. In two experiments, the larger particles were deposited and annealed in a mixture of 5% N<sub>2</sub>/H<sub>2</sub> for 1 hr at 450° C and/or house N<sub>2</sub> ( $\sim$  100 ppm O<sub>2</sub> or H<sub>2</sub>O) at 450° C.

Conventional and High Resolution Transmission Electron Microscopy (CTEM and HRTEM) were performed on a Philips 430 TEM using a Lab VI filament operated at 300 keV. Samples were collected by ESP on holey-carbon TEM grids.

With the aerosol produced in an atmospheric pressure Inconel reactor, the question arose whether metal contamination of particles might ensue at the operating temperature of 1273 K. Particle contamination studies were performed using an FEI Technai F20ST 200 keV Scanning/Transmission Electron Microscope, equipped with Electron Energy Loss Spectroscopy (EELS) and Energy Dispersive X-Ray Spectroscopy (EDS) capabilities.

The X-ray photoelectron spectroscopy (XPS) measurements were performed in an VG Instruments M-probe surface spectrometer using monochromatic Al K- $\alpha$  excitation X-rays (1486.6 eV) incident at 35 degrees from horizontal. Emitted electrons were collected by a hemispherical analyzer at a takeoff angle of 35 degrees from the plane of the horizontal sample surface.

PL spectra were collected using an electro-optically modulated 457.9 nm Ar laser pump focused to  $\sim$  1 mm spot size, a liquid nitrogen cooled silicon CCD array, and a grating spectrometer. A liquid-nitrogen cooled Germanium detector with the spectrometer was employed to measure infrared (IR) emission. PL decay traces (lifetime) were collected using a thermoelectrically cooled photomultiplier tube (PMT) and grating spectrometer. PL decay data for all samples were collected within 50 nm of the peak PL intensity wavelength.

The thermophoretic sampler consisted of heated (200°C) laminar flow through a 3 mm diameter nozzle normally impacting on a liquid-nitrogen cooled wafer substrate located

1 mm below the nozzle exit. Although the velocity of the aerosol gas jet leaving the nozzle is too great for complete deposition, a representative sample of particles moving through the developing boundary layer above the wafer fragment is deposited.<sup>49,127,141</sup> Modeling in Femlab<sup>TM</sup> indicates  $\sim 4\%$  of the particles deposit.

The ESP sampling was performed using the same physical device used for thermophoretic collection, and with the cold finger replaced with an electrode and Teflon wafer fragment holder. The electric field applied between nozzle and wafer electrode is  $\sim 5 \frac{kV}{cm}$ .

The radial differential mobility analyzer, RDMA, provides a convenient high resolution tool for measuring the particle size distributions of aerosol particles.<sup>150,151</sup> This data is not easily obtainable when particles are grown in a solid matrix and often is inferred from a limited dataset. The RDMA, as used in this configuration, sizes particles after leaving the reactor, before any exposure to the ambient air. Thus, particle size distributions reported herein are sampled before native oxide growth or after thermal oxide growth. Comparison to PL spectra (core size) is used to determine the oxide thickness of particles after exposure to oxygen, either in the relatively cool ambient air or within the reactor.

From RDMA data, the number distribution,  $n(\log_{10}(d_p))$ , of particles is characterized,

$$\frac{dN_p}{d\log_{10}(d_p)} = n(\log_{10}d_p) \quad (4.1)$$

where  $n(\log_{10}(d_p))$  is the number of particles in the size interval from  $\log_{10}(d_p)$  to  $(\log_{10}(d_p) + d\log_{10}(d_p))$  and  $N_p$  is the total number of particles.

Absorption by these particles, which are much smaller than the excitation wavelength and therefore in the Rayleigh regime, is proportional to their volume. The absorption is

weighted by the volume, i.e.,

$$\alpha(\log_{10}(dp)) \propto n(\log_{10}(dp)) \left( \frac{d_p}{d_{p,ref}} \right)^3 = n_v(\log_{10}(dp)) \quad (4.2)$$

where  $d_{p,ref}$  is the mode-size diameter. The  $n_v(d_p)$  distribution is normalized,

$$\hat{n}_v(\log_{10}(dp)) = \frac{n_v(\log_{10}(dp))}{\max \left( n_v(\log_{10}(dp)) \left( \frac{d_p}{d_{p,ref}} \right)^3 \right)}. \quad (4.3)$$

The absorption by particles in the size interval from  $d_p$  to  $(d_p + dd_p)$  is, therefore, proportional to the volume distribution,  $n_v(d_p)$ , i.e.,

$$\alpha(d_p) \propto d_p^3 dd_p = n_v(d_p) dd_p. \quad (4.4)$$

Assuming that the maximum PL intensity originates from the particle at  $\hat{n}_v(\log_{10}(dp))_{max}$  provides a benchmark for estimating the core size of this particle and its corresponding oxide shell thickness. The core size of the luminescing particle is determined using the Ledoux-modeled<sup>83</sup> pressure corrected Delerue correlation,<sup>33,56</sup>

$$E_{PL} = E_g + \frac{3.73}{d_p^{1.39}} + \frac{0.881}{d_p} - 0.245 \quad (4.5)$$

where  $E_g = 1.12$  eV and  $d_p$  is the luminescing particle diameter in nanometers.

The normalized PL intensity spectrum is fitted to a polynomial function for intensities greater than  $0.5I_{max}$ ,

$$\hat{I} = \frac{I(\lambda)}{I_{max}} = \sum_i^n c_i \lambda^i \quad (4.6)$$

where  $I$  is the intensity and  $\lambda$  the wavelength.

The emission rate is assumed proportional to absorption, with emission efficiency treated as invariant with changes in particle size. The efficiency and rate assumptions have been shown to be valid in a narrow region of particle sizes,<sup>43,82</sup> and are used here to illuminate trends in growth of the oxide. Emission rates drop considerably as particles approach sizes wherein quantum confinement is no longer observed, but the magnitude of the decrease as a function of particle size is still under debate in the literature, although using the phenomenological model from Kapoor<sup>67</sup> may be of interest here.

The peak particle size,  $\hat{n}_v(d_p)_{max}$  is assumed to have a luminescent core size that matches the wavelength of peak PL intensity. This provides an estimate of the oxide thickness. For HTO-coated particles, the shell thickness,  $th_{shell}$ , is simply half the difference between RDMA-size,  $d_{p,RDMA}$ , and the luminescent core size,  $d_{p,PL}$ ,

$$h_{shell} = \frac{1}{2} (d_{p,RDMA} - d_{p,PL}) \quad (4.7)$$

but for native oxide-coated particles, this value is estimated using a mass balance from RDMA-size (pure Si), the corresponding core size from PL, with the difference suggesting an oxide thickness,

$$\frac{4}{3}\pi \left(\frac{d_{p,RDMA}}{2}\right)^3 \rho_{Si} = \frac{4}{3}\pi \left[ \left(\frac{d_{p,PL}}{2} + h_{shell}\right)^3 - \left(\frac{d_{p,PL}}{2}\right)^3 \right] \rho_{SiO_2} \frac{\mathcal{M}_{Si}}{\mathcal{M}_{Si} + \mathcal{M}_{O_2}} - \frac{4}{3}\pi \left(\frac{d_{p,PL}}{2}\right)^3 \rho_{Si} \quad (4.8)$$

where  $\mathcal{M}_{Si}$  and  $\mathcal{M}_{O_2}$  are the molecular weights for Si and SiO<sub>2</sub> respectively. Using bulk density parameters and assuming a stoichiometric oxide, the resulting mass balance is cubic in  $d_{p,PL}$  and the relevant root is determined using Newton's interpolation method where

$$f(x) = d_{p,PL},$$

$$f(x)_{n+1} = f(x)_n + \frac{df(x)_n}{dx}. \quad (4.9)$$

The oxide is considered to contain stoichiometric quantities of Si and O<sub>2</sub>. No data were collected to analytically determine the ratios. As silicon aerosol nanoparticles have shown tendencies to not photoluminesce for some developmental period of the native oxide,<sup>83,117</sup> this assumption has some justification.

Between 0.5 $\hat{I}_{max}$ , the distribution of particle data is fitted to the normalized PL intensity spectrum, wherein  $\hat{I} \approx \hat{n}_v(d_p)$ , using a sum of least squares method. The particles are fitted with the trend,

$$h_{shell}(j) = h_{shell}(j = 0)e^{\left(-\log_{10}\left(\frac{h_{shell}(j=J)}{h_{shell}(j=0)}\right)\left(\frac{j}{J}\right)\right)} \quad (4.10)$$

where  $j$  is an index of the number of data points between the half-maximum intensity and  $J$  is the largest index.

The RDMA data are captured with a similar exponential ramp in  $d_{p,RDMA}$ . For oxide thicknesses that increase with particle size, such as the HTO-coated particles, the two exponential ramps grow with an equal ratio, and a linear increase in oxide thickness with particle size is observed. For oxide thicknesses that decrease with particle size, such as newly formed native oxide on the particles, the two exponential ramps are additive and the trend observed fits the discretized equation

$$h_{shell}(j) = h_{shell}(j = 0)e^{\left(-\log_{10}\left(\frac{d_{p,RDMA,j=J}}{d_{p,RDMA,j=0}}\right)\left(\frac{j}{J}\right)^2\right)}. \quad (4.11)$$

For the graphs that follow, this function was then extrapolated to 0.2 $\hat{I}_{max}$  of the particle mode frequency to provide a range of diameter size to oxide thicknesses over the luminescent

range.

For these calculations, the native oxide thickness may be overestimated, as sub-stoichiometric ratios,<sup>83</sup> particularly near the Si-SiO<sub>2</sub> interface, are often observed in luminescent nanocrystals. For larger particles, as the equal-rate assumption is no longer valid, oxide thickness is also overestimated. Our calculations, therefore, provide a lower bound of oxide thickness within the validity of the equal emission rate assumption.

### 4.3 Results and Discussion

Figure 4.1 shows particles imaged using high resolution transmission electron microscopy (HRTEM) and their associated particle size distributions characterized with the RDMA and electrometer for silicon nanoparticles without, Figs. 4.1(a)–4.1(b), and with, Figs. 4.1(c)–4.1(d), thermal oxide coatings. Particle size distributions are typically reported in the change of number of particles,  $N_p$ , with logarithmic changes in diameter,  $d_p$ , hence,  $\frac{dN}{d\log d_p}$  vs.  $d_p$ , to illustrate the polydispersity of the particles. The particle size distributions of the former do not include the effects of native oxide formation; the thermal oxide particles were sized after oxidation. Due to the residence time in the plumbing between the reactor outlet and the RDMA, non-coalescent coagulation increases the particle size and the breadth of the size distribution. This observation is confirmed by the lack of particles in HRTEM images that corresponds to the lower mobility, 15–20 nm particles, detected by the RDMA. For the particles with a native oxide, the distribution shows the majority of particles between 7.5–10.5 nm, and a mode size of 8.5 nm. The HTO-coated particles have a mode size at 10 nm, with a narrower range of sizes. The narrower range results from reducing the precursor concentration in the reactor. From the HRTEM images, Fig. 4.1(d), the HTO oxide is typically thicker,  $\sim 2$  nm, and more uniform than the native oxide. The image

of small,  $\sim 6$  nm native oxide-coated silicon nanoparticles, Fig 4.1(b), with lattice fringes is rarely seen in HRTEM images and may be attributable to inhibition of oxidation from contact with adjacent particles.

The HRTEM image of HTO-coated particles in Fig. 4.1(d) shows qualitative agreement of size between RDMA and TEM. Lattice fringes are seen in some particle cores revealing a crystalline core that is 4–6 nm in diameter with a surrounding oxide thickness of 1.5–2 nm.

Similarly-sized native oxide-coated nanoparticles were collected on a Germanium surface by thermophoretic deposition. Figure 4.2 shows a spectral PL trace, its corresponding decay trace at  $\lambda=900$  nm, and the averaged particle size distribution recorded throughout deposition onto the Germanium. The PL decay fits a stretched exponential,<sup>63</sup>

$$I_t = I_0 e^{-(\frac{t}{\tau})^\beta} \quad (4.12)$$

where  $\tau = 91\mu\text{s}$  and  $\beta = 0.69$ , in good agreement for exciton recombination in well-passivated oxide-coated silicon in a dense ensemble.<sup>19</sup> This parameter is considered a measure of interparticle interaction with  $\beta = 1$  indicating non-interacting particles or sparse ensembles of particles. The variation of PL decay with changes in nanoparticle size also stretches this function.<sup>50</sup> The spectral breadth of the PL signal has been attributed to the spread in core size,<sup>58</sup> to inhomogeneous strain<sup>56</sup> of the lattice from variations in the lattice parameter, and from pressure induced by the oxide layer growth and homogeneous separation of the valence and conduction bands.<sup>134</sup>

HTO-coated particles, collected on silicon by ESP, Fig. 4.3(c), of a broad distribution of particles up to  $\sim 20$  nm did not luminesce within the detection limits of the CCD. They were further processed in  $\sim 50$ –100 ppm oxidant ( $\text{O}_2$  and  $\text{H}_2\text{O}$ ) in house  $\text{N}_2$  for time intervals

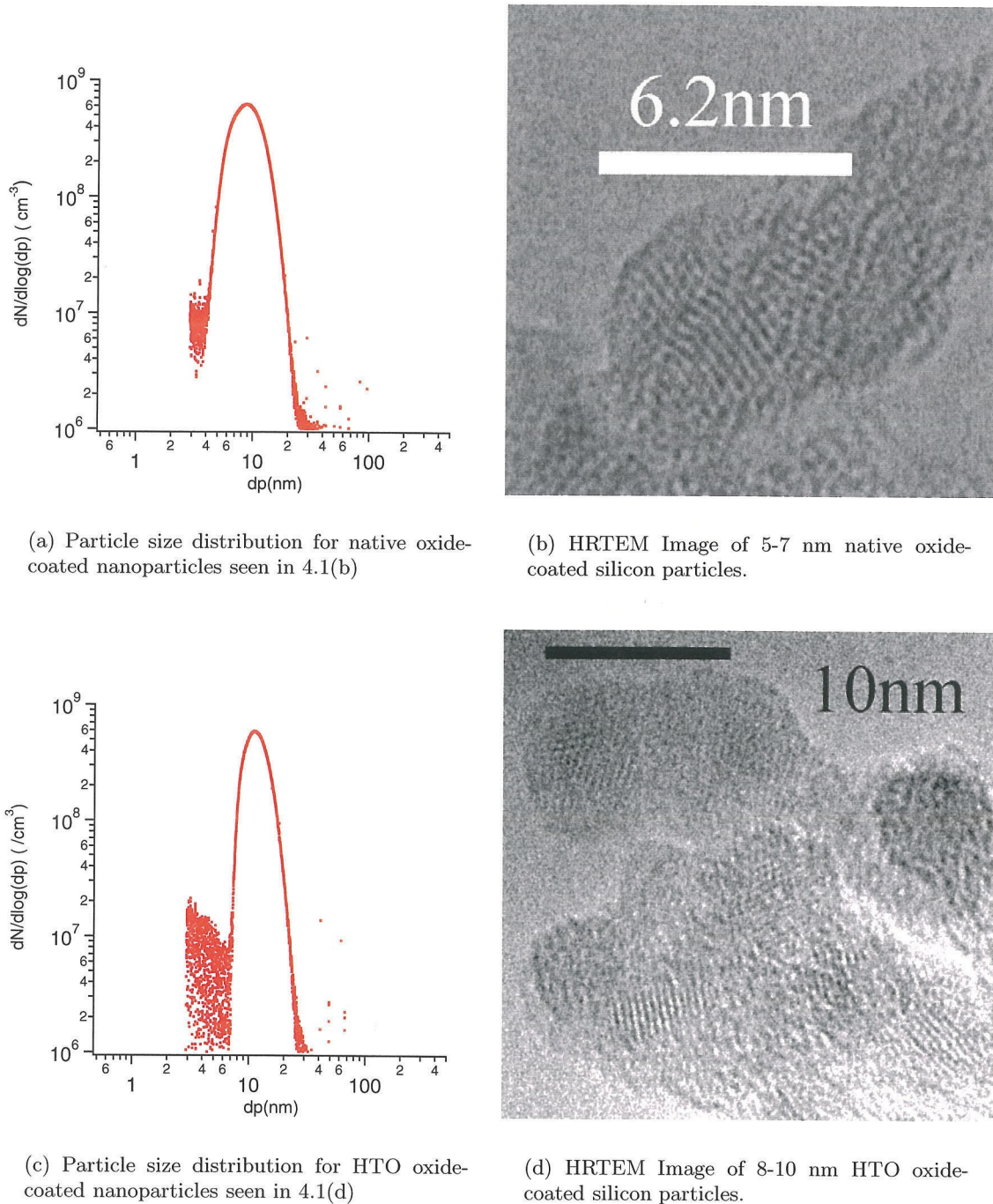
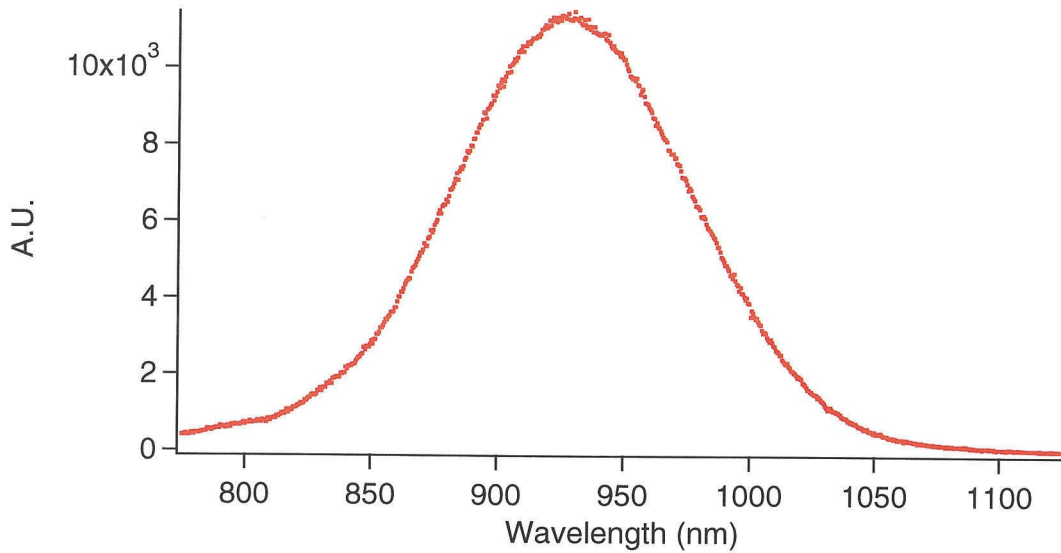
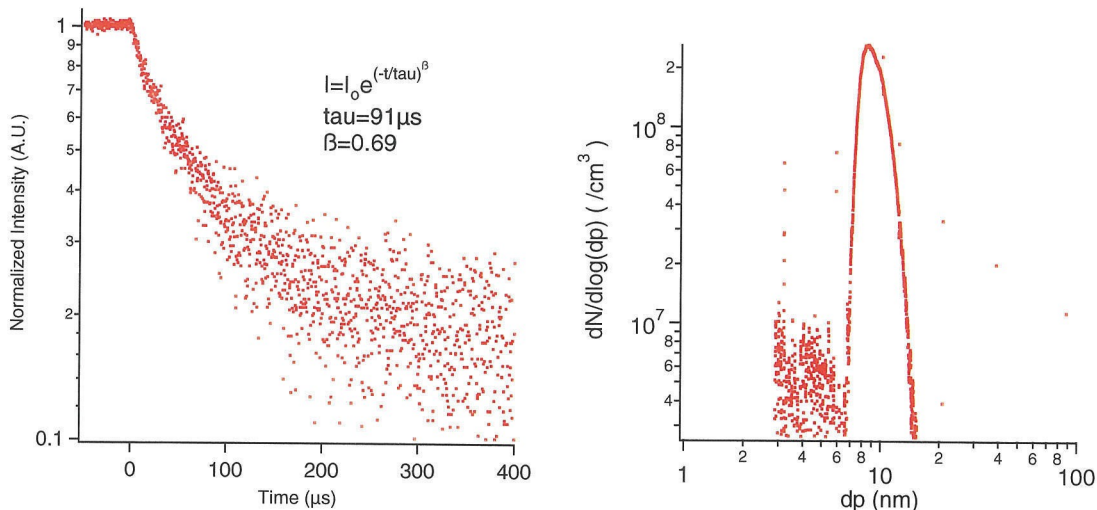


Figure 4.1: HRTEM images and corresponding particle size distributions from RDMA of silicon nanoparticles from the mixing reactor.



(a) Spectral trace for PL from native oxide-coated silicon nanoparticles.



(b) PL decay trace.

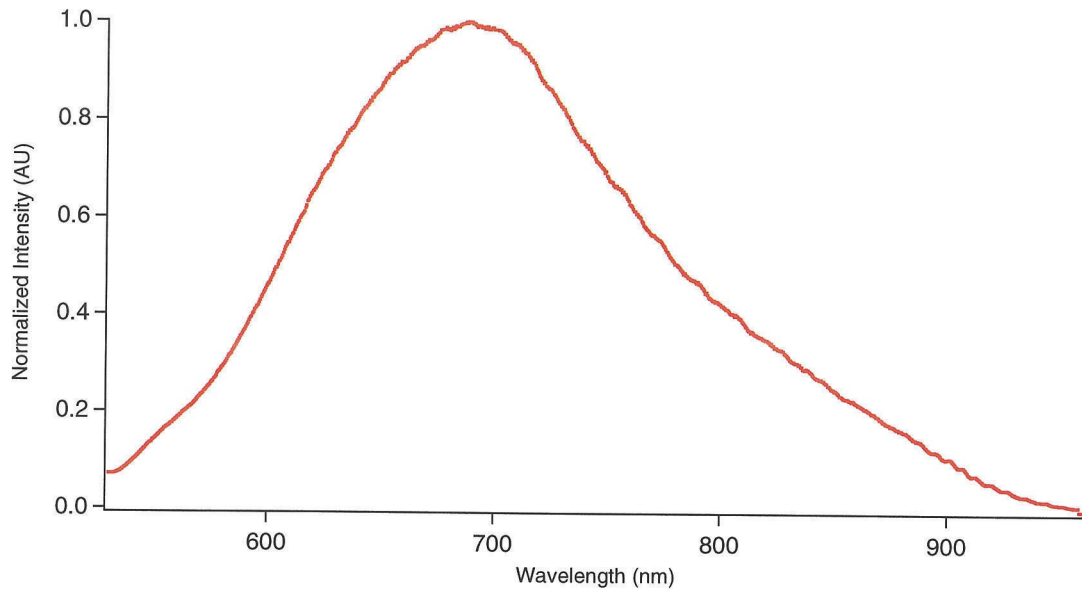
(c) Particle size distribution of native oxide-coated silicon nanoparticles used in PL study.

Figure 4.2: PL, PL decay, and particle size distribution from native oxide-coated silicon nanocrystals.

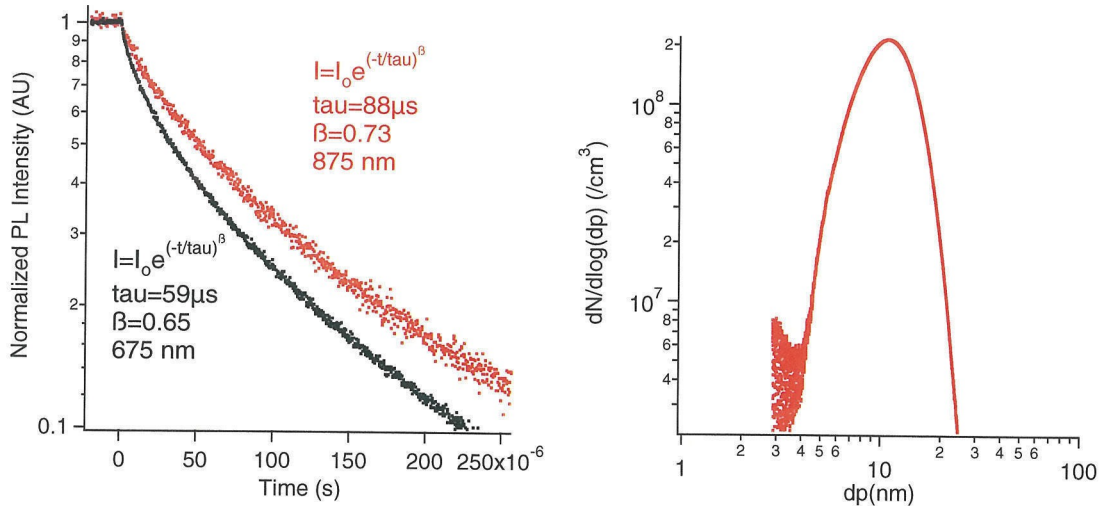
ranging from 10–70 min at 673 K and subsequently annealed in a 5% H<sub>2</sub>/N<sub>2</sub> mixture for 1 hr at 723 K. Particles in the oxidizing environment for more than 40 min showed PL, Fig. 4.3(a), with PL decay times, Fig. 4.3(b), consistent with exciton recombination in Si.<sup>107</sup> PL decay is prolonged at longer wavelengths, consistent with the increase in particle size. The oxide growth rate predicted by the Massoud model<sup>32,87</sup> at 673 K is negligible, so further growth of the oxide shell is not expected. However, kinetic theory predicts many collisions of oxidants with the nanoparticles' surface. Dangling bonds may be passivated at this relatively low temperature. The peak of the PL spectrum varied little whether the particles were processed for 40 min or 70 min, but the intensity increased, suggesting that dangling bonds were being nullified, but little additional oxidation (i.e., particle core shrinking) was occurring. The  $\beta$  values are typical of a dense ensemble of interacting particles.<sup>19</sup>

Figure 4.4 compares the PL spectral emissions from originally similarly sized nanoparticles, one group with an HTO grown shell and the other a native oxide shell. The measured particle size distributions are nearly identical, Fig. 4.4(b), but the PL spectral emission for the HTO-coated particles is blueshifted  $\sim$  100 nm with respect to the native oxide particles, indicating a smaller crystalline core size and thicker oxide.<sup>33,56</sup> Moreover, PL decay time is reduced for the HTO-coated particles, also consistent with a smaller core size.<sup>43,103</sup> PL decay was recorded at 750 nm for HTO-coated particles and 850 nm for the native oxide-coated particles. The  $\beta$  value of 0.63, lower than typically reported values near 0.7, calculated for the PL decay is suggestive of greater interaction between these particles.

Figure 4.5 shows particle size distributions of collected particles and estimated oxide thicknesses for particles with a native oxide. While the shell thickness varies amongst the samples, the trend of increasing shell thickness toward smaller sizes is similar. Previous studies suggest that the shell thickens with continual exposure to the air.<sup>83</sup> Seto observed<sup>117</sup>



(a) PL spectral trace for particles further oxidized for 60 min in house N<sub>2</sub>.



(b) PL decay traces at 675 nm and 875 nm.

(c) Particle size distribution of original silicon nanoparticles before further oxidation.

Figure 4.3: PL, PL decay, and particle size distribution from HTO-coated silicon nanocrystals.

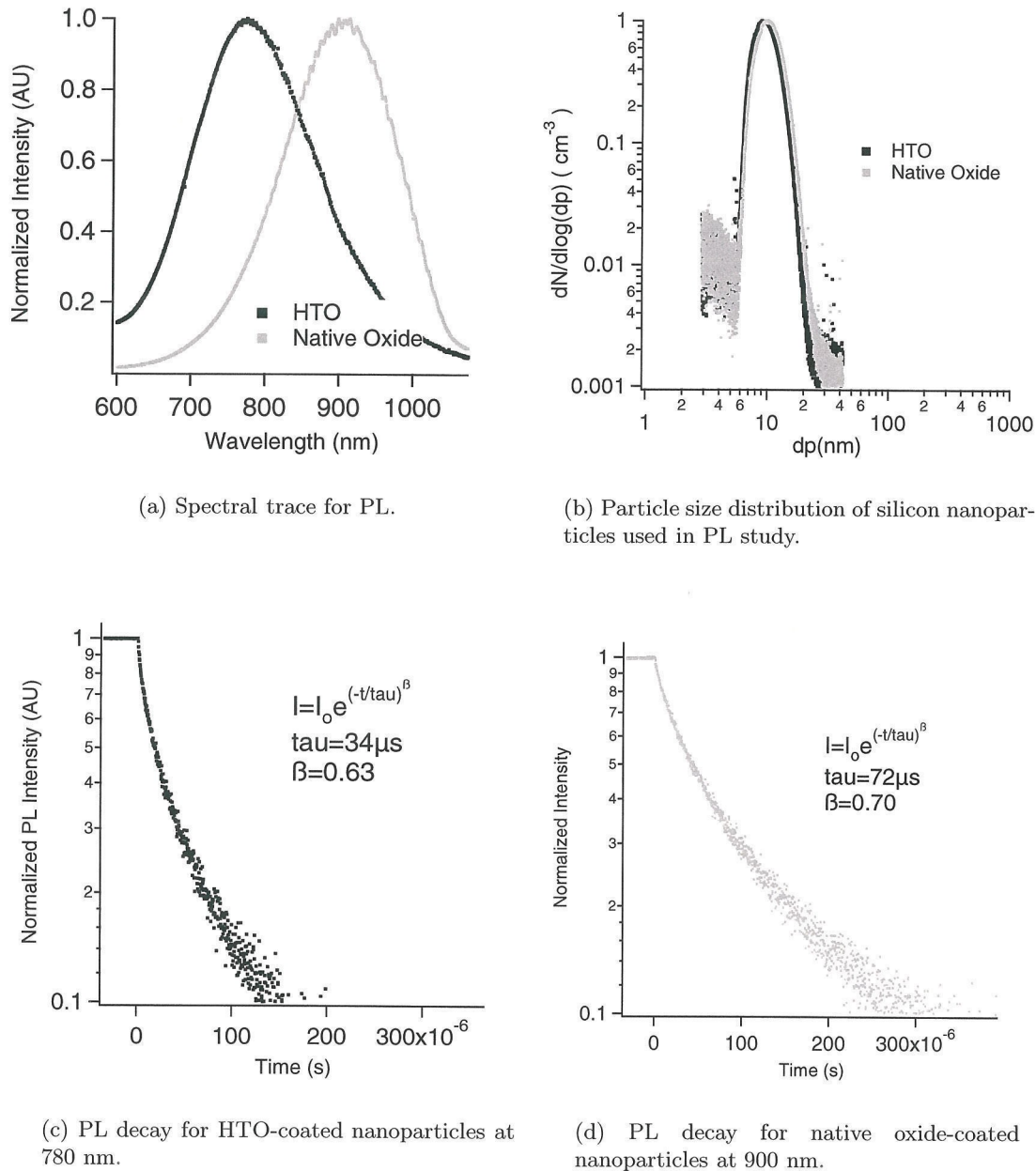


Figure 4.4: PL, PL decay, and particle size distributions from similarly sized oxide-coated silicon nanocrystals. Native oxide-coated particles are exposed to O<sub>2</sub> after characterization with the RDMA.

from HRTEM that lattice fringes could only be seen in particles larger than 4–5 nm diameter and suggested that the amorphous character of the particles arose from the relative high surface energy of these particles.<sup>121</sup> The trend seen here is consistent with Seto's observations and implies that the native oxide growth is both quick and catastrophic for smaller particles.

The two PL spectra, corresponding to NO-2 and NO-3 in Fig. 4.5(c), were collected within 48 hours of PL study and were luminescent. However, the NO-1 sample did not luminesce when first collected. After thermal treatment for 60 min at 673 K in house N<sub>2</sub>, luminescence was observed, without further annealing in forming gas. The small size of the particles seen in the original NO-1 particle size distribution suggests that lack of PL may have been a function of a poorly passivated silicon surface rather than particle size.

The PL trace from NO-4 in Fig. 4.5(c) was observed seven days after particle collection. Its calculated shell thickness lies between that of the young native oxide and a thermal oxide, consistent with observations of increased oxide growth over time by Ledoux.<sup>83</sup> The calculated thickness seen in the trace is likely skewed larger for larger particle sizes as the equal-efficiency/rate assumptions become invalid. Ledoux and others report a strong drop-off in PL efficiency for larger sizes of silicon nanocrystals.

TEM images, Fig. 4.6, obtained within 48 hours of particle exposure to the ambient air also suggest this initial trend of shell growth. The large particles have relatively thin shells of 0.5–1.5 nm. Greater oxidation is observed in the images orthogonal to the [111] lattice fringe lines, consistent with silicon planes oxidizing at different rates.<sup>87</sup>

With HTO-coated particles, the calculated oxide thickness increases with particle size, as seen in Fig. 4.7, as it does in the HRTEM images. (Fig. 4.8) Calculated oxide thickness in samples HTO-2, HTO-3, and HTO-5 group well. Both the particle size distribution and

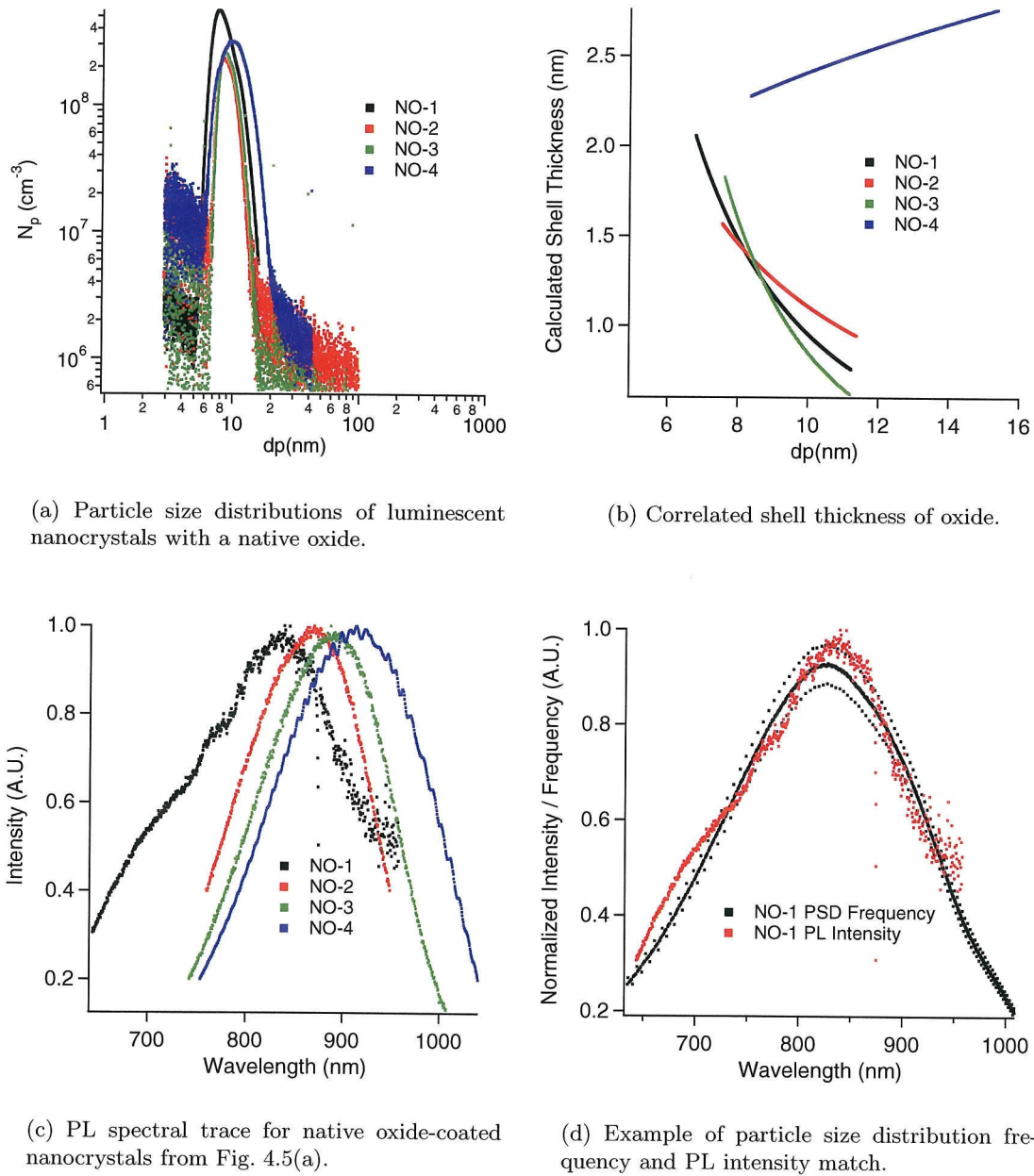


Figure 4.5: Data matched PL Intensity to RDMA particle size characterization for native oxide-coated particles.

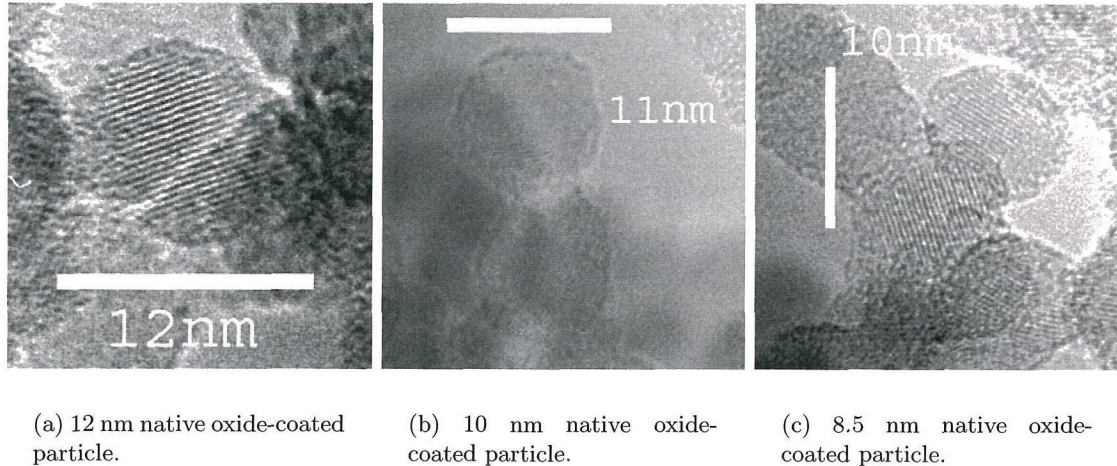


Figure 4.6: HRTEM images of native oxide-coated particles.

oxide thickness are larger in trend for sample HTO-1 and both significantly smaller for HTO-4. Both may result from the equal efficiency/rate assumption not being valid at the larger sizes of particles, since the growth parameters were little varied at the reactor.

The sample HTO-6-60min contained larger particles that did not luminesce initially. After annealing for 1 hr in house  $N_2$ , luminescence was observed. The corresponding particle size distribution indicates that, assuming a well-passivated oxide surface, there were sufficient numbers of small particle cores to observe luminescence, but the lack of a blue-shift in luminescence may indicate a poorly passivated surface from incomplete mixing in the reactor or that exciton energy from small particles may be transferred to larger particles over a finite distance.

HRTEM images, seen in Fig. 4.8, show silicon nanoparticles with an HTO-grown oxide coating. These nanoparticles exhibit a more uniform and thicker oxide at the sizes shown, in agreement with the calculated thickness. The large shell thicknesses,  $\sim 3\text{--}4$  nm derived from the data matching were neither confirmed nor denied by HRTEM images. The size is likely influenced also by the equal rate/equal efficiency assumption.

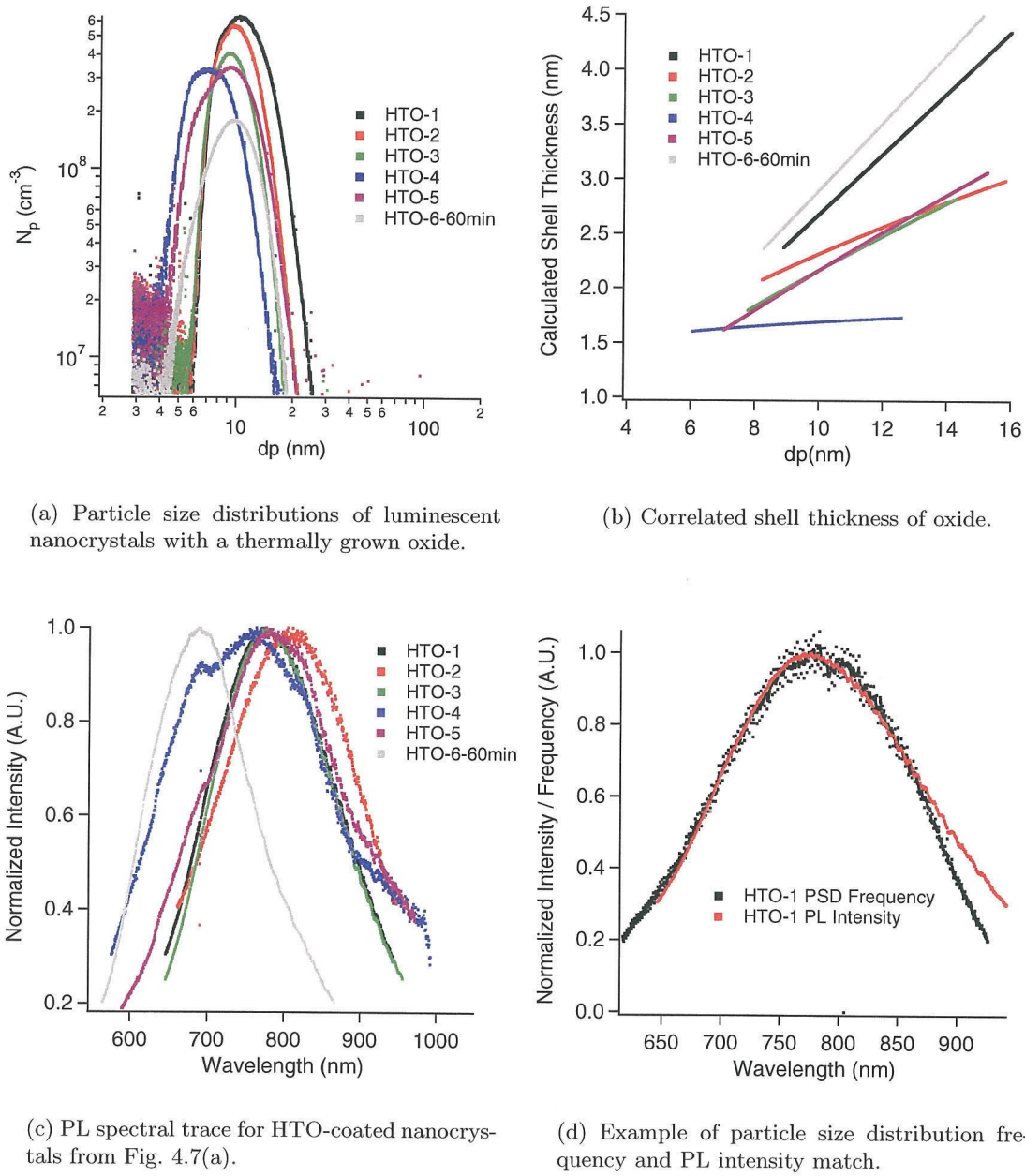


Figure 4.7: Data matched PL Intensity to RDMA particle size characterization for HTO-coated particles.

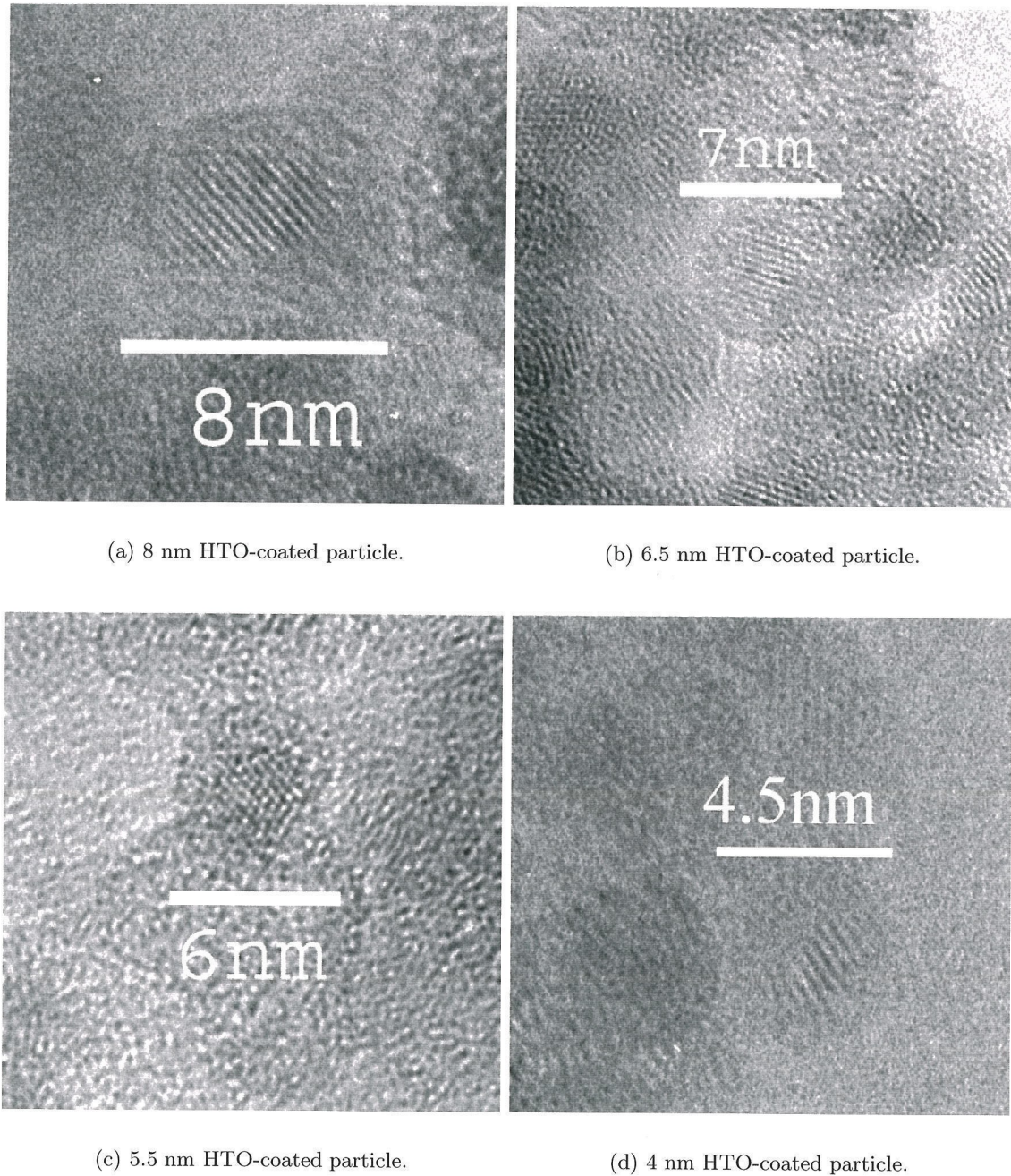


Figure 4.8: HRTEM images of HTO-coated particles showing greater uniformity of shell thickness than observed on native-oxide coated particles.

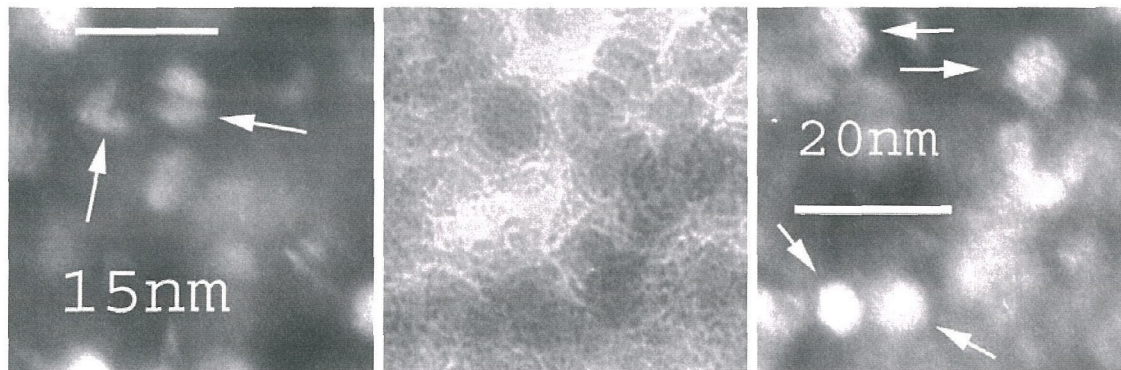
Trace	Median Diameter (nm)	Median Wave-length (nm)	Median Diameter Absorption Corrected (nm)	Core Diameter (nm)	Oxide Thickness (nm)	$\tau_{Decay}$ ( $\mu$ s)	$\beta$	$\tau_{Decay}$ wavelength (nm)
NO-1	7.7	839	8.3	6.7	1.4			
NO-2	8.4	885	9.1	7.8	1.2	91.0	0.69	900
NO-3	8.5	865	8.8	7.4	1.3			
NO-4	9.9	912	11.2	8.3	2.5	72.5	0.70	850
HTO-1	11.4	775	12.9	5.9	3.5			
HTO-2	11.0	804	11.3	6.4	2.4			
HTO-3	10.3	770	10.3	5.8	2.2	34.0	0.63	750
HTO-4	8.6	762	9.1	5.7	1.7			
HTO-5	10.1	775	10.4	5.9	2.2			
HTO-6	10.6	685	11.6	4.8	3.5	58.9	0.65	675
HTO-6	10.6	685	11.6	4.8	3.5	88.0	0.73	875

Table 4.1: Summary of particle size and calculated core diameter/shell thicknesses for median particles and applicable photoluminesce data.

In Fig. 4.9(a), a darkfield image of a pair of 8 nm doublet particles suggests that some particles may crack during oxidation, leaving a wedge within the particle for further oxidation to develop. With sufficient time in the furnace, these particles are more likely to be completely consumed than intact particles of the same size.

The particle cores shown in Fig. 4.9(c) range from faceted to nearly spherical. The faceted particle in the upper right corner suggests that intense oxidation may break some particles into small crystallites. If the formation of crystallites leaves grain boundaries at this silicon-oxide interface, this may also provide sites for nonradiative exciton recombination. The brightfield image included in Fig. 4.9(b) pairs with the image of Fig. 4.9(c), showing that the collected particles were well agglomerated on the TEM grid. Some intensity drift is seen in the darkfield image from the long exposure time.

Particles were collected and analyzed to determine whether metal was evaporating from



(a) Oxidation appears to wedge some particles and crack them open to further oxidation.

(b) Brightfield image of particles seen in (c).

(c) Aerosol nanoparticles appear with both faceted and spherical morphology.

Figure 4.9: TEM images of various morphologies of HTO-oxide coated nanoparticles.

the Inconel reactor and condensing onto the nanocrystals. A search for contaminants found no detectable contamination within the threshold of methods applied. HTO shell particles were studied using XPS and only peaks for silicon, oxygen, and carbon were observed. The carbon peak is likely a result of chamber contamination. However, the sensitivity of XPS is limited to  $\sim 5\%$ , several orders of magnitude greater than the 1 metal ion per nanoparticle ( $\sim 10000$  Si atoms) needed for PL quenching. Thus XPS confirmed only that there was no bulk contamination coming from the reactor.

Particles were also studied under a FEI Technai F20ST 200 keV Scanning/Transmission Electron Microscope, equipped with EELS and EDS capabilities. Electron Energy Loss Spectroscopy (EELS) and Z-contrast analysis of a single particle may be interpreted as evidence of contamination.<sup>88,89</sup> The particle size distributions for the three samples are seen in Fig. 4.10.

Particles with a native oxide, Sample A5 seen in 4.11, showed strong evidence of bulk silicon with EELS, Fig. 4.11(a), high contrast under High Angle Annular Darkfield (HDAAF)

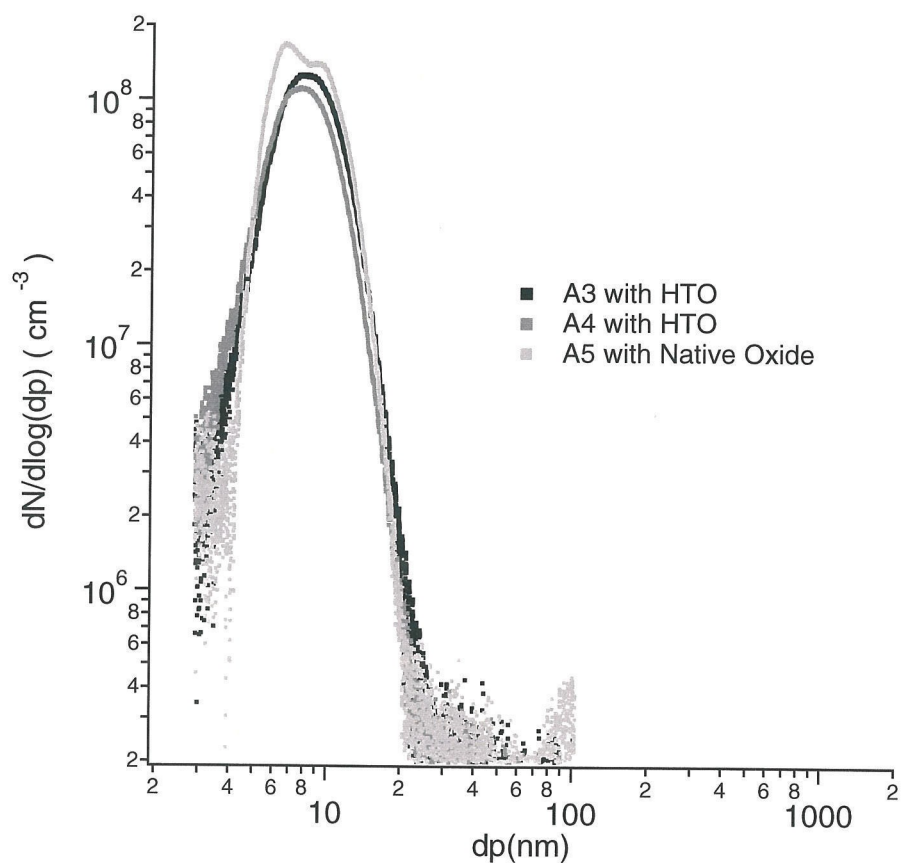
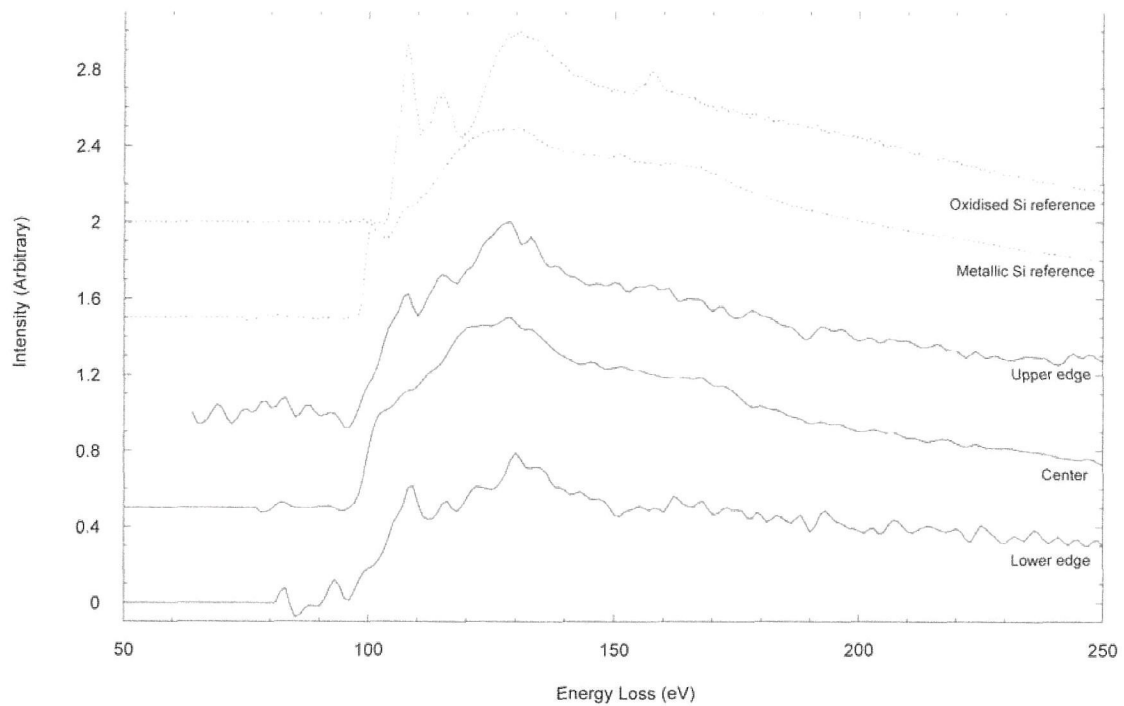


Figure 4.10: Particle size distributions of particles used in EELS study.

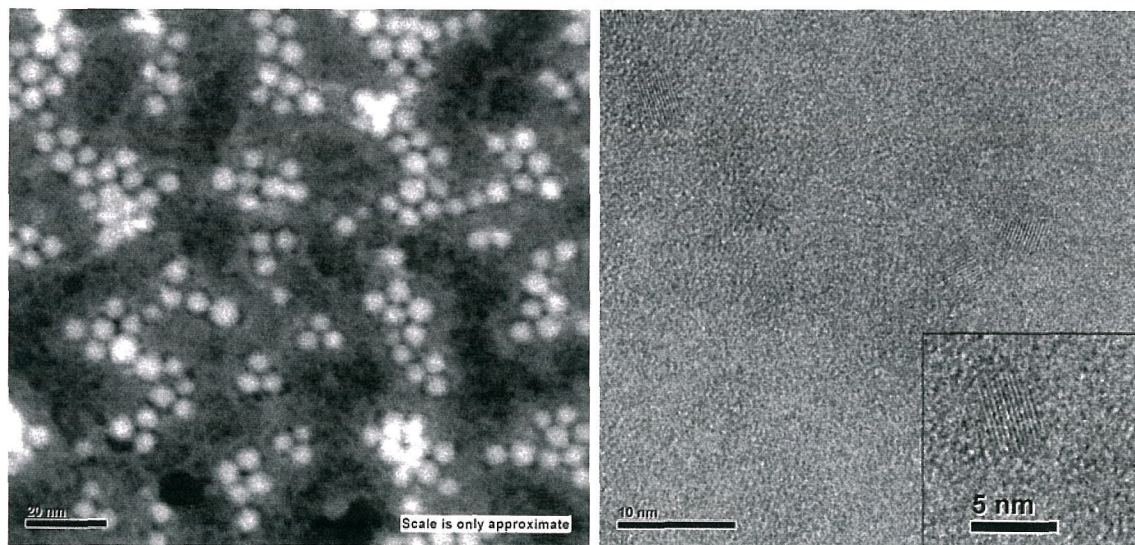
Imaging, Fig. 4.11(b), and lattice fringes under HRTEM, Fig. 4.11(c).

HTO-coated particles, Sample A4 seen in Fig. 4.11, loaded into the scope in a cryogenically cooled stage also showed evidence of  $\text{SiO}_x$  and Si under EELS and strong Z-contrast of the particles. Sample loading onto the cold stage condensed a water vapor film that quickly dissipated under the electron beam, but may have allowed surface tension to draw particles into clumps, Fig. 4.11(b), and thickened the oxide shells leaving Si cores, Fig. 4.12(c), as little as 2–3 nm.

HTO-coated particles, Sample A3 seen in Fig. 4.13, were loaded into a non-cooled sample holder. No condensation occurred on the particles and the particles remained intact on the grid (Fig. 4.13(b)). EELS spectra indicates both silicon and its oxide (Fig. 4.13). Quantification of the EELS spectra up to an energy loss of 1000 eV estimated an Fe concentration of up to 3%, but there was no visible discernable Fe L edge in the spectrum (first and second derivatives to the spectrum did not indicate a feature presence of Fe L). This apparent Fe concentration is thought to be an artifact, leaving only evidence for the presence of silicon, oxygen, and carbon.



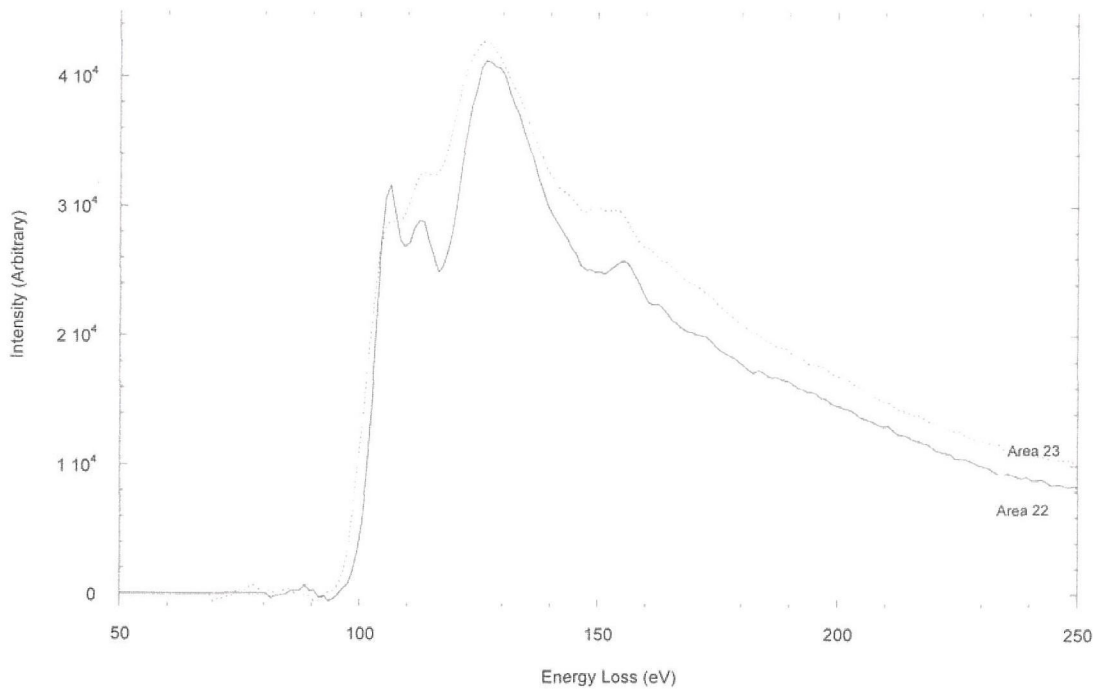
(a) EELS spectra at particle edges and center of an 8 nm native oxide-coated particle. Top two traces are reference traces for bulk Si and  $\text{SiO}_2$ .



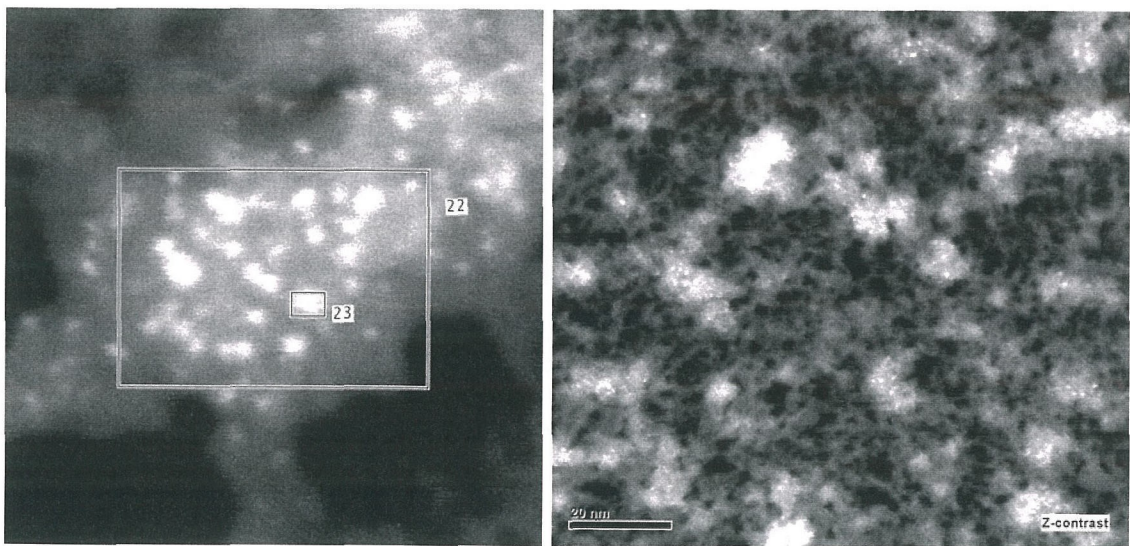
(b) HAADF image of particles with native oxide.

(c) HRTEM image of particles with native oxide.

Figure 4.11: EELS, HRTEM, and HAADF from contamination studies on particles made in Inconel reactor.



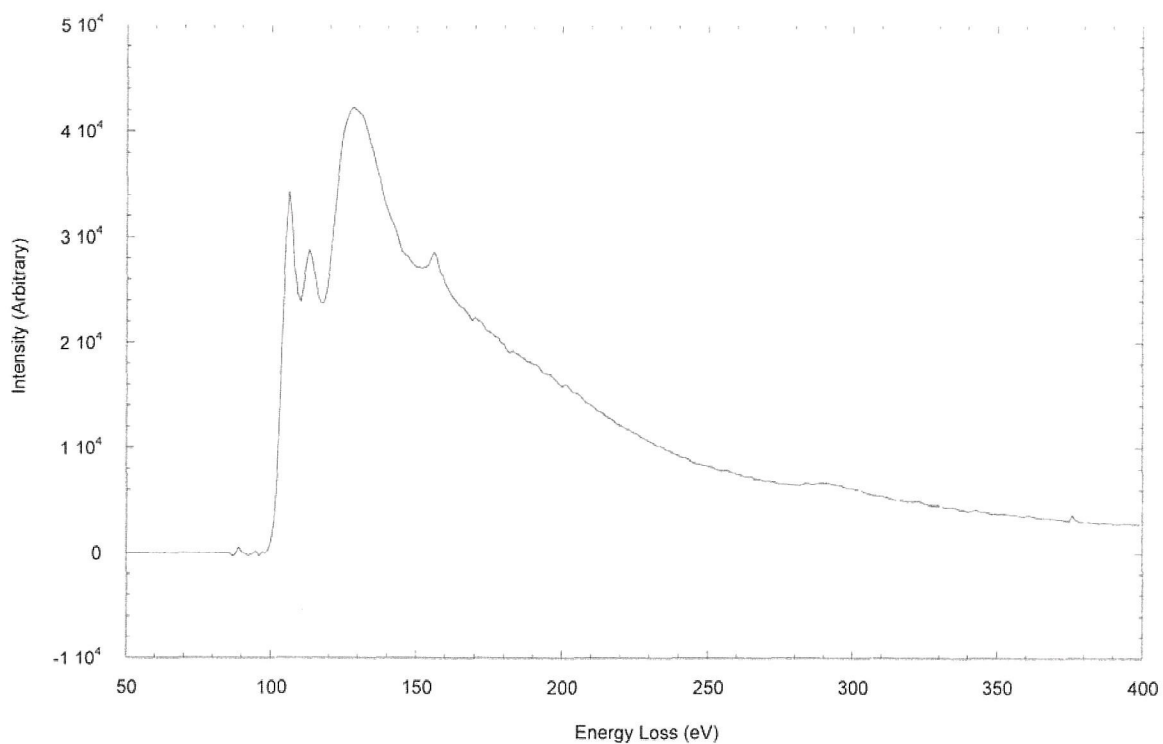
(a) EELS spectra from Areas 22 and 23 seen in Fig. 4.12(b). The top two traces in Fig 4.11(a) are reference traces for Si and  $\text{SiO}_2$ .



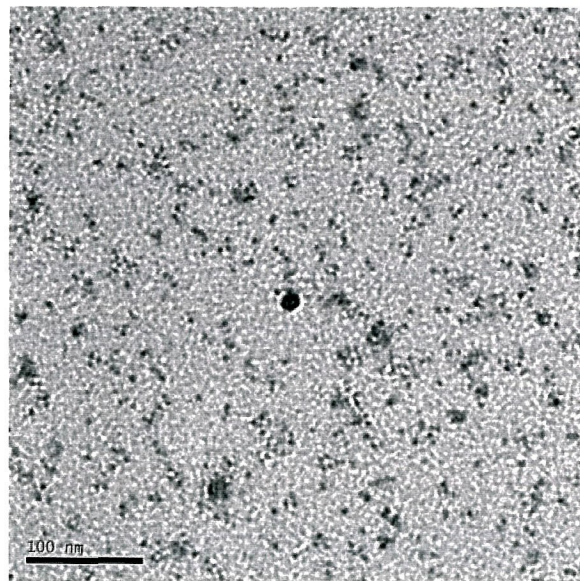
(b) HAADF image of particles with HTO oxide, apparently further oxidized by water during sample loading in a cryogenically cooled sample holder.

(c) Z-Contrast image shows crystallite structures of 1-2 nm.

Figure 4.12: EELS, Z-Contrast, and HAADF from contamination studies on particles made in Inconel reactor.



(a) EELS spectra on particles seen in Fig. 4.13(b). The top two traces in Fig. 4.11(a) are reference traces for Si and  $\text{SiO}_2$ .



(b) Conventional TEM image of particles with HTO oxide.

Figure 4.13: EELS and conventional TEM images from contamination studies on particles made in Inconel reactor.

#### 4.4 Conclusions

Using an RDMA for online particle size characterization of photoluminescent oxide-coated silicon nanocrystals demonstrates differing trends in oxidation. Particles with an HTO-coated oxide have more uniform oxide shells at all sizes and the oxide thickness increases with particle size. Native oxide-coated particles initially exhibit thicker oxides for small particles, with particles less than 5 nm becoming consumed by the oxidation process, and the oxide layer decreasing in thickness as particle size increases. Over time, the oxide layer thickness for these particles increases, approaching similar thicknesses calculated for the HTO-coated particles. Larger, bulk-size, silicon nanoparticles require additional passivation before photoluminescence from quantum-confined exciton emission is observed. While photoluminescence quenching for the largest particles studied is likely due to size, for mid-size particles it may indicate an incomplete or inhomogeneous oxide shell with non-radiative recombination sites. For smaller particles an energy transfer mechanism may quench photoluminescence until larger particles are well passivated. Studies by EELS, EDS, and XPS found no evidence of metal contamination from the Inconel reactor. Evidence from PL spectra and PL decay time are consistent with exciton recombination in silicon nanocrystals, but  $\beta$  parameters tend to lower values, suggesting greater energy interaction amongst the dense ensembles of particles. TEM imaging and EELS analysis demonstrate that particles contain crystalline cores with oxide shells of varying thickness depending upon growth conditions. Particles from the reactor show semiconductor quality, insofar as the existence of a PL trace is evidence of particle purity.

## Chapter 5

# Reactor Fouling And Seeding

### Abstract

Fouling of narrow diameter laminar flow nucleating aerosol pyrolysis reactors rapidly reduces both particle numbers and particle sizes when the shape of the particle size distribution remains similar, the particle number concentration is observed to decay linearly with time. A reactant-free laminar flow sheath shows some promise of inhibiting fouling in one configuration. While fouling might be eliminated through better reactor design, a different strategy for driving nucleation may be a superior alternative. A microplasma discharge reactor that seeds a turbulent mixing reactor demonstrated stable particle number and size production over tens of hours of continuous operation. We present some early results of hybridization of a turbulent mixing reactor with a microplasma-discharge seed reactor.

### 5.1 Introduction

Numerous studies have examined aerosol synthesis of semiconductor nanoparticles by the evaporation/condensation method,<sup>23</sup> externally heated laminar flow reactors,<sup>145</sup> laser ablation,<sup>57,149</sup> flame pyrolysis,<sup>106,133</sup> and other methods. Most of the studies have focused on control of particle size, crystallinity, and/or the extent of agglomeration. Ostraat<sup>102</sup>

employed a multistage laminar flow reactor to synthesize nonagglomerated nanoparticles comprised of 5–10 nm diameter single crystal silicon cores that were encased in a silica shell. These composite nanoparticles were synthesized under clean conditions, deposited immediately onto 200 mm diameter silicon wafers, and processed through an industrial semiconductor fabrication plant to produce novel nonvolatile memory devices. In these memories the nanoparticles served as a discontinuous floating gate, rendering the charge retention of the memory more robust than conventional devices with a continuous floating gate. Although the performance of the devices synthesized by this route and the properties of the materials synthesized in other reactors are very promising, a number of challenges remain to be overcome before aerosol technology is routinely integrated in microelectronics processing.<sup>38</sup> Foremost is reluctance to introduce particles into the manufacturing process after decades of work aimed at removing particles from the cleanroom and processing tools. Skepticism about the use of aerosols in device fabrication will only fade after additional demonstrations of the unique capabilities of aerosol synthesis, and further demonstrations that aerosol routes can be advantageously employed without risk to the expensive tools and processes involved in microelectronics fabrication.

The study of nanoparticle aerosols need not be limited to applications in solid state devices or environmental impact. An emerging application for silicon nanoparticles is that of luminescent biological tracers.<sup>91</sup> These particles are typically formulated in colloidal suspensions. Liquid phase synthesis facilitates greater mass production due to the greater density of the fluid phase and to tight size control through manipulation of interparticle forces, but possibly at the expense of flexibility in composition and heterogeneous structure. Solid phase synthesis is also a well-established method for fabricating homogeneous particles embedded in matrices, but harvesting these particles for use in other applications is a costly

process.

In contrast, aerosol synthesis may offer a solution to producing a wide range of harvestable, size-selected nanoparticles. Continuous production in a flow environment offers flexibility in both composition control and methods of deposition. But these advantages typically are achieved at the expense of mass production. Flagan and Lunden<sup>38</sup> showed that increases in aerosol nanoparticle production rates are best achieved by reducing the residence time in the reactor. In recent years, mass quantities of condensable products have been realized using laser,<sup>57</sup> spark, arc, microplasma,<sup>113</sup> or flame-induction decomposition methods, but these methods often induce intense nucleation and thus coagulation aerosols.

Laminar flow reactors that have been the focus of much work to date are not well suited to the production environment. Due to the long residence times in most laminar flow reactors, particle number concentrations must be kept low to prevent runaway agglomeration. The low flow rates, combined with the low number concentrations, lead to low production rates. Successful incorporation of aerosol nanoparticle deposition into a process such as device fabrication will require that deposition times be competitive with conventional process steps. Higher throughput processes that maintain control over nanoparticle properties while minimizing contamination are therefore needed.

A recent demonstration of a turbulent mixing reactor<sup>60</sup> showed particle production in excess of  $10^9 \text{ cm}^{-3}$ . However, particle deposition on the walls degraded its performance over time. Similar degradation has been observed in each of the relatively narrow tube laminar flow reactors studied earlier. Examination of the larger quartz tube reactors used earlier also showed that there was particle deposition in the nucleation and exit regions, but reactor performance was not noticeably degraded since the larger available volume limited the effect of deposition during labscale operations.

Fouling of narrow diameter laminar flow aerosol reactors rapidly reduces both particle numbers and particle size, limiting the effective operation of these reactors to tens of hours before flow chokes and the reactor fails. Although some reactors, notably metal reactors, may be mechanically cleaned to restore the original performance, the need for consistent output over longer periods of time remains. Fouling is most apparent in the early reaction region where precursors decompose, nucleate, and form small clusters. In decomposition reactors, heat transfer from the walls provides the energy to initiate the reaction. This close proximity to the reactor wall combined with slow convection and the relatively large diffusivity of the small clusters ensure rapid transport to the reactor walls, scrubbing and filtering up to 99% of the reactant.

What is clearly needed is a reactor that can combine the features of high nucleation rate reactors with the robustness of the laminar flow reactor, while preventing runaway particle agglomeration. A promising alternative is to generate seed particles with an intense reaction such that the nuclei rapidly grow into slower moving clusters before significant loss occurs. However, this high rate reactor would be sufficient for developing only the smallest nanoparticles due to inherent limits to the rate of particle growth. Nucleation must be quenched quickly, usually by dilution, to prevent the accumulation of such large numbers of particles that coagulation becomes the primary growth mechanism. Hybridization of the microplasma reactor, while limiting nucleation, with a turbulent mixing reactor may allow efficient generation of controlled numbers of particles, and a means to add additional mass while ensuring densification and/or crystallization.

This chapter will present evidence of fouling for several configurations of reactors and initial data of a hybridized microplasma/turbulent mixing reactor. Effects of fouling with time on the particle number production will be shown. A reactor employing a laminar

sheath flow around the nucleating particles shows some promise in reducing fouling. Characterizing particle distributions from the microplasma-seed turbulent reactor with a radial differential mobility analyzer, we show evidence of thermally induced particle densification. We introduce additional cold reagent, observe evidence of vapor deposition growth, and avoid simultaneous homogeneous nucleation.<sup>98</sup>

## 5.2 Experimental Methods & Design

### 5.2.1 Reverse Flow Shell & Tube Assembly

These experiments used a 7.525/9.525 mm annular nucleation region followed by flow reversal and exit through a 6.35/4.35 mm or 3/5 mm exit tube. The silane containing feed is introduced in the annular region where it is heated both internally from the exiting gas and externally by convection and conduction from the furnace insulation. The exit tube is positioned within the annular space so the tube opening is physically located just inside the furnace hotzone. As the flow enters the hotzone of the reactor, it is heated and the reaction begins. The flow then quickly reverses direction and exits the reactor through the inner tubing. At the point of flow reversal, an opposing flow is also drawn into the inner flow tube, as illustrated in Fig. 5.1, that is preheated by passage through a 15 cm hotzone maintained between 1273 K and 1523 K.

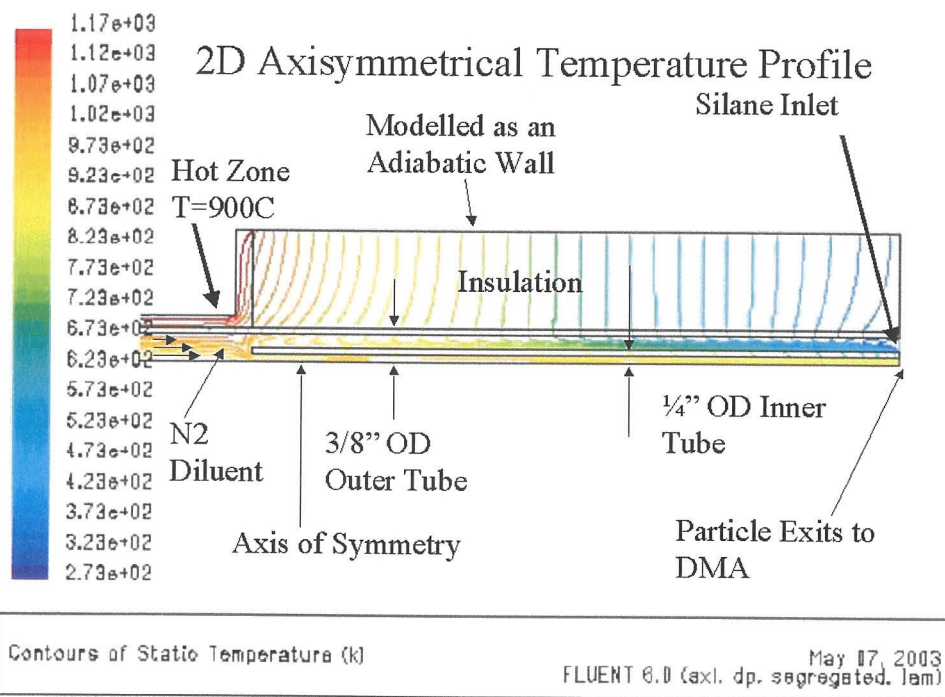


Figure 5.1: Isotherms of Laminar Shell & Tube Reversing Flow Aerosol Reactor modeled in Fluent<sup>TM</sup>.

### 5.2.2 Shell & Tube Nucleation/Growth with Subsequent Mixing Jet

This configuration featured a shell-in-tube laminar nucleation and quenching zones followed by a pair of mixing jets to introduce additional reagents for heterogeneous particle development. Although a fused quartz reactor was first tried (to ensure cleanliness), it was too fragile for extended use. Experiments were, therefore, performed using a reactor made from Inconel-625. A 4.35/6.35 mm tube inserted into a 12.7 mm OD cavity. This cavity tapered by  $45^\circ$  to a 4.35 mm ID tubing. A 39.1 mm growth chamber followed with this diameter. At the end of the growth chamber a pair of radially opposing 1 mm mixing jets allowed the introduction of preheated  $O_2$  into the aerosol stream. Both the annular flow  $N_2$  and mixing jet  $O_2$  were preheated to  $\sim 1273$  K.

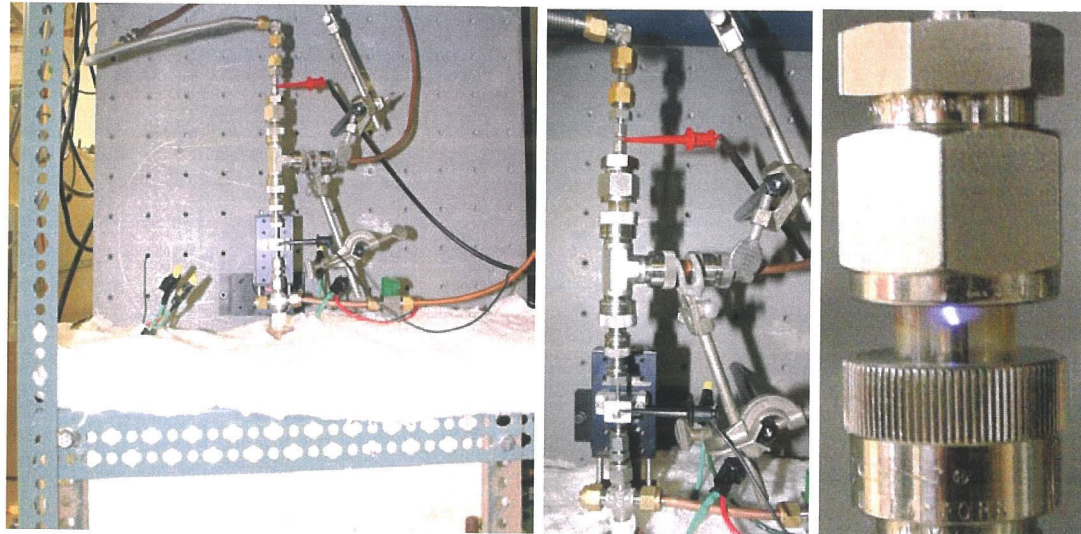
A laminar nucleation zone and mixer were employed to inhibit fouling seen in earlier narrow diameter reactors. Preheated  $N_2$  is introduced in an annular space around the nucleation zone, heating the tubing and inducing silane decomposition as near its outlet as possible. With laminar mixing following nucleation, the aerosol is limited by diffusional processes for both thermal and mass transfer.

### 5.2.3 Laminar Flow Nucleation, Turbulent Mixing Jets Reactor

This configuration is comprised of narrow, 3.9 mm, inlet tubing wherein  $SiH_4$  decomposition and nucleation occurs. Two pairs of 1 mm radially opposed mixing jets, separated by 39.1 mm, are preheated to 1273 K before introduction into the aerosol flow. The first jet supplies  $N_2$  diluent, the second jet  $O_2$  as an additional reagent. This reactor has been described in more detail previously.<sup>60</sup>

### 5.2.4 Microplasma-Seeded Turbulent Mixing Jets Reactor

The microplasma reactor is described in more detail elsewhere.<sup>113,114</sup>  $\text{SiH}_4$  is decomposed in a hollow cathode plasma jet, Fig. 5.2 struck in Ar. A sheath of  $\text{N}_2$  gas is introduced around the discharge, mixing with the aerosol stream downstream of the hollow anode. Additional reagent may be added with the sheath  $\text{N}_2$  flow, or downstream via a Tee-assembly at the furnace entrance. The furnace is maintained at a constant temperature between 973 K–1273 K. This reagent/aerosol mixture is heated by conduction from the hotwall during laminar flow, inducing reaction and increasing the primary particle size by vapor deposition growth. The concentration of the reagent must be kept sufficiently low to avoid homogeneous nucleation.<sup>98</sup> In the furnace, preheated  $\text{N}_2$  in a ratio exceeding 5:1 with the aerosol stream is introduced through a pair of mixing jets to raise the temperature of the aerosol to sufficiently high temperature, thermal energy for densification.



(a) Microplasma discharge assembly above Turbulent Mixing furnace. (b) Microplasma assembly. (c) Discharge struck in argon.

Figure 5.2: Microplasma Discharge Assembly Above Turbulent Mixing furnace.

### 5.3 Results

#### 5.3.1 Fouling in Reverse Flow Shell & Tube Assembly

In this work with the reversing flow reactor, the outlet tubing was as small as 3 mm inside diameter. Conductive heating in the narrow annulus between the inner and outer tubes induces silane pyrolysis and particle nucleation. The discoloration in the wall of the quartz tube, Figure 5.4, shows thin film at the cold region upstream of the reactor hotzone. This deposition pattern most likely results from vapor deposition at temperatures too low to nucleate and grow particles. Farther downstream, the film develops a texture, presumably due to deposition of small, high diffusivity particles. This begins the fouling process. Coalescence of particles is limited at the relatively low reactor temperatures. Farther downstream, the texturing of the surface becomes the dominant deposition profile, and the build-up begins to extend into the flow from the surface. This fouling, now macroscopic in nature, may lead to a filtering effect on the aerosol, as suggested by the gradual decrease in both the number and size of particles observed in on-line particle size distribution measurements with the RDMA. The continuous transport of reactant gas and ultrafine particles to the tube walls eventually produces dendritic structures on the wall that may filter particles, as seen in Fig. 5.5.



Figure 5.3: From right to left: far right: Thermophoretic deposition of cooling nanoparticles leaves light brown coating on inside of exit tubing; middle: Silicon film deposits, likely from CVD; far left: fouling on the outer side of the inner tubing. Tube outer diameter is 6.35 mm.

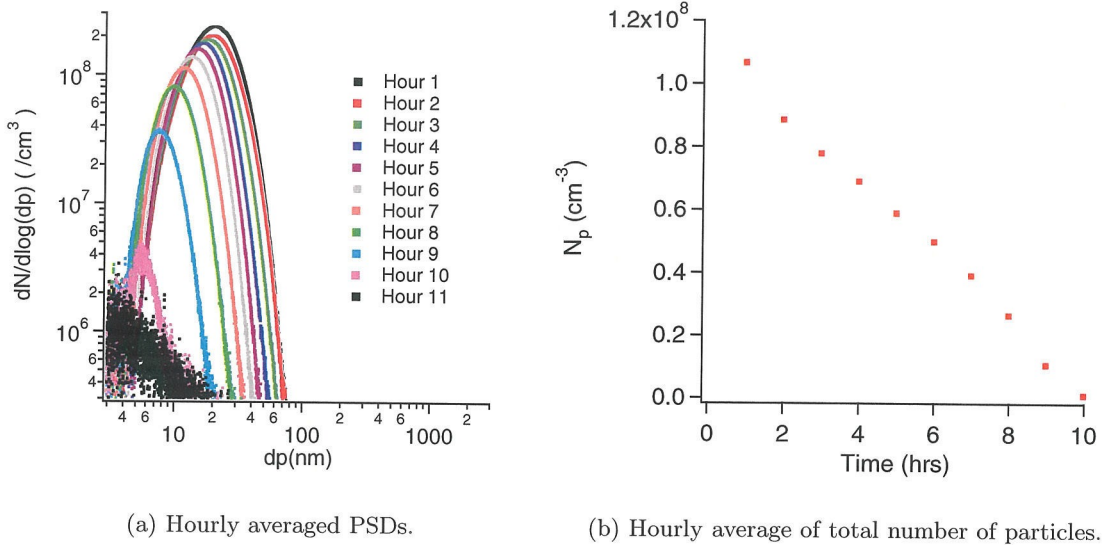


Figure 5.4: Effect of fouling on particle distribution over time.

A log-log plot of the particle size distribution reveals that, for this reactor, the trend is seen as a consistent linear decrease in the number concentration. Fouling constricts the reactor tubing, increasing the flowrate of the aerosol stream. As the velocity of reactant increases and the deposited silicon inhibits conductive heat transfer from the hotwall, the rate of silane decomposition is reduced. Particle numbers are decreased. With this additional loss of reactant, and the filtering effect that discriminates towards removing larger particles, the size measured at the RDMA concurrently is also decreased. The effectiveness of filtering increases as the buildup creates a more tortuous path for the aerosol, in spite of the increased velocity. Figure 5.4 shows the performance degradation over 11 hours of continuous operation with constant inputs of 200 sccm of 50 ppm SiH<sub>4</sub> in N<sub>2</sub> mixed with 300 sccm N<sub>2</sub> at 1273 K. In the last two hours, the degradation becomes catastrophic.

Figure 5.5 is an image of the reactor side internal tubing in the shell-in-tube assembly. The original inside tube diameter was 4.35 mm. Figure 5.5(b) is an image the same tube that shows the extent of the macroscopic buildup which has filtered particles and begun

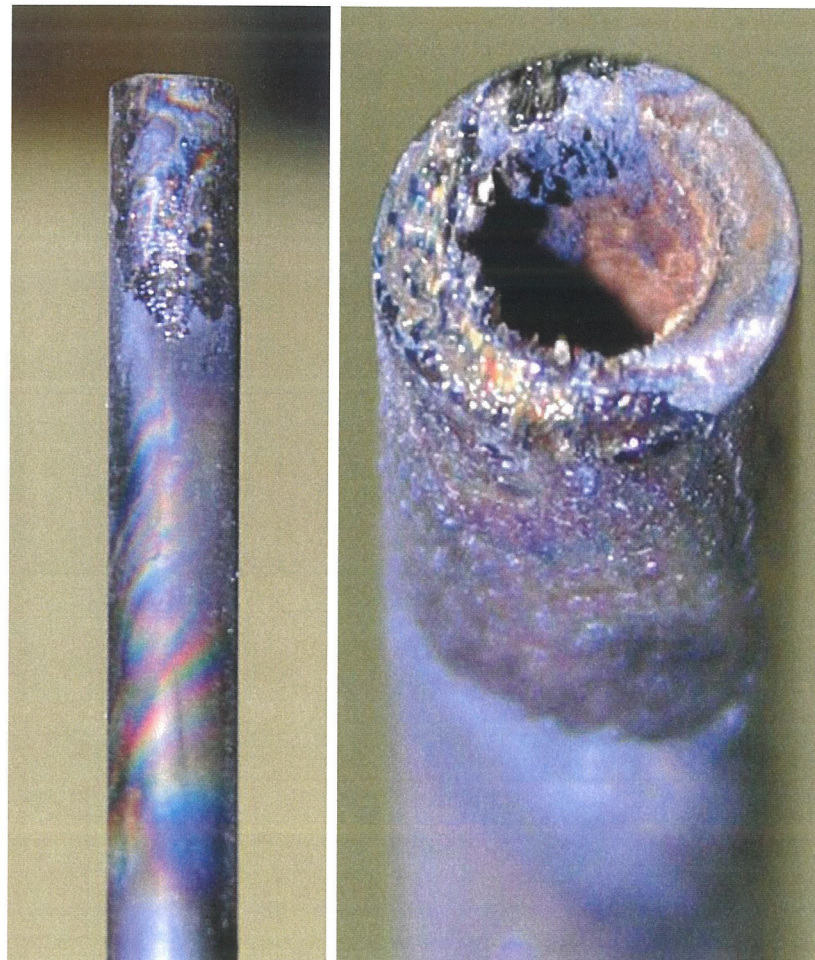
choking gas flow. In another series of experiments, the final tube diameter, when removed from the reactor, was  $\sim 1$  mm.

### 5.3.2 Fouling in Shell & Tube Nucleation/Growth With Subsequent Mixing Jet

With this configuration, at higher flowrates, fouling of the reactor was temporarily reduced. Fig. 5.6(a) shows the time evolution of reactor product from RDMA characterized traces. These PSDs are of an agglomerate aerosol, but there is little change observed over the seven hour period of operation. The increase in particle numbers over time, Fig. 5.6(b), and coincides with a small decrease in the mass output, indicating that fouling is occurring, albeit at a slower rate. The reduction effect is more dramatic than the graphs suggest since the concentration of  $\text{SiH}_4$  used in this experiment was  $\sim 433$  ppm, 5–10 times more than used in later studies. This reactor was not studied in much detail. Although narrower size distributions of smaller particles could be made by adjusting feed concentration and flowrate, particles numbers dropped considerably at sizes less than 18 nm. At lower flowrates and lower concentration of  $\text{SiH}_4$ , fouling proceeded much more rapidly as nucleation and early particle growth occurred entirely within the narrow diameter inlet tubing.

### 5.3.3 Fouling in Laminar Flow Nucleation, Turbulent Mixing Jets Reactor

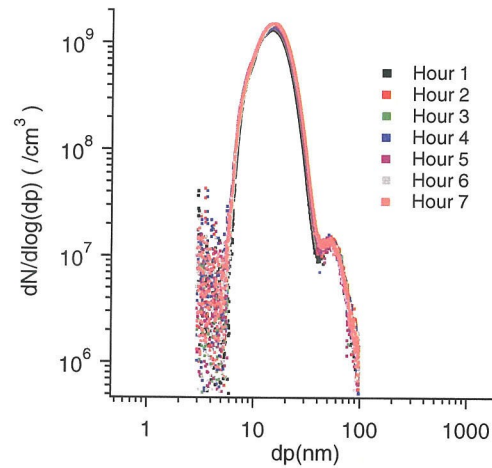
Although this configuration is subject to fouling, it also had the greatest throughput of  $\sim 10$  nm nanoparticles. This reactor has the advantage that mechanical cleaning restores performance and has been subjected to numerous fouling and cleaning iterations. Fouling occurs a few centimeters before the first pair of mixing jets, constricting the diameter of



(a) Fouling on outer wall of 6.35/4.35 mm tubing. A gradual transition from film deposition to particulate fouling is seen.

(b) Visible structures seen in close up of 6.35/4.35 mm tubing fouling.

Figure 5.5: Images from reverse flow, shell-in-tube reactor of fouling deposits that lead to tube constriction, performance degradation, and reactor failure.



(a) Hourly averaged PSDs.

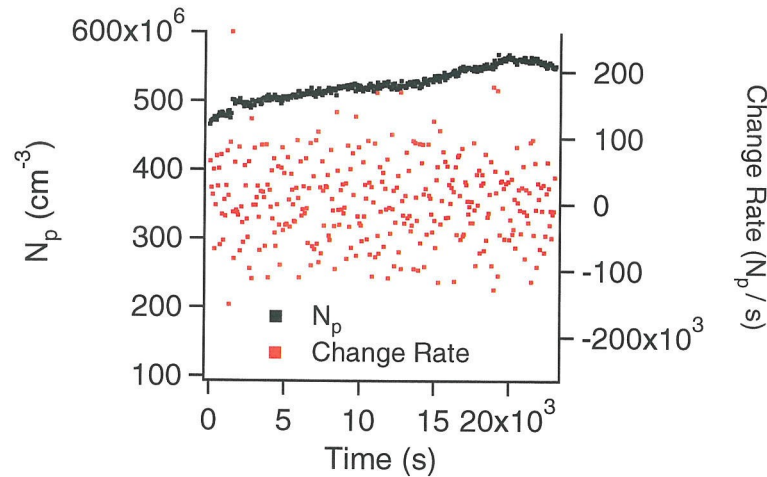
(b) Total number of particles,  $N_p$ , per scan with RDMA, and rate of change.

Figure 5.6: Effect of fouling on particle distribution with time observed from the shell and tube nucleation/growth with subsequent mixing jet reactor.

the tubing. With flowrate remaining constant, the velocity of the flow increases through the constriction, while decreases are seen in particle size and number. Figs. 5.7–5.8 show the trends in PSD evolution over time as well as the decreasing rate of particle production. This rate is also a linear decrease, similar to that observed in Fig. 5.4. The particle number production could be temporarily increased by decreasing the flowrate of the reactant stream. This flowrate change corresponded to an increase in precursor concentration that fueled additional nucleation. However, the increased particle number production was only temporary. Fig. 5.7(b) contains a series of points around  $10^4$  s wherein particle numbers are temporarily suppressed, but follow a similar trend of decreasing. The abruptness of the change in number of particles characterized, and the similarly abrupt return to the original trendline, suggest that an electronic malfunction temporarily affected data collection. It is unlikely that this signature results from a change in the furnace temperature or a change in the reactant concentration.

Efforts to model the nucleation zone in Femlab using a simplified reaction (Simplified Reaction (SR) Model) with no kinetic barrier to nucleation or coagulation) were not successful, but some trends emerged. First, reactant loss to the walls of a low molecular weight species with a large diffusivity, such as  $\text{SiH}_4$ , is significant. Second, if the sticking parameter of  $\text{SiH}_4$ , or any of the decomposition products, to a cluster is not unity,<sup>21</sup> the loss of these species to the walls also significantly enhances fouling. As clusters grow, thermophoretic effects begin to drive clusters towards the cooler center of the tubing, and fouling is quickly curtailed.

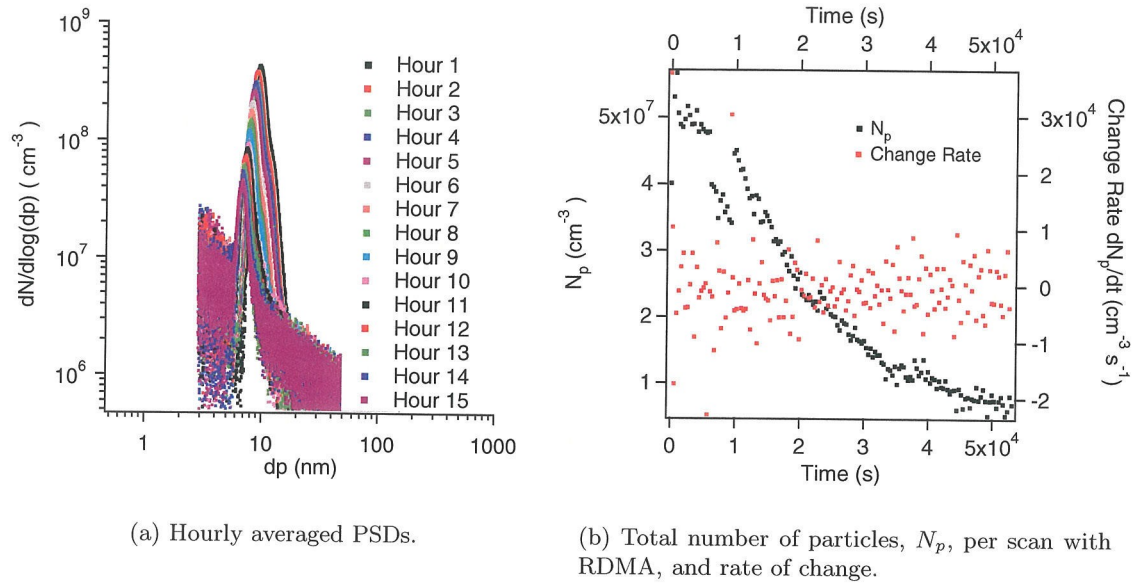


Figure 5.7: Effect of fouling on particle distribution with time observed from the laminar flow nucleation, turbulent mixing reactor.

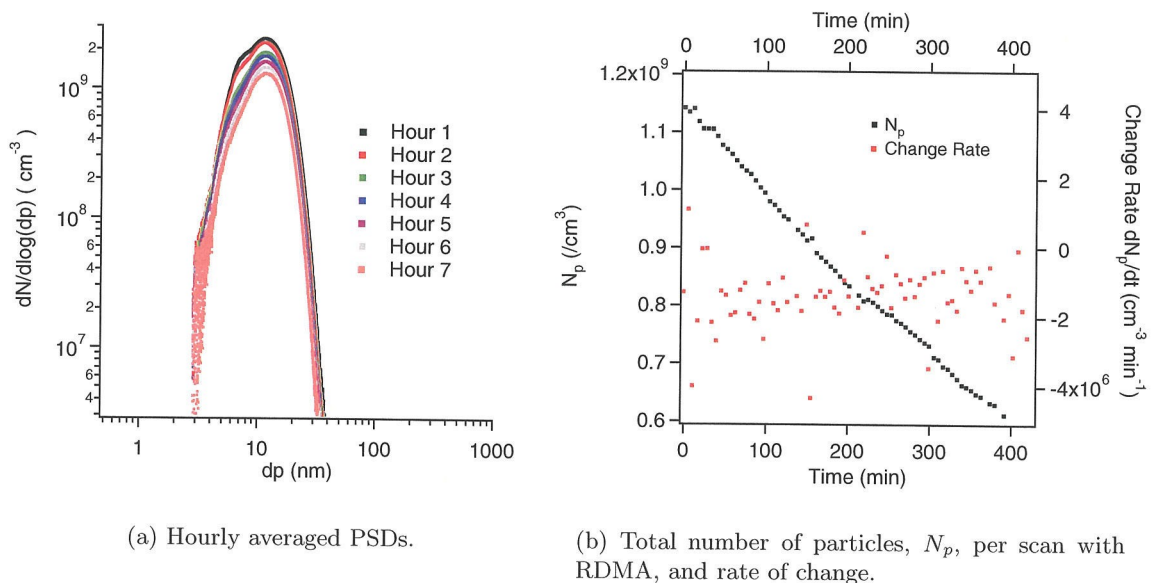


Figure 5.8: Effect of fouling on particle distribution with time observed from the laminar flow nucleation, turbulent mixing reactor.

### 5.3.4 Microplasma-Seeded Turbulent Mixing Reactor

Increasing throughput in the mixing reactor is limited by the onset of agglomeration within the laminar flow nucleation zone. Even though the comparatively slow thermal transport inhibits nucleation, it also favors wall fouling and agglomeration. Hence, further increases in particle number and size will likely be achieved by seeding a series of mixing zones with particles nucleated via an accelerated energy transport mechanism wherein the residence time may also be engineered to be orders of magnitude faster. Such an energy transfer is possible via pathways such as plasma, arc, laser, or flame induction. Sankaran demonstrated extremely fine nanoparticles, less than 3 nm, generated from an atmospheric pressure discharge struck in Argon.<sup>113</sup> Particle size was typically below the detection limit of a RDMA,  $\sim 3$  nm, unless a coagulation aerosol was allowed to form and evolve to a measurable size. Images of the microplasma/turbulent mixer setup are shown in Fig. 5.2.

Experiments performed with a microplasma discharge to seed a turbulent mixing annealing/growth furnace further demonstrate that particles may be both densified with increased thermal energy and/or grown to larger sizes by vapor deposition.<sup>57</sup> Figure 5.9 shows PSDs of silicon particles nucleated in a microplasma discharge struck in Argon that pass into a turbulent mixing reactor wherein mixing  $N_2$  is introduced at a ratio of 4 : 1 at various temperatures. As the temperature of the mixing reactor is increased, the mobility of the particles characterized decreases to an asymptotic limit, indicating that sintering has occurred.<sup>26,79,116</sup> It does not, however, indicate complete densification<sup>97,147</sup> since the time scale for the various densification mechanisms are affected by the initial particle morphology. Note, however, that fouling losses are not evident when seeding the turbulent mixing reactor, a very promising result for increasing reactor output.

In Fig. 5.10, seed particles generated in the microplasma combine with additional silane

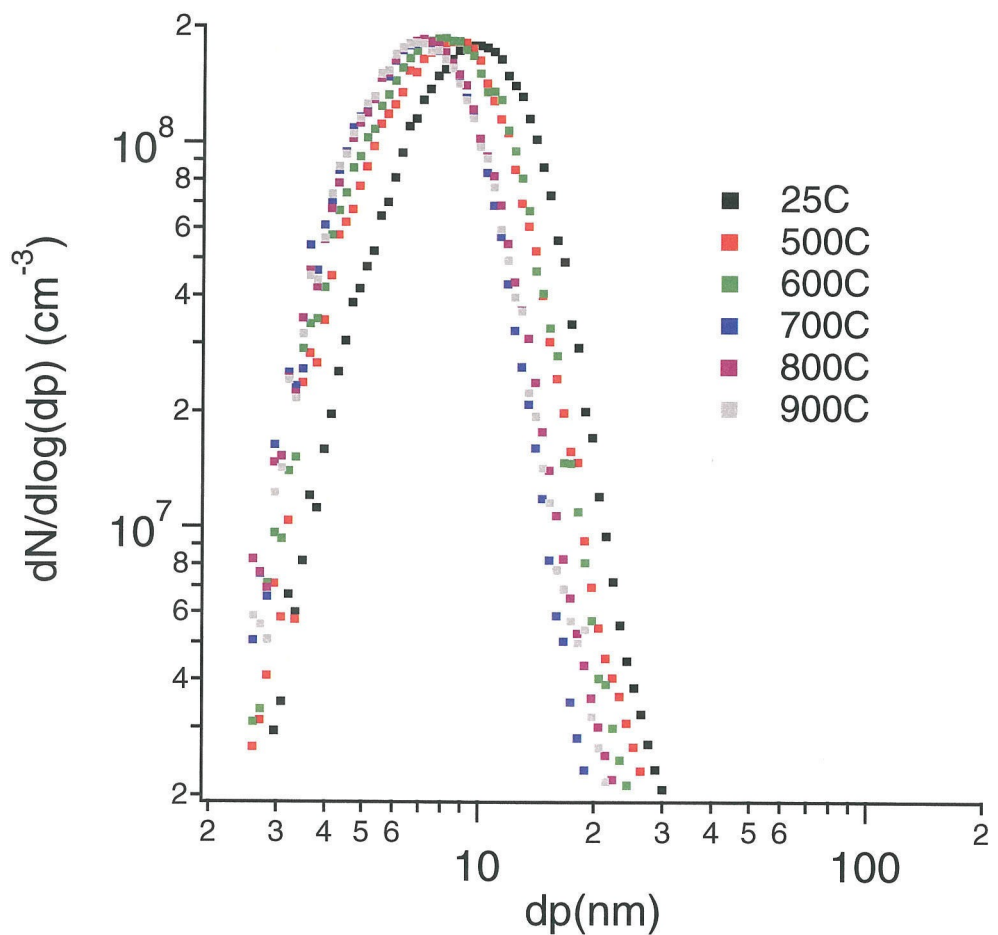


Figure 5.9: Densification of silicon particles from a microplasma discharge in Argon seeding a turbulent mixing reactor.

in a laminar flow tube before introduction into a heated turbulent mixing reactor. For precursor concentrations low enough to inhibit homogeneous nucleation, a shift to larger particle size with little corresponding effect on number is demonstrated. This experiment warrants further study with a DMA, currently being characterized, that is capable of sizing seed particles of  $\sim 1$  nm, since the initial number distribution of seed particles is unclear with the current characterization equipment.

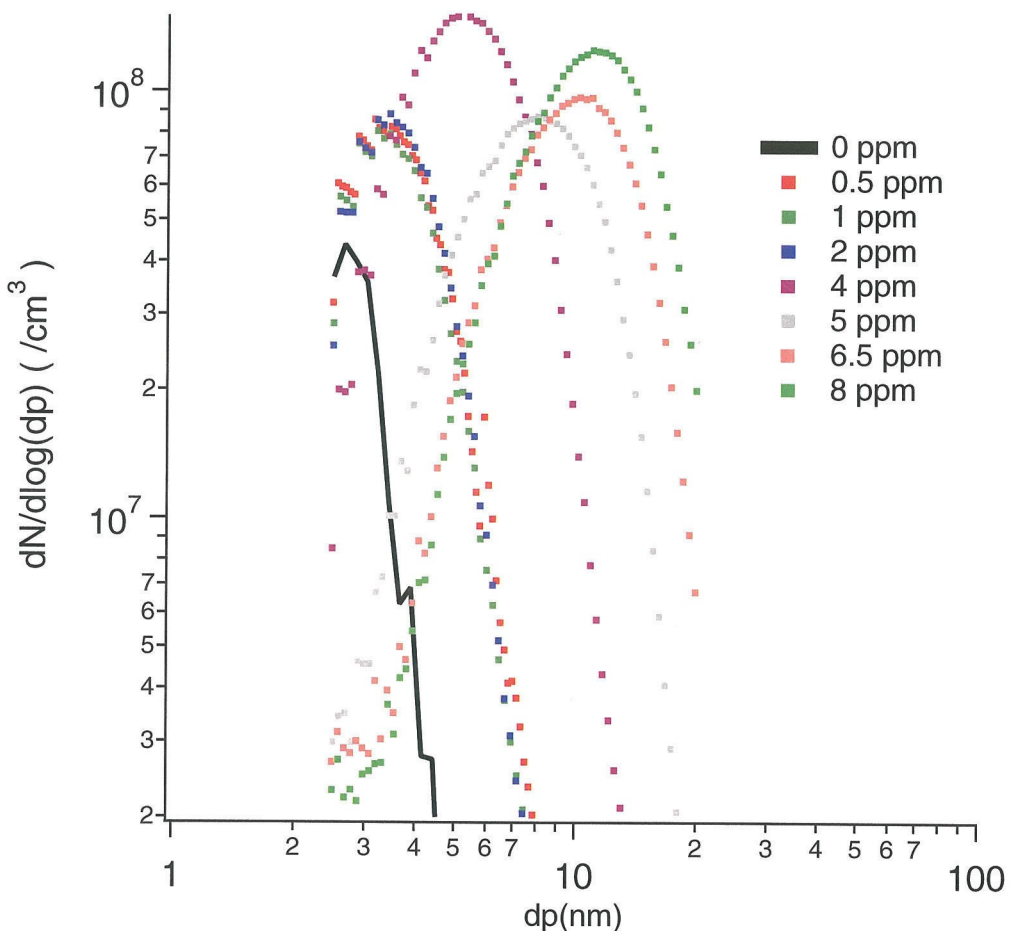


Figure 5.10: Densification of coagulated silicon nanoparticles from a microplasma discharge in Argon seeding a turbulent mixing reactor.

Another interesting feature of the microplasma discharge reactor is the potential to produce condensable vapors from a wide range of materials, including organics.<sup>114</sup> Successful

incorporation of the two schemes may allow narrow, size tunable distributions of a vast array of homogeneous and heterogeneous nanoparticles.

The use of quick transport mechanisms to deliver additional reagents or energy opens the door to study the engineering of nanoparticle aerosol reactors. For nearly monodisperse aerosol with involved mixing processes on a timescale short compared to coagulation, there is no ambiguity in deciphering the past history of the aerosol or predicting its future growth.

## 5.4 Conclusions

Small volume/low residence time reactors are necessary for the production of small nanoparticles. However, catastrophic fouling in the nucleation regions of laminar flow reactors suggests that improvements are necessary. The quick mixing achieved from narrow diameter jets that preserves the small sizes of particles in small volume reactors may also facilitate additional growth of seed particles. Combining the technologies of the microplasma discharge reactor and the quick mixing small volume thermal reactor may be a means to increase particle numbers while decreasing particle size without the cost of quickly fouled reactors.

## Chapter 6

# Experimental Evidence of an Inherent Monodisperse Particle Production Regime of Sinclair-LaMer Aerosol Reactors

### Abstract

Although most aerosol reactors produce particles with the relatively broad particle size distribution,  $\sigma_G \approx 1.45$ , typical of growth by coagulation, a number of studies produced narrower distributions,  $\sigma_G \approx 1.1$ , by operating under conditions where growth is dominated by vapor deposition. The particle size distributions produced by several laminar flow nanoparticle synthesis reactors have been examined to probe the factors that lead to these differences in performance. In some cases, coagulation downstream from the particle synthesis region determines the form of the particle size distribution. By reducing the residence times between the reactor and the measurement point or by quenching coagulation through rapid dilution at the reactor outlet, the inherent capabilities of aerosol synthesis reactors are revealed. For a wide range of operation of laminar flow nanoparticle synthesis reactors, vapor losses to the tube wall suppress homogeneous nucleation and enable production of uniform nanoparticles. For atmospheric pressure decomposition of silane, the size of sili-

con nanoparticles produced under such conditions increases with increasing tube diameter, consistent with the decreasing precursor flux to the wall.

## 6.1 Introduction

To fabricate small, 20 nm or less, particles without compromising particle numbers from Sinclair-LaMer<sup>122</sup> reactors in which the primary mechanism of particle growth is vapor deposition, the residence time must be kept short to avoid agglomeration.<sup>38</sup> Increases in precursor concentration yields larger particle size and particle concentration. However, even small increases in the precursor concentration can dramatically increase the number of nuclei formed.<sup>7</sup> As the particle number concentration in the reactor increases, agglomeration becomes increasingly difficult to avoid,<sup>81,145</sup> both within the reactor and in the downstream plumbing and characterization equipment. Alam<sup>7</sup> et al. observed narrowed size distributions when the precursor's temperature was slowly raised along the length of a laminar flow reactor, limiting the increase in the decomposition and nucleation rates while favoring growth of the nuclei and small particles via vapor deposition.<sup>146</sup> In this growth mode, the depletion of precursor<sup>6</sup> limits additional nucleation as the temperature continues to increase, preserving a narrowed distribution of particle sizes. Monodisperse particle size distributions,  $\sigma_G \approx 1.2$ , were reported.  $\sigma_G$  is the geometric standard deviation of a log-normal distribution. Such narrow size distributions are attractive where particle size is important, and even narrower distributions are needed in many applications.

A recent implementation of a turbulent mixing reactor demonstrated nearly monodisperse 8-12 nm heterogeneous aerosol nanoparticles,  $\sigma_G \approx 1.1$ , with a crystalline silicon core and oxide shell, fabricated at concentrations approaching  $10^9$  particles/cm<sup>3</sup>. This reactor employed a laminar nucleation zone wherein a gentle thermal ramp facilitated vapor de-

position onto nuclei, followed by a fast quench diluent supplied through turbulent mixing jets.<sup>30</sup> The monodispersity observed with those particle distributions is not limited to this class of reactors, but is observed in other so-called Sinclair-LaMer laminar flow reactors. In fact, laminar flow reactors seem well suited to the production of monodisperse aerosols; these result when nucleation rates are hindered sufficiently that chemical vapor deposition becomes the dominant growth mechanism.

On-line measurements of particle size distributions in the nanometer size regime are typically made by differential mobility analysis.<sup>23</sup> This technique requires that a known charge distribution<sup>40,142</sup> exist on the particles. This charge is generally imparted by exposing the aerosol to an ambipolar ion-cloud produced by ionizing radiation in a so-called neutralizer. The volume of the typical neutralizer may be larger than the volume of the reactor in which the aerosol forms, contributing to unacceptable coagulation of particles. The resulting “apparent” particle size distribution measured with the DMA bears little resemblance to that leaving the reactor. If, however, such biases could be eliminated (or minimized), differential mobility analysis provides a fast and convenient method for characterizing aerosol nanoparticles as they are produced.

To first order, the characteristic time for particle-particle collisions,  $\tau_{coag}$ , at the prevailing particle number concentration,  $N_p$ , can be estimated as

$$\tau_{coag} = \frac{2}{KN_p}. \quad (6.1)$$

As nanoparticles are much smaller than the mean-free-path of the gas molecules, the collision

frequency function,  $K$ , is that for free-molecular particles, which can be expressed as,<sup>40</sup>

$$K = \frac{\pi}{4} (d_{pi} + d_{pj})^2 (\bar{c}_i^2 + \bar{c}_j^2)^{\frac{1}{2}} \quad (6.2)$$

where  $d_{px}$  is the diameter and  $c_x$  is the mean velocity of the  $x^{th}$  particle. The mean molecular speed is given by,

$$c_x = \frac{8k_B T^{\frac{1}{2}}}{\pi m_x} \quad (6.3)$$

where  $k_B$  and  $T$  are the Boltzmann constant and temperature, respectively, and  $m_x$  is the mass of the  $x^{th}$  particle. For particles of equal diameter,  $d_p$ , this expression reduces to

$$K = 4 \left( \frac{6k_B T}{\rho_p} \right)^{\frac{1}{2}} d_p^{\frac{1}{2}}. \quad (6.4)$$

In this free-molecular size regime,  $K$  is only a weak function of particle size and temperature, so the characteristic time for coagulation is determined by the particle number concentration. For monodisperse 20 nm particles,  $K \approx 10^{-9} \frac{cm^3}{s}$ .

However,  $K$  increases dramatically for particles of unequal size, since both the higher mobility of the small particle and the larger cross-sectional area of the larger particle increase the collisional frequency. Thus, this estimation method places an upper bound on  $\tau_{coag}$ . At low flowrates, or for large  $N_p$ , particle characterization may be skewed to larger apparent sizes by coagulation of smaller particles. The presence of a small number of larger particles can dramatically reduce the number concentration of the smaller ones at the reactor outlet.

The present paper employs experiments performed with a number of different reactor configurations to examine the conditions that enable production of uniformly sized nanoparticles. All of the reactors studied are laminar flow tubular reactors in which silane undergoes

Reactor	Diameter (mm)	Hotzone	Reactor Material	Temp. (K)
RD1-1	17 mm	15 cm	Quartz	1273–1523
RD1-2	7.53 mm	15 cm	Quartz	1273–1523
RD1-3	1.75 mm	15 cm	Stainless Steel	1273
RD2-1	6.35 mm – 7.53 mm		Quartz	1273–1523
RD2-2	5 mm – 7.53 mm		Quartz	1273–1523
RD3	4.35 mm	3.9 cm	Inconel	1273
RD4	3.9 mm	3.9 cm	Inconel	1273

Table 6.1: Configurations of laminar flow nucleation reactors used.

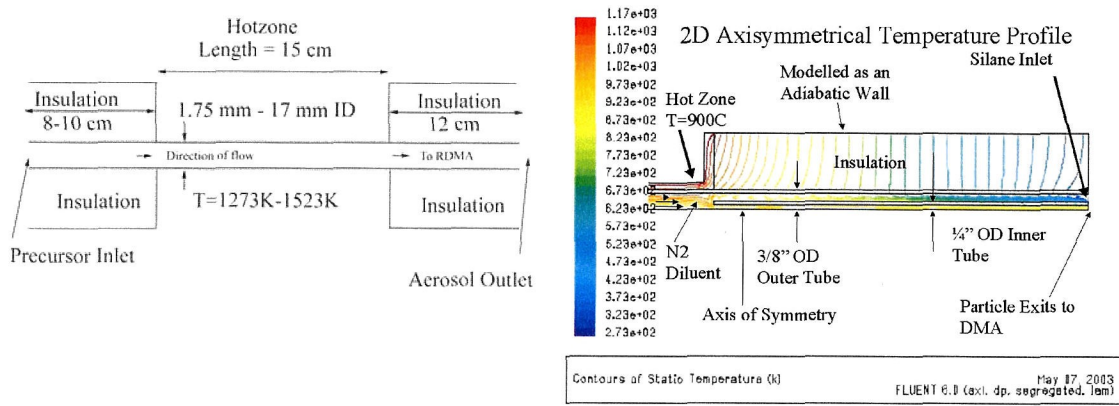
thermal decomposition in a nitrogen carrier gas at atmospheric pressure. Operation of each reactor can range from production of uniformly sized nanoparticles to formation of more broadly distributed coagulation aerosols. The discussion that follows examines the factors that enable the former, more desirable, mode of operation.

## 6.2 Experimental Methods & Design

Each of the four reactor configurations employs a laminar flow zone for particle nucleation, with different downstream configurations for reaction quenching, particle growth/densification, or particle annealing. Cold, dilute silane in nitrogen is introduced through insulated tubing into a furnace hotzone that is maintained at a fixed temperature between 1173 K–1523 K. Between the cold entrance and the furnace hotzone, thermal conduction from the hotzone heats the tube wall and the reactant mixture, initiating silane decomposition well upstream of the entrance into the furnace hotzone. We sought to study the effect on the measured particle size distribution of manipulating both the thermal ramp, through adjusting flowrate and temperature, and the onset of agglomeration, through a variety of approaches to cooling and/or diluting the product aerosol. Table 6.1 summarizes the differences in configurations and supplies a nomenclature for the following discussion.

### 6.2.1 Reactor Configurations

Reactors RD1, Fig. 6.1(a), are single tube reactors with a 15 cm hotzone between 8–12 cm lengths of entrance/exit insulation. Tube diameters ranged from 1.75 mm–17 mm. Particle nucleation and growth begin in the conduction-heated tube upstream of the furnace hotzone; particle densification and crystallization continue within the hotzone. This configuration has been widely studied and reported in the literature, both experimentally and theoretically.<sup>44,79,97,128,144</sup>



(a) RD1: Single tube reactors.

(b) RD2: Reversed flow shell & tube reactor.

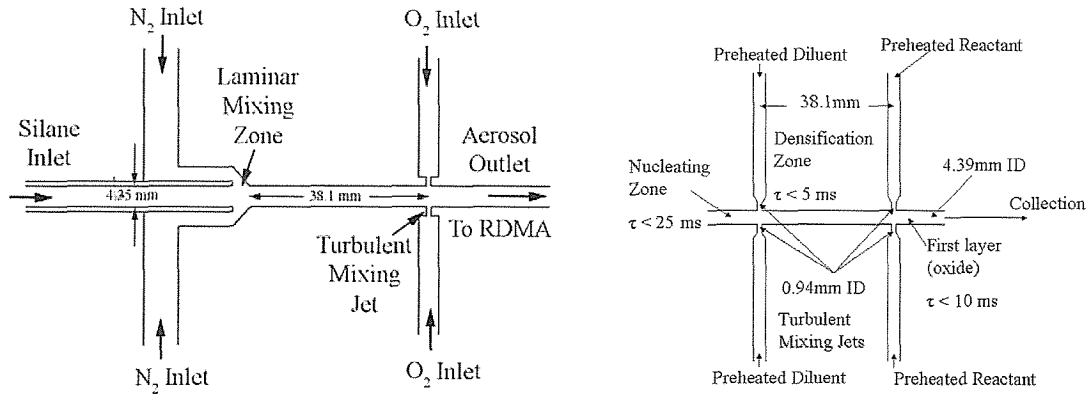
Figure 6.1: Two configurations of quartz laminar flow reactors. (a) RD1: Single tube reactors. (b) RD2: Reversed flow shell and tube reactor.

Reactors RD2, Fig. 6.1(b), employ a counterflow shell and tube configuration. The silane containing feed is introduced in the annular region where it is heated both internally from the exiting gas and externally by convection and conduction from the furnace. The exit tube is positioned within the annular space so the tube opening is physically located just inside the furnace hotzone. A counter flow of  $\text{N}_2$  diluent (1273–1523 K) mixes with the reaction stream; the diluted reactants, reaction products, and aerosol exit the reactor through the inner tube. Particles are quickly removed through the exit tubing by reversing

the flow. In some experiments, relatively large amounts of reversing flow were used to quench the reaction and dilute the particle concentration. The exit tubing size ranged from 3–4.35 mm ID with 5–6.35 mm OD. The outer annulus ID was 7.53 mm.

Reactor RD3, Fig. 6.2(a), is a co-flow shell & tube assembly consisting of a 4.35 mm ID inner tube within a 12.7 mm ID annulus. Although a fused quartz reactor was first tried (to ensure cleanliness) it proved to be too fragile for extended use. Experiments were, therefore, performed using a reactor made from a high temperature alloy of Inconel. Preheated N<sub>2</sub> diluent, 1273 K, is introduced coaxially and contacts the inner tube along a 19.1 mm length, heating the fluid within the inner tubing, wherein the aerosol forms in a manner as already described. At the confluence, the outer tube is tapered 45° from 12.7 mm to 4.35 mm, thus accelerating the flow and reducing the overall residence time as the two streams join in a laminar flow. A short length downstream, 39.1 mm, additional diluent is supplied through opposed impinging jets to quench coagulation. This configuration was designed to combine the laminar nucleation and laminar quenching zones of the previous configuration and provide a second stage of rapid dilution in the present experiments, although it has been used in other studies as a two stage reactor in which oxygen was introduced in the mixing jets to grow a thermal oxide coating on the silicon nanocrystal cores. Both the annular flow N<sub>2</sub> and mixing jet gases were preheated to ~ 1273 K.

Reactor RD4, Fig. 6.2(b), consists of a narrow (from 3.9 mm or 1.75 mm) diameter inlet tube followed by successive pairs of radially opposed mixing jets wherein the gas flow is preheated before introduction into the aerosol flow. It is similar to RD3 except that instead of performing the first dilution in a laminar mixing zone, a pair of small diameter opposed jets produce intense turbulence to both supply and rapidly mix preheated nitrogen with the aerosol. While nucleation still occurs within a laminar flow, the diluent



(a) RD3: Shell and tube nucleation zone with downstream turbulent mixing jet.

(b) RD4: Laminar flow with multiple mixing jets.

Figure 6.2: Two configurations of laminar flow nucleation reactors made from Inconel.

now rapidly quenches agglomeration, and ensures a homogeneous environment for further particle development. A second pair of jets is located 39.1 mm downstream through which additional reagents may be introduced. Application of this reactor to the synthesis of core/shell nanoparticles has been described in more detail previously.<sup>30,60</sup>

### 6.2.2 Nanoparticle Characterization

Particles were brought to a known steady-state charge distribution using a TSI 3077 model  $^{85}\text{Kr}$  neutralizer with an internal volume of  $\sim 100$  ml. Particle size distributions were then measured by using a radial differential mobility analyzer<sup>23</sup> (RDMA) coupled to a Faraday-cage filter system with a fA-resolution ( $10^{-15}$  A) electrometer for detection of the transmitted particles. A diluent gas was mixed with the aerosol before classification with the RDMA, delaying the onset of agglomeration,<sup>145</sup> and preserving the characteristics of the particles that exited the reactor. The RDMA was operated in scanning mode<sup>140</sup> and

data inversion was performed by the method of Collins.<sup>28</sup>

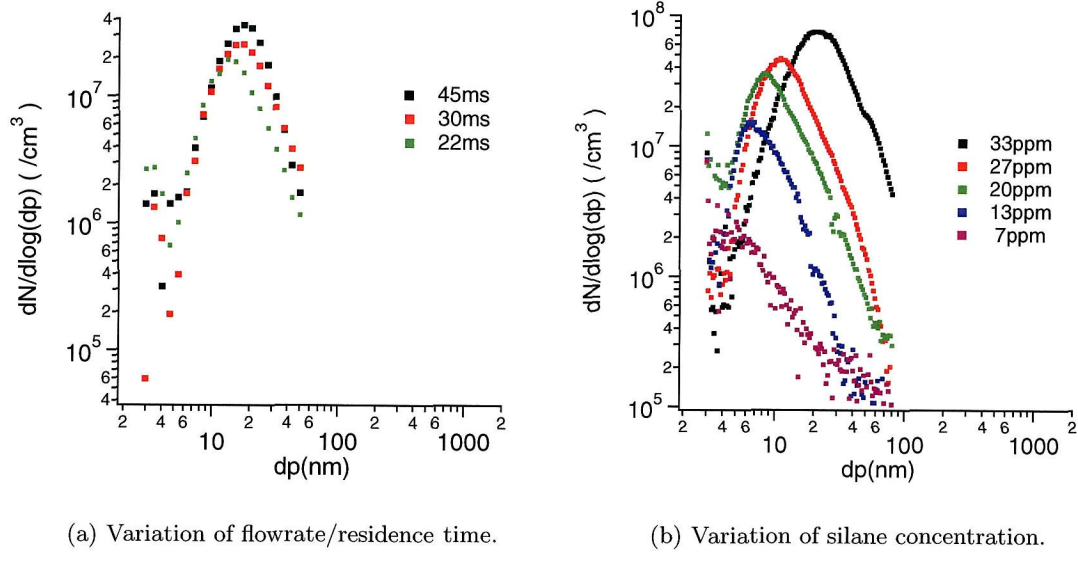
## 6.3 Results

### 6.3.1 Measurement Validation

Particle size distribution measurements were made in early experiments by first passing the aerosol en-masse through a <sup>85</sup>Kr neutralizer before sending it to the RDMA. Particle size distributions measured downstream of a large diameter reactor, RD1-1, are shown in Fig. 6.3. Figure 6.3(a) shows that the particle size decreases slightly as the reactor residence time decreases. The size distributions are broad, as expected for an aerosol that has grown primarily by coagulation. The shapes of the size distributions at different residence times are similar, suggesting that the aerosol has approached the asymptotic, “self-preserving particle size distribution.<sup>81,145,147</sup> Figure 6.3(b) shows a much more dramatic variation when reducing the precursor concentration, along with some apparent changes in the shape of the size distribution.

Figure 6.4(a) shows particle size distributions measured using a smaller diameter reactor, RD1-2, at 1423 K. Trends with particle size with residence time or reactant concentration are similar to those observed with the larger reactor. There is some narrowing of the size distribution with this smaller reactor, but not to the degree of monodispersity reported in recent studies.

Figure 6.4(b) shows particle size distributions from RD1-3, a reactor made from 1.75 mm ID stainless steel (SS) tubing. Although they are polydisperse, an interesting feature is seen at 20 ppm, where the size distribution appears to have a mode wherein a sharp increase in the number of small particles is followed by gradually decreasing numbers of larger



(a) Variation of flowrate/residence time.

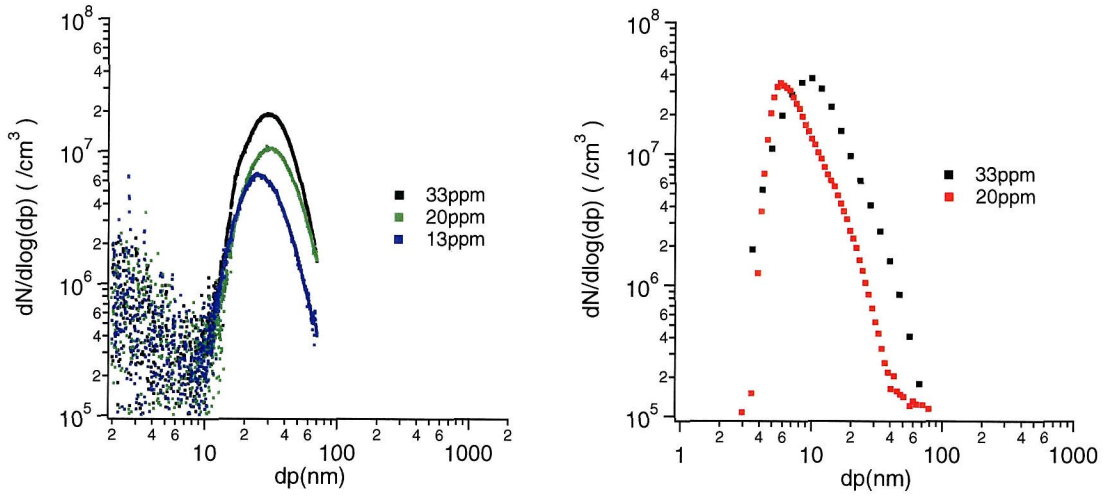
(b) Variation of silane concentration.

Figure 6.3: Typical particle size distributions from RD1 with 17 mm diameter.

particles. It is suggestive that larger particles were agglomerates of the left-mode sub-10 nm particles. Unfortunately, rapid fouling of the small diameter tubing prevented more detailed explorations of this hypothesis.

The broad size distributions produced by all three implementations of these single tube reactors, even with a short residence time in the SS tubing reactor,  $\sim O(10 \text{ ms})$ , strongly suggested that aerosol coagulation have been occurred outside the reactor, in transit to the RDMA.

To explore this possibility, the aerosol produced by RD1-2 operated at a total flowrate of 600 sccm was further diluted before neutralization. Because the residence time in the passage from the reactor through the neutralizer to the RDMA was  $\sim 20 \text{ s}$ , the aerosol was diluted to reduce the number concentration below  $N_p = 5 \times 10^7 \text{ cm}^{-3}$ , corresponding to a coagulation time of 20 s for 20 nm diameter particles. Size distributions (not shown) indicate that the extent of agglomeration decreases as the diluent flow increases.



(a) Effect of concentration variation in particle size distributions from RD1-2

(b) Effect of concentration variation in particle size distributions from RD1-3.

Figure 6.4: particle size distributions from RD1 type reactors.

These experiments revealed that the high particle concentrations in the stream exiting the reactors led to unacceptable coagulation within the plumbing and, in particular, the large volume of the neutralizer; this coagulation resulted in size distributions at the RDMA that were quite similar in shape and size, irrespective of the nature of the aerosol leaving the reactor.

To avoid the long residence time within the neutralizer volume, an alternate aerosol neutralization method was introduced; rather than passing the aerosol through the neutralizer, it was mixed with particle-free, ion-rich N<sub>2</sub> that had been processed through the neutralizer as illustrated in Fig. 6.5. The steady-state ion concentration of the gas that is produced in the neutralizer persists for a small but finite time after the fluid leaves the ionizing environment. 90% decay of charged species removed from a ionized radiation source are reported in NRD, Inc., literature occurring within  $\sim O(1\text{ s})$ . Particle characterization appeared to greatly reduce this coagulation bias when this ion-rich neutralizer diluent was

mixed in ratios of at least 2:1. As the flow ratio from the neutralizer is increased from 2x through 16x, Fig. 6.5(a), the particle diameter and height of the particle size distribution mode is unaltered although a small reduction in the number of larger particles is seen, consistent with reduced agglomeration from shorter residence time in the neutralizer. In Figs. 6.5(b) - 6.5(c), a narrower range of dilution ratios is explored while characterizing a polydisperse aerosol. Little apparent change in the particle size distribution is observed between 2x and 3x dilution. To conserve gas in experiments with reactor RD2, the following particle size distributions are recorded at 2x dilution.

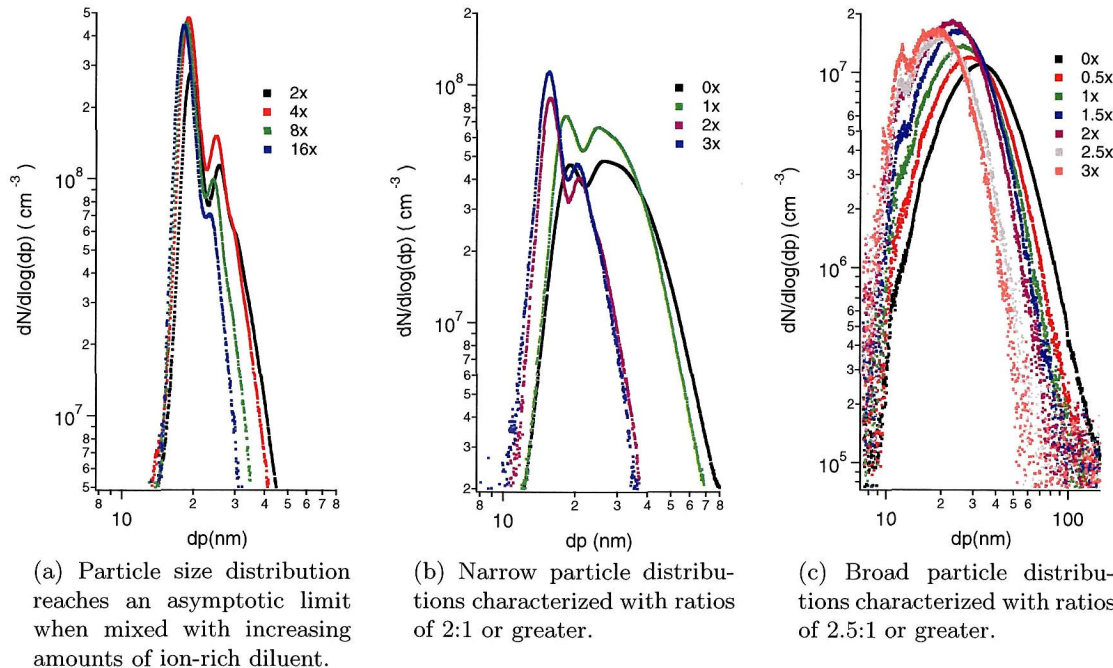


Figure 6.5: Dilution of aerosol with ion-rich gas in ratios greater than 2:1 significantly reduce the agglomeration bias seen in particle size distributions. Traces are corrected for dilution.

Experiments with reactors RD3 and RD4 were neutralized in a more efficient manner. An aerosol-containing flow of 135 sccm was rapidly mixed with 405 sccm of ion-rich gas that was delivered through an impinging jet. Particle size distributions were observed to

reach an asymptotic particle size distribution at similar dilution ratios as seen in Fig. 6.5.

### 6.3.2 Product Particle Characterization

Having identified an aerosol charging approach that minimizes coagulation within the neutralizer, the nature of the particles produced by the different reactors was explored.

#### 6.3.2.1 RD1: Laminar Flow Single Tube Reactors And Particle Characterization

At relatively low flow rates in RD1-2, the gas heats quickly, leading to rapid nucleation. The relatively long residence time allows coagulation to grow large, polydisperse particles with the size distributions shown in Fig. 6.6(a). At higher flow rates, the heating rate is reduced, as is the number of particles emerging. Nucleation is prolonged by the resulting slow reaction, yielding a broad, polydisperse aerosol with smaller size particles, as shown in Fig. 6.6(b). At intermediate flow rates, Fig. 6.6(c), a bimodal peak is observed. The 600 sccm traces, seen in Fig. 6.6(c), are very narrow, indicating that conditions existed wherein growth by vapor deposition has occurred, simultaneously suppressing nucleation and allowing particle growth without significant agglomeration. The resulting distribution shows a monodispersity similar to that observed in the turbulent mixing reactor.<sup>60</sup> A data fit, Fig. 6.6(c), of the narrow mode, indicates  $\sigma_G \approx 1.1$ . The second mode in this trace were doublet particles. Increasing the precursor concentration from 25 ppm to 50 ppm increases the breadth of the coagulation mode, an early approach toward the self-preserving size distribution aerosol.

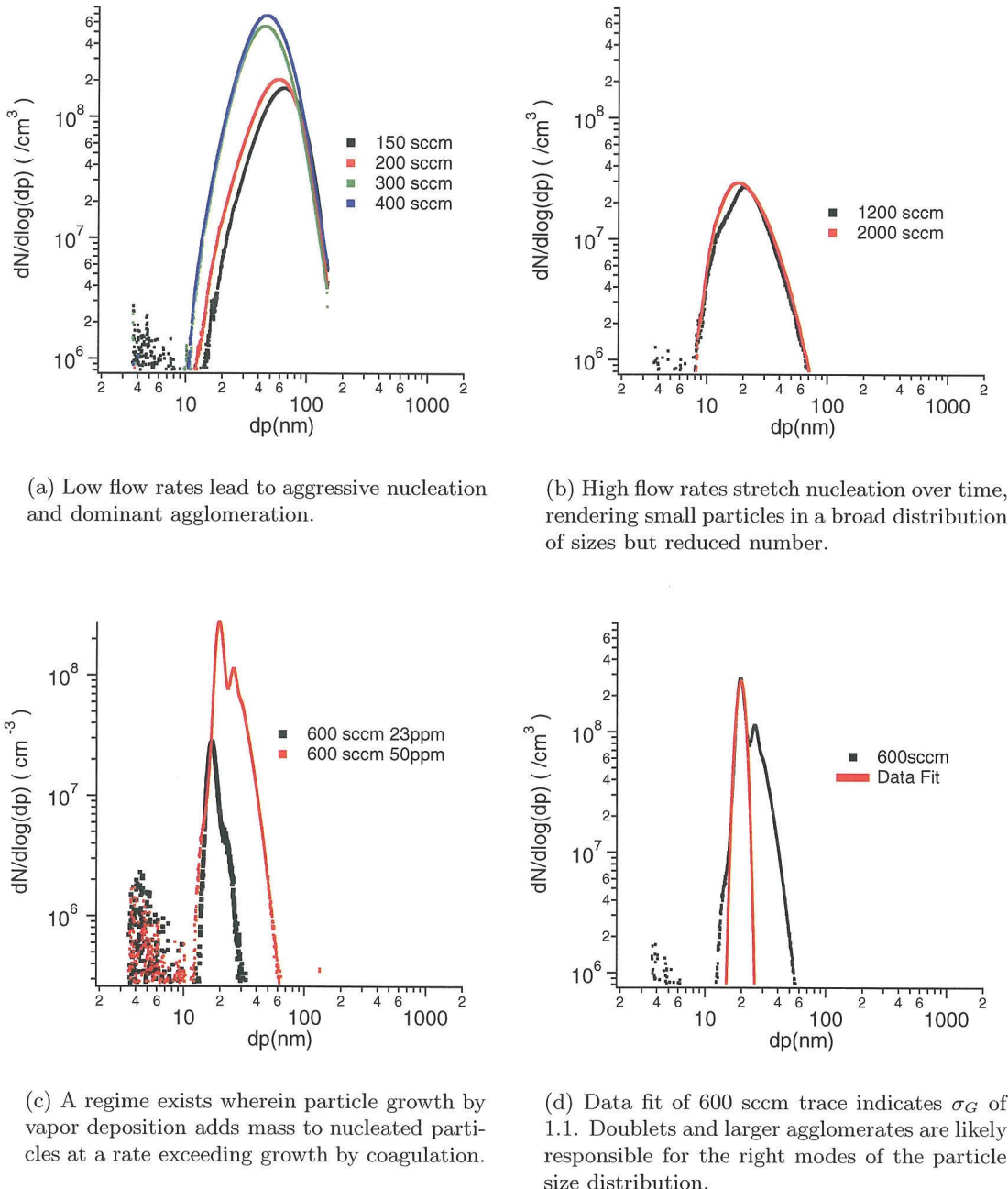


Figure 6.6: Particle size distributions from 15 cm hotzone at 1023 K single 7.525 mm I.D. fused quartz tube laminar flow aerosol pyrolysis reactor with 50 ppm reactant silane.

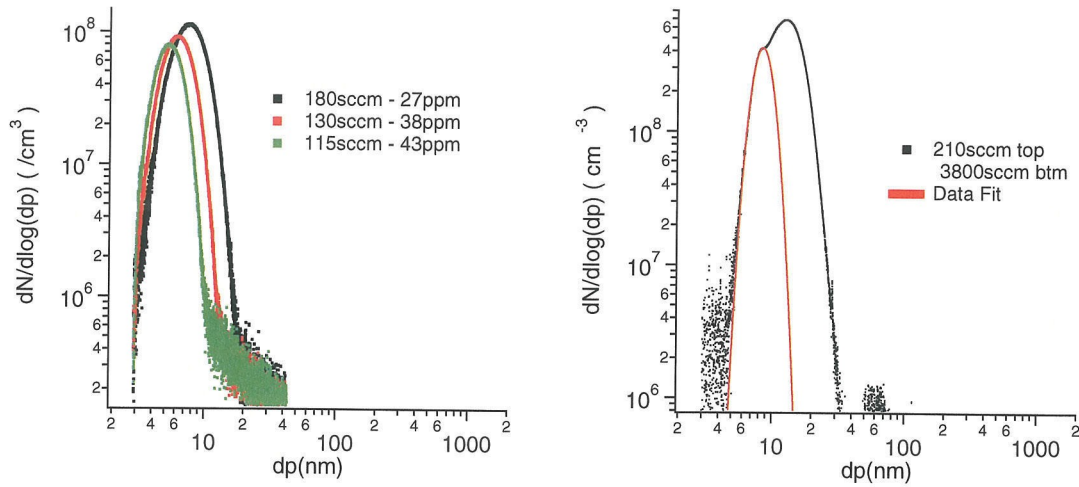
### 6.3.2.2 RD2: Reverse Flow Shell & Tube Assembly

This configuration produced higher particle numbers than did the single tube, RD1, reactors while also narrowing the size distribution. The modeled temperature profile seen in Fig. 6.1(b) suggests that the temperature rise produces nucleation both near the inner tubing and the outer tubing, creating large numbers of particles. However, this reactor was prone to fouling and to unstable recirculating flow zones near the exit tubing evidenced by large particles modes (not shown) in the particle size distributions. Within recirculation zones, particles collect and coagulate into much larger mobility diameter particles.

Operation at low flowrates is shown in Fig. 6.7(a). A low silane concentration limits nucleation, and the small precursor-containing flow ensures a single nucleation event. The broad size distribution reveals a coagulation aerosol as expected given the long residence time in the reactor, but as the silane concentration increases and the nucleating flowrate decreases, the size distribution shifts to smaller sizes and lower number concentrations. The geometric standard deviation,  $\sigma_G$ , for the three traces are 180 sccm/27 ppm,  $\sigma_G \approx 1.32$ , 130 sccm/38 ppm,  $\sigma_G \approx 1.29$ , and 115 sccm/43 ppm  $\sigma_G \approx 1.26$ . At low flowrates, reactants and small nuclei can diffuse to the reactor walls, thereby reducing the number of particles available for coagulation in spite of the higher precursor concentrations.

Figure 6.7(b) shows the size distribution obtained when a 235 sccm flow of 100 ppm  $\text{SiH}_4$  is reacted and quenched by a high 3800 sccm  $\text{N}_2$  flow. A narrow mode is evident on the left side, corresponding to  $\sim 8\text{--}12$  nm particles, with  $\sigma_G \approx 1.17$ .

This mode is repeated and better isolated in the size distribution seen in Fig. 6.8. The narrowness of the particle size distribution is attributed to conditions wherein nucleation occurs slowly enough that numbers of nucleated particles remain small enough such that growth by vapor deposition is the dominant growth mechanism. However, the appearance



(a) Variation of both nucleation flowrate and SiH<sub>4</sub> concentration with fixed 20 sccm quench flow.  
 (b) 210 sccm nucleation and 2865 sccm quench flow.

Figure 6.7: Particle distributions observed from RD2 for variations silane concentration at 1273 K for low nucleation flowrate.

of two distinct modes may result from heating the precursor within the annulus from both the internal tubing and external hotwall. Heat transfer from the large combined exit flow preheats the inlet precursor flow earlier, inducing earlier nucleation, thus increasing the particle's residence time. The precursor flow is simultaneously heated from the outer hotwall, but this heating occurs deeper into the reactor, Fig. 6.1(b), where the SiH<sub>4</sub> concentration is reduced, but not yet depleted. Nucleation may also occur here, near the outer wall, leading to two particle modes that experience different growth conditions; the late developing mode producing fewer particles, with less coagulation, and therefore remaining more monodisperse.

These results suggest that, when relatively slow forward convection prevents the fluid temperature from rising too quickly, particles competitively intercept reactant diffusing toward the wall, growing independently by a vapor deposition process. This reaction condition

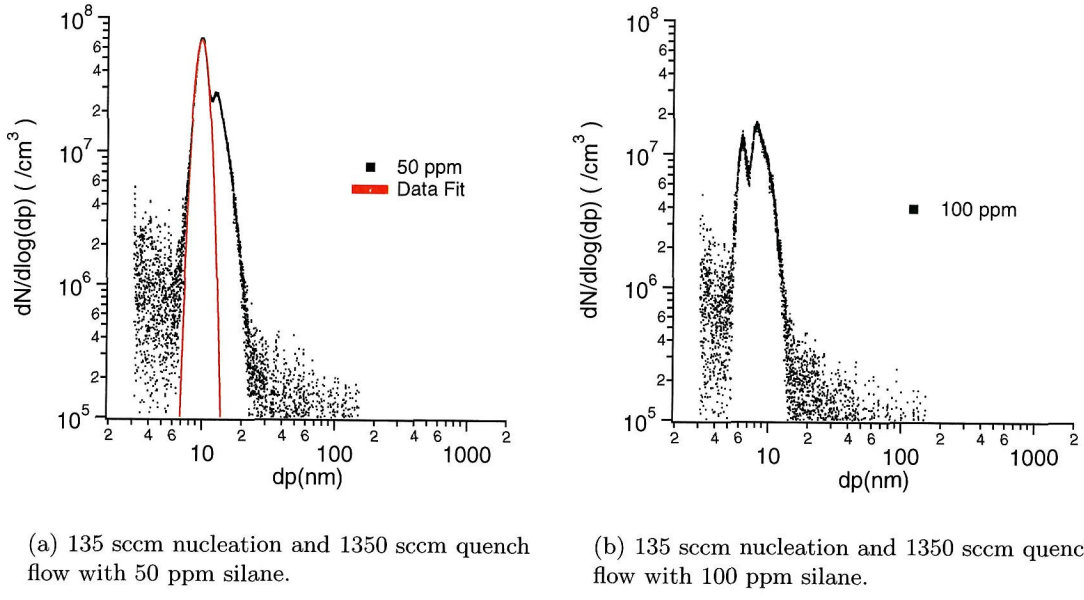


Figure 6.8: Particle distributions observed in RD2 for variations in silane concentration at 1273 K for large comparative difference in bottom to top flow.

suggests that the Damkohler II number is sufficiently greater than unity. This Damkohler II parameter is defined,

$$Da^{II} = \frac{kr_h}{\bar{u}} \quad (6.5)$$

where  $k$  is the reaction rate,  $r_h$  is half of the hydraulic diameter,

$$r_h = \frac{1}{2} \left( \frac{4A_c}{P_w} \right) \quad (6.6)$$

where  $A_c$  is the cross-sectional area,  $P_w$  is the wetted perimeter, and  $\bar{u}$  is the average flowrate. Moreover, the relatively slow flow with fast moving molecular species ensures the mass Peclet number,

$$Pe_m = \frac{\bar{u}r_h}{\mathcal{D}} \quad (6.7)$$

where  $\mathcal{D}$  is the diffusivity of silane in nitrogen, remains near unity. The combination of these

two conditions favors independent particle growth from a continuous source of reactant that is diffusing radially from the cooler reactor regions. For a low enough particle concentration, quenching the reaction at the precise time, before the onset of runaway agglomeration,<sup>145</sup> may yield much larger numbers of small, monodisperse particles than observed in coagulation aerosols. However, the quenching (mixing) timescale must be short compared with the overall residence time to ensure a homogeneous, dilute mixture that can be removed before significant agglomeration begins. Designing a reactor with a precisely engineered quench that freezes the particle distribution development before agglomeration dominates without introducing unstable flow was the goal of the development of the mixing reactor.

### 6.3.2.3 RD3: Shell and Tube Nucleation/Growth With Laminar Quench

Figure 6.9 shows size distributions for various precursor concentrations and flowrates with a  $N_2$  dilution of 1800 sccm and a mixing jet dilution of 400 sccm. In Fig. 6.9(a), the precursor flowrate is varied between 200 sccm and 400 sccm while the silane concentration in that flow is fixed at 100 ppm. A narrow, small particle mode is evident throughout; it narrows and becomes more pronounced as flowrate is increased. As the precursor flowrate increases, cooler precursor penetrates deeper into the reactor, the nucleation rate is reduced, as is the agglomeration rate. The large particle mode,  $\sim 80$  nm, is thought to result from particles that agglomerated in a recirculation zone within the tapered cavity at the end of the nucleation zone tubing.

For a fixed precursor flow of 200 sccm, Fig. 6.9(b), varying the silane concentration dramatically affects the product size distribution. With the increased nucleation rates at higher feed concentrations, agglomeration dominates, and the aerosol shifts from the monodisperse aerosol produced at lower concentration to a polydisperse, coagulation aerosol.

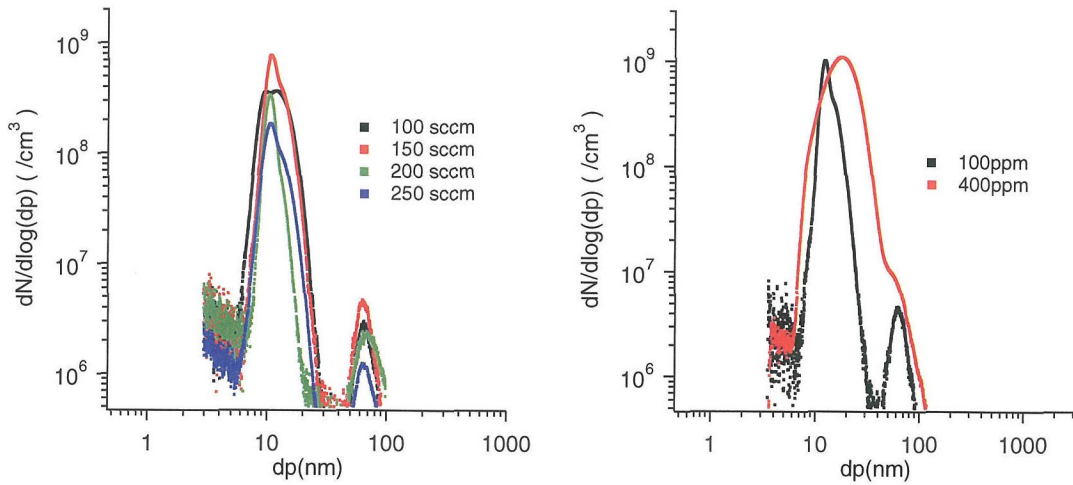


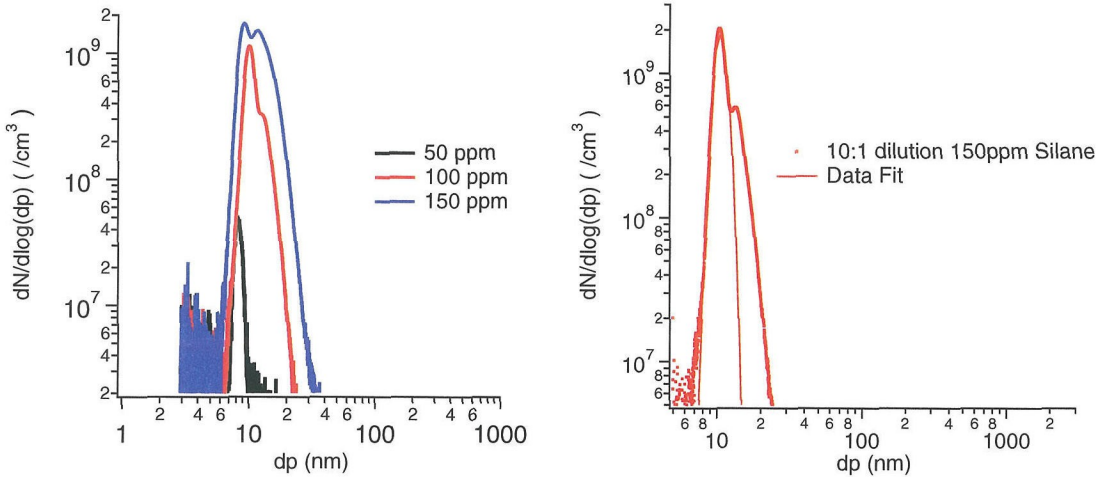
Figure 6.9: Particle distributions observed for nucleation in RD3, an inconel shell & tube with turbulent mixer reactor.

The laminar quenching zone and turbulent mixing jets employed in this configuration allow larger numbers of particles than was observed with the reactors examined above. Moreover, the localized vapor deposition particle growth at relatively low flowrates and low silane concentration lead to narrow size distributions similar to those observed with RD2.

#### 6.3.2.4 RD4: Laminar Flow Nucleation, Turbulent Mixing Quench

RD4 provides a well-defined, abrupt quench of particle coagulation. The resulting size distributions, shown in Fig. 6.10, can be extremely narrow. The lowest precursor concentration examined, 50 ppm, produces a very narrow peak with all particles between 7 and 10 nm as synthesized. It is important to note that no particle classification was needed to produce this monodisperse aerosol. Increasing the precursor concentration to 100 ppm enhanced nucleation; the resulting particle concentrations were too high to avoid significant agglomeration, even with quenching by dilution. The size distribution is broader than at

the lower precursor concentration, initially the mode is narrow and of low enough mobility to indicate the presence of doublet particles. Large excesses of precursor, i.e., the 150 ppm trace, yields a broader size distribution, indicative of significant coagulation.



(a) Increased polydispersity in particle size distributions as precursor concentration is varied.

(b) Curve fitted to left mode of a particle distribution with  $\sigma_G$  of 1.1. Decreasing precursor concentration removes the right mode.

Figure 6.10: Initial monodisperse peak observed from RD4 for a variety of inlet concentrations.

Another trend revealed by Fig. 6.10(a) is the change of particle size with changes in the feed concentration. The smallest particles recorded, with a peak of 7 nm, were grown with a feed concentration of 50 ppm. Increasing the silane concentration generated higher concentrations (up to 10x more) of slightly larger particles but did not appear to significantly affect the monodispersity of this mode. Increasing the concentration further actually decreased the size of the first mode. These trends suggest that in the monodisperse regime, particles develop independently from each other. Increasing the precursor, within limits, increases the particle size and number as long as particles continue to develop independently. Excessive precursor drives enhanced nucleation, accelerating depletion of precursor. Vapor deposition onto larger numbers of nuclei limits growth, so smaller particles result.

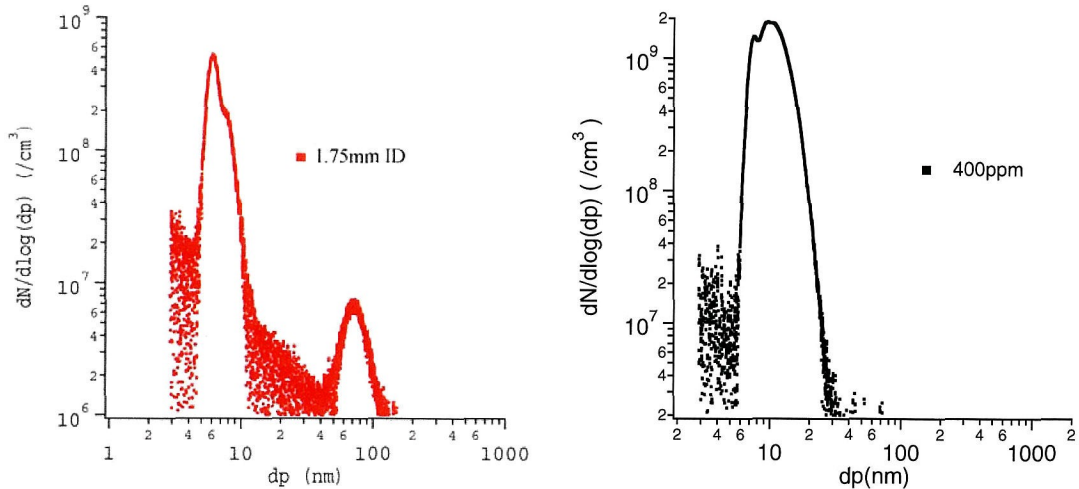
The increased number of particles assures that agglomeration will broaden the particle size distribution.

Fitting the fine mode of the 100 ppm trace to a log-normal size distribution suggests that the initial aerosol had a  $\sigma_G$  as little as 1.1, much smaller than that of the so called self-preserving distribution ( $\sigma_G \approx 1.45$ ) produced by free-molecular coagulation.

These particles have previously been examined using both conventional and high resolution (TEM and HRTEM) transmission electron microscopy. They were observed to be dense, single crystalline particles of uniform size; thus it appears likely that the second (larger diameter) peak results from coagulation of the smaller particles into doublets during passage through the cooler post-reactor, plumbing.

Narrowing the diameter of the inlet tubing decreased the size of particles. Size distributions observed when the 3.9 mm nucleation zone tubing was replaced with a 1.75 mm SS tube show a large particle mode, Fig. 6.11(a), suggestive of agglomeration of particles near the tube end. Attaching a 7° conical nozzle to the end of the tubing to remove the recirculation associated with the step increase in diameter eliminated this large particle mode, as shown in Fig. 6.11(b). The decrease in the size of particle formed in the narrower inlet tubing suggested that final particle size may be adjusted by changing the reactor diameter.

Figure 6.12 compares normalized size distributions from the different reactors discussed earlier in this paper. The trend is fairly consistent, i.e., small diameter reactors produce small particles when the reactors are operated in the monodisperse mode. In Fig. 6.12(a), the trace names are the inner diameters of the tubing wherein nucleation occurs. Trace '1.75 mm-1' corresponds to the trace in Fig. 6.11, but with the 80 nm particle mode removed. Trace '1.75 mm-2' is the '20 ppm' trace from Fig. 6.4(b). Trace '3.93 mm' is the '100 ppm' trace from Fig. 6.10(a). Trace '4.35 mm' is the '100 ppm' trace from Fig. 6.9(a).



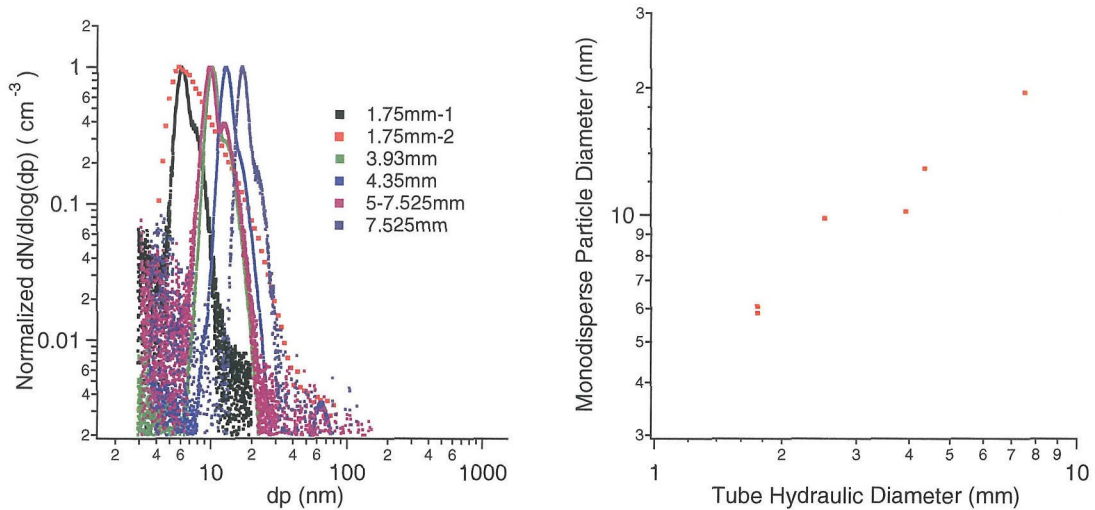
(a) Particle size distribution recorded when particles nucleate within a 1.75 mm diameter tubing feeding RD4, the turbulent mixing reactor. Large mode of particles likely arises from particle agglomeration in recirculating flow located at end of 1.75 mm tubing.

(b) Large particle mode eliminated when using 7° conical inlet nozzle.

Figure 6.11: Particle size distributions recorded from RD4 from nucleating silicon nanoparticles in a 1.75 mm ID SS tube.

Trace ‘5 mm–7.525 mm’ is the trace from Fig. 6.8(a). This particle size distribution trace is from RD2-2, the name indicates both the inner and outer dimension of the shell and tube assembly. Trace 7.525 mm is from an experiment similar, i.e., reduced precursor concentration, to those observed in the ‘2x’ trace of Fig. 6.5(b). A systematic increase in particle size with tube diameter is apparent.

Figure 6.12(b) shows a plot of the mode diameter in the monodisperse regime vs the reactors’ hydraulic diameter. (Eq. 6.6) A trend of increasing particle-mode size proportional with increasing reactor cross-sectional area is evident, but the results are affected by several factors: reactors were operated at different temperatures, and the optimum size/number distribution was not sought in each case. Reaction kinetics for all configurations are similar, with nucleation occurring in a laminar flow environment, gently heated from a non-isothermal



(a) Normalized particle size distributions for largest “monodisperse” particle size recorded from the various configurations of reactors

(b) The mode-sized particle, from the particle size distributions seen in Fig. 6.12(a), increases with hydraulic diameter (Eq. 6.6) of the reactor.

Figure 6.12: Mode-sized particle of monodisperse particles from reactors RD1-RD4 increase with reactor diameter.

wall, at similar (atmospheric) pressure.

## 6.4 Modeling

A simplified reaction model, without coagulation, (SR Model)<sup>97</sup> in Femlab<sup>TM</sup>, was constructed. The reactor was modeled, using RD4 parameters, as a 3.9 mm inlet tube with 50 ppm silane in nitrogen introduced at 150 sccm and heated by a hotwall. The hotwall contained a linear temperature gradient varying from room temperature at the inlet to 1273 K at the reactor. SiH<sub>4</sub> decomposition is modeled as governed by a first-order reaction where,

$$\frac{dc}{dt} = -kc \quad (6.8)$$

where  $c$  is the SiH<sub>4</sub> concentration and the reaction rate coefficient,  $k$ , is estimated as<sup>97</sup>,

$$k = 10^{12.9} e^{-\frac{25768}{T}} \quad [s^{-1}]. \quad (6.9)$$

Observation of silicon deposits on the reactor walls, after many hours of aerosol production, suggested that, at low temperature, there was little or no loss of precursor, but as the temperature increased, the wall served as a sink of increasing strength. Vapor deposition of thin film silicon appeared at temperatures well below that of significant silane decomposition. Deeper into the reactor, the character of the deposits became increasingly granulated. To simplify the boundary condition without imposing non-isothermal adsorption/reaction expressions, an empirical fit to wall deposition profiles observed in the lab was modeled using the decomposition rate and an arbitrary timescale,

$$c_{wall} = c - kc\Delta t. \quad (6.10)$$

Using  $\Delta t = 1$  s, the model shows vapor deposition beginning on the tubewall at temperatures  $\sim 100$  K below particle deposition at the tubewall, similar to the pattern observed in the laboratory. Vapor deposition growth of particles is accounted for by,

$$\nabla \bullet (-\mathcal{D} \nabla c_3) = R - u \bullet \nabla c_3 \quad (6.11)$$

where  $R$  includes the flux of  $\text{SiH}_4$  to the surface of  $c_2 N_A$  particles, with radius  $r_m$  for  $\text{SiH}_4$  and  $r_p$  for the particle.  $N_A$  is Avagadro's constant.  $R$  is determined,

$$R = \pi (r_p + r_m)^2 \bar{c}_v c \sigma c_2 N_A \quad (6.12)$$

with the mean velocity of  $\text{SiH}_4$  as,

$$\bar{c}_v = \sqrt{\frac{8k_B T}{\pi m}}. \quad (6.13)$$

A sticking parameter of unity,  $\sigma = 1$ , was assumed, and  $u$  contains both the convective transport in the fluid and the thermophoretic terms,  $v_t$ ,

$$v_t = -Th \frac{\mu}{\rho T} \nabla T \quad (6.14)$$

where  $\mu$  is the gas viscosity,  $\rho$  is the gas density and  $Th = 0.5$  is an experimentally determined dimensionless parameter.<sup>39</sup>

Tabulation of silane concentration,  $c$ , monomer/particle concentration,  $c_2$ , and silicon gained by vapor deposition,  $c_3$ , is tracked in each cell of the model. Particle size is determined from the number of silicon units per particle,  $\frac{c_3}{c_2}$ . This arbitrarily limits each cell to

contain a single particle size, which is then used to calculate diffusivity,  $\mathcal{D}$ , for transport as well as the surface area for additional vapor deposition. To account for concurrent transport of  $c_2$  and  $c_3$ , equal diffusivities are applied within each cell.

As the flux of unreacted  $\text{SiH}_4$  to monomer units (or clusters) is initially two orders of magnitude greater than the decomposition predicted by Equation 6.8, the model typically failed to converge. Vapor depositional growth is affected by the reactive sticking parameter,  $\sigma$ , but use of the bulk silicon parameter,<sup>21</sup> failed to predict any particle production. It appears that all decomposed silane and all monomer units diffused to the wall and were lost. This extreme is not observed and the bulk silicon reactive sticking parameter is too small to address the physics of the nuclei and small particles.

To assist model convergence,  $\sigma = 1$  was assumed and the rate of vapor deposition onto monomers or particles was set to zero below 795 K, which is a few degrees below the temperature at which silane decomposition leading to nucleation would dominate. The model then converged, producing the results seen in Figs. 6.13–6.15. Predicted particle sizes were smaller than observed, Fig. 6.13, but the number concentration, Fig. 6.14, is of the correct order of magnitude. The mixing cup average particle concentration at the reactor outlet, Fig. 6.15, is  $\sim \mathcal{O}(10^{10} \text{ cm}^3)$ , comparable to concentration upstream of the 10:1 dilution by turbulent mixing jets in reactor RD4.

This model, while arbitrary in some parameters, suggests several trends: (i) Silane decomposition and monomer production begins near the wall, with loss of both species that consuming nearly all the reactant (99%+). Non-uniform flow patterns, i.e., plumes, from intense wall heating are not needed (but aren't discounted) to explain the magnitude of silane loss.<sup>31</sup> (ii) Thermophoresis assists particle preservation by driving larger clusters towards the center of the reactor as illustrated by the depletion region seen near the wall,

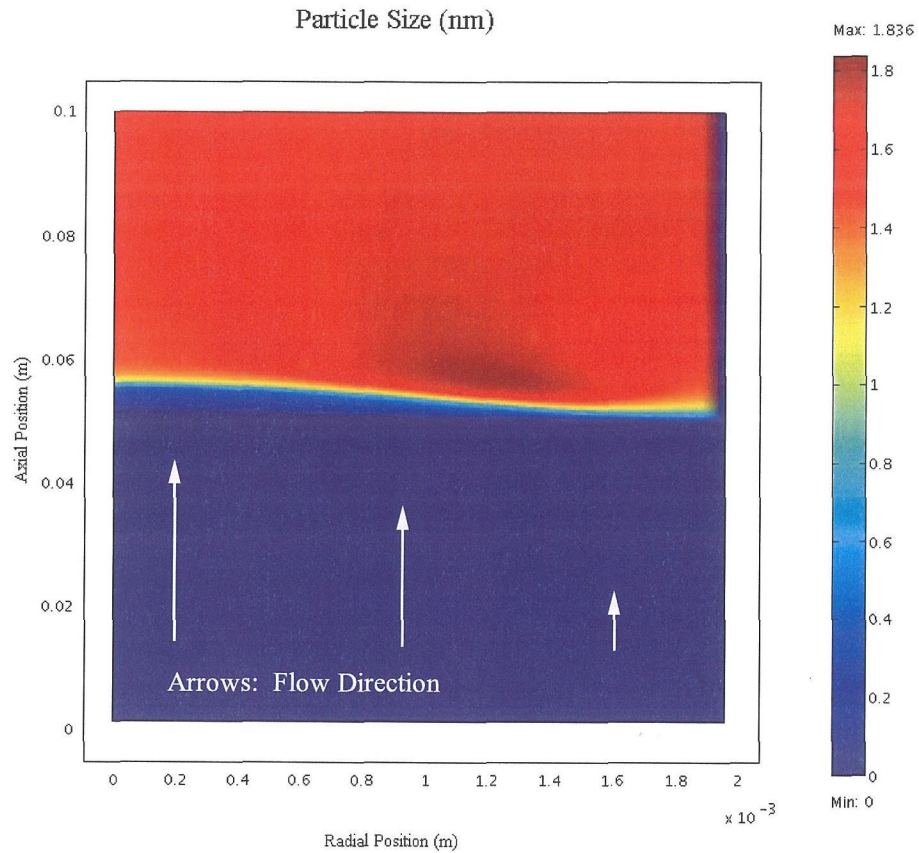


Figure 6.13: Predicted size of nanoparticles from modeling in Femlab<sup>TM</sup>.

Fig. 6.14, at a rate exceeding the Brownian diffusion rate to the reactor wall. (iii) Particles grow by vapor deposition from silane that is diffusing radially outward towards the sink at the hotwall, suggesting that larger monodisperse particles can be made in larger diameter reactors. (iv) The use of turbulent mixing jets at the exit of reactor in the model would both dilute the particle concentration and disperses the particles spatially, preventing immediate agglomeration.

Besides the arbitrary reactive temperature for vapor deposition and the lack of a suitable reactive sticking coefficient for all particle sizes at all temperatures, the model predicts parti-

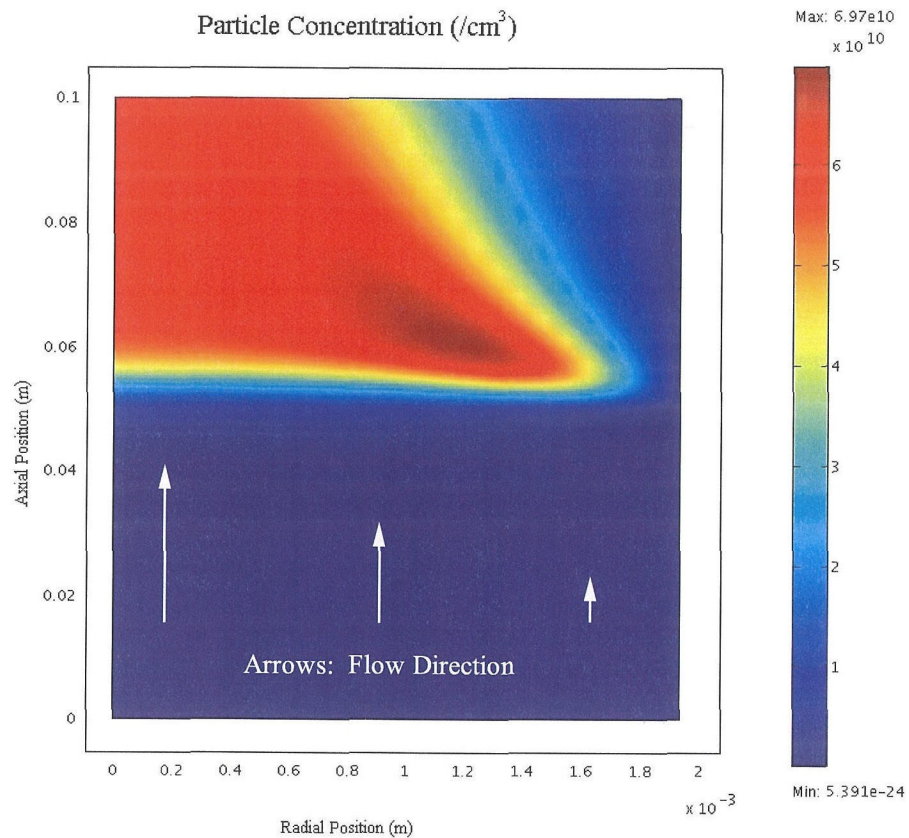


Figure 6.14: Particle concentrations from modeling. The effect of thermophoretic transport is clearly seen in the image.

cles size less than observed. While reducing the activation temperature for vapor deposition would have the effect of reducing losses to the hotwall and increasing the modeled particle size at the outlet, the model failed to converge with implementation of lower activation temperatures.

Wu and Flagan<sup>145</sup> found that implementation of a pyrolytic generated condensable vapor in a thermal ramp reduced nucleation and allowed growth by vapor deposition to compete and suppress additional nucleation, thus maintaining a narrower size distribution. Nguyen and Flagan<sup>97</sup> proposed a model for aerosol growth that incorporated both chemical vapor

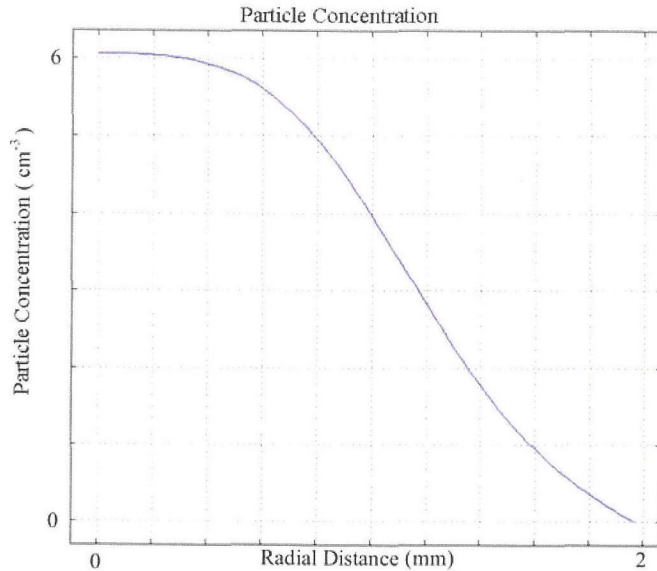


Figure 6.15: Particle flux at reactor exit in  $\text{cm}^{-3}$ .

deposition on developing particle surfaces and coagulate growth. The narrow distributions seen in the turbulent mixing reactor, and the low particle density laminar flow reactor, suggest that nucleation has been inhibited sufficiently that particle-particle interactions are minimal, and each particle exists in an environment essentially isolated from other particles, allowing individual particle growth to occur by either vapor deposition or contact with other near-monomer units. This environment exists only as a number of factors coincide. These factors include a gentle thermal ramp, produced by a combination of the temperature ramp of the inlet tubing entering the hotzone of the furnace and a reduced flowrate of reactants, wherein nucleation rate is constrained to produce few enough particles that agglomeration may be temporarily suppressed. The other factor is a supersaturation that is not overzealous, a condition that is assisted by diffusional loss of reactant to the heated walls in a laminar flow reactor.

At a temperature less than that needed for thermal decomposition, a silane sink exists at the inlet walls of the reactor tubing. Hence a concentration gradient of silane exists that

facilitates further silane loss in the region where decomposition begins. Silane decomposition species are a relatively mobile species that, in the absence of sufficient reactant may also be lost to the walls. However, if sufficient precursor remains, these nuclei may grow and become subject to a thermophoretic force that inhibits further loss while particles lose diffusional mobility. Thermophoretic velocities are  $\sim O(0.1 \frac{mm}{s})$  and are not fast enough to overcome Brownian diffusion for the highly mobile species of small nuclei and precursor decomposition products.

## 6.5 Conclusions

A regime of operation for production of monodisperse,  $\sigma_G \approx 1.1$ , nanoparticles exists in Sinclair-LaMer type silane pyrolysis aerosol reactors. Particle growth by vapor deposition is favored over agglomeration when thermal transport to the reactant stream is hindered, thus reducing the formation of nuclei and clusters. High diffusivity products, both decomposition species and small nucleated clusters, form near the hotwall wherein the majority of products may be lost to the reactor walls. Small nuclei that migrate inwardly towards the cooler center of the reactor, grow larger from precursor that is diffusing radially outward. Monodisperse particle growth is favored when the  $Da^{II}$  remains large while nucleation is limited when  $Pe_m$  is  $\sim O(1)$ . Thermophoretic transport assists the preservation of the developing particles by driving them away from the hotwall to the cooler reactor center. The mode-sized particle of the particle size distribution is typically larger for larger diameter reactors. Particle size of the narrow production mode is tunable only within a small range of sizes, but the number produced may be varied by well over an order of magnitude. The turbulent mixing jet reactor preserved this mode by both diluting the aerosol concentration and dispersing concentrated particles into a homogeneous mixture, delaying the onset of significant agglomeration. Using multiple jets in series, the narrowness of nanoparticle distributions may be preserved while additional growth layers are added. With suitable precursors, nanoparticles of materials other than silicon are expected to exhibit similar growth behavior.

## Chapter 7

# Particle Collection

### Abstract

Modeling of nanoparticle collectors, an electrostatic precipitator (ESP), and a thermophoretic precipitator (TD), predicts nearly 100% efficiency for charged sub-20 nm particles with the ESP and 4% efficiency by the TD. Collection efficiency decreases as particle size increases in the ESP, affecting the interpretation of particle size or numbers based on transmission electron microscope (TEM) images. A proposed turbulent mixing aerosol virtual impactor aerosol collector is suggested although modeling of the design is incomplete.

### 7.1 Introduction

Collection tools in the lab for particles fabricated in aerosol reactors include an electrostatic precipitator, a thermophoretic precipitator, and bubblers using a “degassed” liquid. These methods are inefficient, usually collecting less than 5% of the particles that pass through the device. Although these small numbers of particles may be sufficient for some studies or even fabrication of small devices, they are not suitable for projects requiring greater particle density or for fabricating larger devices. A 300 mm thermophoretic chamber was designed, in part, to efficiently collect the majority of particles made within the constraint

of a 12-hour collection period. Interpretation of photoluminescence studies on oxide-coated nanoparticles is hindered without an estimate of particle density. When collected particles did not luminesce, questions arose as to whether enough particles were collected. When particles luminesced, it was difficult to determine a luminescence efficiency without an accurate estimation of collection density.

However, supplying nanoparticles in a liquid medium for collaborative efforts with other projects was severely hindered by the lack of an efficient collector. Ostraat<sup>100</sup> observed that liquids must be degassed, removing virtually all oxidants, before silicon nanoparticles remain stable in size within the solution. Failure to properly degas the collection liquid led to changes in particle size, i.e., the particles restructured in the liquid into a size different than that observed in the feed aerosol. Moreover, it is preferable to use a small volume of liquid  $\sim O(ml)$  to keep the collection density high, and separately degas a liquid prior to contact with the nanoparticles.

This section discusses modeling of the devices already in use and presents some initial design ideas for an efficient liquid collector of nanoparticles.

## 7.2 Design

### 7.2.1 Turbulent Mixing Virtual Impaction Aerosol Collector

With particle production typically above  $10^8 \text{ cm}^{-3}$  and occasionally as high as  $10^9 \text{ cm}^{-3}$ , particle collection on TEM grids was routine. But collection in a liquid medium for use in biological studies proved challenging.

The device proposed contains little new design, rather a combination of a pair of designs, a condensational nucleus growth region followed by an impactor. A typical condensation

nucleus counter<sup>4,90,126</sup> supplies a condensable vapor onto “seed” particles wherein heterogeneous nucleation occurs and growth continues by condensational vapor deposition.<sup>148</sup> Once the particles reach sizes that incident light scatters onto an optical detector, the number of particles can be determined. With the addition of an impaction, or virtual impaction, region after growth region, the aerosol particles may be collected taking advantage of their now increased aerodynamic drag. Since it is desired to collect all the particles, the volume of the growth region needs to be large enough to ensure growth to  $\sim O(\mu\text{m})$  sizes. Growth may be accomplished relatively quickly as Wang<sup>76?</sup> demonstrated with a fast mixing condensational nucleus counter.

However, the particles from the turbulent mixing reactor are too small for efficient aerodynamic sizing, and too numerous to simultaneously grow all in a single stage to the desired size. For example, growth of  $10^8 \text{ cm}^{-3}$  to  $1 \mu\text{m}$  would require a volumetric fraction of 7% vapor. Collection across a virtual impaction plane is preferable to electrostatic collection (inefficient). Thermophoretic deposition is also ruled out: to create the thermophoretic driving force necessary for quick collection would likely require temperatures too high to maintain a liquid coating on the particles.

This proposed scrubber design incorporates aspects of condensational growth, aerodynamic sizing, and fast mixing concepts. A fraction of the aerosol stream,  $\sim 10\%$ , is diverted, using pressure-balanced flow into a concentric tube within a shell-in-tube assembly. Turbulent mixing jets supply vapor-laden diluent, wherein condensational growth enlarges particles to aerodynamically selectable size. The remainder of the “dry” aerosol passes through an annular region outside the condensational growth chamber.

At the exit of the growth chamber, where the “dry” particles and the coated aerosol particles rejoin, quick mixing jets deliver additional vapor-laden diluent into the heteroge-

nous mixture. Rapid mixing, with sufficient vapor pressure to avoid evaporation from the particles, would initiate a coagulation event that would quickly scavenge the small particles into the larger, heterogeneous aerosol while preserving the size for separation across a virtual impaction plane.

If the condensational growth method proves to require too much time or forced cooling, then the scavenging droplets may be formed using an atomizer and grown to the appropriate size. The advantage of using either of these methods is that a condensable vapor may be degassed externally from the aerosol production system.

Once the two particle streams are reintroduced and mixed, the characteristic time for coagulation, and thus a minimum time of passage for collection of the particles can be estimated considering the distribution as a bimodal group of particles at a primary size of  $\sim 10$  nm and a collection size of  $\sim 1 \mu\text{m}$ . This bimodal distribution seeks to take advantage of the increased coagulation “power” of the large particles. For  $10^7 \text{ cm}^{-3}$  “wet” particles and  $10^8 \text{ cm}^{-3}$  “dry” particles, the coagulation/collection time is  $\sim 0(\text{s})$ , slower than the mixing times, but much quicker than thermophoresis.

A first-order estimate of the time required for coagulation for a concentration of  $N$  particles may be obtained from the rate equation,

$$\frac{dN}{dt} = -\frac{1}{2}K(D_{pi}, D_{pj})N^2. \quad (7.1)$$

For an initial number of particles,  $N_o$ , the solution to this equation is,

$$N(t) = \frac{N_o}{1 + \frac{t}{\tau_c}} \quad (7.2)$$

where the characteristic time for coagulation is obtained,

$$\tau_c = \frac{2}{K(D_{pi}, D_{pj}) N_o}. \quad (7.3)$$

The Brownian coagulation coefficient may be estimated as follows,<sup>39,40</sup>

$$K(D_{pi}, D_{pj}) = 2\pi(D_i + D_j) \left( \frac{D_{pi} + D_{pj}}{D_{pi} + D_{pj} + 2g_{ij}} + \frac{8(D_i + D_j)}{\bar{c}_{ij}(D_{pi} + D_{pj})} \right)^{-1} \quad (7.4)$$

where,

$$g_{ij} = \left( g_i^2 + g_j^2 \right)^{\frac{1}{2}} \quad (7.5)$$

$$g_i = \frac{1}{3D_{pi}l_i} \left( (D_{pi} + l_i)^3 - (D_{pi}^2 + l_i^2)^{\frac{3}{2}} \right) - D_{pi} \quad (7.6)$$

$$l_i = \frac{8D_i}{\pi\bar{c}_i} \quad (7.7)$$

$$D_i = \frac{kTC_c}{3\pi\mu D_{pi}} \quad (7.8)$$

$$\hat{c}_i = \left( \frac{8kT}{\pi m_i} \right)^{\frac{1}{2}}. \quad (7.9)$$

To collect particles without employing a real impactor that might require a drip system, subject to clogging, a virtual impaction plane is suggested, wherein the fluid changes direction faster than the aerodynamic response of the micron-sized particles. Particles cross fluid streamlines and pass through the plane into a relative quiescent zone wherein they may precipitate into a collection vessel. Fluid flowrates through a small diameter nozzle, up to incompressible limits, would improve particle collection efficiency.

Previous studies of impactors<sup>14,15</sup> suggest that the nozzle diameter to impaction plane have a ratio between 1.4 and 1.9 and the impaction radius to nozzle radius should be from

1–1.9.<sup>36,55,84,85,131</sup>

Initial modeling demonstrated that a virtual impaction plane orthogonal to the fluid flow in a radial geometry could not restrain the fluid from entering the collection chamber as the momentum of the fluid was sufficient to overcome any pressure boundary from the collection vessel. Thus, for the near sonic flow velocities one might wish to employ, this geometry would prove limiting. Borrowing a concept from the turbulent mixer and chemical engineering rule of thumb, i.e., a disturbance in an isotropic fluid tends to be resolved within a pathlength of the order of the critical dimension of the fluid, one could conceive of a virtual impaction plane at the narrow end of a convergent nozzle geometry in which the fluid enters orthogonally to the virtual impaction plane, but is allowed to bend and exit in the divergent nozzle. In this configuration, it was found that a 45° nozzle was sufficient to constrain fluid flow from entering the collection chamber at velocities approaching the speed of sound. These results are consistent with an analytical solution from a potential flow model for fluid by Ravenhall and Forney.<sup>110</sup>

However, modeling of this virtual impactor proved to be challenging. Modeling was performed in Femlab<sup>TM</sup> using standard  $\kappa-\epsilon$  turbulent flow model. When the model failed to converge, it often indicated unstable flow within the modeled geometry and could be interpreted as a poor design. Models for a few geometries succeeded in converging; however, modeling of particle transport using the 3D PDE mode was not completed successfully.

For labscale collection flowrate,  $\sim 5000$  sccm or less, constrained to a maximum of near sonic or supersonic flow, nozzle diameter, and keeping the device within personally machineable dimensions, the nozzle diameter was constrained to 1 mm.

Several nozzles were modeled, including a straight jet nozzle, a nozzle pinched to 1 mm diameter and then expanded with a constant angle taper or a curved geometry. Modeling

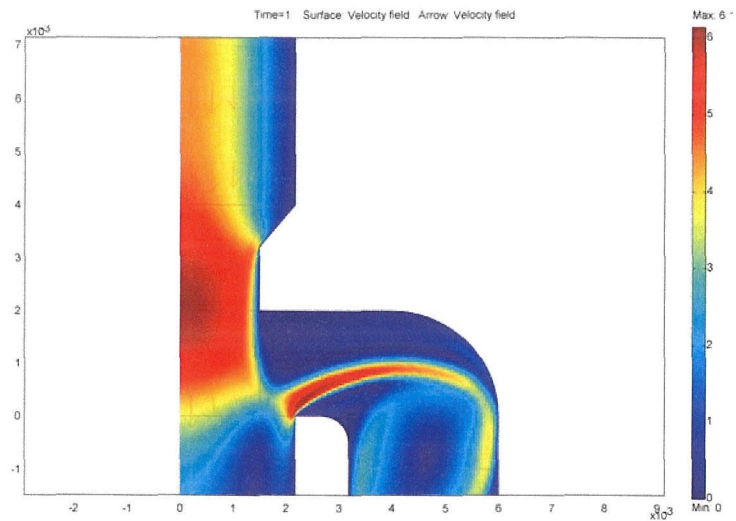
results indicate that the exit flow is not properly constrained unless the gap distance below the exit jet surface is a fraction of the jet diameter, typically  $\frac{1}{4}$  or less. See Figs. 7.1–7.2.

In Fig. 7.1(a), a 3 mm diameter nozzle is projected over a virtual impaction plane that is 1.4x wider than the diameter. The gap is 2 mm. Even for a flowrate of 2000 sccm, the exiting flow shows instability when the exit annulus is too large. Figure 7.1(b) shows a 3 mm jet diameter that is allowed to diverge at  $15^\circ$  until its diameter is 1.5x the minimum. A flowrate of only 1000 sccm is modeled. The virtual impaction plane is the same diameter as the constriction in the jet. Although the expansion in the jet limits recirculation in the exit flow, the narrowness of the virtual impactor diameter may limit efficiency.

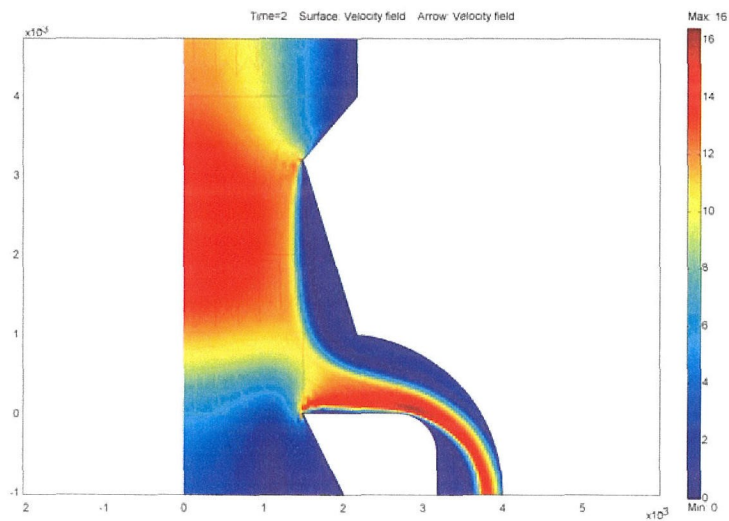
Figure 7.2 illustrates flow through two nozzles of 0.5 mm diameter. In Fig. 7.2(a), the nozzle is straight and the exit gap is 1 mm. The flow is modeled without a virtual impactor opening, i.e., as an actual impaction surface. Although the flowrate is 1000 sccm, sufficient momentum in the flow exiting the jet delays flow divergence and leads to unstable flow downstream, making model convergence difficult to achieve. Figure 7.2(b) uses a discretized hyperbolic exit from the nozzle with a 0.2 mm gap and 5000 sccm flowrate. Here the exiting flow remains stable until it is far enough downstream that its effect on impactor performance would be minimal. The velocity arrows in these plots are reproduced with the same length to indicate direction of fluid motion.

Modeling a downstream venturi, Fig. 7.3, to alleviate the pressure fluctuations that lead to unsteady flow in the earlier models did not appear to produce a workable solution. Fluid still penetrated into the collection chamber and induced enough slowly recirculating flow that many particles would likely remain entrained and exit through the venturi.

Introducing an additional diverging space void for turning the fluid above the impaction plane using a  $45^\circ$  tapered wall offered the greatest promise for a working design. This



(a) 3 mm nozzle diameter, 2000 sccm flow, 1 mm exit gap. Exit flow is not constrained downstream.

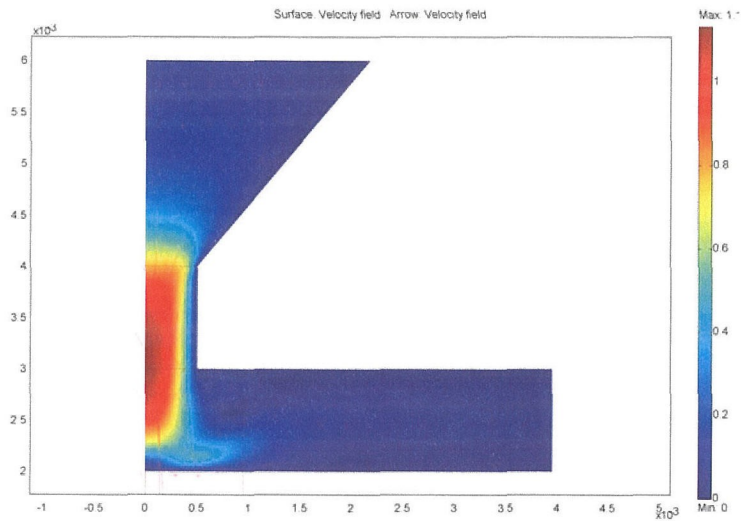


(b) 3 mm nozzle diameter, 1000 sccm flow, 2 mm exit gap. Exit flow is largely constrained.

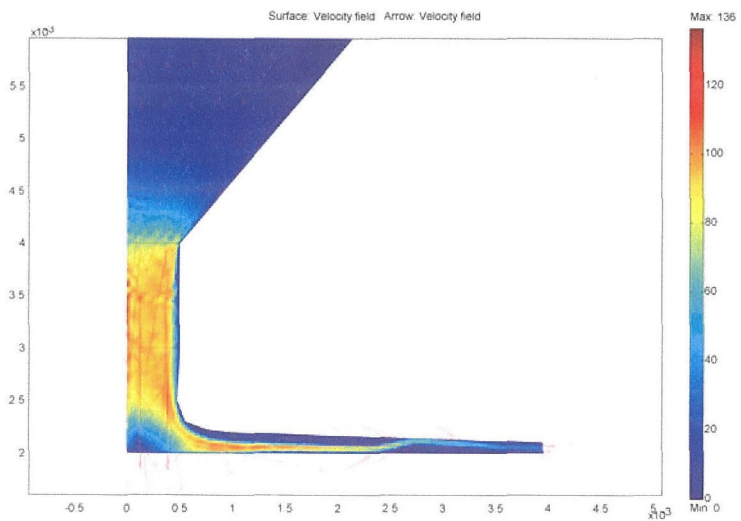
Figure 7.1: Exit gap adjustments for 3 mm diameter nozzle.

angle fits the rule of thumb for the disturbance in the flow exactly, wherein the channel diameter and turning depth exactly match in size. However, the incoming jet still needed modification. If the jet nozzle was kept straight, sufficient momentum existed in the flow to penetrate the collection chamber, Fig. 7.4, preventing the model from converging, and in real terms, likely indicating unstable flow.

The introduction of a region for fluid to change direction was robust enough that the model was capable of converging with alternate nozzle geometries, including a smooth-curved, Fig. 7.5(a), exit and a discretized hyperbolic nozzle, Fig. 7.5(b), exit.



(a) 1 mm nozzle diameter, 1 mm exit gap. Exit flow is not constrained with 1000 sccm flowrate.



(b) 1 mm nozzle diameter, 5000 sccm flow, 0.2 mm exit gap. Exit flow is largely constrained.

Figure 7.2: Exit gap adjustments for 1 mm diameter nozzle.

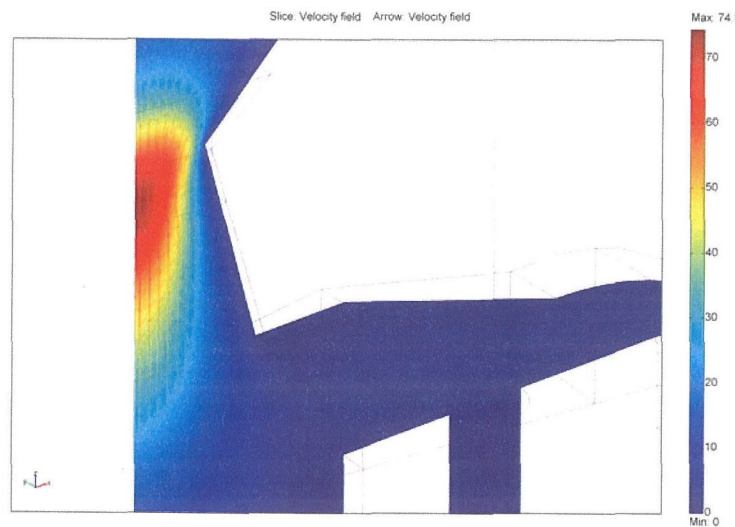


Figure 7.3: 15° tapered nozzle with a venturi downstream in 1 mm exit gap. Impaction flow still penetrates the collection chamber.

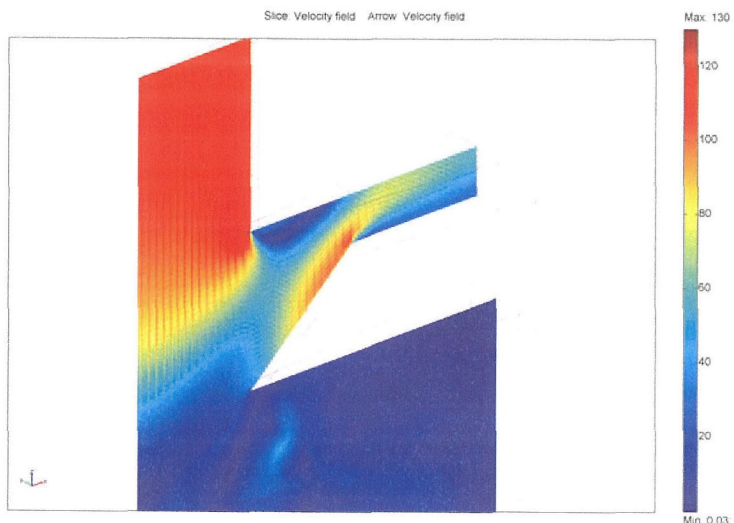


Figure 7.4: Velocity profile using a straight jet modeled in Femlab.



(a) Curved nozzle with 0.2 mm exit gap and  $45^\circ$  turning zone.



(b) Discretized hyperbolic nozzle with 0.2 mm exit gap and  $45^\circ$  turning zone.

Figure 7.5: Exit gap adjustments for 3 mm diameter nozzle.

### 7.2.2 Electrostatic Precipitator

Collection of charged aerosol particles by electrostatic precipitation offers a degree of efficiency, speed, and precision that is superior to thermophoresis. Particles from the turbulent mixing aerosol reactor are well-formed single, spherical particles wherein the aerodynamics are well understood. While charged particles drift in an electric field at velocities wherein Brownian diffusion is relatively unimportant, lack of a charging tool with efficient throughput hinders this technology from being implemented as the method of choice. When charging using an ambipolar ion source such as an  $^{85}\text{Kr}$  neutralizer, the nanoparticles used in these studies are typically singly charged particles, but with efficiencies less than 5%,<sup>2,40,142,143</sup> severely limiting the collection efficiency.

For labscale collection on TEM grids and wafer fragments, we have employed a device with a 2 mm diameter nozzle in an electrostatic precipitator typically operated with a 2000 V bias across a  $\sim 1$  mm gap. However, not being involved in the design of the device, there was uncertainty as to the efficiency of collection, especially as the flowrate of the reactor used in these studies was typically 2x–5x greater than used with the previous reactors.

Charged particles moving in a fluid subject to an electric field may be described as follows:

$$m_p \frac{d\bar{v}}{dt} = \frac{3\pi\mu D_p}{C_c} (\bar{u} - \bar{v}) + q\bar{E}. \quad (7.10)$$

At steady state, or as in the RDMA where the particles are moving orthogonally to the fluid, the drag force and electrical force are balanced,

$$\frac{3\pi\mu D_p}{C_c} \bar{v}_e = q\bar{E} \quad (7.11)$$

where  $\bar{v}_e$  is the electrical migration velocity. The electrical mobility,  $B_e$ , may then be defined

as

$$B_e = \frac{qC_c}{3\pi\mu D_p}. \quad (7.12)$$

Modeling in Femlab<sup>TM</sup> was performed to predict collection characteristics for a wide variety of conditions. Electric potential across the 1 mm gap was varied from 1000 V to 3000 V. Particle sizes ranged from 2.5 nm to 20 nm. Flowrates were adjusted between 1000 sccm and 3000 sccm. A 3 mm diameter collection stage modeled the TEM grid used in actual collection. Results are shown in Figs. 7.6–7.8. At all flowrates and applied potentials, the smaller nanoparticles are seen to be completely deposited on the collection surface. However, the larger particles, 20 nm and presumably greater, do not deposit with similar efficiency. Hence, interpreting particle size distributions of polydisperse aerosol using TEM counts is skewed towards overreporting smaller-sized particles.

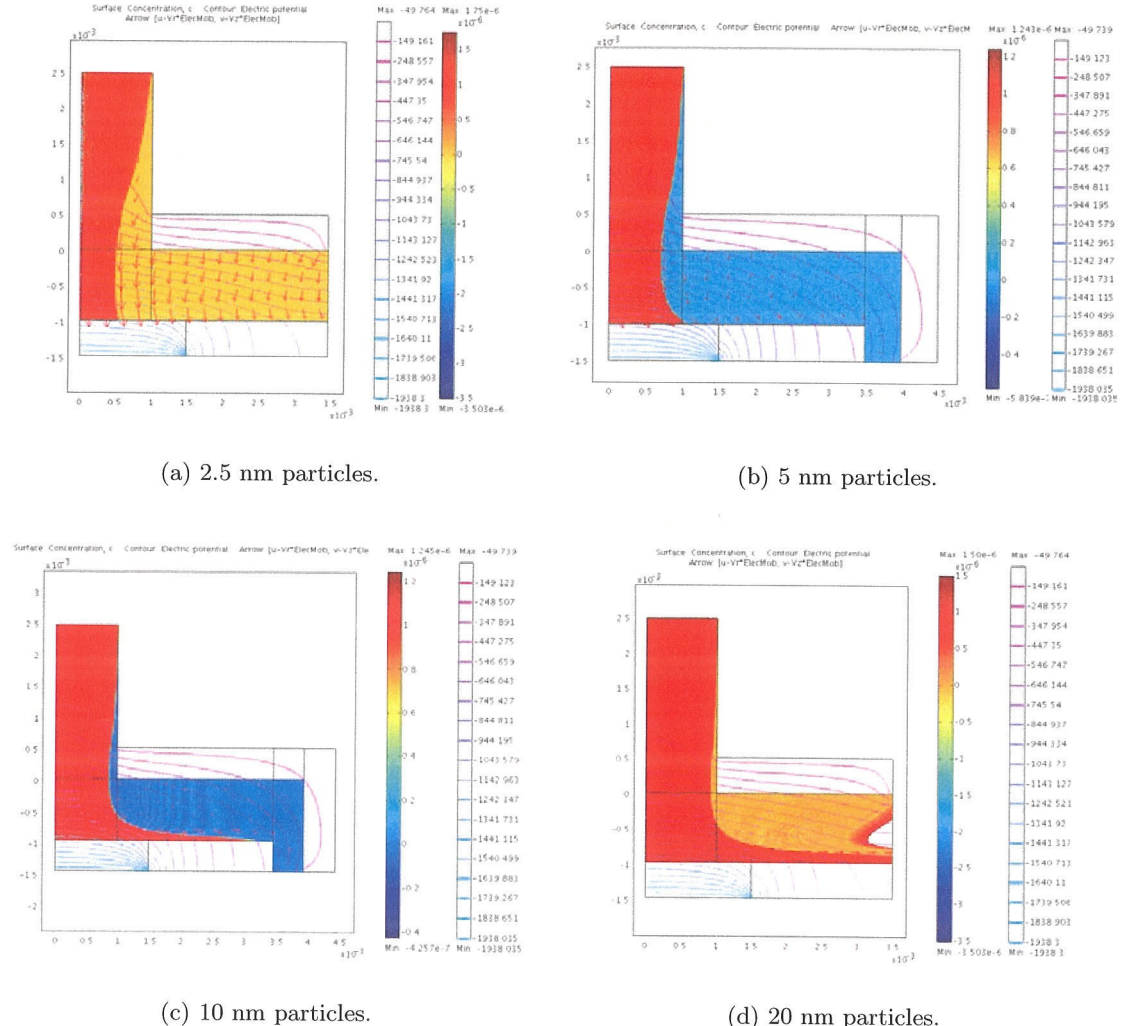


Figure 7.6: Deposition modeling on 3 mm TEM Grid with a 2000 V electric field across a 1 mm gap and 2000 sccm flow through nozzle.

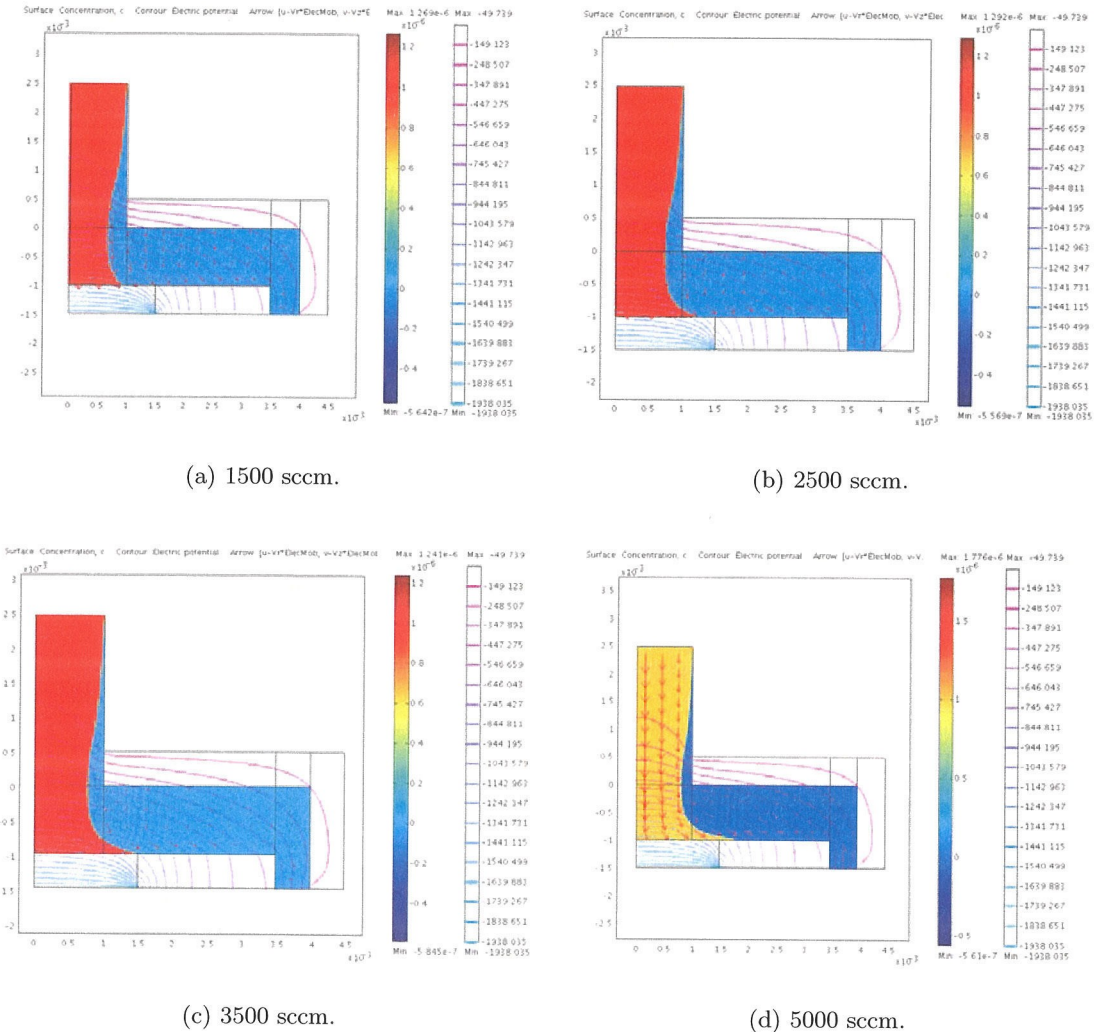


Figure 7.7: Deposition modeling of 5 nm particles on 3 mm TEM Grid with a 2000 V electric field across a 1 mm gap with varied flowrates.

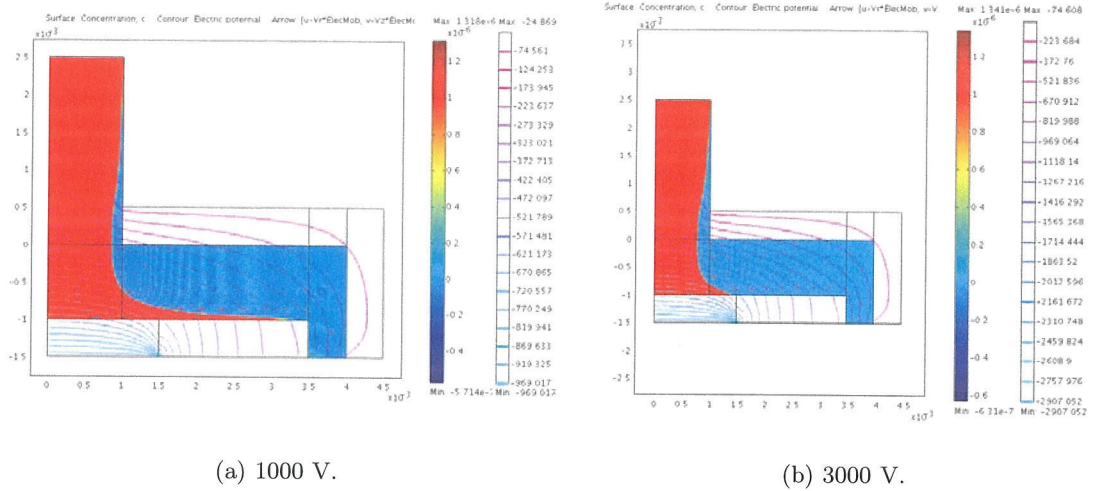


Figure 7.8: Modeling of deposition of 5 nm particles onto a 3 mm TEM Grid with various electric field strengths across a 1 mm gap and using 5000 sccm flowrate.

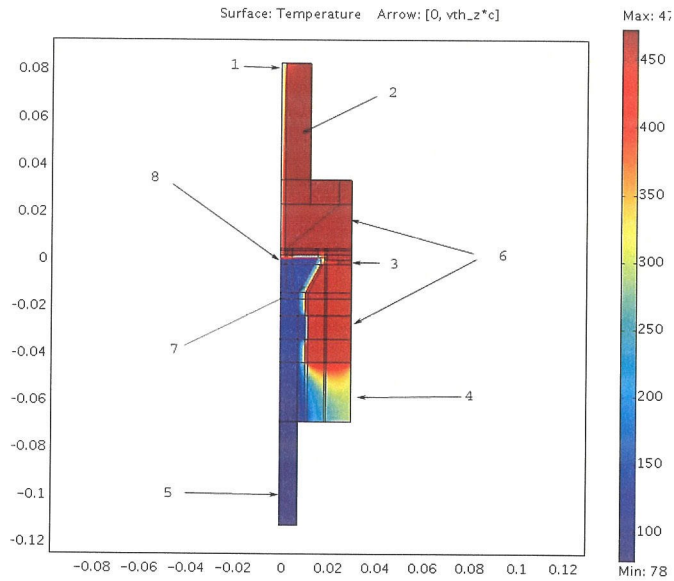
### 7.2.3 Thermophoretic Depositor in ESP Housing

Photoluminescence studies of particles collected by ESP were hindered, in part, by the scattering of incident laser light during analysis, especially with relatively a large laser output of 100 mW. Aerosol particles were deposited in heaps  $\sim$  2 mm in diameter that were visible to the naked eye. Around the particle deposits were dark, scorch-like markings, possibly from arcing during deposition. Electrical breakdown could occur during the deposition of large numbers of charged particles at high concentrations, or if the gap between the electrodes is too narrow. The effect of arcing on the particle morphology or behavior was not investigated, but eliminating the unwanted experimental parameter motivated building an alternate collector.

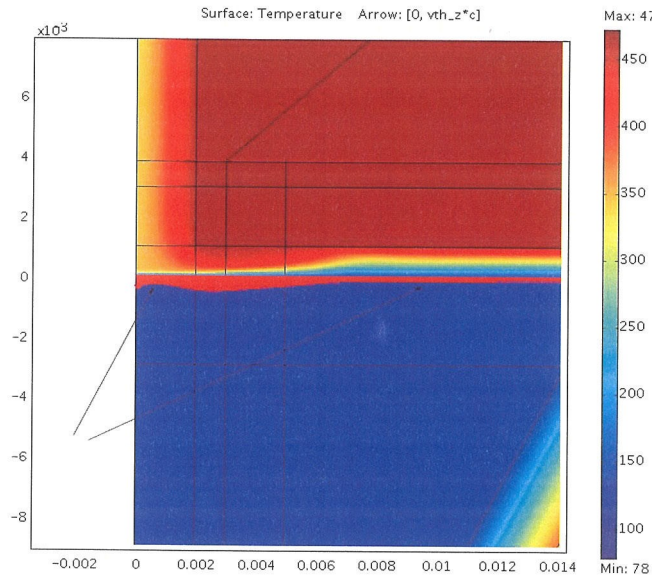
For low to moderate flowrates and for the size distributions produced in the lab, thermophoretic diffusion<sup>141</sup> is efficient and non-discriminatory in effecting particle movement. While the flowrates were too large through the 2 mm diameter nozzle to efficiently collect

most of the particles, particles that diffuse into the boundary layer<sup>49,127</sup> near the stagnation point of the impacting jet would likely diffuse to the surface and deposit.

To collect samples, a wafer-fragment stage, Fig. 7.9(a), was attached to a cold-finger stage that could be inserted through the bottom of the ESP tool and dipped into liquid nitrogen to provide the cold sink for thermophoresis. Teflon was machined to fit between the cold-finger stage and the aluminum ESP housing (borrowed from a cascade impactor) to limit thermal conductivity into the cold finger. The top housing was replaced with a brass inlet heater tape housing that could be connected using Swagelok<sup>TM</sup> fittings. Viton o-rings sealed the top and bottom chambers, limiting the heater to temperatures less than 473 K during operation. Styrofoam was used to insulate the top of a 500 ml dewer filled with liquid N<sub>2</sub> from the ESP/TD housing into which the cold finger was placed.



(a) Thermal profile and thermophoretic flux arrows of thermophoretic collector.



(b) Concentration profile and thermophoretic flux arrows (seen as red band above the arrows) over wafer holder in collection area. Background color indicates temperature.

Figure 7.9: Modeling of thermophoretic flux of particles. In (a), the numbers correspond to:  
 1. Aerosol inlet. 2. Brass heater tape housing. 3. Aerosol outlet. 4. Styrofoam insulator.  
 5. Brass cold finger dipped into liquid N<sub>2</sub>. 6. Aluminum housing. 7. Teflon insulator. 8.  
 Wafer fragment housing/deposition area.

The liquid nitrogen evaporated fully over a period of 45–60 min, limiting deposition to this timeframe. A 20 min period of thermal equilibration with the room was necessary before exposing the sample to the humidity in the room air, otherwise a frost layer would immediately form on the chilled sample and cold finger, damaging the nanocrystals. A darkfield TEM image, Fig. 7.10, of a frosted sample contained a 25 nm particle with a 7–8 nm crystalline core and an 8–9 nm thick shell.

Integration of particle flux in Femlab<sup>TM</sup> over the inlet and a 5 mm radial deposition area indicated that about 4% of incoming particles deposit. The thermophoretic flux arrows, Fig. 7.9(b), indicate that deposition is neither non-uniform nor widely varying over the deposition area.

#### 7.2.4 Thermophoretic Liquid Trap

The need to efficiently collect aerosol particles in a liquid medium motivated some modeling work to determine an efficient method of collecting particles in a small volume of liquid. Typically, aerosol particles were collected using a gas-liquid exchange by bubbling the aerosol containing gas streams through columns of degassed liquid using flowrates,  $\sim 2000$  sccm, that required liquid volumes of  $\sim 100$  ml or more. Fine porous frits created small bubbles to enhance transfer efficiency, but with this comparatively large volume of liquid needed to

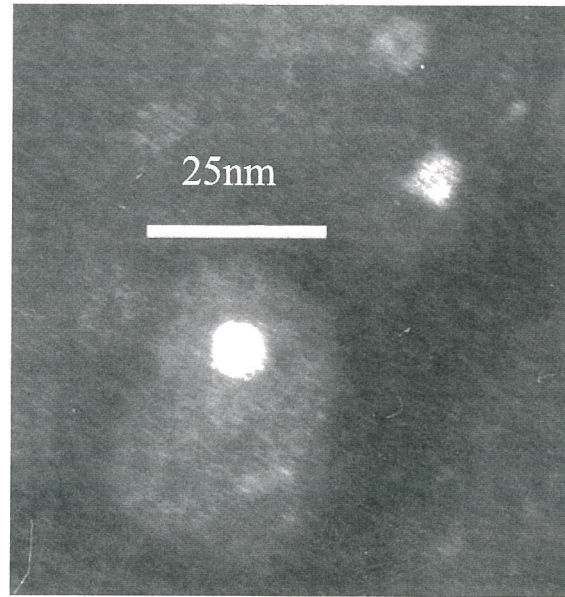


Figure 7.10: Darkfield image of silicon core particle and oxide shell after exposure to frost.

enhance transfer time and avoid aerosolizing the collection medium itself, collection periods needed were greater than the time the reactor took to foul. The evaporation of relatively higher vapor pressure liquids (at room temperature) such as water or methanol also was a factor contributing to the inefficiency of this method, as collection time decreased with the decreasing liquid column height.

Preferably the liquid volume should be kept to a minimum to avoid a long collection time while collecting a suitable concentration. The device needs to be sealed with an inert environment during particle collection and subsequent transport and evaporation needs to be suppressed. It is reasonable that this collection method may be accomplished with a device analogous to the wafer deposition chamber. A long, thin, liquid well with a gas channel above may be cooled from below and heated above the gas providing the necessary thermophoretic driving force. The liquid well volume can be kept small by using channels, if needed, within the liquid well. Channels also would reduce the possibility of the liquid being pushed out of the well by the moving gas above. Modeling of thermophoretically driven particles into a liquid channel is shown in Figs. 7.11–7.16.

Using Femlab<sup>TM</sup>, a 2D model of a liquid channel 10 cm long (5 cm into the page) is cooled from the bottom by contact with either a liquid N<sub>2</sub> (200 K) or water-containing (300 K) heat exchanger. A 1 cm deep gas channel above the liquid is resistively heated from the top. Sealing the collection chamber using o-ring type seals made of PTFE or Viton would limit the top temperature to less than 500 K, thus this is the top temperature modeled. PTFE and Viton are typically used to avoid contamination. Gas flow is laminar, and the entrance region may be heated or cooled as needed. At the gas liquid interface, a slip boundary condition is employed, but liquid recirculation is not modeled as implementation of this movement prevented model convergence. In Fig. 7.11(a) and Fig. 7.11(b), with respective

flowrates of 1000 sccm and 1500 sccm, no preheating of the inlet aerosol and using a water exchanger (300 K) at the bottom predicted that thermophoretic collection is less than 50% of the entering aerosol.

In Fig. 7.12(a) and Fig. 7.12(b), the flowrate is increased to 2000 sccm while the aerosol is preheated to 500 K. Fig. 7.12(a) is modeled with water cooling while Fig. 7.12(b) is modeled with liquid N<sub>2</sub> cooling. With the increased flowrate and a similar temperature drop, thermophoretic transport is predictably reduced. In contrast, the thermophoretic flux arrows indicate relatively greater transport near the inlet than seen in Figs. 7.11(a)–7.11(b). This is attributable to the increased temperature gradient above the cooled liquid near the entrance formed by preheating the gas. However, only a little improvement in collection is predicted with the enhanced cooling from liquid N<sub>2</sub> compared to room temperature water cooling.

Reducing the flowrate, Fig. 7.13, while preheating to 500 K and using water cooling also did not achieve enough collection. Although there is slightly greater transport at 1000 sccm, in each case less than 50% of the particle concentration is driven into the liquid well. The similarity of each of the models suggested that using a longer chamber may have a greater effect than reducing flowrate.

The modeled device was reconfigured for a chamber 20 cm long (3 cm into the page) to keep the residence time similar. The gap depth remained unchanged at 1 cm. The model flowrate was set at 2000 sccm, cooling was by liquid N<sub>2</sub> cooling, and the introduction of the aerosol was at room temperature. In Fig. 7.14, the model predicts that just over half the entering particle concentration is driven to the liquid well. The longer length model also demonstrated that reducing the gap height, thus strongly increasing the temperature gradient, would likely have the greatest effect on increasing collection. This is not surprising,

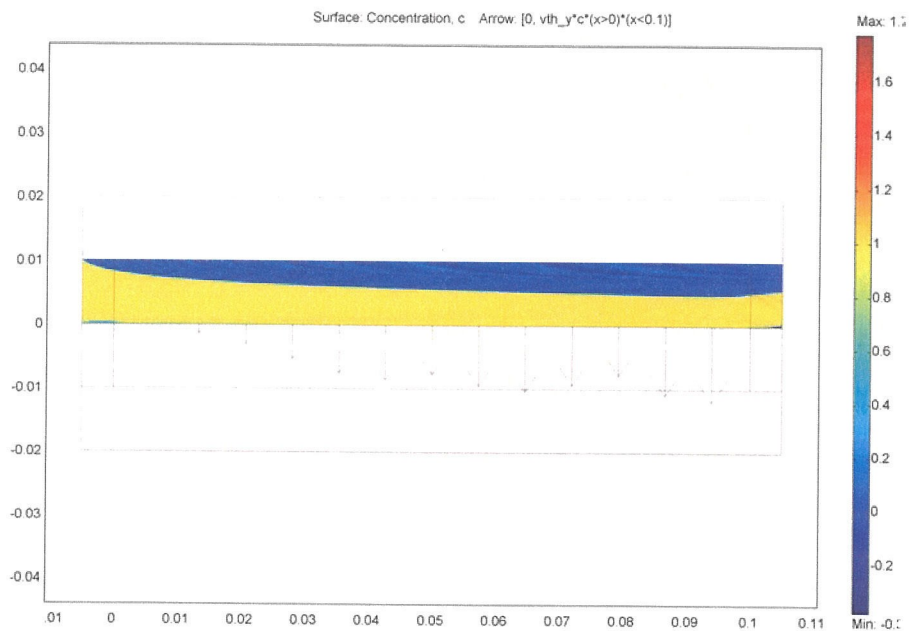
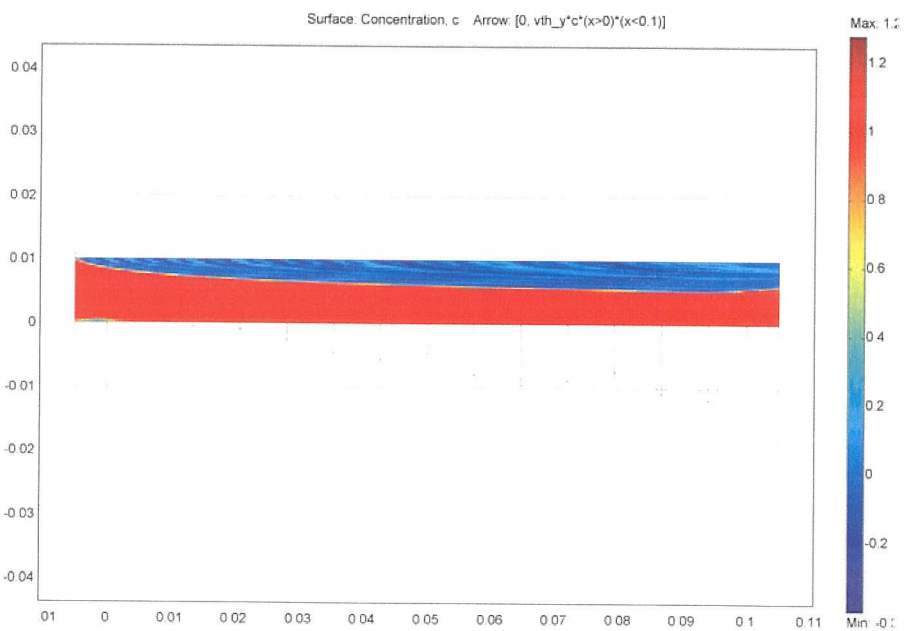
(a) 1500 sccm, 300 K inlet, H<sub>2</sub>O cooled.(b) 2000 sccm, 300 K inlet, H<sub>2</sub>O cooled.

Figure 7.11: Collection efficiencies less than 50% are predicted for a chamber 10 cm x 5 cm x 1 cm.

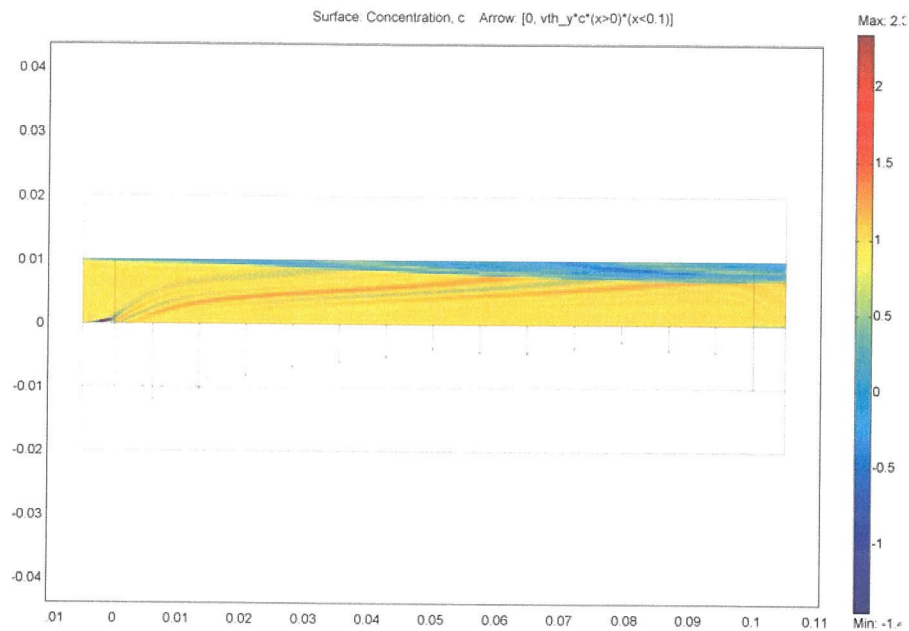
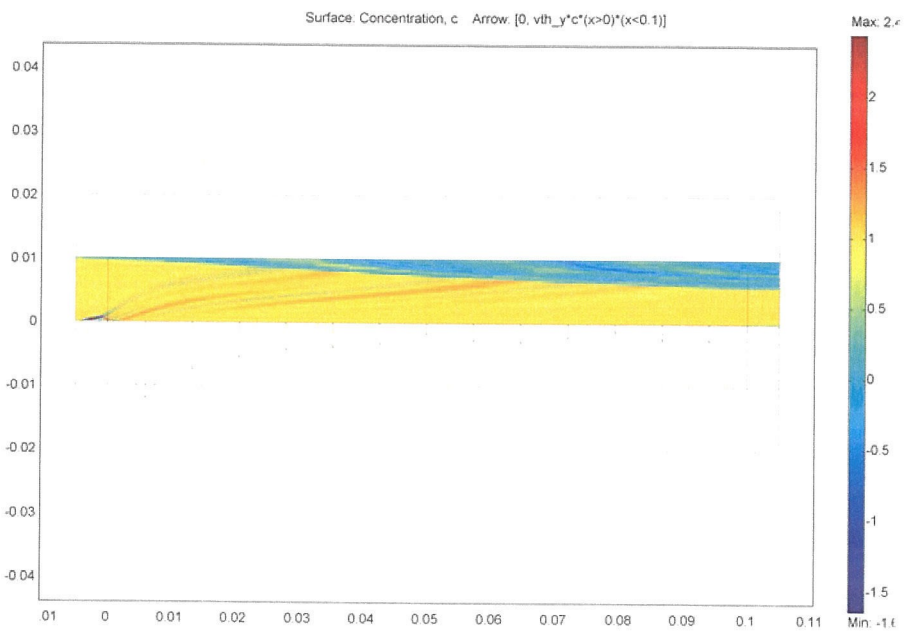
(a) 2000 sccm, 500 K inlet, H<sub>2</sub>O cooled.(b) 2000 sccm, 500 K inlet, N<sub>2</sub> cooled.

Figure 7.12: Collection efficiency improves using a liquid nitrogen cooled surface, but remains unsuitably low.

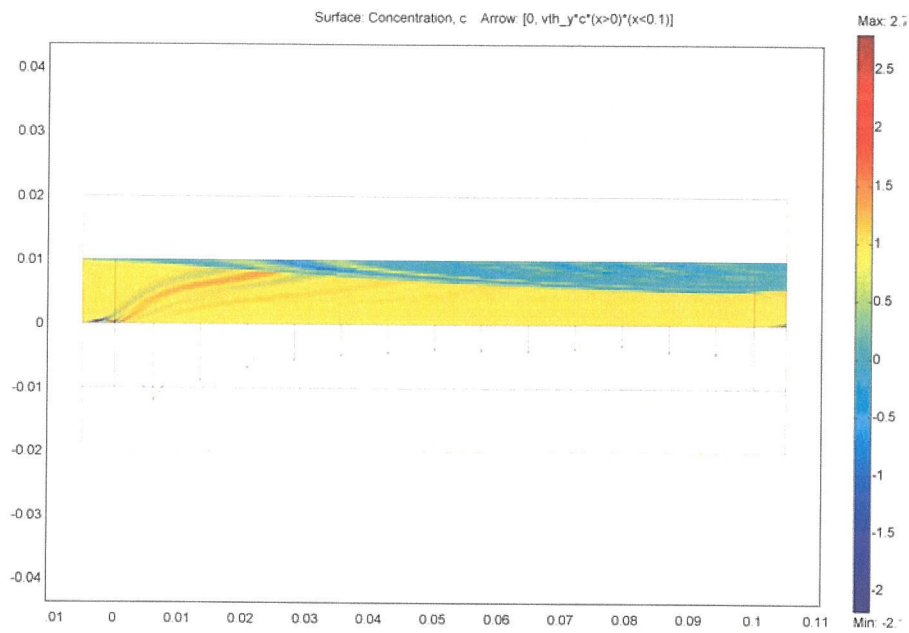
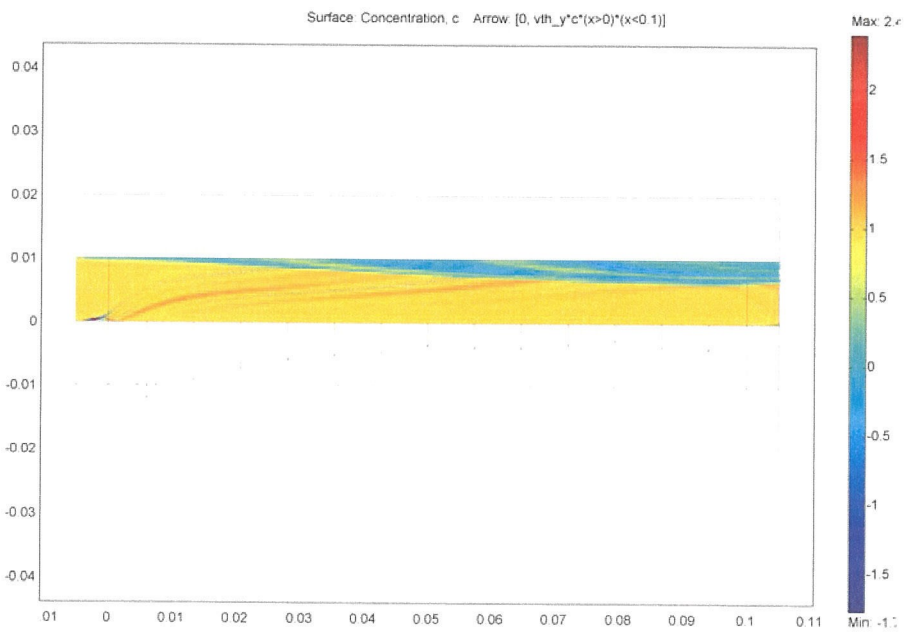
(a) 1000 sccm, 500 K inlet, H<sub>2</sub>O cooled.(b) 1500 sccm, 500 K inlet, H<sub>2</sub>O cooled.

Figure 7.13: Low flowrates with a water-cooled system, still yields low collection efficiency.

but utilization could lead to flowrates strong enough to blow the liquid out of the well.

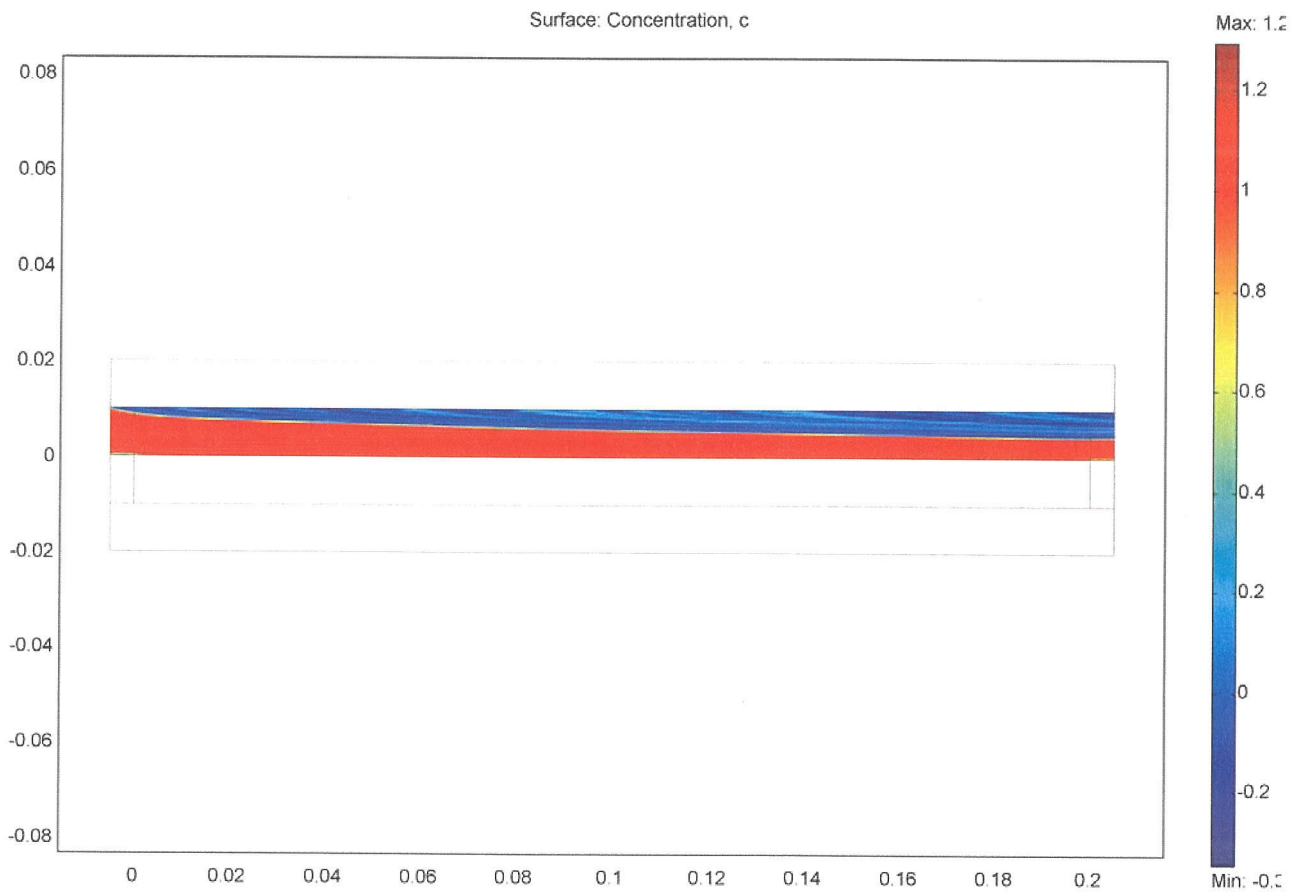
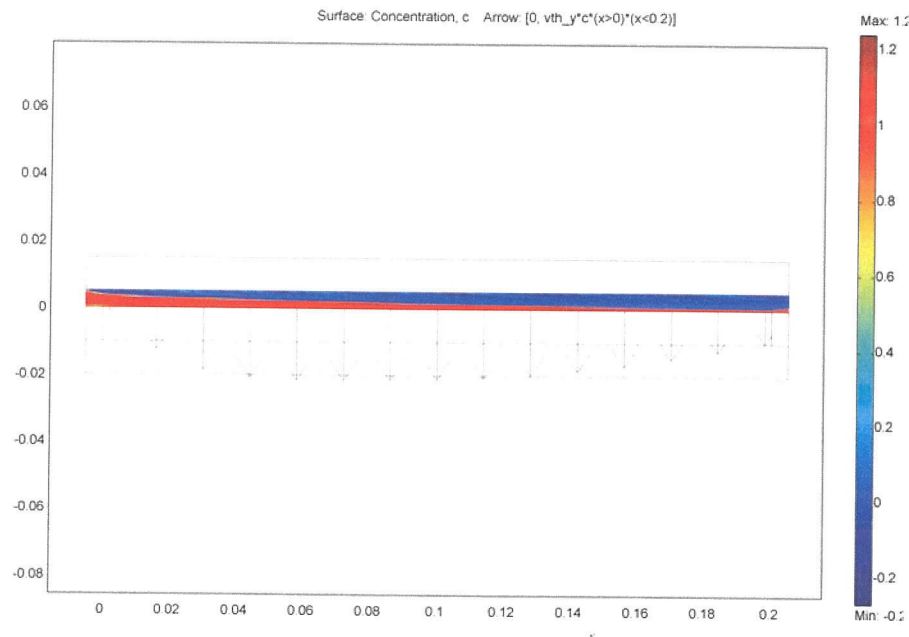
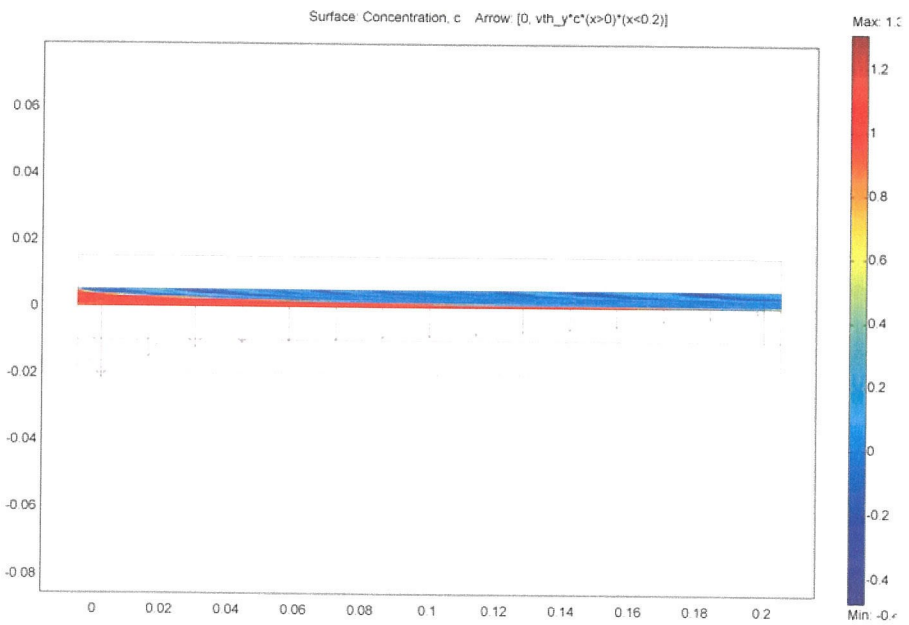


Figure 7.14: Longer collection length yields greater collection of particles.

With the gap height set at 12.7 cm, model results are seen in Figs. 7.15–7.16. The faster flowrates of 2000 sccm were modeled. Very little difference is seen whether the cold side is at room temperature or liquid N<sub>2</sub> cooled, although virtually all of the particles are expected to be collected when using liquid N<sub>2</sub>. An advantage to using liquid N<sub>2</sub> for cooling is the reduction of vapor pressure for more volatile liquids, increasing viscosity and reducing the possibility for the liquid to be blown out of the well. However, it requires constant replenishment of the liquid N<sub>2</sub> throughout the collection period.

An alternate scenario using water cooling that is nearly as efficient as using liquid N<sub>2</sub> involves preheating the aerosol to 400 K as seen in Fig. 7.16. This configuration has the advantage of requiring less maintenance, i.e., not replacing liquid N<sub>2</sub>, during operation. The thermophoretic flux arrows indicate that this configuration may produce the most uniform deposition over the entire liquid well, which may be advantageous if collecting into viscous fluids.

(a) 2000 sccm, 300 K inlet,  $\text{H}_2\text{O}$  cooled.(b) 2000 sccm, 300 K inlet, liquid  $\text{N}_2$  cooled.Figure 7.15: Comparison of  $\text{H}_2\text{O}$  and liquid  $\text{N}_2$  cooled 20 cm x 3 cm x 0.5 cm collectors.

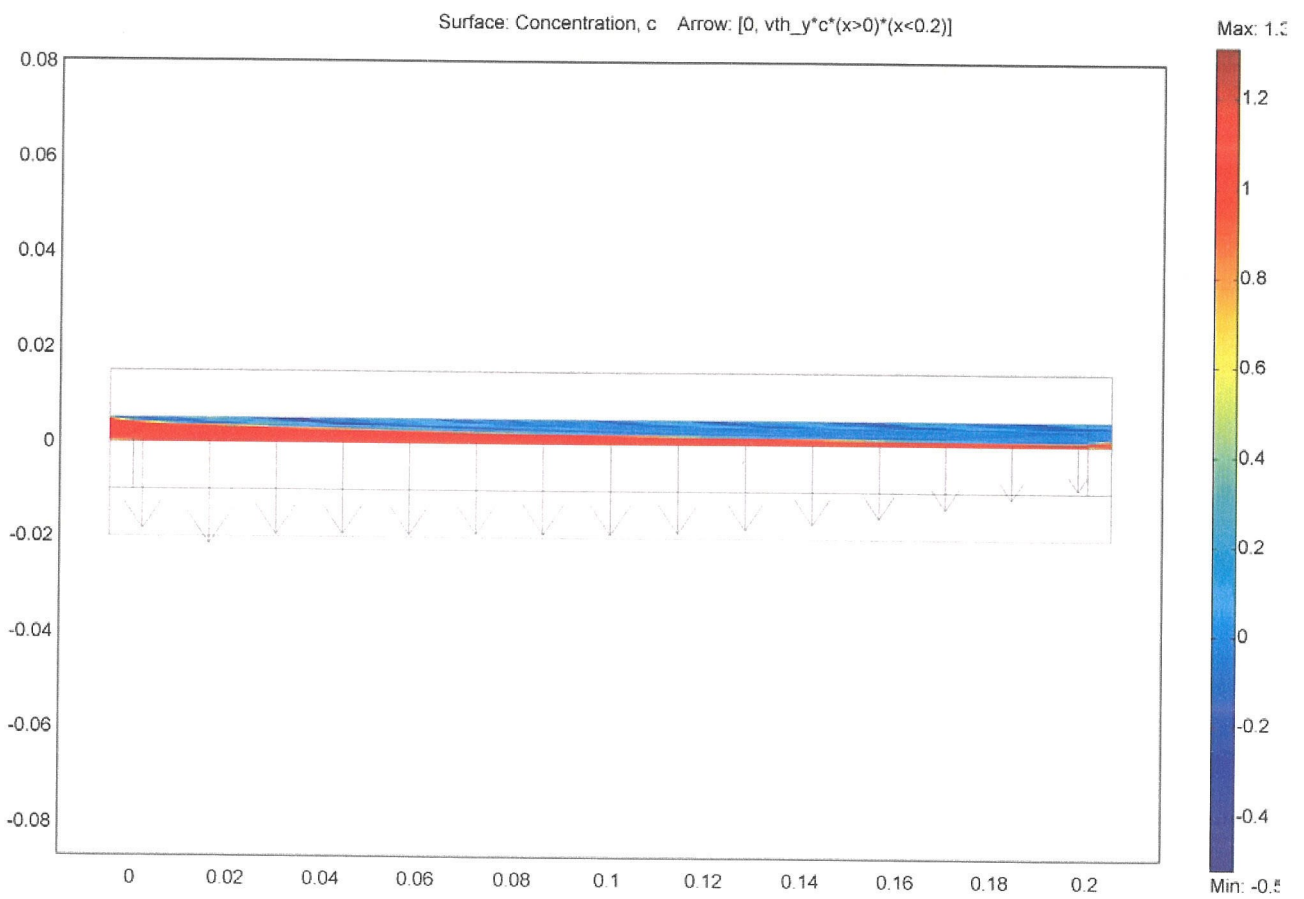


Figure 7.16: Thermophoretic flux arrows are most uniform for this design in this configuration with 2000 sccm, 400 K inlet,  $\text{H}_2\text{O}$  cooled.

## Chapter 8

# Appearance of Bipolarly Charged Particles

### Abstract

Aerosol particles fabricated at 1273 K in a turbulent mixing reactor constructed from Inconel were detected to have a bipolar distribution of electrical charge. The charge distribution is less than that obtained at steady-state within a so-called neutralizer, although negatively charged particles outnumbered positively charged particles in ratios of  $\sim 1.25 : 1$  or greater. Radioactive contamination of the metal as a charging source was briefly investigated, but no detectable radioactivity was found. The source of the charge has not yet been identified.

### 8.1 Introduction

Aerosol charging is attracting renewed interest as a means of achieving precise deposition control of nanoparticles using electrostatic precipitators. Electrostatic precipitation is fast and can eliminate the smearing effect caused by Browning diffusion during aerosol transport. A distribution of nanoparticles might be deposited with such precise size selectivity that, for very small nanoparticles, characterization of size-related properties may become discernable. For broader applications, an efficient unipolar charger that preserves the ma-

jority of sub-10 nm nanoparticles has not been made, although recent progress approaches 50% efficiency.<sup>3,64,80,94,118,119</sup>

Some charging may occur during the formation of an aerosol in a high temperature reactor, particularly for sub-10 nm particles. This charging is limited and unipolar,<sup>41</sup> and has been attributed to a thermal charging mechanism.<sup>68</sup> The origin of the charging mechanism for the bipolar charge observed was not determined.

Enhanced agglomeration<sup>1</sup> or ion-induced nucleation has not been observed for bipolarly-charged particle distributions within the observed size range.

## 8.2 Design

Particles were fabricated in the turbulent mixing aerosol reactor described within this thesis. Aerosol streams were sent directly from the reactor to the RDMA and a fA-resolution electrometer without passage through, or mixing of ion-rich gas from, a neutralizer. The polarity of the potential applied to the RDMA was reversed to measure quantities of particles of either charge.

## 8.3 Results

A fraction of the sub-20 nm particles leaving the turbulent mixing reactor are charged. While others have reported unipolar-charged nanoparticles exiting reactors and attributed the mechanism to thermal charging, these particles were observed to have a bipolar distribution, with a greater proportion of particles carrying a negative charge. Figure 8.1 shows that this proportion is  $\sim 25\%$ , similar to the steady-state charge distribution predicted by Fuchs,<sup>40,143</sup> such as obtained in an aerosol neutralizer.

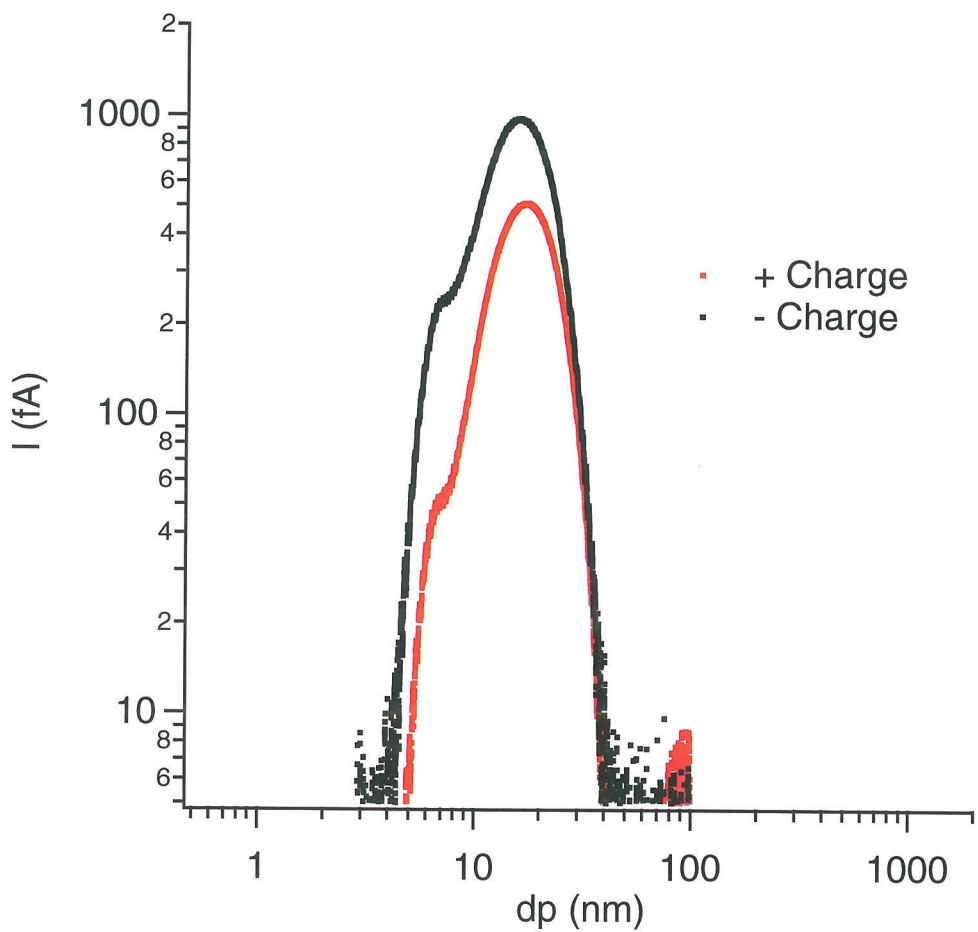
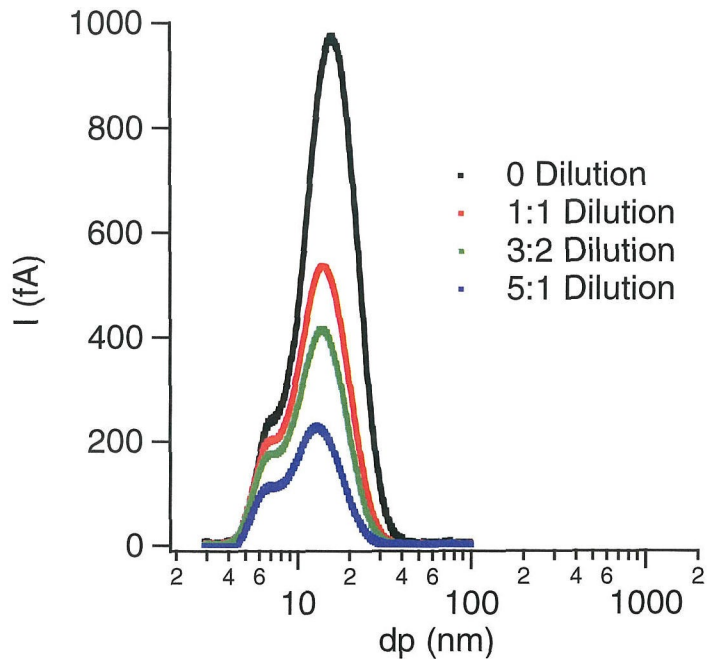


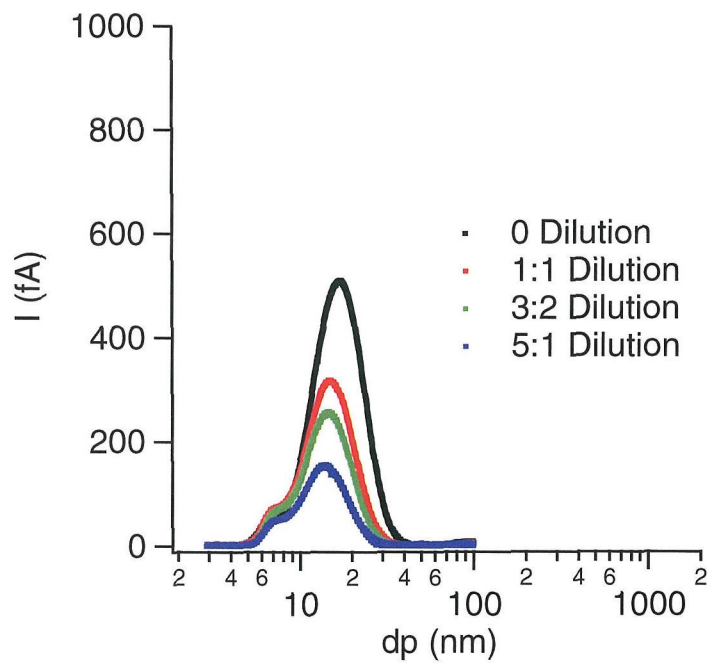
Figure 8.1: Current in fA measured with an electrometer from charged particles immediately exiting Inconel Reactor.

The particles were mixed in a 0.125" Swagelok<sup>TM</sup> Tee with various ratios of N<sub>2</sub> leaving a neutralizer, similar to that explained in Chapter 2, but without a turbulent jet to accomplish quick mixing, no asymptotic current limit was measured for either species of charged particle. See Figure 8.2. The number of charged particles per unit volume of aerosol increases with increased ion-rich N<sub>2</sub> but the increase is less than linear, Fig. 8.3, with the dilution ratio. Thus the bipolar charge distribution is less than the steady-state that would be obtained in an aerosol neutralizer.

However, it is highly unlikely that thermionic emission of nitrogen at 1273 K could create this charge distribution. Charging sources within the apparatus were briefly investigated, both with a pico-roentgen sensitive Geiger counter and by physically removing the aerosol neutralizer from the reactor proximity. The metals in the furnace and reactor assembly tested negatively for radioactive contaminants. The charge distribution was unaltered when the neutralizer was removed from the vicinity. Thus it is unlikely that the origin of the bipolar distribution is from a leaking neutralizer.



(a) Negatively Charged Particles.



(b) Positively Charged Particles.

Figure 8.2: Current measured at electrometer from charged particles exiting reactor with various ratios of ion-rich  $N_2$  from  $^{85}Kr$  neutralizer.

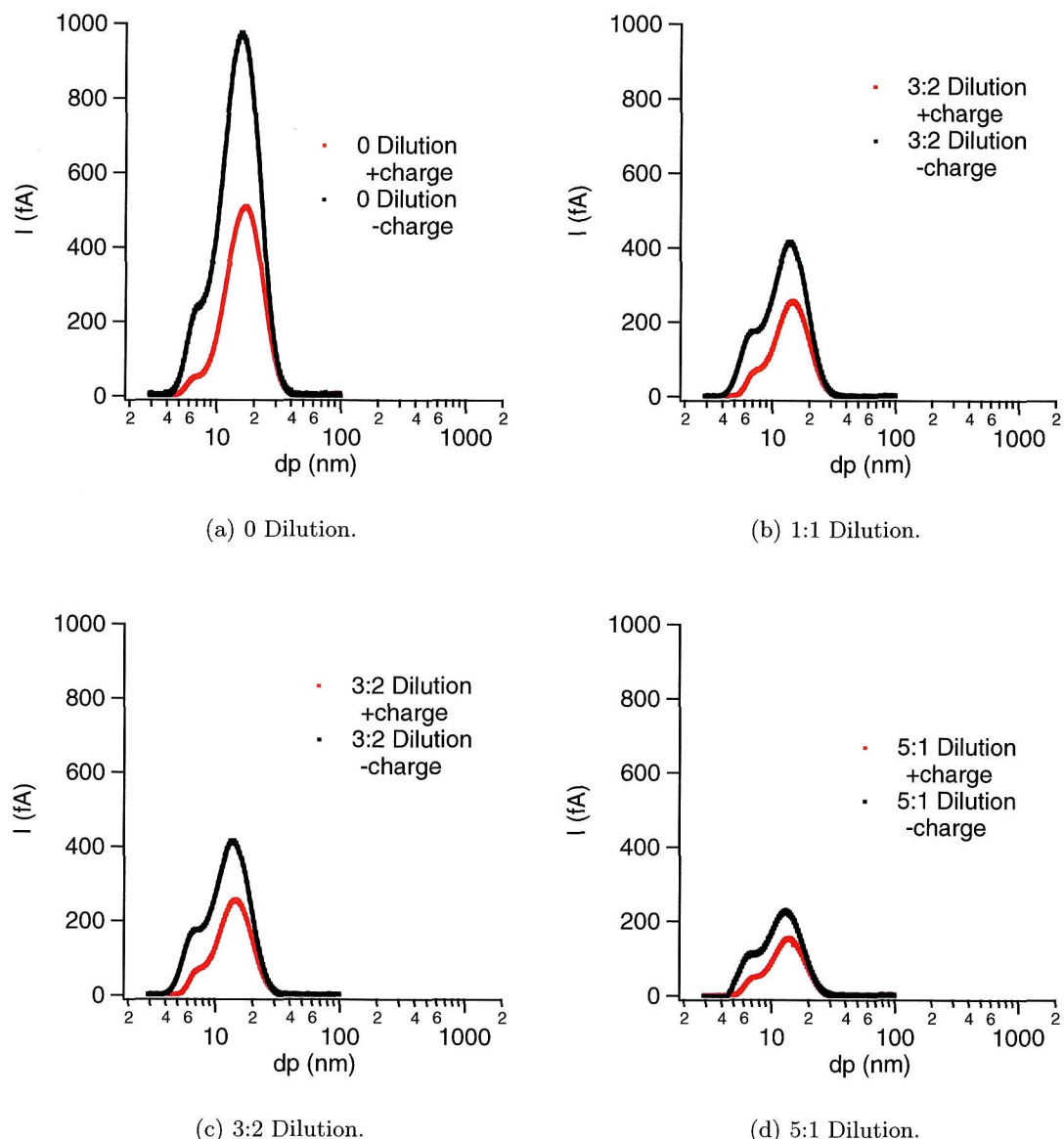


Figure 8.3: Current measured at electrometer from charged particles exiting reactor with various ratios of ion-rich  $N_2$  from  $^{85}\text{Kr}$  neutralizer.

Kousaka<sup>77</sup> reported that aerosols could acquire charge during formation. Whether charging was unipolar or bipolar was dependent on the formation method and the material being aerosolized. For example, CaCO<sub>3</sub> particles appeared to be charged mechanically during passage through a glass venturi. No mechanism was proposed for charge transfer from the venturi surface to the aerosol. Similarly, the turbulent mixing of the reactor jets is a mechanical mixing process.

## 8.4 Conclusions

Further investigation into the charging mechanism is warranted, even if only to demonstrate that the first test for radioactive contamination in the reactor metals was a false negative. If radioactivity testing remains negative, then the charging mechanism becomes more interesting. If a charging mechanism can be shown to be reliably repeatable, characterization of high particle density ultrafine aerosols may be accomplished with less particle loss to the plumbing and reduced agglomeration during the charging-time process.

## Chapter 9

# Conclusions

We have demonstrated that particle number production can be significantly improved without sacrificing monodispersity or particle purity. Although fouling limits the present application of the turbulent mixing reactor to a few hours of operation, scaling the reactor to larger diameter tubing may increase the mass throughput to  $\sim \frac{\text{mg}}{\text{hr}}$  and reduce the immediate impact of fouling. Long-term improvements will require re-design of the nucleation region. Preventing nucleation near a sink and allowing particles to grow reduces their mobility and the potential for particle loss. One potential alternative, apart from re-design, is to seed the reactor using a microplasma discharge reactor. The turbulent mixing reactor can function as a growth, densification, and annealing reactor to produce well-formed, heterogeneous core-shell structures with a minimum of agglomerates.

Photoluminescence spectra collected from the oxide-coated nanoparticles is consistent with models of quantum-confined, exciton recombination in silicon. Observation of spectra is evidence of contaminant-free particles. However, to make aerosol-made nanoparticles available to different applications, an efficient collection tool is needed in which particles may be dispersed and stored in liquids and made available to collaborators. The use of photoluminescent silicon nanoparticles as biological markers has drawn recent interest, as do questions over the toxicity of nanoparticles.

We have shown uniform coverage of nanoparticles by thermophoretic deposition on 150 mm wafers and, by modeling, expect similar coverage on 300 mm wafers. The chamber design permits deposition on smaller surfaces. This tool can be used for the fabrication of nanoparticle-containing devices, for studies of particle stability, or to collect catalysts that facilitate growth of materials such as carbon nanotubes. Particle adhesion studies of ensembles of small nanoparticles on surfaces are needed to address industry concerns over contaminating cleanrooms from dislodging aerosol-made nanoparticles. As microelectronics device dimensions shrink, defect-free growth of device components becomes more difficult. Aerosol made nanoparticles of key device components can be “perfected” in an ex-situ process and deposited uniformly without damage to device components already present. This advantage may make aerosol-engineered nanoparticles an important component of micro-electronic fabrication.

# Appendix A

## Additional Information

### A.1 Reactor Design—First Order Analysis

For particles developing independently of each other, the growth rate for a surface reaction limited by availability of reactant can be estimated by the flux of reactant to a particle's surface. If one further assumes a sticking parameter,  $\sigma$ , of unity at the particle's surface, then the growth rate is estimated using a vapor-particle mass balance where  $a_p$  is the particle radius;  $t$  is time;  $m_i$ ,  $C_i$ ,  $\mathcal{M}_i$ , and  $\rho_i$  are the mass, concentration, molecular weight, and density of the  $i^{th}$  species;  $n_v$  is the number concentration of particles per unit volume;  $c_v$  is the Boltzmann average velocity of the vapor phase reactant;  $T$  is temperature; and  $k_B$  is the Boltzmann constant. The subscripts  $x_p$  and  $x_v$  refer to the particle and vapor phase, respectively, elsewhere,

$$\frac{\Delta m_p}{\Delta t} = \frac{\Delta m_v}{\Delta t}. \quad (\text{A.1})$$

In the free molecular regime,

$$\frac{4}{3}\pi\rho_p \frac{\partial a_p^3}{\partial t} = 4\pi a_p^2 \frac{n_v \bar{c}_v}{4} m_v \quad (\text{A.2})$$

where the mean free path of reactant is given by

$$\bar{c}_v = \sqrt{\frac{8k_B T}{\pi m_i}}. \quad (\text{A.3})$$

For growth of particles from vapor condensation of silane.

$$m_v n_v = \rho_v = \mathcal{C}_{SiH_4} \mathcal{M}_{SiH_4}. \quad (\text{A.4})$$

Thus,

$$\frac{\partial a_p}{\partial t} = \frac{c_v \mathcal{M}_{SiH_4} \mathcal{C}_{SiH_4}}{4 \rho_p}. \quad (\text{A.5})$$

However,  $\mathcal{C}_{SiH_4}$  is depleting, requiring a mass/mole balance on the  $SiH_4$ ,

$$\frac{dn_{SiH_4}}{dt} = \text{condensation rate} = \frac{\bar{c}_v}{4} \mathcal{C}_{SiH_4} 4\pi a_p^2 \quad (\text{A.6})$$

where  $n_{SiH_4}$  represents molecules of  $SiH_4$ . At isobaric conditions,  $n_{SiH_4} = \mathcal{C}_{SiH_4} V$ . Accounting for reactions with  $N_p$  particles,

$$\frac{d\mathcal{C}_{SiH_4}}{dt} = \frac{N_p}{V} \frac{\bar{c}_v}{4} 4\pi a_p^2. \quad (\text{A.7})$$

Substituting  $\bar{N}_p$  for the number per unit volume,  $\frac{N_p}{V}$ , yields,

$$\frac{d\mathcal{C}_{SiH_4}}{dt} = \bar{N}_p \bar{c}_v \pi a_p^2. \quad (\text{A.8})$$

Eliminating the time parameter,  $t$ , from (A.2) and (A.8) yields the parametric ODE,

$$d\mathcal{C}_{SiH_4} = \frac{4\bar{N}_p\pi a_p^2 \rho_p}{\mathcal{M}_{SiH_4}} da_p. \quad (\text{A.9})$$

Solving for  $a_p(\mathcal{C}_{SiH_4})$  from a small cluster size,  $a_{p,o}$ , and initial silane concentration,  $\mathcal{C}_{SiH_4,o}$ ,

$$\mathcal{C}_{SiH_4}(t) - \mathcal{C}_{SiH_4,o} = -\frac{4\bar{N}_p\pi\rho_p}{3\mathcal{M}_{SiH_4}} (a_p^3(t) - a_{p,o}^3). \quad (\text{A.10})$$

Inserting (A.10) into (A.2) and solving where

$$K = \frac{\bar{c}_v \bar{N}_p \pi}{3} \quad (\text{A.11})$$

and

$$R^3 = \frac{3\mathcal{M}_{SiH_4}\mathcal{C}_{SiH_4,o}}{4\bar{N}_p\pi\rho_p} + a_{p,o}^3 \quad (\text{A.12})$$

yields

$$\frac{1}{6R^2} \log \left( \frac{R^2 + Ra_p + a_p^2}{(R - a)^2} \right) + \frac{1}{R^2\sqrt{3}} \arctan \left( \frac{2a_p + R}{R\sqrt{3}} \right) \bigg|_{a_{p,o}}^{a_p(t)} = Kt \bigg|_0^{t^*}. \quad (\text{A.13})$$

This first-order analysis does not take into account precursor loss to other sinks such as radial diffusion and deposition at the reactor wall. It also assumes a sticking factor of unity for all molecular contact with the developing particle.

Similarly, for a first-order growth analysis of a thermal oxide modeled as limited by transport of  $O_2$  to the surface,

$$m_v n_v = \rho_v = \mathcal{C}_{O_2} \mathcal{M}_{O_2}. \quad (\text{A.14})$$

Thus

$$\frac{\partial a_p}{\partial t} = \frac{c_v \mathcal{M}_{O_2} \mathcal{C}_{O_2}}{4 \rho_p}. \quad (\text{A.15})$$

For  $\text{SiO}_2$  growth into Si, the density varies only mildly, and a straightforward solution to this ODE assuming 15%  $\text{O}_2$  in the reactor, estimates the initial growth rate as

$$t = 3.238 \times 10^2 \Delta a_p. \quad (\text{A.16})$$

For 15%  $\text{O}_2$  in the reactor, this predicts a time-scale for a surface monolayer of an oxide layer formation of tens to hundreds of nanoseconds.

## A.2 Inconel Turbulent Mixing Reactor Fluent Modeling

The turbulent mixing reactor was modeled with the 3D  $\kappa - \epsilon$  turbulent flow solver in Fluent<sup>TM</sup>. The images from the modeling, however, were not published with the paper describing this reactor. These images are included here.

A short residence time reactor not operating entirely in a laminar flow regime requires a non-analytical study of the heat transfer and fluid flow profiles. Within the guidelines imposed by the various residence time limitations, CFD modeling identified a range of successful operation parameters wherein fabricated particles could nucleate, grow, and be expected to be crystalline. It also identified operating profiles that should be avoided, where recirculation within the reactor would lead to large agglomerate particles, or low temperatures would prevent densification or inhibit nucleation. The effectiveness of the mixing jets also could be qualitatively studied under multiple flowrates.

To examine the heat transfer and flow characteristics of the reactor, a 3D representation was modeled using Fluent<sup>TM</sup>. The solver was the standard  $\kappa - \epsilon$  model that accounted for the turbulent mixing regions. The reactor was modeled as a 3D cylinder as illustrated, Fig. A.1, that was comprised of entrance/exit tubing with convection to the atmosphere, insulated preheating/cooling zones, and the reactor with two concentric pairs of normal mixing jets. The reactor surface was assumed to be at a steady-state temperature of 1000°C, with impinging jet flow also entering at 1000°C. The insulated sections' radial surfaces were assumed to be adiabatic while axial thermal transport was coupled within the solver. Convection to the incoming and outgoing tubing was described using a convection coefficient of 15 W m<sup>-2</sup> K<sup>-1</sup> with  $T_\infty$  at 300 K. Incoming reactant entered at room temperature (300 K) and the exit pressure from the reactor was atmospheric.

## CFD Modeling Assumptions

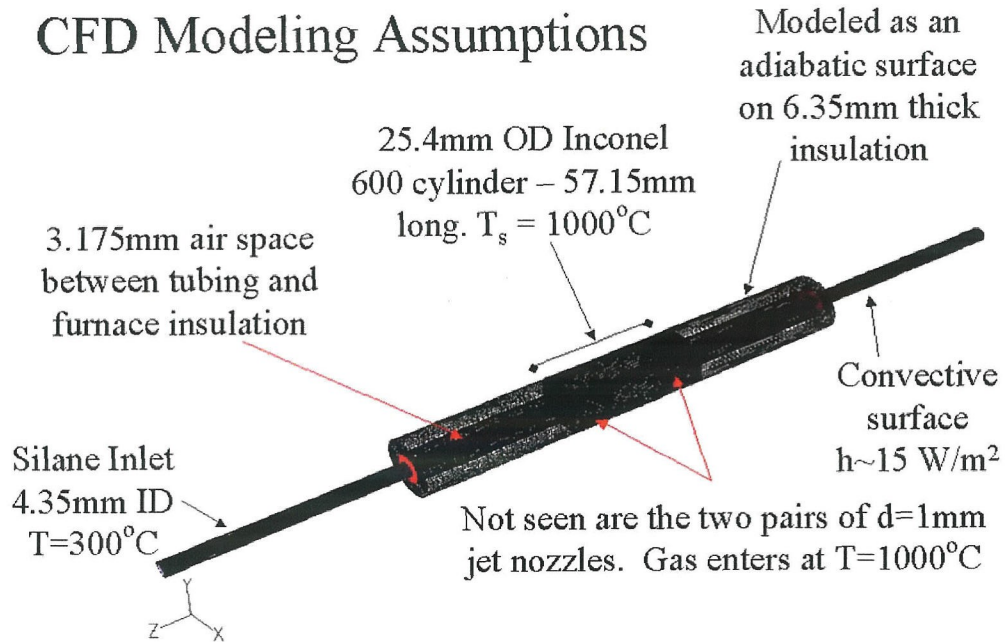
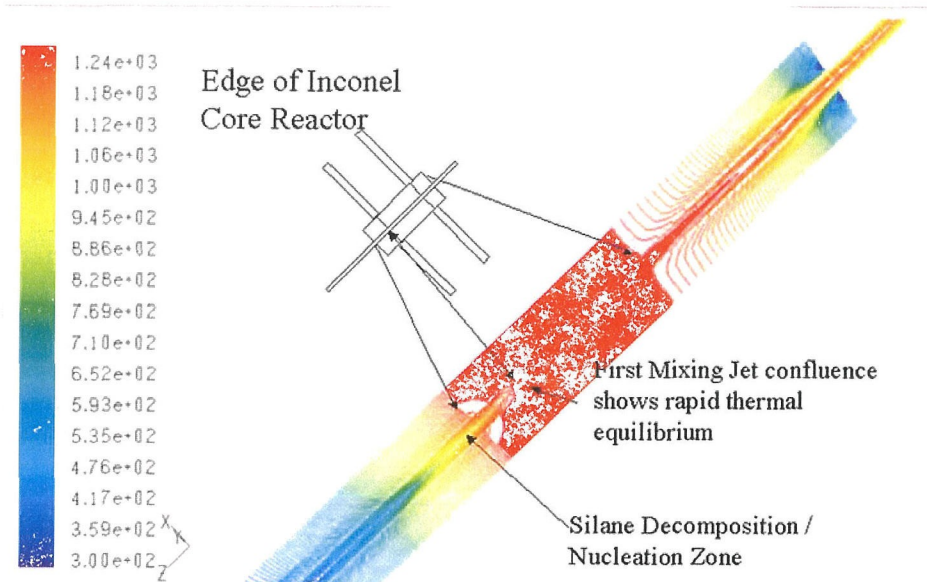


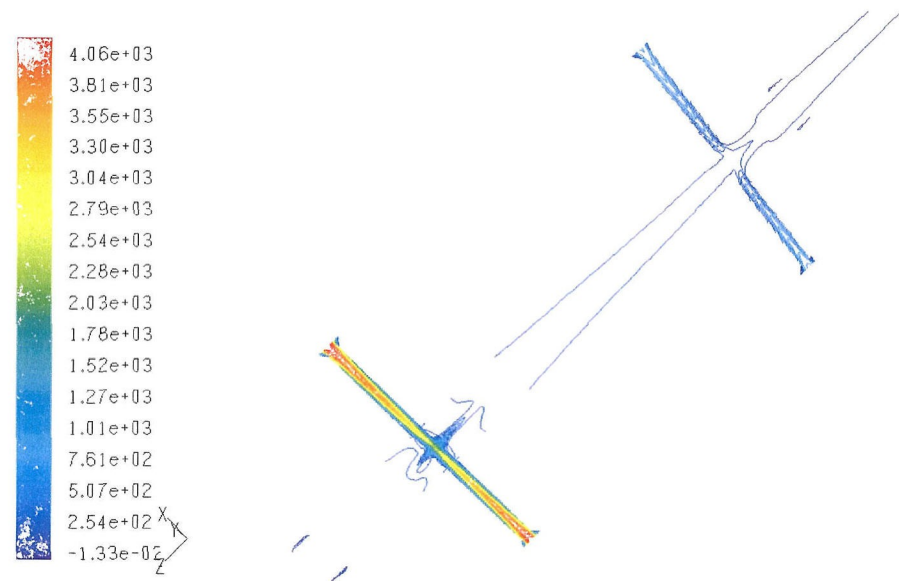
Figure A.1: Meshed grid from Gambit for CFD modeling in Fluent<sup>TM</sup>.

Figures A.2–A.3 shows representative temperature, pressure, and velocity contours for operation with 2400 sccm total flow (180 sccm nucleation flow, 1800 sccm quenching flow, and 400 sccm oxidizing flow) at a 10:1 dilution flowrate. Fig. A.2(a) indicates thermal equilibrium in the mixing jet zone. With the ratio of thermal diffusivity to molecular diffusivity,  $\frac{\alpha}{D}$  is of  $\sim O(1)$ , the modeled decay of thermal fluctuations from mixing is similar to the decay of concentration fluctuations. The pressure contour plot is included, Fig. A.2(b), to show model convergence.

Similar features remain in the temperature profile when modeled flowrates are increased by 5x, provided the ratio of nucleation flow to first mixing jet flow,  $\sim 10x$ , is also maintained (see Fig. A.4). For reactors scaled to larger sizes to produce a higher throughput or those hybridized with an alternate nucleation source, this robustness can further decrease processing time for nanoparticles and allow greater mass throughput. However, these flowrates



(a) Temperature contours with peak temperature filled in as a solid color to indicate the structure of the reactor.



(b) Pressure contours.

Figure A.2: Temperature and pressure contour plots of reactor with flowrates of 180 sccm Nucleation zone, 1800 sccm first jets, 400 sccm second jets.

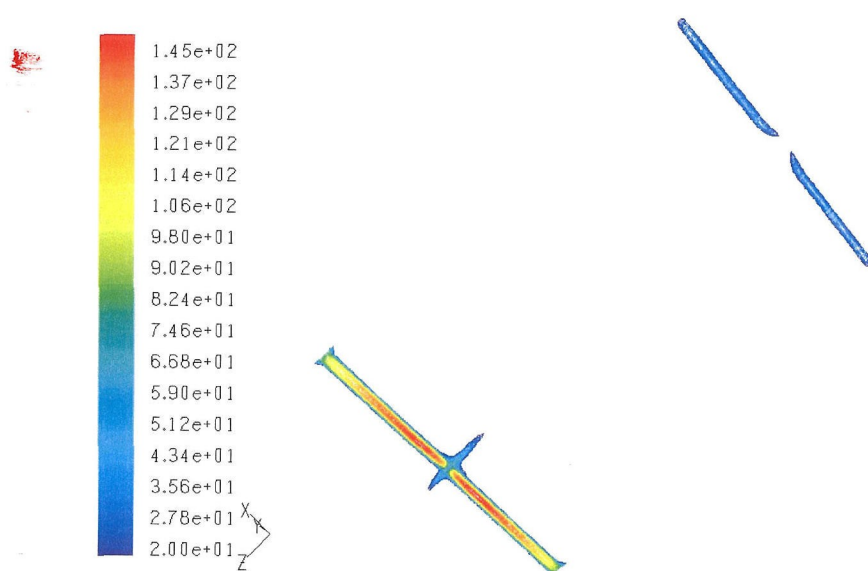
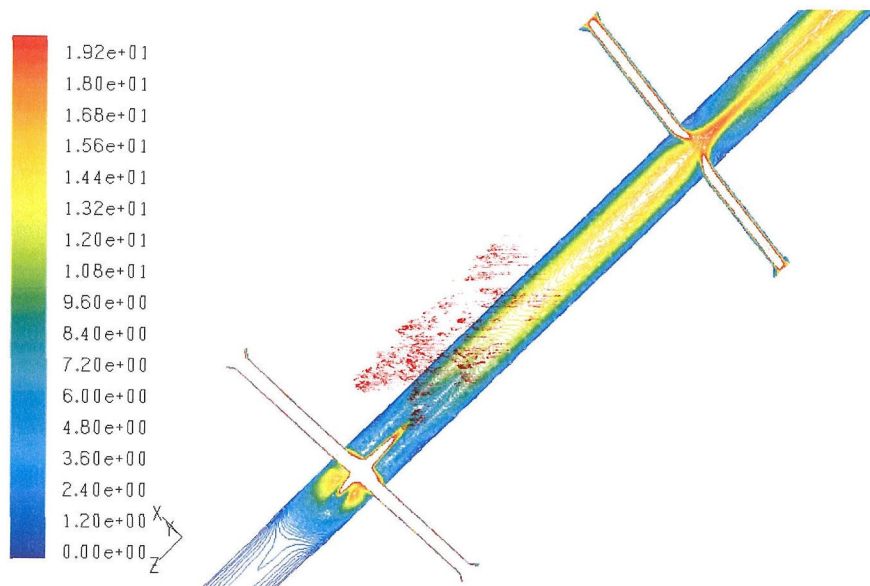


Figure A.3: Velocity contour plots of reactor with flowrates of 180 sccm Nucleation zone, 1800 sccm first jets, 400 sccm second jets.

were not used in experiments with this reactor since it was observed that flowrates even 3x greater than those seen in Figs. A.2–A.3 led to broader size distributions, even with the same flow ratios. The broader size distribution likely rises from increased nucleation at the local level as, with less time for diffusional losses, concentrations remained locally higher during the passage through the reactor.

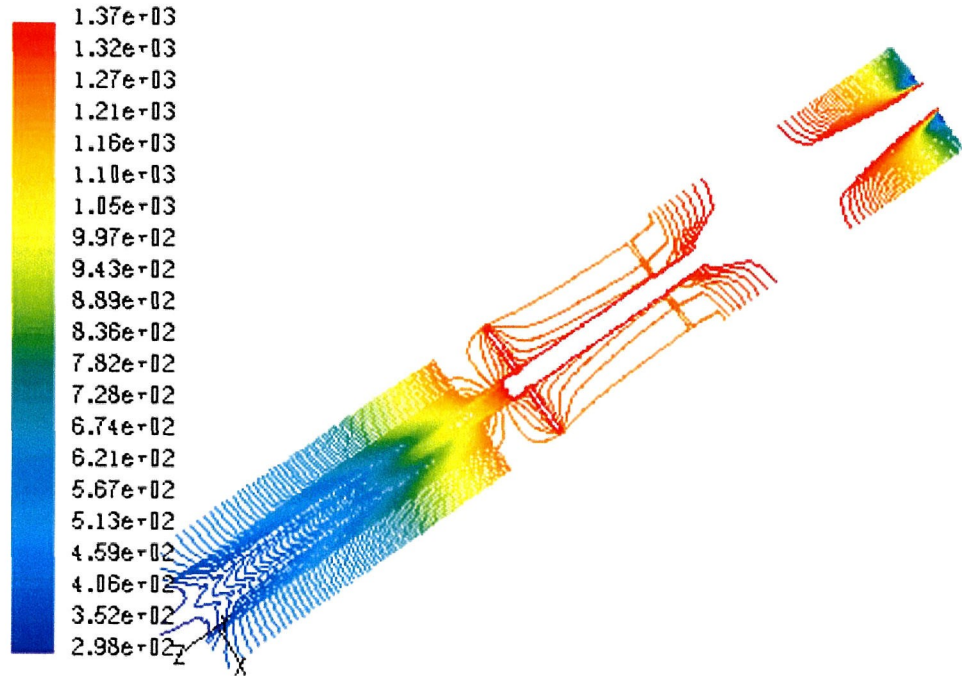
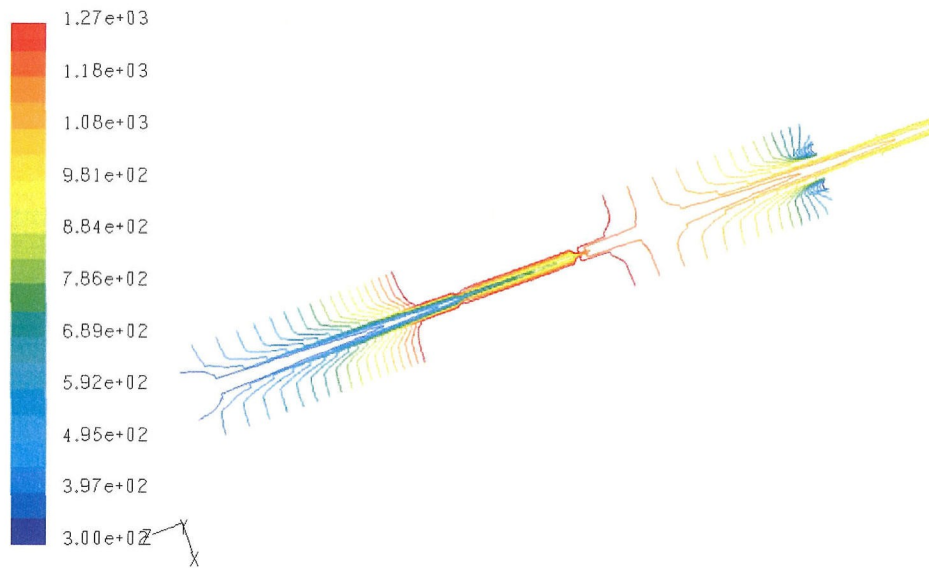
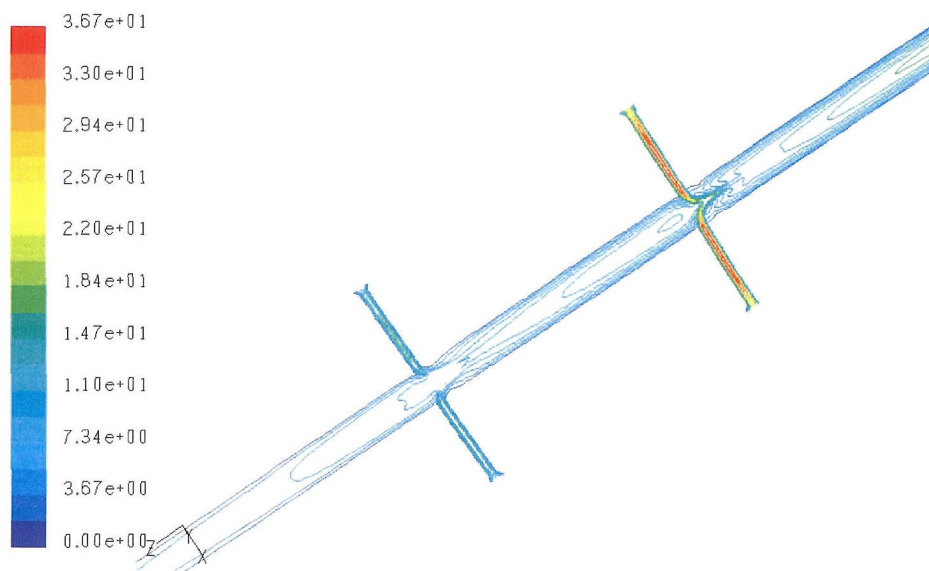


Figure A.4: Temperature contour when increasing nucleation and first mixing jet flow rates by 5x over those shown in Figs. A.2–A.3.

In contrast, Figs. A.5(a)–A.5(b), for a fast nucleation flow, 1800 sccm, and slow mixing flow, 180 sccm, modeling results predict a lack of suitable temperature for silane decomposition.



(a) Temperature contour 1800 sccm nucleation flow, 180 sccm mixing jet.



(b) Pressure contour 1800 sccm nucleation flow, 180 sccm mixing jet.

Figure A.5: Contour plots of reactor with 1800 sccm nucleation and 180 sccm first mixing jet flowrates.

### A.3 Particle Charging From Neutralizer

Central to RDMA analysis is charging the particles in a known way. This is normally achieved by passing the aerosol through a so-called neutralizer in which the particles are exposed to an electrically neutral ambipolar ion cloud produced by an ionizing radiation source, e.g., a sealed capsule of  $^{85}\text{Kr}$ .<sup>40,142</sup> Initial experiments revealed that the high particle concentrations in the stream exiting the present reactor led to unacceptable coagulation within the large,  $\sim \text{O}(10^2)$  ml, volume of the neutralizer. The characterized particle distribution was now broadened and size shifted to larger diameter particles. To prevent post reactor agglomeration during passage of the aerosol through the neutralizer, a portion of the aerosol was mixed with particle-free  $\text{N}_2$  that had been processed through the neutralizer. The ion-cloud found within an aerosol neutralizer will decay over some finite period after the carrier gas leaves the neutralizer. In principle, if an aerosol can be mixed into the decaying ion cloud much faster than it decays, the aerosol may asymptotically approach the steady-state charge distribution gained within a neutralizer.

Experiments were performed at a range of ratios of the ion-rich  $\text{N}_2$  diluent to aerosol to ensure that this new charging system resulted in the asymptotic charge distribution as predicted by the Boltzmann charging model. Figure A.6 shows the dilution-correction particle concentrations measured using the RDMA (Radial Differential Mobility Analyzer) as the dilution rate is increased. The steady-state charge distribution was assumed in this evaluation, so the concentration estimates can be considered quantitative only at dilution ratios great than 3:1 ( $\text{N}_2$  from neutralizer to aerosol from reactor) where the concentration approaches an asymptotic value. The observation that the inferred concentration does not change with increased dilution beyond this value strongly suggests that the desired

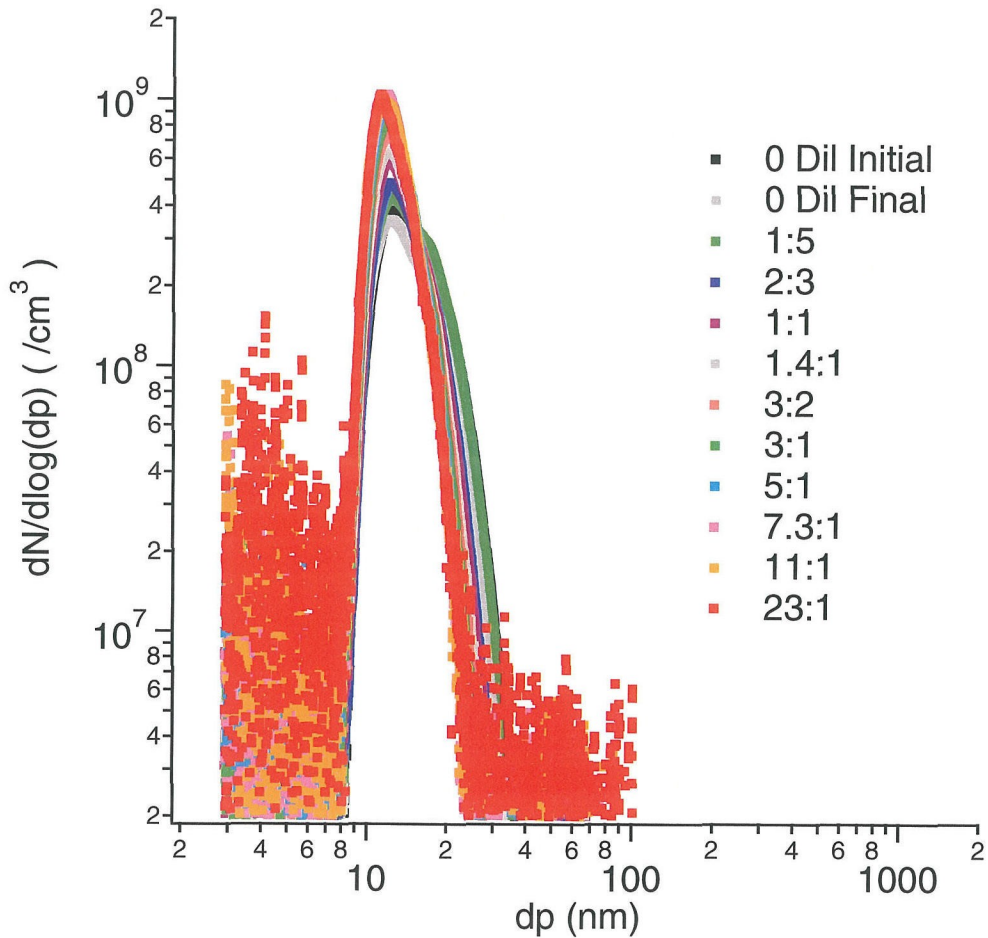


Figure A.6: Asymptotic particle distribution measured, assuming steady state charge distribution on particles, with various ratios of ion rich gas well mixed with particles.

steady-state charge distribution has been achieved. All observations from the turbulently mixed reactors, unless noted otherwise, are reported as having been made with a neutralizer dilution ratio of 7:1.

#### A.4 Coagulation & Densification

Flagan and Lunden<sup>38</sup> describe initial coalescence where a mechanism of surface diffusion initiates fusing of silicon nanoparticles. The characteristic time for neck growth, ( $\tau_s$ ), using the classical sintering model is,

$$\tau_s = \frac{a_m}{B(T)} = \frac{a_m}{AT^\gamma} e^{\frac{E}{RT}}. \quad (\text{A.17})$$

Further densification can be characterized by grain-boundary diffusion using a surface area based linear rate law.<sup>73</sup> This time constant,  $\tau_f$ , is,

$$\frac{da_p}{dt} = -\frac{1}{\tau_f} (a_p - a_{sph}) \quad (\text{A.18})$$

where  $a_p$  is the surface area of an initially necked biparticle and  $a_{sph}$  the surface area of the final coalesced single particle. Estimating  $\tau_f$  from an isothermal process overestimates the time of actual exothermic coalescence,<sup>96,147</sup>

$$\tau_f = \frac{3k_B T_p N}{64\pi\sigma_s D_{eff}} \quad (\text{A.19})$$

where  $k_B$  is the Boltzmann constant,  $T_p$  is the temperature of the system,  $N$  is the number of silicon atoms comprising the coalescing sphere,  $\sigma_s$  is the bulk silicon solid-state surface tension, and  $D_{GB}$  is the solid-state grain boundary diffusion coefficient,

$$D_{eff} = D_{GB} \left( \frac{\delta}{d_p} \right) \quad (\text{A.20})$$

with  $\delta$  is the grain-boundary width,  $d_p$  is the small particle diameter, and the diffusion coefficient has an Arrhenius behavior,

$$D_{GB} = A e^{-\frac{B}{T_p}}. \quad (\text{A.21})$$

The time required for two 8 nm particles to coalesce into one 10 nm particle is of  $\sim O(\mu s)$ .

In order to ensure that the coalesced particle forms a single crystal, an  $\sim O(ms)$  residence time is provided to allow annealing within the reactor.

## A.5 Particle Distributions

This material was originally included with Chapter 6, but was superfluous or redundant to the theme discussed. It is included here as additional information on reactor behavior during conditions of changing flowrates or feed concentration.

### A.5.0.1 RD2: Reverse Flow Shell & Tube Assembly

Figure A.7 are PSDs observed while increasing the precursor concentration for similarly slow reactant flow and large quench flow. Coagulation aerosols are evident, Fig. A.7(a), but the number of particles characterized at the peak, even with the quench dilution, shows nearly a 10x improvement over the single tube laminar flow reactor.

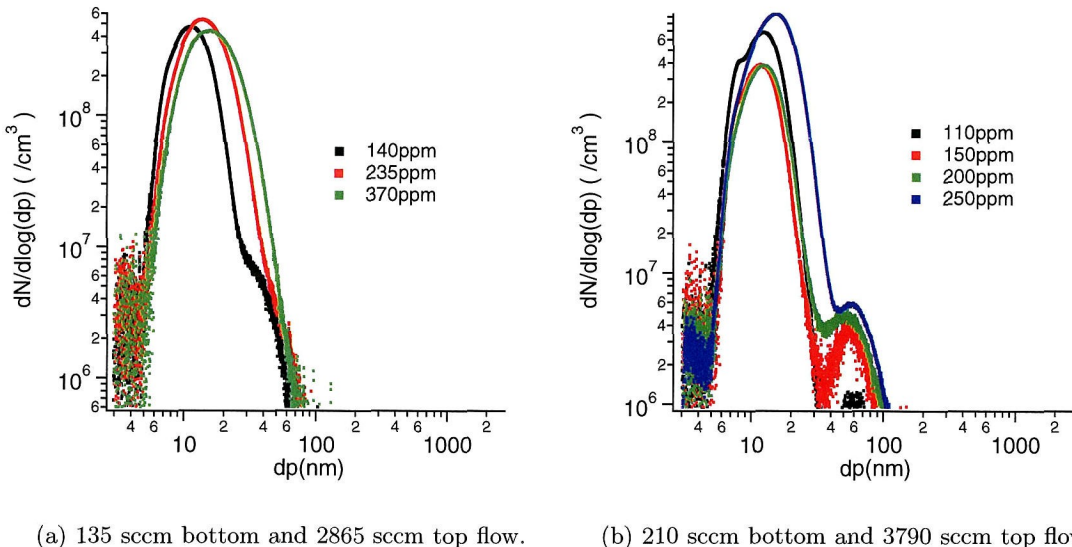


Figure A.7: Particle distributions observed for variations in silane concentration at 1273 K for large comparative difference in bottom to top flow.

#### A.5.0.2 RD3: Shell and Tube Nucleation/Growth with Subsequent Mixing Jet

In Fig. A.8 PSDs are seen for various nucleation flowrates and concentrations with a  $\text{N}_2$  dilution of 1800 sccm and a mixing jet dilution of 400 sccm. In Figs. A.8(a)–A.8(b), the nucleation flowrate is varied between 100 sccm and 400 sccm while the silane concentration is fixed at 100 ppm. The experiments were conducted on different days, wherein changing conditions in the recirculation zones affected the measured particle numbers. But, the trends seen in the PSDs are consistent. A narrow, small particle mode is evident throughout and is increasingly dominant as flowrate is increased. As the nucleation flowrate increases, the heat transfer rate decreases, the nucleation rate is reduced as is the agglomeration rate.

For fixed nucleation flowrates of 200 sccm, Fig. A.8(c), and 250 sccm, Fig. A.8(d), variation of the silane concentration demonstrates a similar effect on the highly monodisperse mode. With the increased nucleation rates at higher feed concentrations, agglomeration dominates and the monodisperse mode is no longer observed.

A final pair of experiments, Fig. A.9, compare the results from early operation of the reactor at low feed concentration to operation after the recirculation problem had self-rectified, presumably by agglomerate particle deposition. In Fig. A.9(a), a combination of lower silane concentration, 45 ppm, at a high nucleation flowrate, 600 sccm, shows a small primary particle size of  $\sim 12 \text{ nm}$ , but the slow laminar mixing time contributes to growth in particle sizes up to 40 nm—either from agglomeration or the lack of complete densification. In Fig. A.9(b), with a slower nucleation flow of 175 sccm and additional silane precursor, the particle distribution is narrower, indicating increased densification, and the distribution appears to have arisen from a nearly monodisperse collection of 8–12 nm particles. The peak height of these left-most shoulders is fairly consistent over many experiments, and appear to correlate to a local event of particle growth by vapor deposition

at a short timescale, and then agglomeration over a larger timescale as determined before dilution inhibits coagulation.

#### **A.5.0.3 RD4: Laminar Flow Nucleation With Subsequent Mixing Jet**

A second configuration, Fig. A.10, was made with an additional pair of mixing jets in between the quench and thermal oxide jets. This additional inlet provided some flexibility in introducing additional quenching flow or additional reagent.

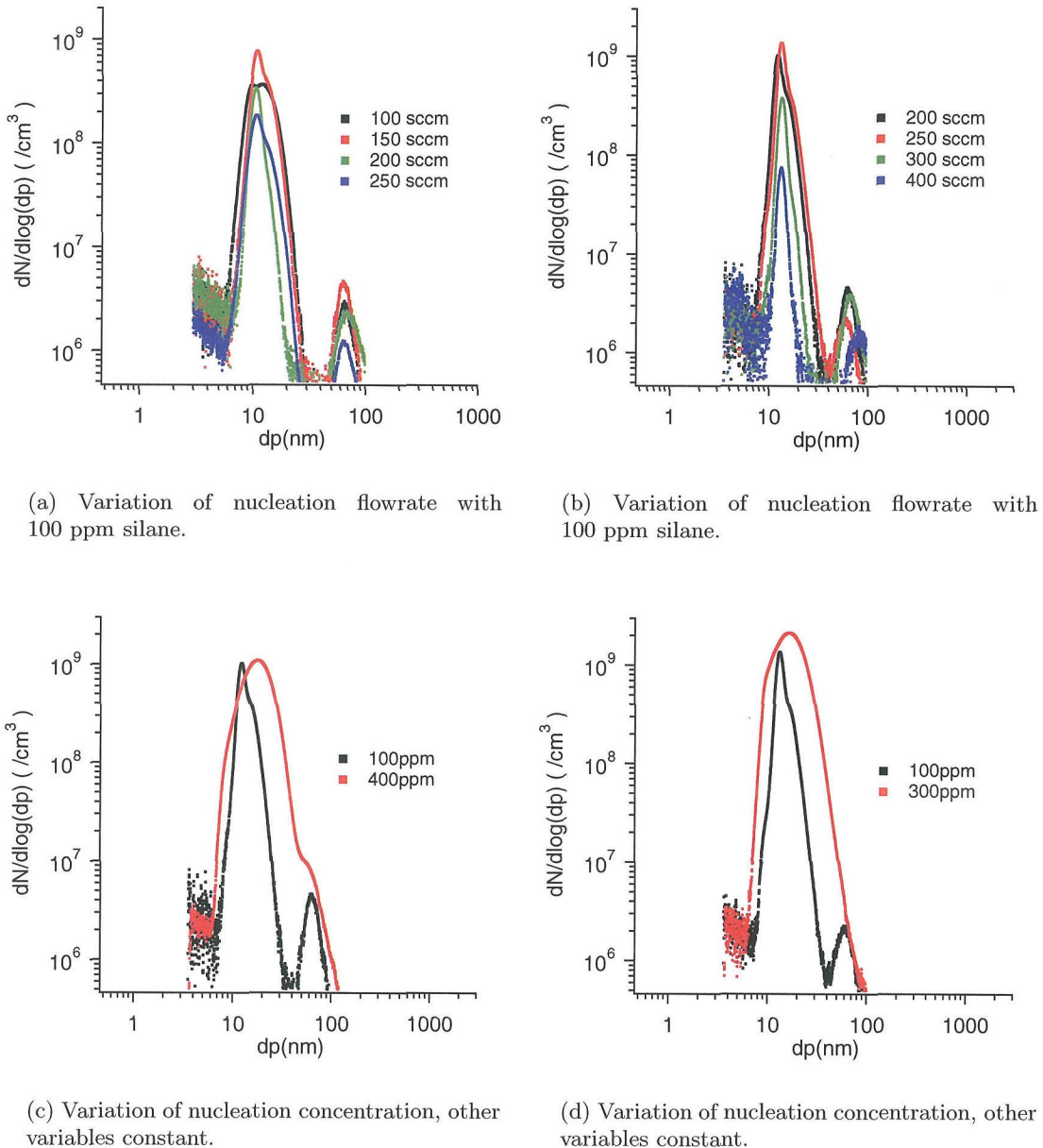


Figure A.8: Particle distributions observed for nucleation in RD3, an inconel shell and tube with turbulent mixer reactor.

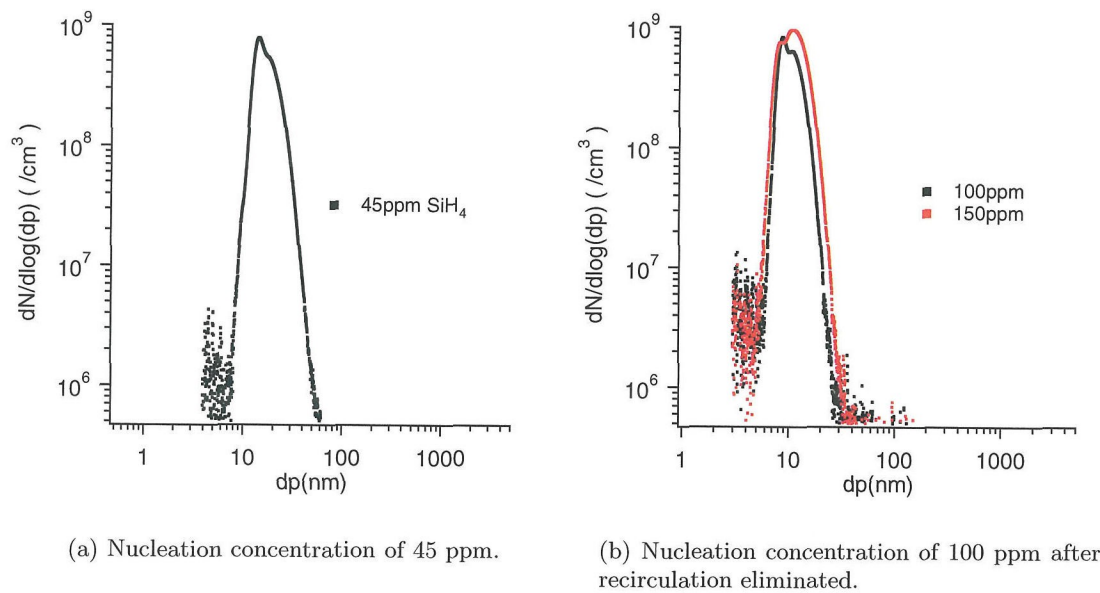


Figure A.9: Particle size distributions from RD3 at relatively lower concentration of  $\text{SiH}_4$ .

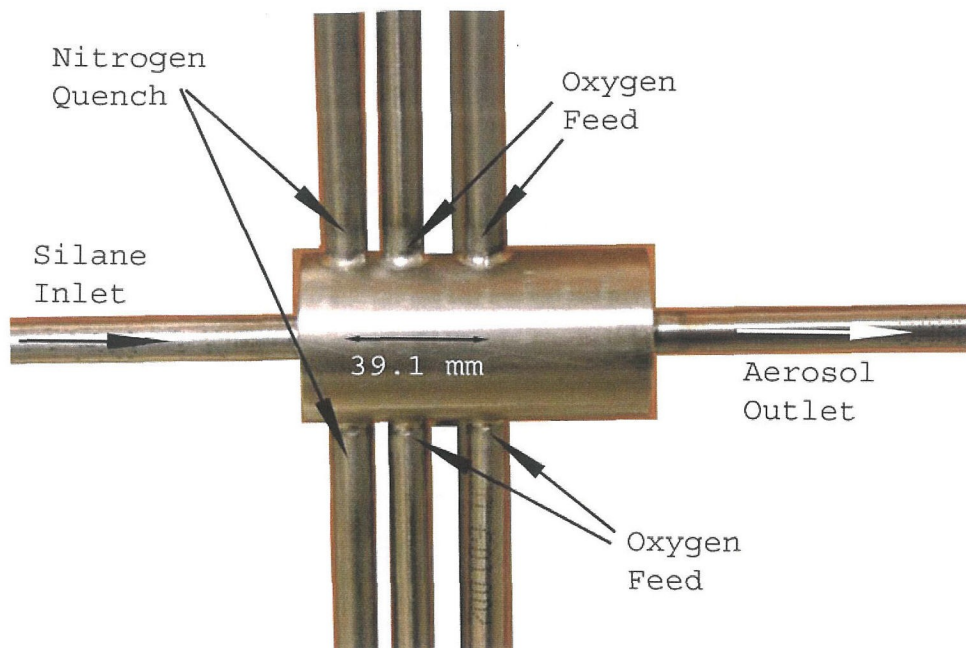


Figure A.10: Image of mixing reactor, RD4, described in ??.

## Appendix B

# CAD Drawings And Software Code

### B.1 300 mm Thermophoretic Deposition Chamber Drawings

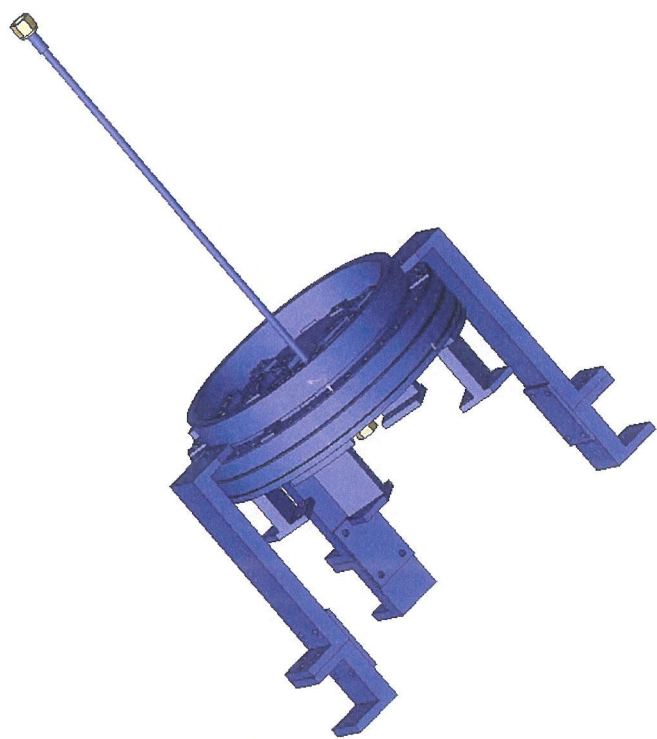


Figure B.1: Full Assembly.

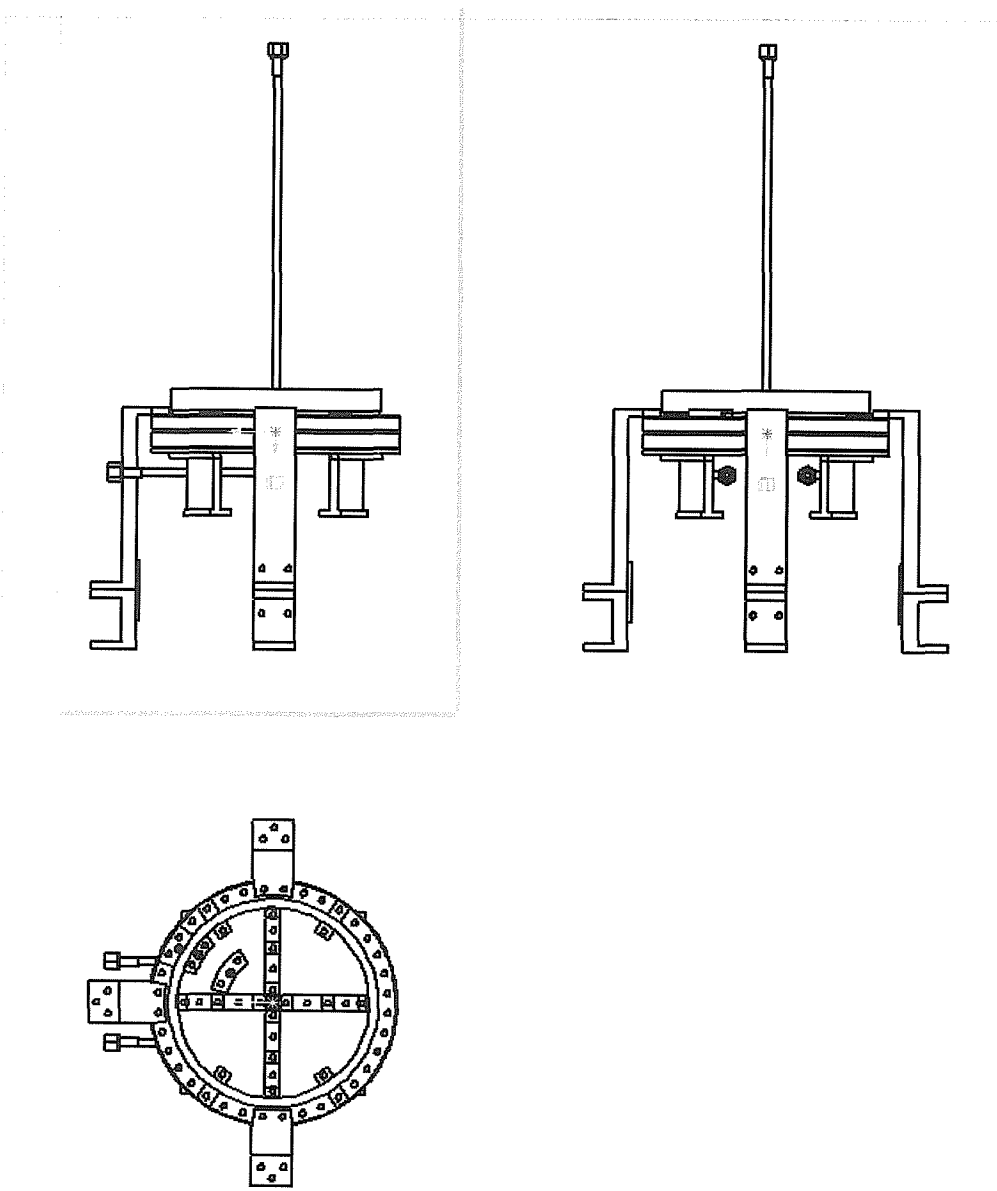


Figure B.2: Full Assembly.

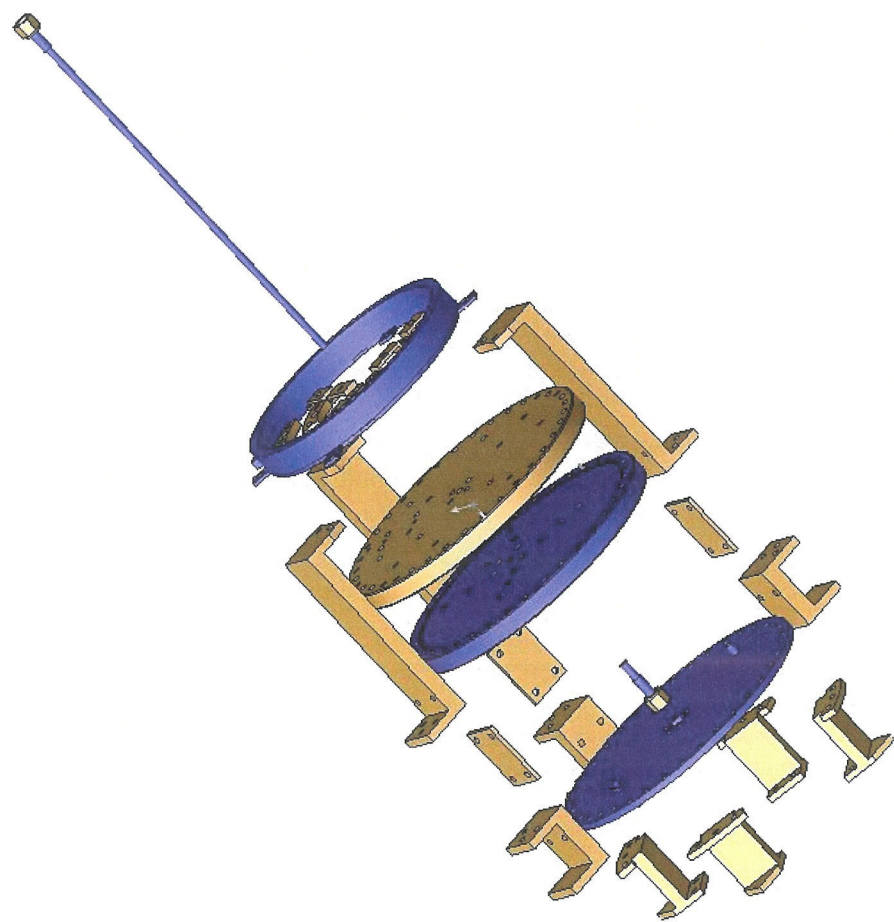


Figure B.3: Full assembly exploded.

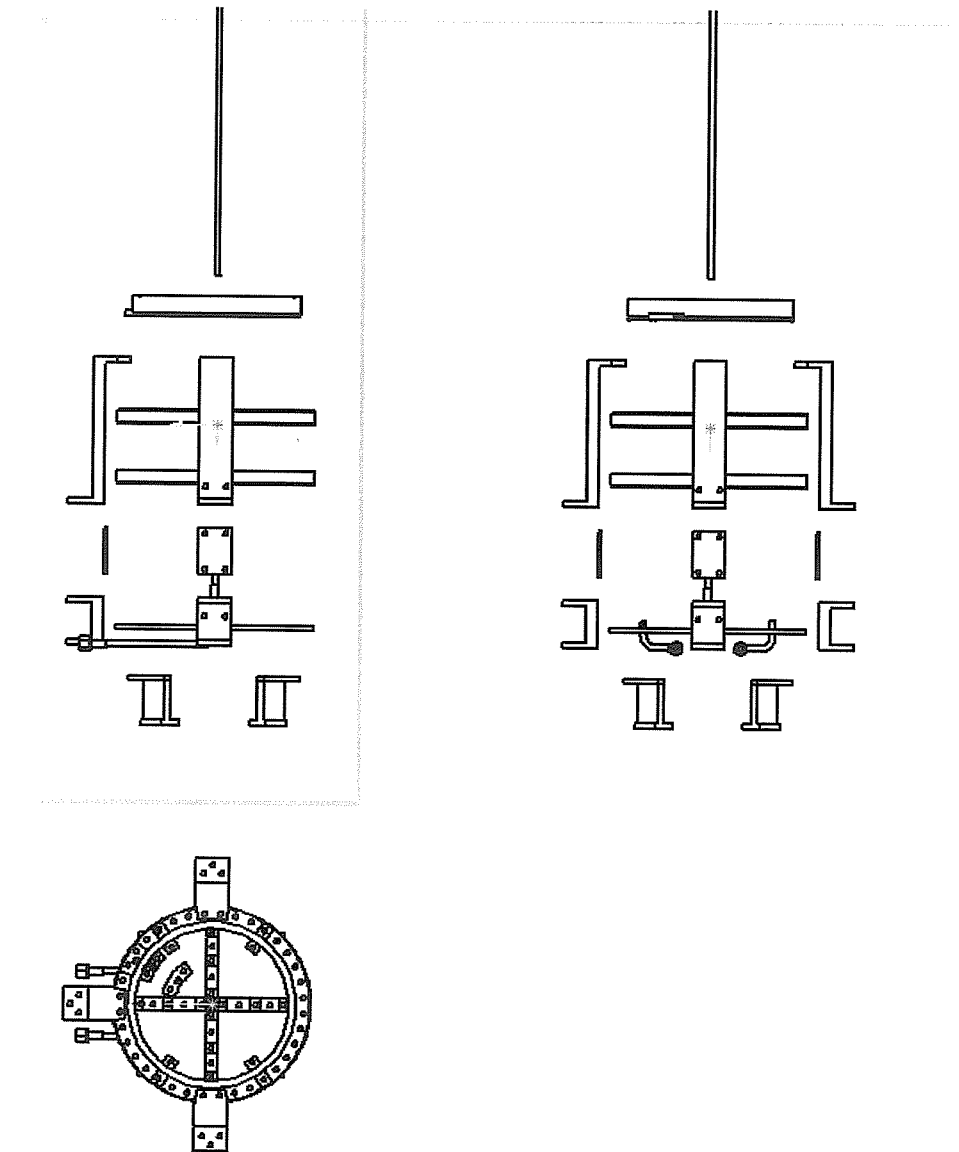


Figure B.4: Full assembly exploded.

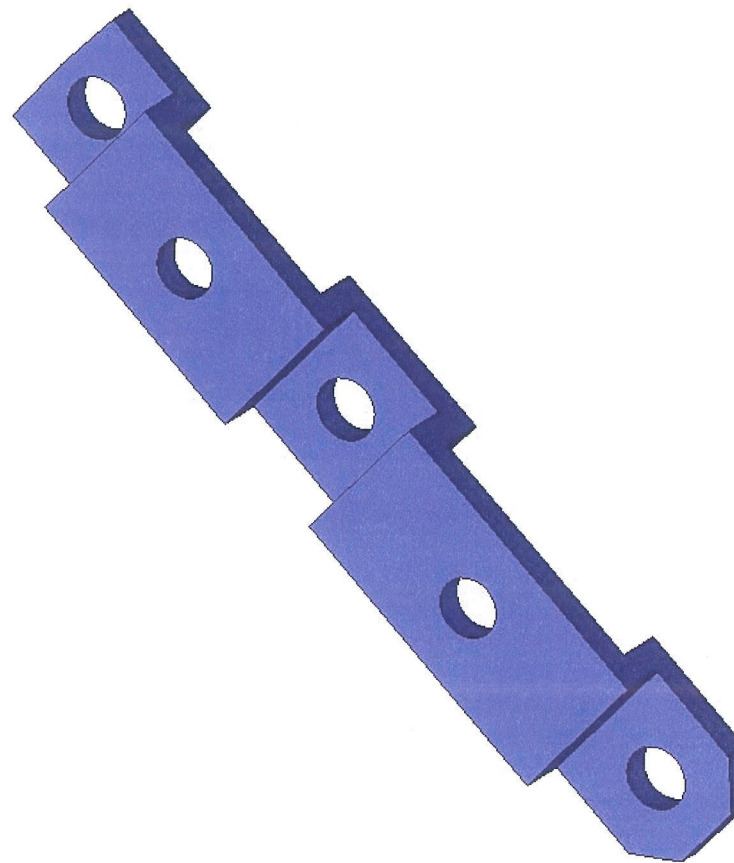


Figure B.5: Ring Heater Clamp.

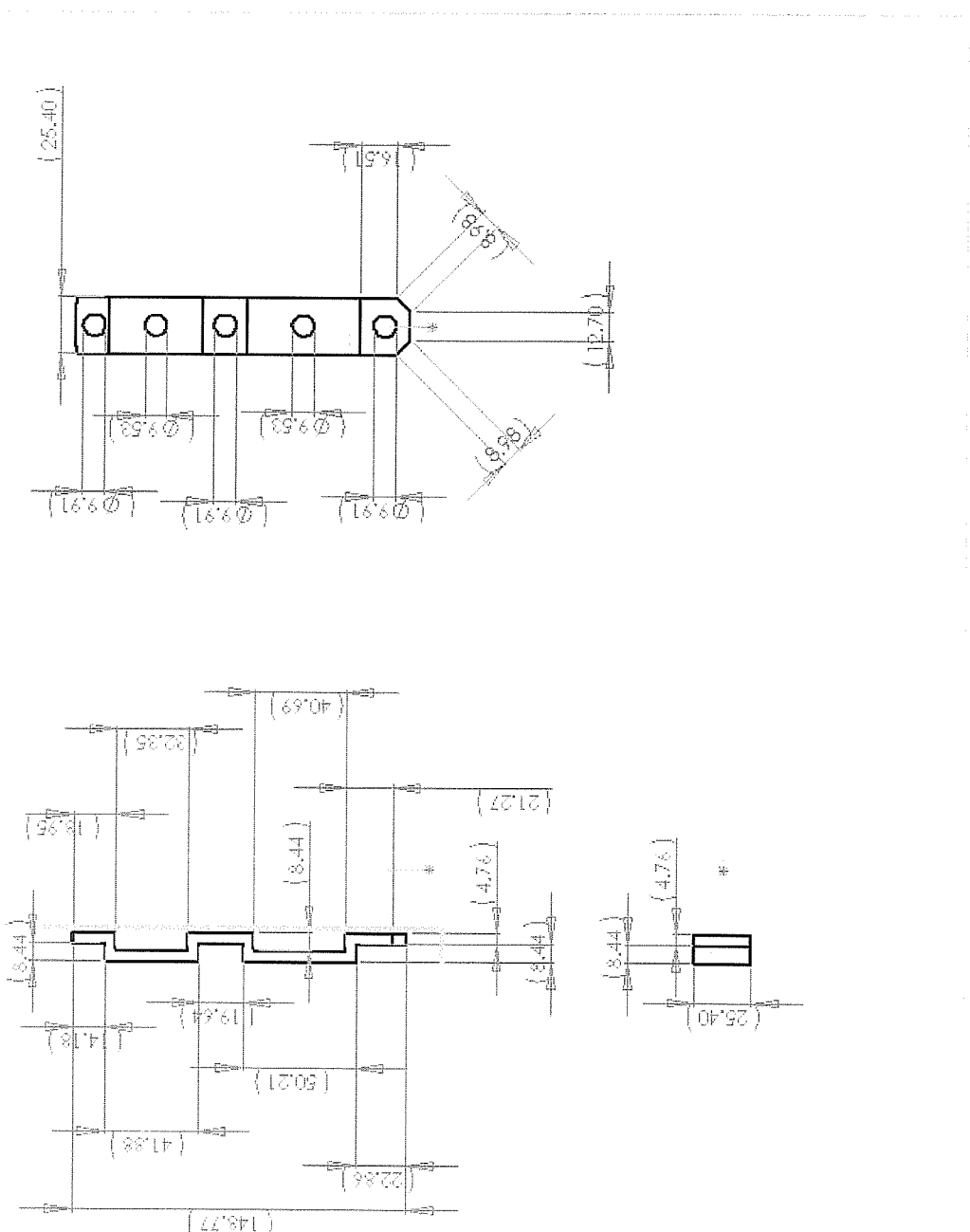


Figure B.6: Ring Heater Clamp.

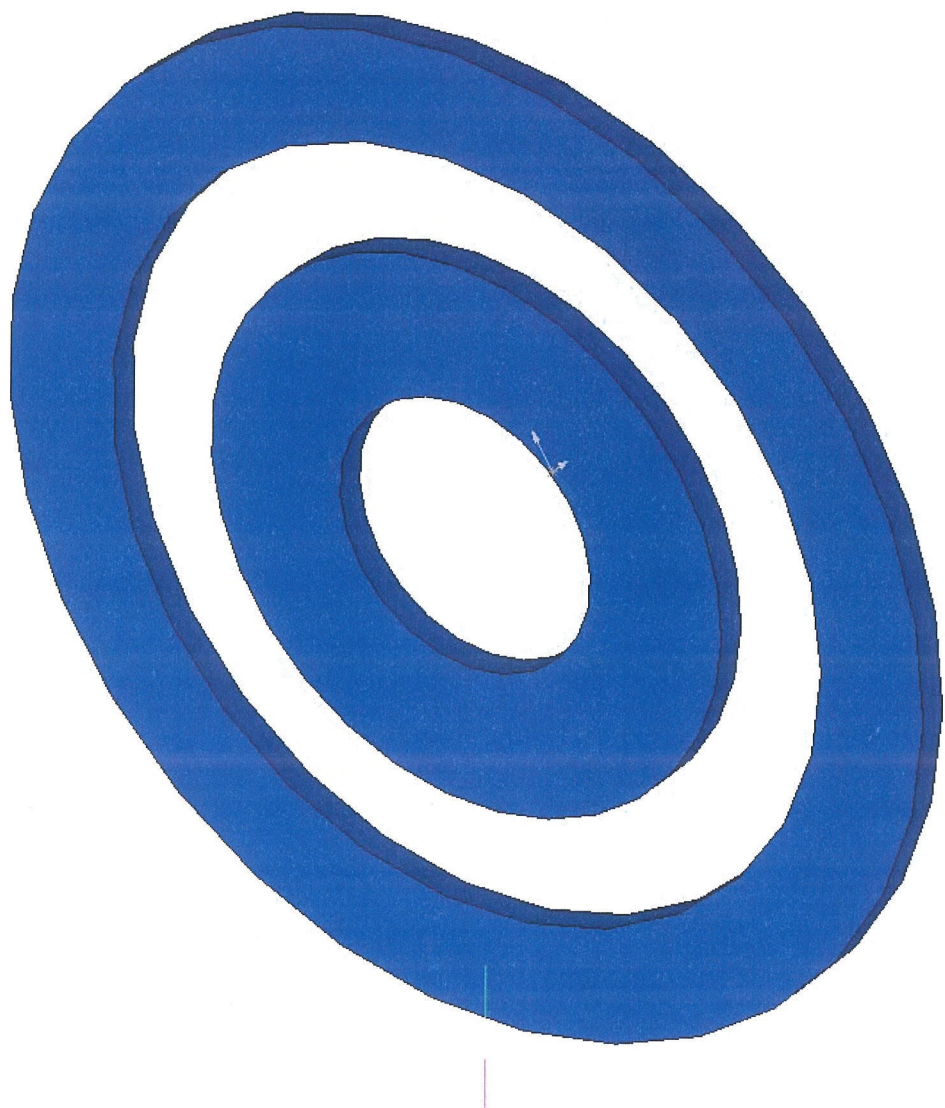


Figure B.7: Ring Heaters.

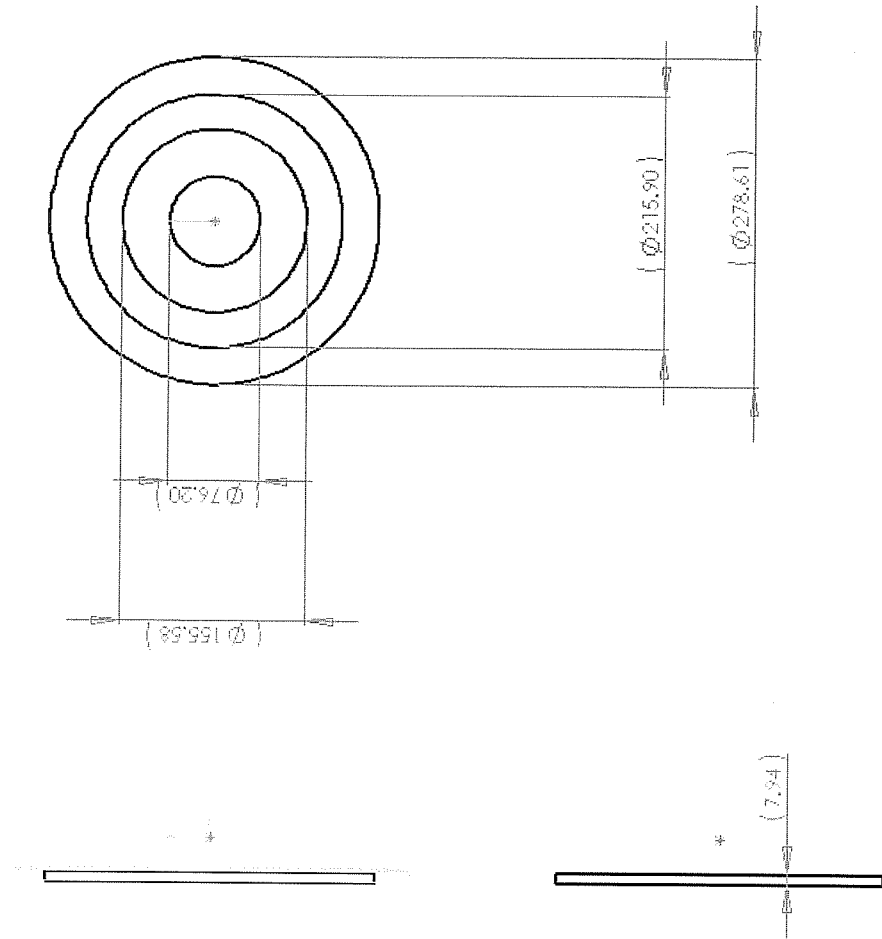


Figure B.8: Ring Heaters.

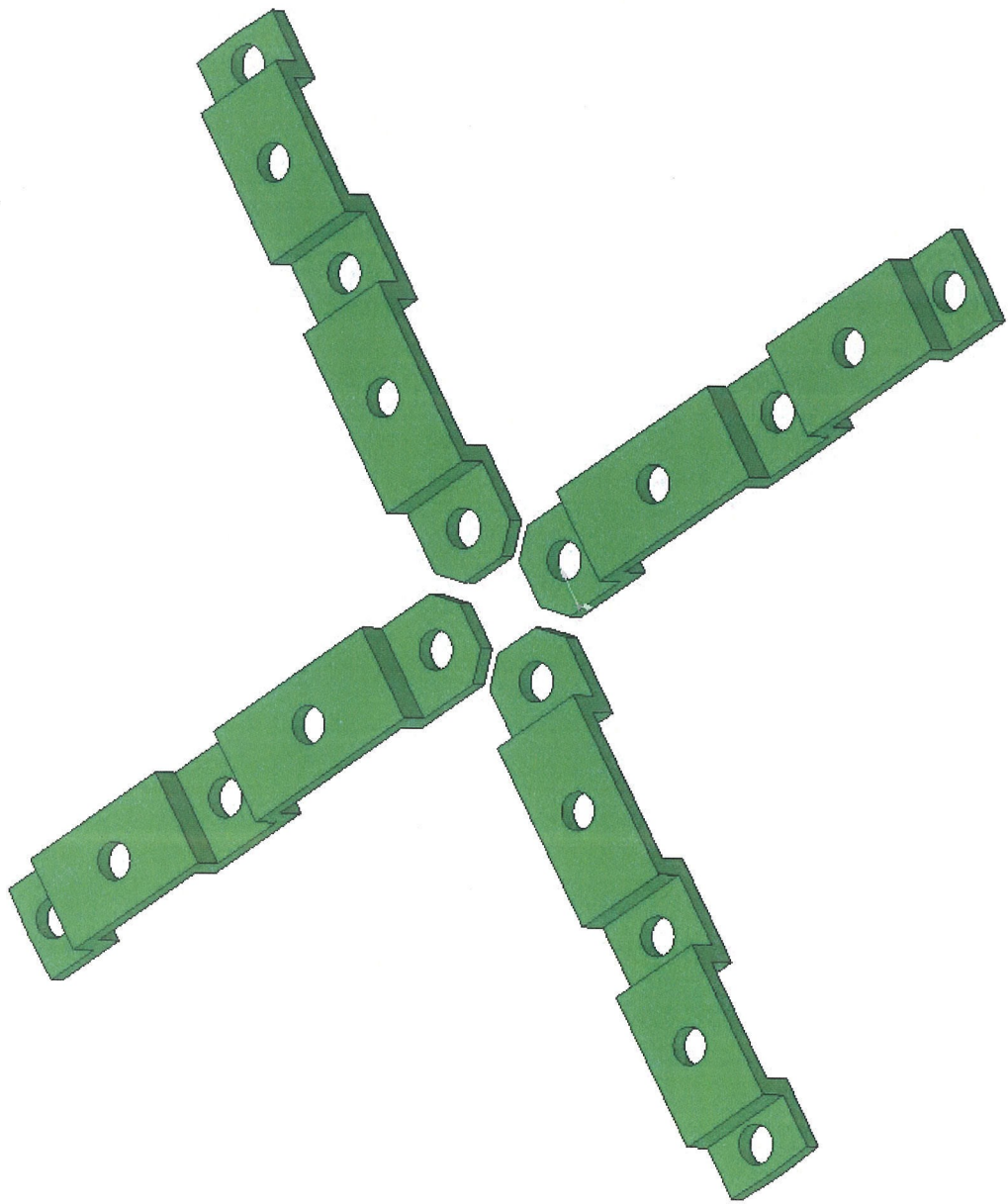


Figure B.9: Ring Heater Clamps.

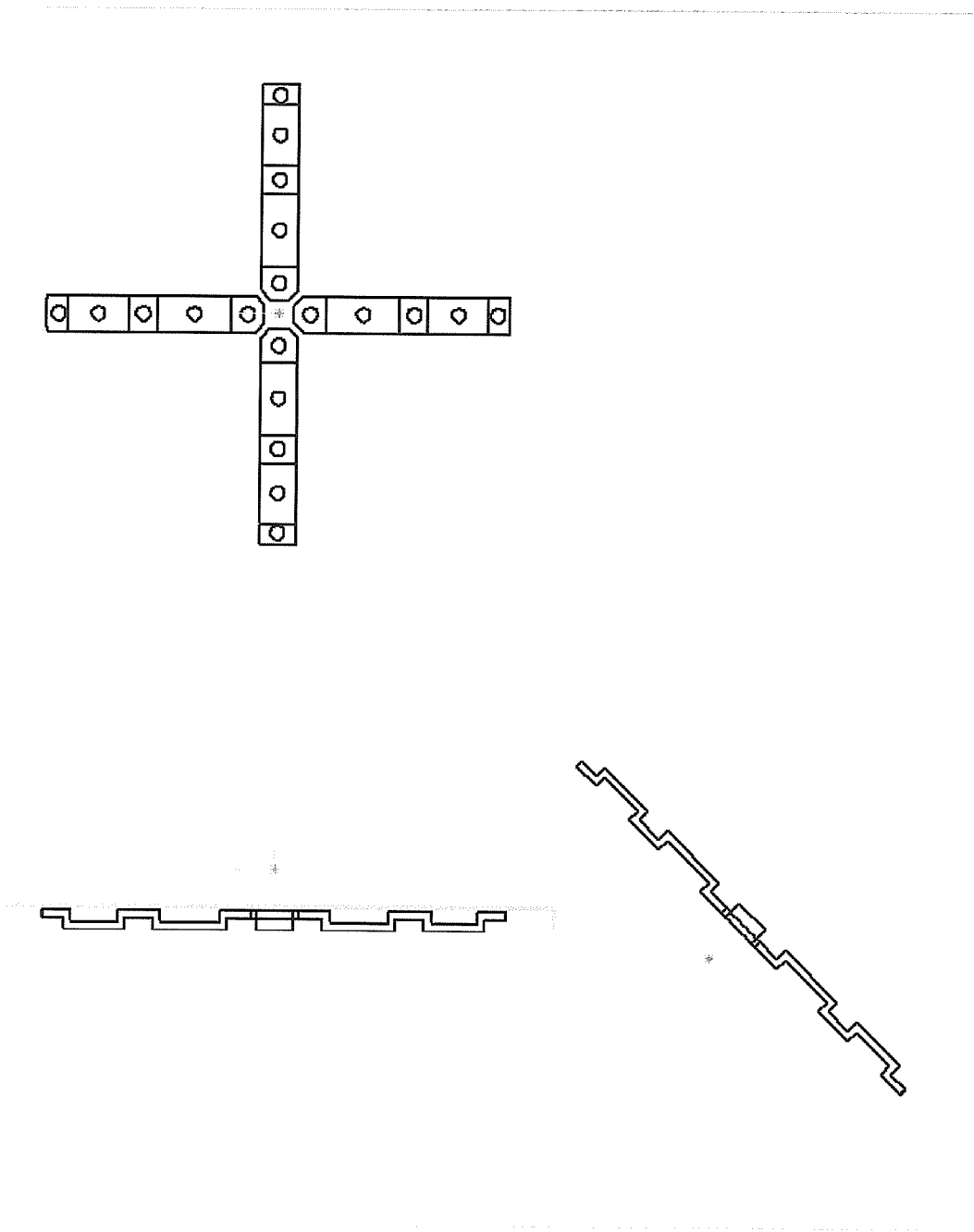


Figure B.10: Ring Heater Clamps.

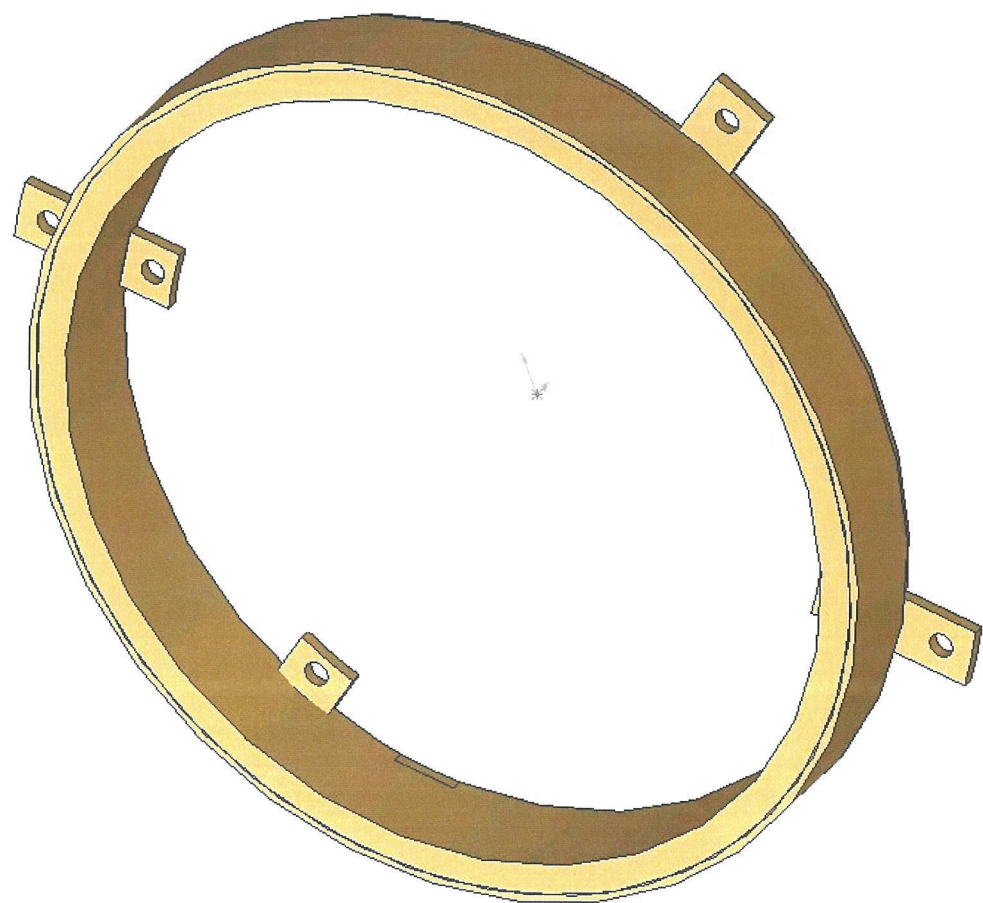


Figure B.11: Band Heater Mount.

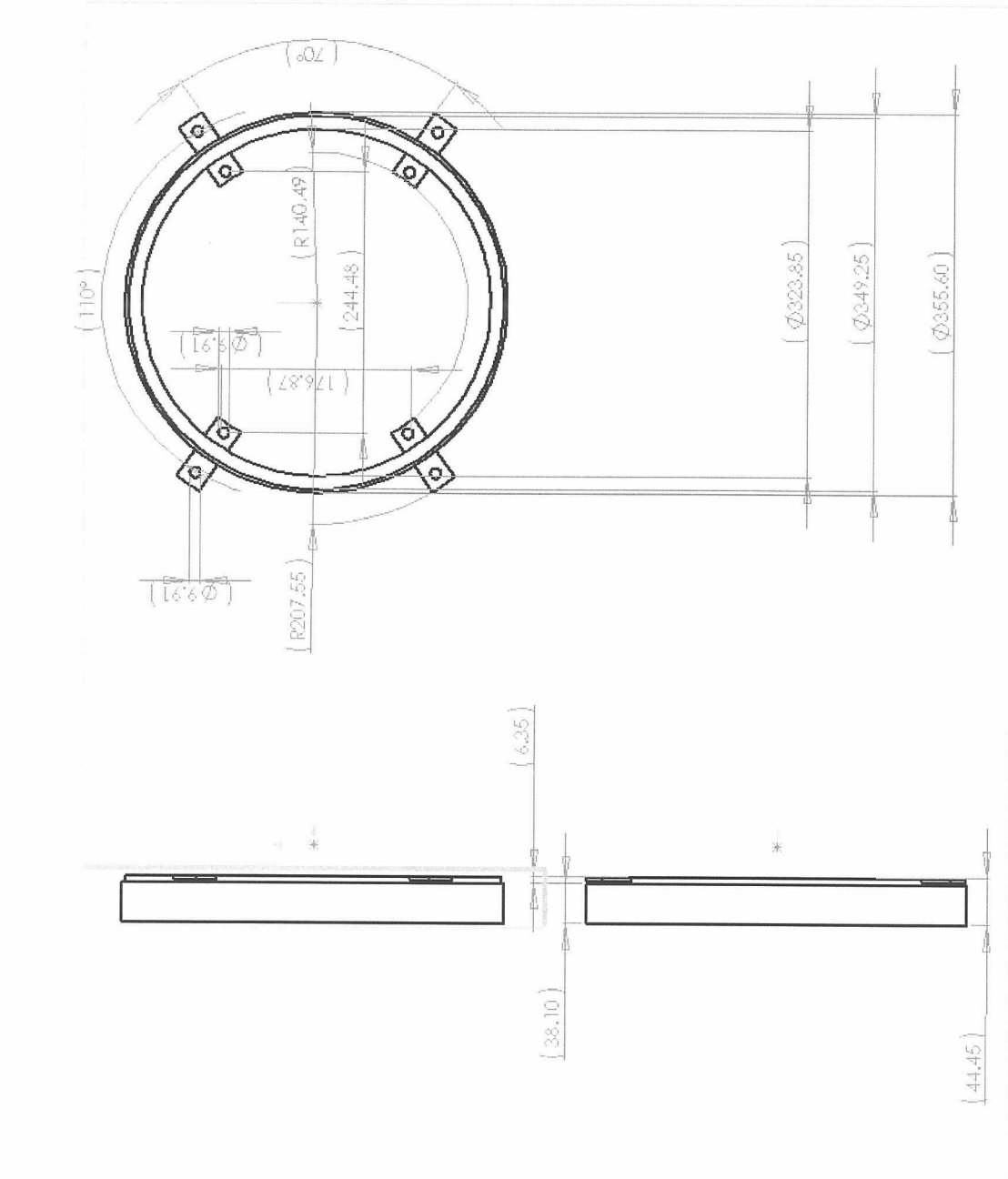


Figure B.12: Band Heater Mount.

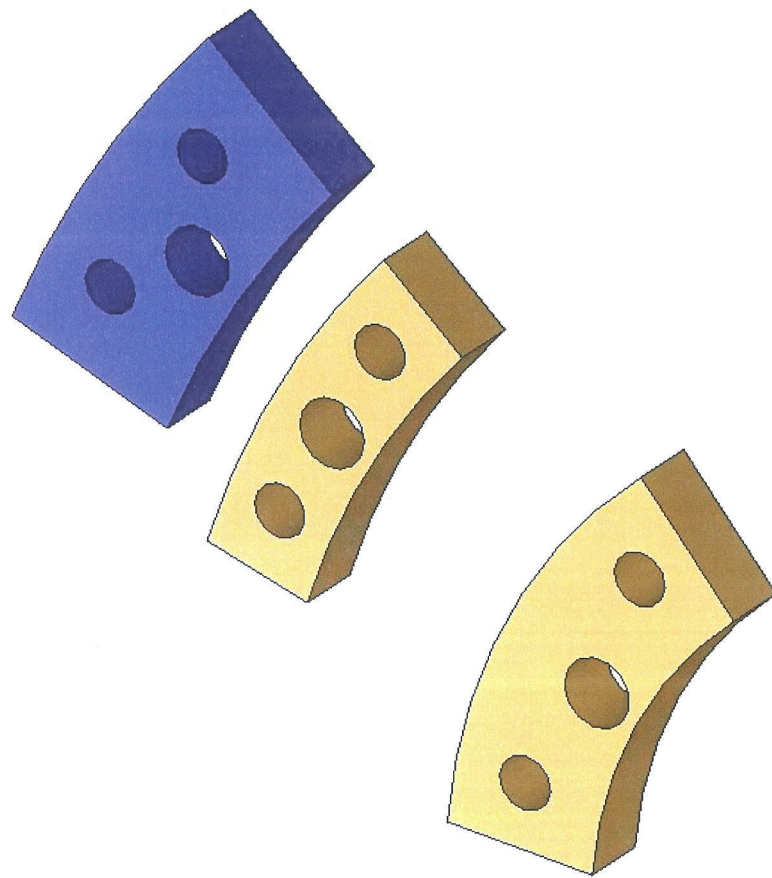


Figure B.13: Mounts for PID controller thermal sensors.

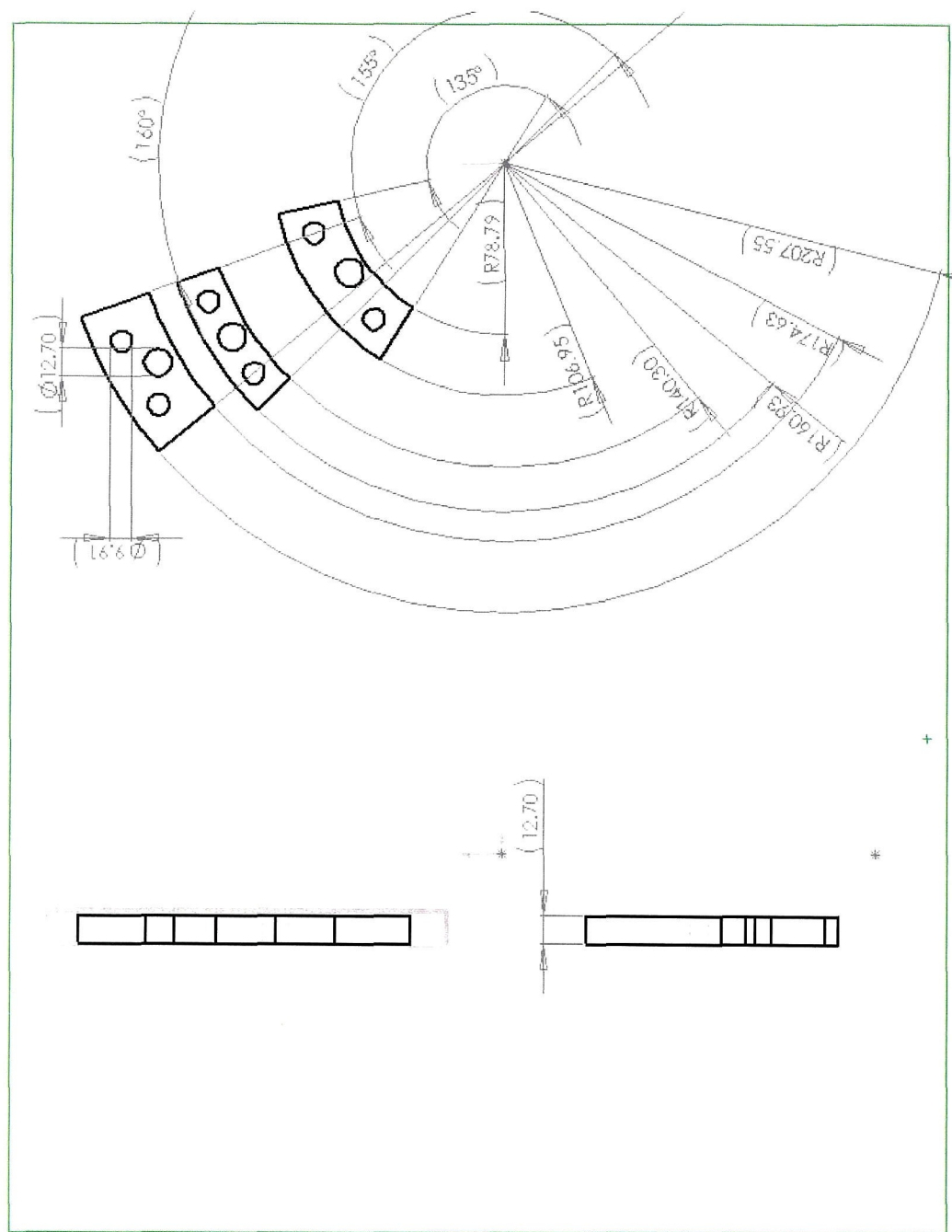


Figure B.14: Mounts for PID controller thermal sensors.

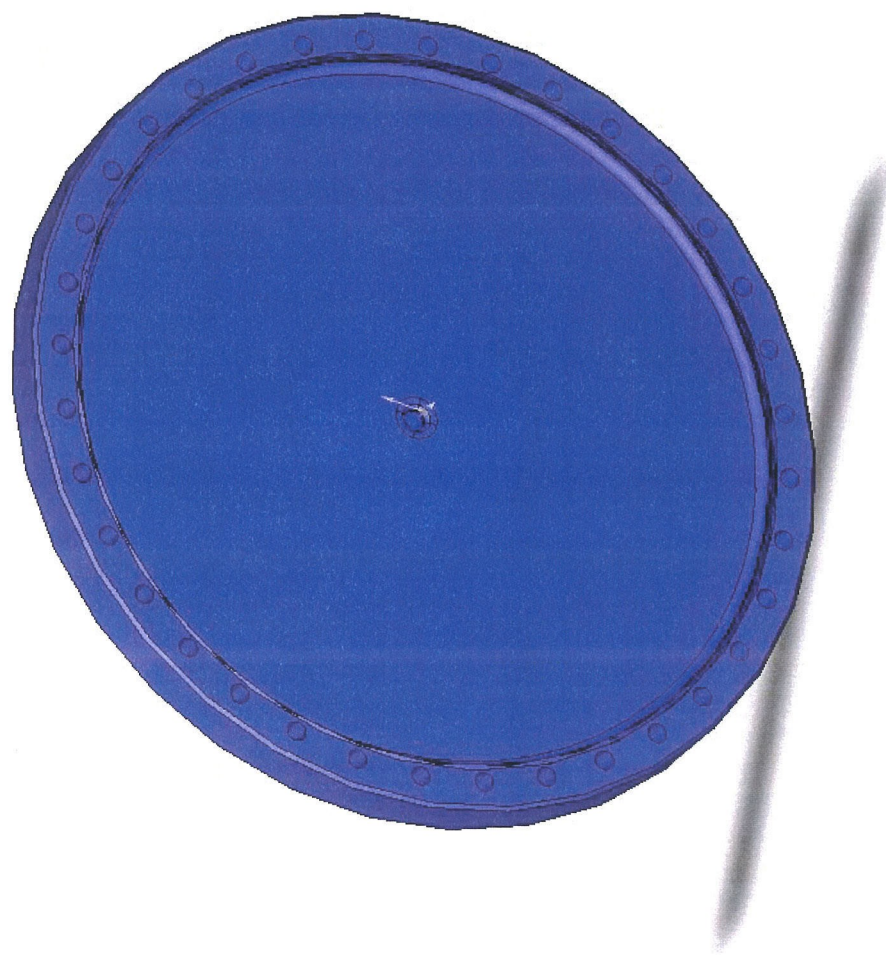


Figure B.15: Top Flange MDC.

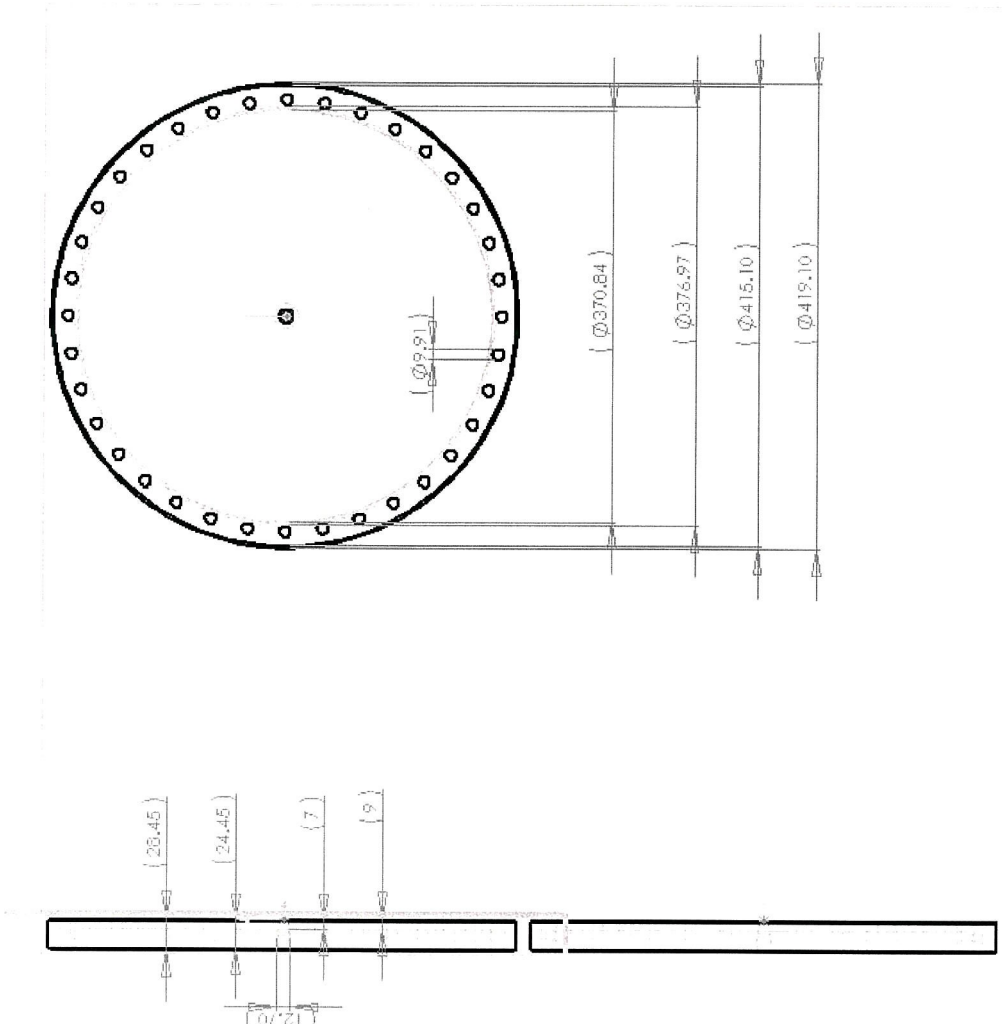


Figure B.16: Top Flange MDC.

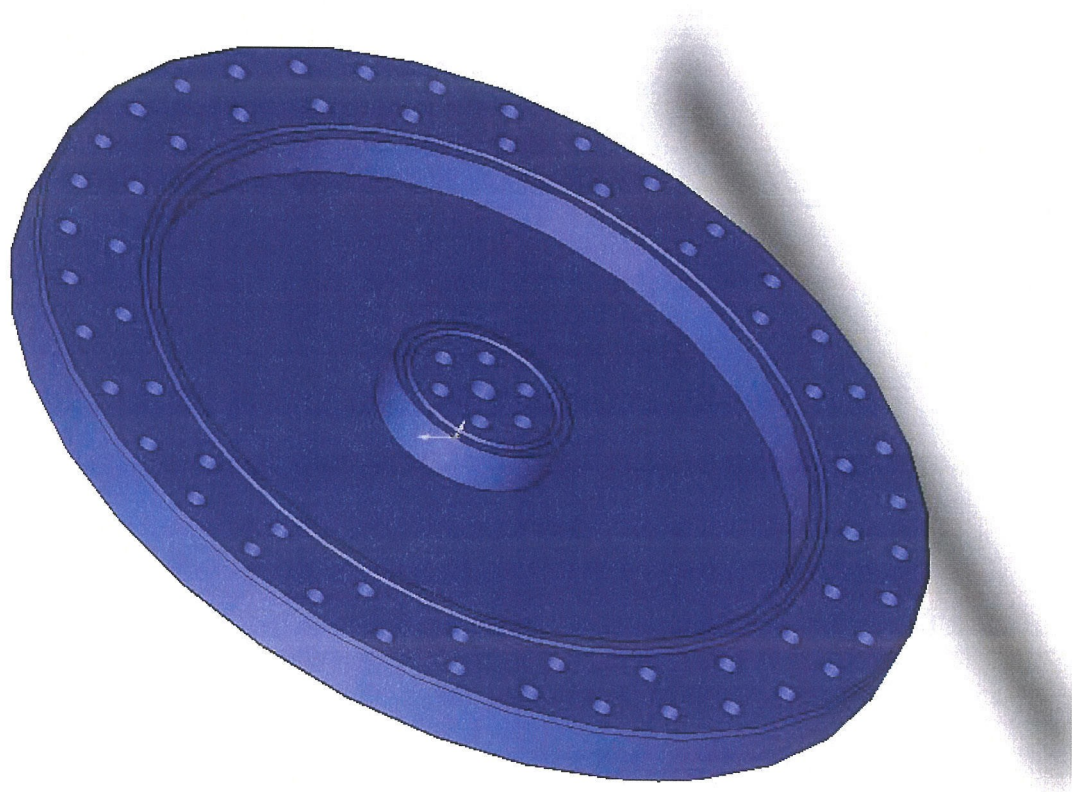


Figure B.17: Bottom Flange MDC.

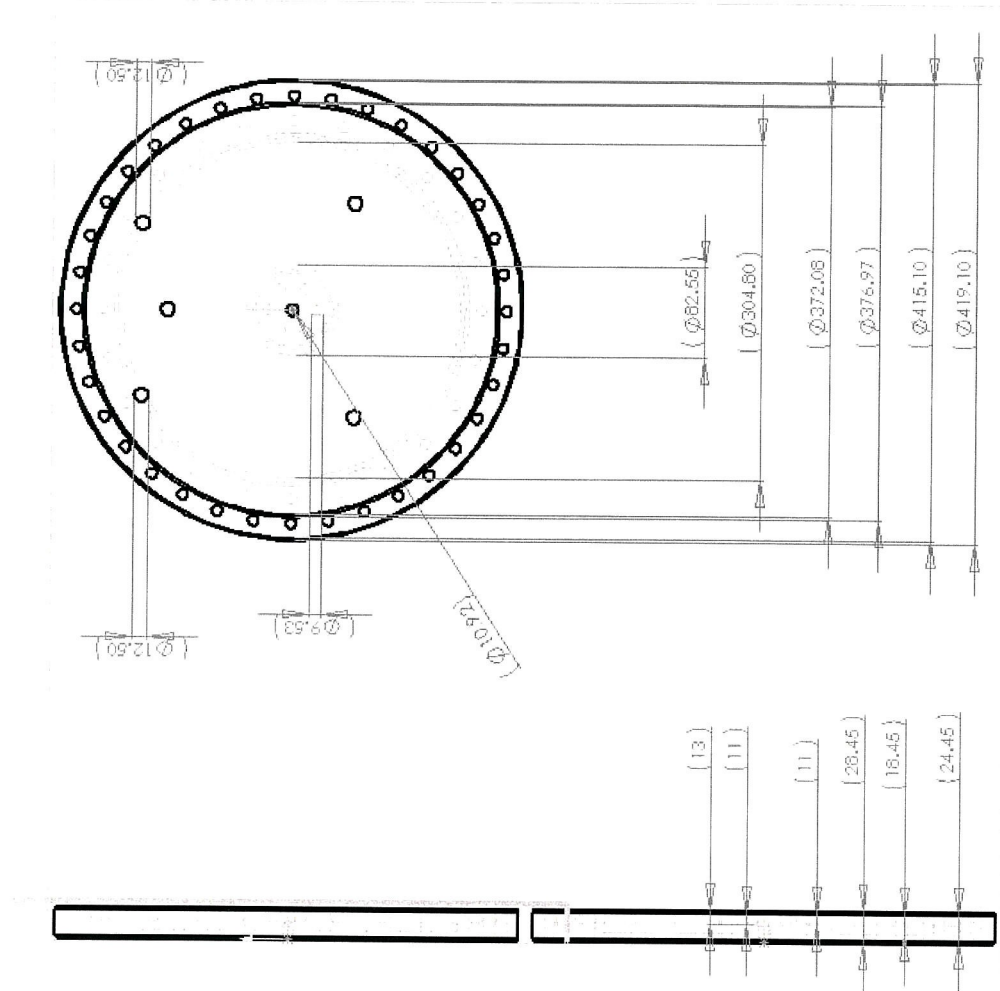


Figure B.18: Bottom Flange MDC.

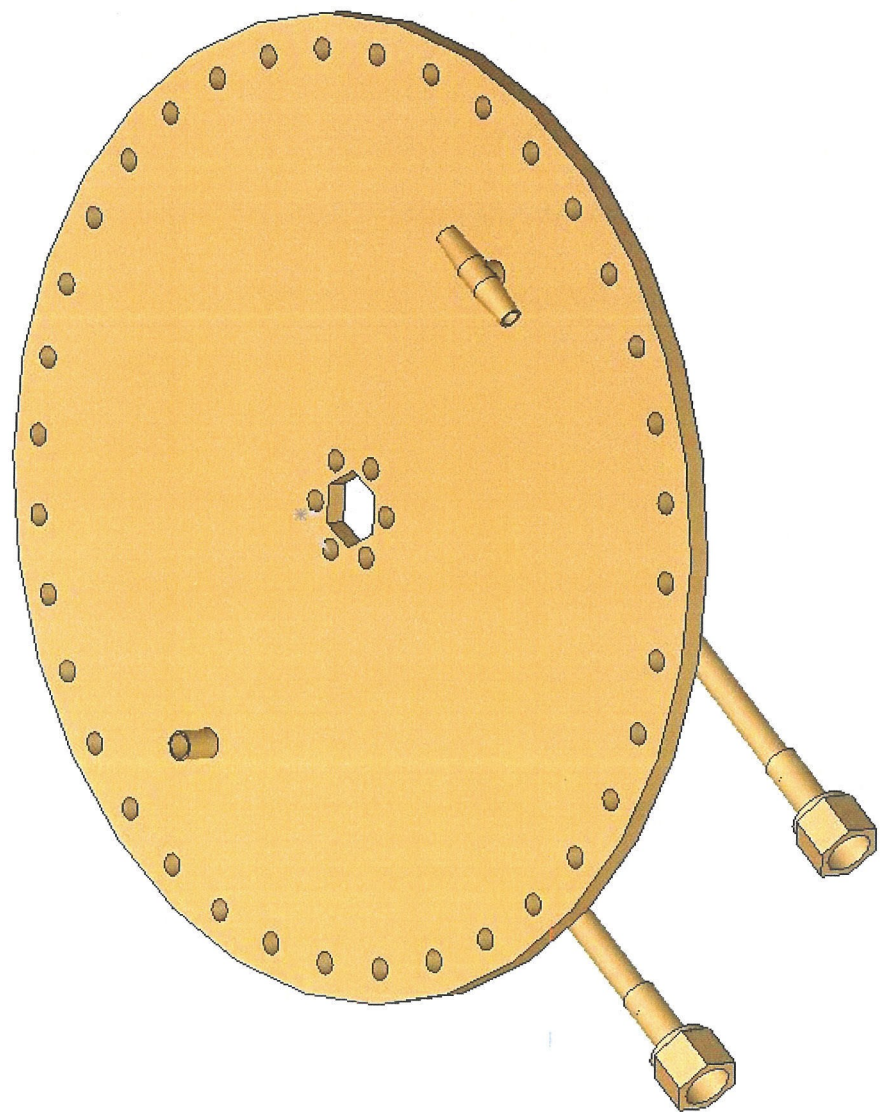


Figure B.19: Water cover plate, inlet jet and nozzle, and outlet port.

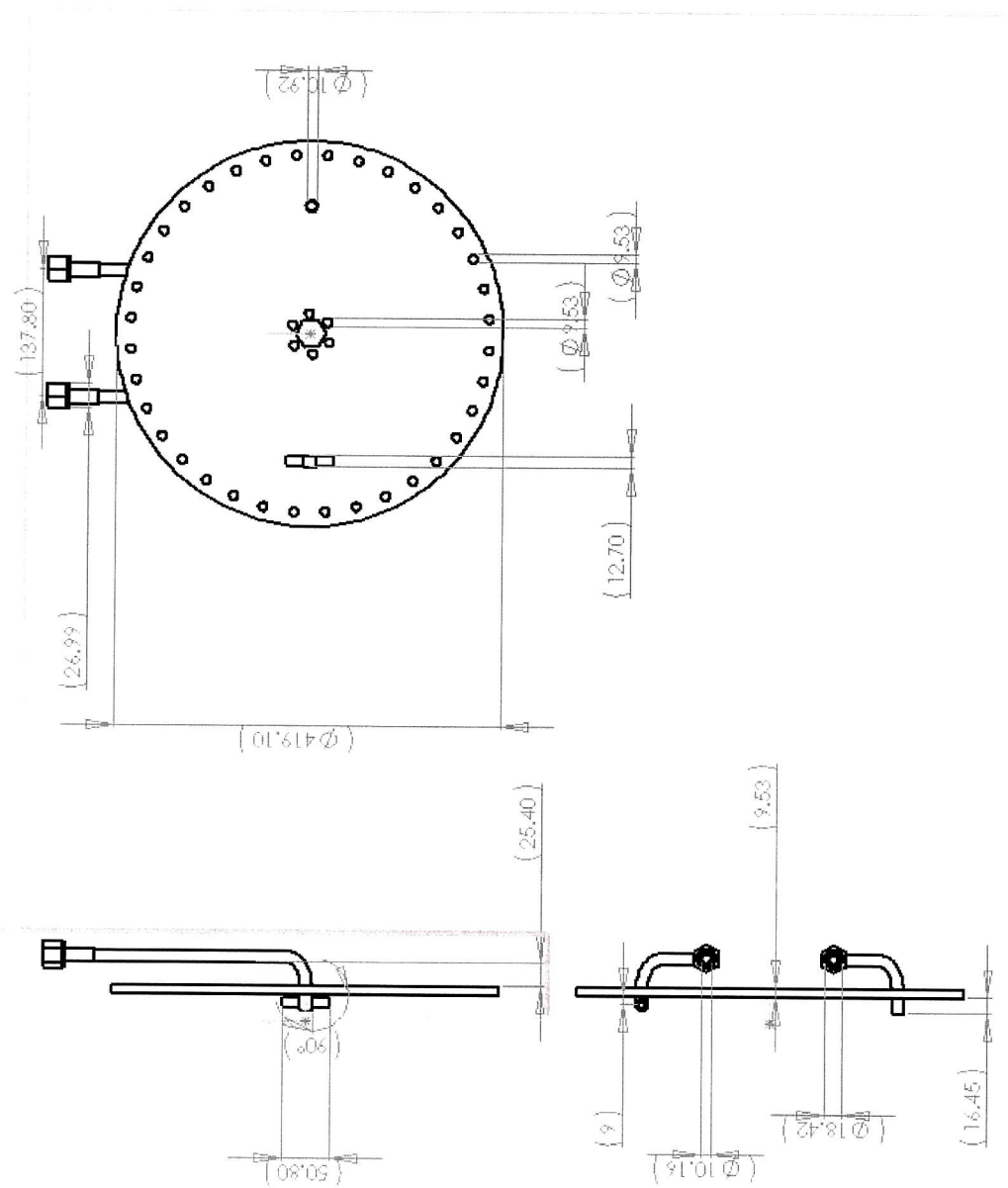


Figure B.20: Water cover plate, inlet jet and nozzle, and outlet port.

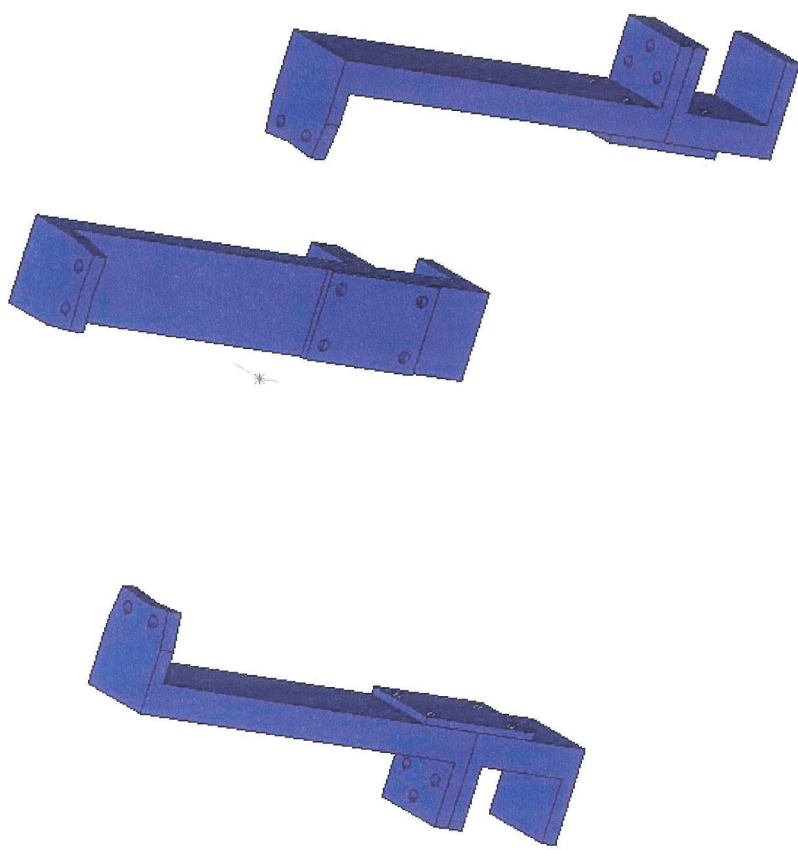


Figure B.21: Legs for supporting Top Flange and Assembly.

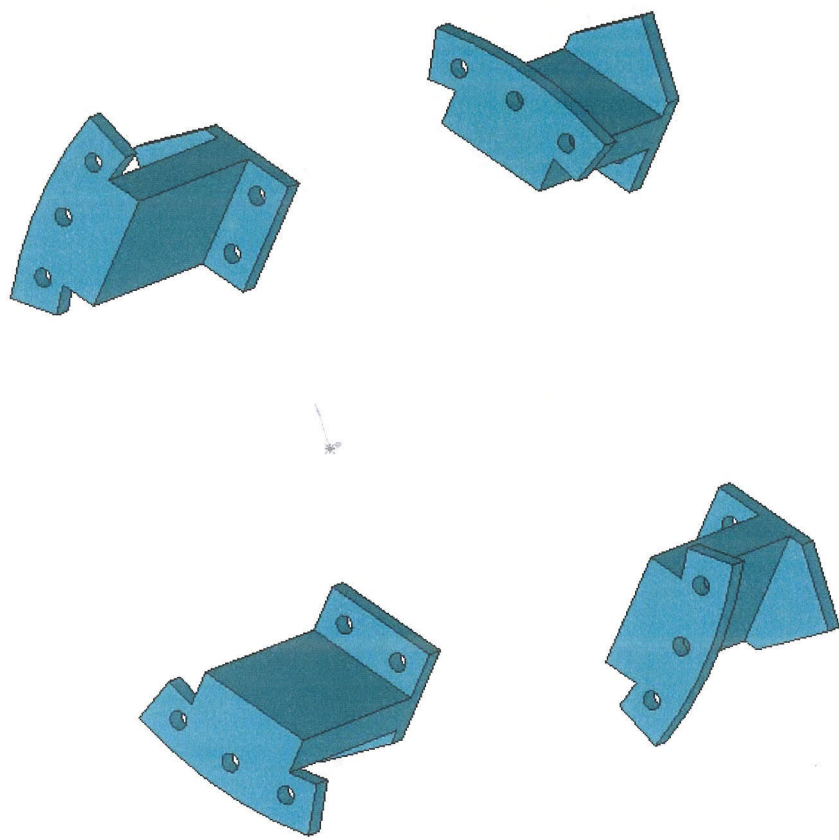


Figure B.22: Legs that mount to bottom flange, water plate, and jackstand.

## B.2 300 mm Quartz Sleeved Forks

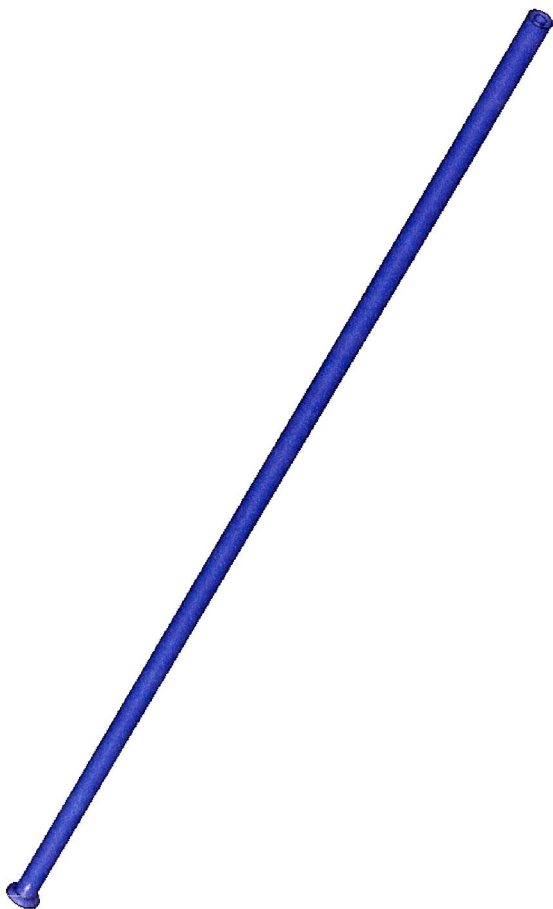


Figure B.23: Quartz Tine to cover SS Forks for 300 mm wafer handling.

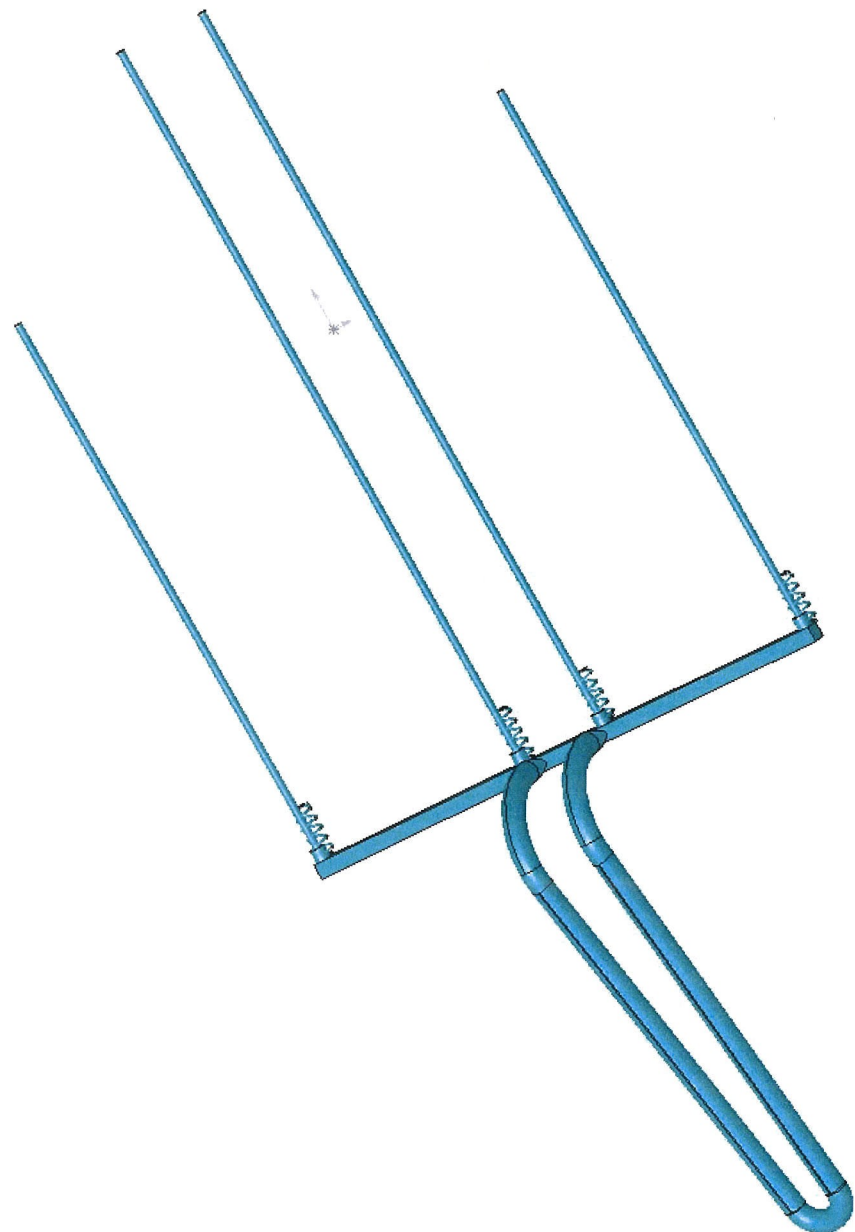


Figure B.24: Forks for 300 mm wafer handling.

### B.3 Software Code

This code is written in C++ for extraction of particle distribution data from Labview output \*.txt output of RDMA discrete-mode data.

```

//      Labview text extraction
//      Written by: Dean Holunga
//      Borland Turbo C++, ver.: 4.0

#include <string.h>
#include <stdio.h>
#include <conio.h>
#include <fstream.h>
#include <stdlib.h>

char temp;
char date[25], timer[25];
char dmin[16], dmax[16], binsize[16];
char Tcount[16], Tset[16], Tmeas[16];
char Qa[16], Qsh[16], Qel[16];
char partconc[30];
char mean[16], median[16], mode[16];
char stndev[16], logdevone[16], logdevtwo[16];
char VRdma[16], IElect[16], Dp[16], numpart[16], dndlogdp[16];
ifstream in1("extract.txt", ios::in);
ofstream out2("out.txt", ios::out);

void search(){
    char name[100];
    char dataget[100];
    int i,j,k;
    ifstream in1("extract.txt", ios::in);
    ofstream out2("out.txt", ios::out);
    FILE *extrct;
    extrct=fopen("extract.txt", "r");

    do {
        fgets(name,100,extrct);
        if(!strcmpi(name, " Vrdma(V)    Ielectrometer(fA)  Dp(nm)      # of
Particles(/s)      dN/dlogDp(/ml)\n")){
            fgets(dataget,100,extrct);
            for(int i=0;i<100;i++){
                temp = dataget[i];
                if (temp=='\t') {
                    VRdma[i]=NULL;
                    j=i+1;
                    k=i+1;
                    i=100;
                }
                else VRdma[i]=temp;
            }
            for(int j=k;j<(k+100);j++){
                temp = dataget[j];
                if (temp=='\t') {
                    IElect[j-k]=NULL;
                    k=j+1;
                    i=j+1;
                    j=k+100;
                }
                else IElect[j-k]=temp;
            }
        }
    }
}

```

Figure B.25: Page 1 of 8 C++ code.

```

        for(int k=i;k<(i+100);k++) {
            temp = dataget[k];
            if (temp=='\t') {
                Dp[k-i]=NULL;
                j=i+1;
                k=i+1;
                i=j+100;
            }
            else Dp[k-i]=temp;
        }

        for(int i=j;i<(j+100);i++) {
            temp = dataget[i];
            if (temp=='\t') {
                numpart[i-j]=NULL;
                j=i+1;
                k=i+1;
                i=j+100;
            }
            else numpart[i-j]=temp;
        }

        for(int j=k;j<(k+100);j++) {
            temp = dataget[j];
            if (temp=='\n') {
                dndlogdp[j-k]=NULL;
                j=k+100;
            }
            else dndlogdp[j-k]=temp;
        }
    }

    out2<<"Date,Time,Dmin,Dmax,BinSize,Tcount,TSett,Tmeas,Qa,Qsh,Qel,PartConc,
Mean,Median,Mode,StndDev,dlog/Dp1,dlog/dp2,VRDMA,IElectrometer,PartDia,NumPart,d
N/DlogDp\n";
    out2<<date<<","<<timer<<","<<dmin<<","<<dmax<<","<<binsize<<","<<Tcount<<
,"<<TSet<<","<<Tmeas<<","<<Qa<<","<<Qsh<<","<<Qel<<","<<partconc<<","<<mean<<",
"<<median<<","<<mode<<","<<stndev<<","<<logdevone<<","<<logdevtwo<<","<<VRdma<<",
"<<IElect<<","<<Dp<<","<<numpart<<","<<dndlogdp;

    }
    while(!strcmpi(name,"Total Particle Concentration(/ml)/n")));
    out2.close();
    in1.close();
    fclose(extrct);
    return;
}

void fnddate(){
    char name[33];
    char dataget[100];
    int i,j,k;

    FILE *extrct;
    extrct=fopen("extract.txt", "r");
}

```

Figure B.26: Page 2 of 8 C++ code.

```

do {
    fgets(name,33,extrct);

    if(!strcmpi(name,"Date & Time of This Measurement\t")){
        fgets(dataget,100,extrct);
        for(int i=0;i<100;i++){
            temp = dataget[i];
            if (temp=='\t') {
                date[i]=NULL;
                j=i+1;
                k=i+1;
                i=100;
            }
            else date[i]=temp;
        }
        for(int j=k;j<(k+100);j++){
            temp = dataget[j];
            if (temp=='\n') {
                timer[k-1]=NULL;
                k=i+100;
            }
            else timer[j-k]=temp;
        }
        fclose(extrct);
        return;
    }
}
while(!in1.eof());
fclose(extrct);
}

void fnddia(){
    char name[100];
    char dataget[100];
    int i,j,k;

    FILE *extrct;
    extrct=fopen("extract.txt", "r");

    do {
        fgets(name,100,extrct);

        if(!strcmpi(name,"Dmin(nm)      Dmax(nm)      # of bins\n")){
            fgets(dataget,100,extrct);
            for(int i=0;i<100;i++){
                temp = dataget[i];
                if (temp=='\t') {
                    dmin[i]=NULL;
                    j=i+1;
                    k=i+1;
                    i=100;
                }
                else dmin[i]=temp;
            }
        }
    }
}

```

Figure B.27: Page 3 of 8 C++ code.

```

        for(int j=k;j<(k+100);j++) {
            temp = dataget[j];
            if (temp=='\t') {
                dmax[j-k]=NULL;
                k=j+1;
                i=j+1;
                j=k+100;
            }
            else dmax[j-k]=temp;
        }

        for(int k=i;k<(i+100);k++) {
            temp = dataget[k];
            if (temp=='\n') {
                binsize[k-i]=NULL;
                k=i+100;
            }
            else binsize[k-i]=temp;
        }
        fclose(exrct);
        return;
    }
}
while(!in1.eof());
out2.close();

fclose(exrct);
}
void fnftime() {
    char name[100];
    char dataget[100];
    int i,j,k;

    FILE *exrct;
    exrct=fopen("extract.txt", "r");

    do {
        fgets(name,100,exrct);
        if(!strcmpi(name,"Settling time(s)  Counting time(s)  Measurement
Interval(s)\n")){
            fgets(dataget,100,exrct);
            for(int i=0;i<100;i++){
                temp = dataget[i];
                if (temp=='\t') {
                    Tset[i]=NULL;
                    j=i+1;
                    k=i+1;
                    i=100;
                }
                else Tset[i]=temp;
            }
            for(int j=k;j<(k+100);j++) {
                temp = dataget[j];
                if (temp=='\t') {
                    Tcount[j-k]=NULL;
                }
                else Tcount[j-k]=temp;
            }
        }
    }
}

```

Figure B.28: Page 4 of 8 C++ code.

```

        k=j+1;
        i=j+1;
        j=k+100;
    }
    else Tcount[j-k]=temp;
}

for(int k=i;k<(i+100);k++) {
    temp = dataget[k];
    if (temp=='\n') {
        Tmeas[k-i]=NULL;
        k=i+100;
    }
    else Tmeas[k-i]=temp;
}

fclose(exrct);
return;
}
}
while(!in1.eof());
fclose(exrct);
}

void fndflow() {
    char name[100];
    char dataget[100];
    int i,j,k;

    FILE *exrct;
    exrct=fopen("extract.txt", "r");

    do {
        fgets(name,100,exrct);
        if(!strcmpi(name, " Qa(l/min)  Qsh(l/min)  Qelectrometer(l/min)\n")) {

            fgets(dataget,100,exrct);
            for(int i=0;i<100;i++) {
                temp = dataget[i];
                if (temp=='\t') {
                    Qa[i]=NULL;
                    j=i+1;
                    k=i+1;
                    i=100;
                }
                else Qa[i]=temp;
            }
            for(int j=k;j<(k+100);j++) {
                temp = dataget[j];
                if (temp=='\t') {
                    Qsh[j-k]=NULL;
                    k=j+1;
                    i=j+1;
                    j=k+100;
                }
                else Qsh[j-k]=temp;
            }
        }
    }
}
}

```

Figure B.29: Page 5 of 8 C++ code.

```

        }

        for(int k=i;k<(i+100);k++) {
            temp = dataget [k];
            if (temp=='\n') {
                Qel [k-i]=NULL;
                k=i+100;
            }
            else Qel [k-i]=temp;
        }

        fclose(extrct);
        return;
    }
}
while(!in1.eof());

fclose(extrct);
}

void fndpartconc(){
    char name[100];

    FILE *extrct;
    extrct=fopen("extract.txt", "r");

    do {
        fgets(name,100,extrct);
        if(!strcmpi(name,"Total Particle Concentration(/ml)\n")){
            fgets(partconc,30,extrct);

            for(int i=0;i<30;i++){
                temp = partconc[i];
                if (temp=='\n'){
                    partconc[i]=NULL;
                }
                else partconc[i]=temp;
            }

            fclose(extrct);
            return;
        }
    }
    while(!in1.eof());

    fclose(extrct);
}

void fndstats(){
    char name[100];
    char dataget[100];
    int i,j,k;

    FILE *extrct;
    extrct=fopen("extract.txt", "r");

    do {

```

Figure B.30: Page 6 of 8 C++ code.

```

        fgets(name,100,extrct);
        if(!strcmpi(name,"Mean Diameter(nm)  Meadian Diameter(nm)      Mode
Diameter(nm)\n")){
            fgets(dataget,100,extrct);
            for(int i=0;i<100;i++){
                temp = dataget[i];
                if (temp=='\t') {
                    mean[i]=NULL;
                    j=i+1;
                    k=i+1;
                    i=100;
                }
                else mean[i]=temp;
            }
            for(int j=k;j<(k+100);j++) {
                temp = dataget[j];
                if (temp=='\t') {
                    median[j-k]=NULL;
                    k=j+1;
                    i=j+1;
                    j=k+100;
                }
                else median[j-k]=temp;
            }
            for(int k=i;k<(i+100);k++) {
                temp = dataget[k];
                if (temp=='\n') {
                    mode[k-i]=NULL;
                    k=i+100;
                }
                else mode[k-i]=temp;
            }
            fclose(extrct);
            return;
        }
    }
    while(!in1.eof());
    fclose(extrct);
}

void fnddev(){
    char name[100];
    char dataget[100];
    int i,j,k;

    FILE *extrct;
    extrct=fopen("extract.txt", "r");

    do {
        fgets(name,100,extrct);
        if(!strcmpi(name,"Standard Deviation of logDp  Deviation of
logDp(84%/50%)  Deviation of logDp(16%/50%)\n")){

```

Figure B.31: Page 7 of 8 C++ code.

```

        fgets(dataget,100,extrct);
        for(int i=0;i<100;i++) {
            temp = dataget[i];
            if (temp=='\t') {
                stndev[i]=NULL;
                j=i+1;
                k=i+1;
                i=100;
            }
            else stndev[i]=temp;
        }
        for(int j=k;j<(k+100);j++) {
            temp = dataget[j];
            if (temp=='\t') {
                logdevone[j-k]=NULL;
                k=j+1;
                i=j+1;
                j=k+100;
            }
            else logdevone[j-k]=temp;
        }
        for(int k=i;k<(i+100);k++) {
            temp = dataget[k];
            if (temp=='\n') {
                logdevtwo[k-i]=NULL;
                k=i+100;
            }
            else logdevtwo[k-i]=temp;
        }
        fclose(extrct);
        return;
    }
}
while(!in1.eof());
fclose(extrct);
}

int main(void)
{
    fnndate();
    fnndia();
    fnftime();
    fnflow();
    fnpartconc();
    fnstats();
    fnpdev();
    search();
    return 0;
}

```

Figure B.32: Page 8 of 8 C++ code.

## B.4 Scanning Algorithm In Labview

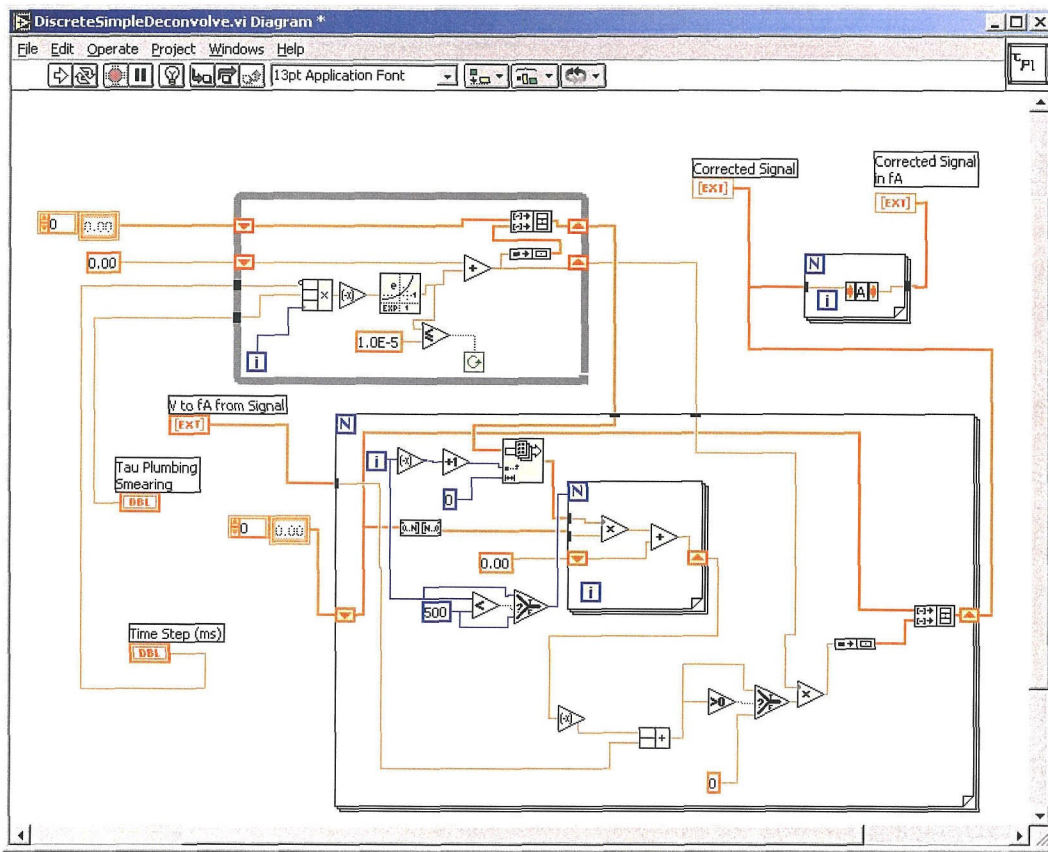


Figure B.33: Labview code for RDMA scanning-mode data inversion algorithm of Collins et al.<sup>28</sup>

## B.5 VB Code For MS Access Data Handling

Output files from the RDMA scanning code are memory intensive. Each file is named “Scan.txt”. Code in MS Access Visual Basic was used to reduce file size and convert them to referential databases.

First, the file “Scan.txt” was linked to the database, then several queries were run using a macro, called “Macro1”. The SQL code for the queries is as follows:

ZCopyScanner: INSERT INTO Scan SELECT Scanner.\* FROM Scanner;

Embedded Query2: TRANSFORM Sum(Scan.[dN/dlogDp(/ml)]) AS [SumOfdN/dlogDp(/ml)] SELECT Scan.[Dp(nm)] FROM Scan WHERE (((Scan.FileNum)>255)) GROUP BY Scan.[Dp(nm)] ORDER BY Scan.[Dp(nm)], [Time] & “-” & [FileNum] PIVOT [Time] & “-” & [FileNum];

Query3: SELECT Query2.\* INTO [output] FROM Query2;

zQuery1: INSERT INTO zDetails ( [Mean Diameter(nm)], [Median Diameter(nm)], [Mode Diameter(nm)], [Standard Deviation of logDp], [Deviation of logDp(84%/50%)], [Deviation of logDp(16%/50%)], [Total Particle Concentration(/ml)], [Dmin(nm)], [Dmax(nm)], [# of bins], [Settling time(s)], [Counting time(s)], [Measurement Interval(s)], [Qa(1/min)], [Qsh(1/min)], [Qelectrometer(1/min)], [Qdiluent(1/min)], [Qsilane(ml/min)], [QO2(1/min)], [QNuet(1/min)], [Temp(K)], [Scan Time (s)], FileNum, [Date], [Time], Tubing, [Silane Mixture (ppm)] ) SELECT DISTINCT Scan.[Mean Diameter(nm)], Scan.[Median Diameter(nm)], Scan.[Mode Diameter(nm)], Scan.[Standard Deviation of logDp], Scan.[Deviation of logDp(84%/50%)], Scan.[Deviation of logDp(16%/50%)], Scan.[Total Particle Concentration(/ml)], Scan.[Dmin(nm)], Scan.[Dmax(nm)], Scan.[# of bins], Scan.[Settling time(s)], Scan.[Counting time(s)], Scan.[Measurement Interval(s)], Scan.[Qa(1/min)], Scan.[Qsh(1/min)], Scan.[Qelectrometer(1/min)], Scan.[Qdiluent(1/min)], Scan.[Qsilane(ml/min)], Scan.[QO2(1/min)],

Scan.[QNuet(1/min)], Scan.[Temp (K)], Scan.[Scan Time (s)], Scan.FileNum, Scan.Date,  
Scan.Time, Scan.Tubing, Scan.[Silane Mixture (ppm)] FROM Scan;

zQuery2: INSERT INTO zData ( [Vrdma(V)], [Ielectrometer(fA)], [Dp(nm)], [# of Particles(/s)], [dN/dlogDp(/ml)], IDNum ) SELECT DISTINCT Scan.[Vrdma(V)], Scan.[Ielectrometer(fA)]  
Scan.[Dp(nm)], Scan.[# of Particles(/s)], Scan.[dN/dlogDp(/ml)], zDetails.IDNum FROM  
Scan INNER JOIN zDetails ON Scan.Time = zDetails.Time;

zQuery4: DELETE Scan.\* FROM Scan;

This final query deletes all duplicated information by emptying the dummy table “Scan”.

# Bibliography

- [1] M. Adachi, K. Okuyama, and Y. Kousaka. Electrostatic Coagulation Of Bipolarly Charged Aerosol Particles. *Journal Of Chemical Engineering Of Japan*, 14(6):467–473, 1981.
- [2] M. Adachi, K. Okuyama, Y. Kousaka, and T. Takahashi. Electrical Charging Of Uncharged Aerosol-Particles Under At Bipolar Ion Concentrations. *Journal Of Chemical Engineering Of Japan*, 13(1):55–60, 1980.
- [3] M. Adachi, F. J. Romay, and D. Y. H. Pui. High-Efficiency Unipolar Aerosol Charger Using a Radioactive Alpha-Source. *Journal of Aerosol Science*, 23(2):123–137, 1992.
- [4] J. K. Agarwal and G. J. Sem. Continuous-Flow, Single-Particle-Counting Condensation Nucleus Counter. *Journal of Aerosol Science*, 11(4):343–&, 1980.
- [5] M. Alam and R. Flagan. An Aerosol Reactor For Silicon Production. *Aerosol Science And Technology*, 2(2):271–271, 1983.
- [6] M. Alam and R. Flagan. Simultaneous Homogeneous Nucleation And Aerosol Growth. *Journal Of Colloid And Interface Science*, 97(1):232–246, 1984.
- [7] M. Alam and R. Flagan. Controlled Nucleation Aerosol Reactors–Production Of Bulk Silicon. *Aerosol Science And Technology*, 5(2):237–248, 1986.

[8] A. Alivisatos. Less Is More In Medicine—Sophisticated Forms Of Nanotechnology Will Find Some Of Their First Real-World Applications In Biomedical Research, Disease Diagnosis And, Possibly, Therapy. *Scientific American*, 285(3):66–73, 2001.

[9] A. Alivisatos. Biological Applications Of Nanocrystals. *Abstracts of Papers of the American Chemical Society*, 227:U117–U117, 2004. Part 1.

[10] A. Alivisatos. Biological Tagging Applications For Single Molecules And Cells Using Semiconductor Nanocrystals. *Abstracts of Papers of the American Chemical Society*, 228:U211–U211, 2004. Part 2.

[11] H. L. Bai, C. C. Chen, C. S. Lin, W. Den, and C. L. Chang. Monodisperse Nanoparticle Synthesis By An Atmospheric Pressure Plasma Process: An Example Of A Visible Light Photocatalyst. *Industrial & Engineering Chemistry Research*, 43(22):7200–7203, 2004.

[12] U. Banin, Y. W. Cao, D. Katz, and O. Millo. Identification Of Atomic-Like Electronic States In Indium Arsenide Nanocrystal Quantum Dots. *Nature*, 400(6744):542–544, 1999.

[13] R. Bird, W. Stewart, and E. Lightfoot. *Transport Phenomena*. John Wiley & Sons, New York, NY, 1st edition, 1960.

[14] P. Biswas and R. Flagan. High-Velocity Inertial Impactors. *Environmental Science & Technology*, 18(8):611–616, 1984.

[15] P. Biswas and R. Flagan. The Particle Trap Impactor. *Journal of Aerosol Science*, 19(1):113–121, 1988.

- [16] J. S. Biteen, N. S. Lewis, H. A. Atwater, and A. Polman. Size-Dependent Oxygen-Related Electronic States In Silicon Nanocrystals. *Applied Physics Letters*, 84(26):5389–5391, 2004.
- [17] H. Branz, L. Liem, C. Harris, S. Fan, J. Flint, D. Adler, and J. Haggerty. Laser-Induced Chemical Vapor-Deposition Of Hydrogenated Amorphous-Silicon-Photovoltaic Devices And Material Properties. *Solar Cells*, 21:177–188, 1987.
- [18] M. L. Brongersma, A. Polman, K. S. Min, and H. A. Atwater. Depth Distribution Of Luminescent Si Nanocrystals In Si Implanted SiO<sub>2</sub> Films On Si. *Journal of Applied Physics*, 86(2):759–763, 1999.
- [19] M. L. Brongersma, A. Polman, K. S. Min, E. Boer, T. Tambo, and H. A. Atwater. Tuning The Emission Wavelength Of Si Nanocrystals In SiO<sub>2</sub> By Oxidation. *Applied Physics Letters*, 72(20):2577–2579, 1998.
- [20] M. Bruchez, M. Moronne, P. Gin, S. Weiss, and A. P. Alivisatos. Semiconductor Nanocrystals As Fluorescent Biological Labels. *Science*, 281(5385):2013–2016, 1998.
- [21] R. J. Buss, P. Ho, W. G. Breiland, and M. E. Coltrin. Reactive Sticking Coefficients for Silane and Disilane on Polycrystalline Silicon. *Journal of Applied Physics*, 63(8):2808–2819, 1988.
- [22] R. Camata, H. Atwater, and R. Flagan. Space-Charge Effects In Nanoparticle Processing Using The Differential Mobility Analyzer. *Journal Of Aerosol Science*, 32(5):583–599, 2001.
- [23] R. Camata, H. Atwater, K. Vahala, and R. Flagan. Size Classification Of Silicon Nanocrystals. *Applied Physics Letters*, 68(22):3162–3164, 1996.

[24] L. T. Canham. Silicon Quantum Wire Array Fabrication by Electrochemical and Chemical Dissolution of Wafers. *Applied Physics Letters*, 57(10):1046–1048, 1990.

[25] W. Cannon, S. Danforth, J. Flint, K. Lai, and J. Haggerty. Synthesis Of Si And  $\text{Si}_3\text{N}_4$  Powders From Laser-Heated Gas-Phase Reactants. *American Ceramic Society Bulletin*, 58(3):337–337, 1979.

[26] W. Cannon, S. Danforth, J. Haggerty, and R. Marra. Processing And Sintering Of Powders Synthesized By Laser-Induced Gas-Phase Reactions. *American Ceramic Society Bulletin*, 59(3):361–361, 1980.

[27] S. Coe, W. K. Woo, M. Bawendi, and V. Bulovic. Electroluminescence From Single Monolayers Of Nanocrystals In Molecular Organic Devices. *Nature*, 420(6917):800–803, 2002.

[28] D. Collins, R. Flagan, and J. Seinfeld. Improved Inversion Of Scanning DMA Data. *Aerosol Science And Technology*, 36(1):1–9, 2002.

[29] V. L. Colvin, M. C. Schlamp, and A. P. Alivisatos. Light-Emitting-Diodes Made from Cadmium Selenide Nanocrystals and a Semiconducting Polymer. *Nature*, 370(6488):354–357, 1994.

[30] S. Corrsin. Simple Theory Of An Idealized Turbulent Mixer. *AICHE Journal*, 3(3):329–330, 1957.

[31] T. M. Damour, S. H. Ehrman, M. N. A. Karlsson, L. S. Karisson, and K. Deppert. Experimental Evidence For Evaporation/Condensation Nonuniform Flow In A Horizontal Aerosol Generator. *Aerosol Science and Technology*, 39(5):444–451, 2005.

- [32] B. E. Deal and A. S. Grove. General Relationship for Thermal Oxidation of Silicon. *Journal of Applied Physics*, 36(12):3770, 1965.
- [33] C. Delerue, G. Allan, and M. Lannoo. Theoretical Aspects of the Luminescence of Porous Silicon. *Physical Review B*, 48(15):11024–11036, 1993.
- [34] D. S. English, L. E. Pell, Z. H. Yu, P. F. Barbara, and B. A. Korgel. Size Tunable Visible Luminescence From Individual Organic Monolayer Stabilized Silicon Nanocrystal Quantum Dots. *Nano Letters*, 2(7):681–685, 2002.
- [35] T. Feng, H. B. Yu, M. Dicken, J. R. Heath, and H. A. Atwater. Probing The Size And Density Of Silicon Nanocrystals In Nanocrystal Memory Device Applications. *Applied Physics Letters*, 86(3), 2005.
- [36] R. Flagan. Probing The Chemical-Dynamics Of Aerosols. *Advances In Chemistry Series*, (232):185–210, 1993.
- [37] R. Flagan. On Differential Mobility Analyzer Resolution. *Aerosol Science And Technology*, 30(6):556–570, 1999.
- [38] R. Flagan and M. Lunden. Particle Structure Control In Nanoparticle Synthesis From The Vapor Phase. *Materials Science And Engineering A-Structural Materials Properties Microstructure And Processing*, 204(1-2):113–124, 1995.
- [39] R. Flagan and J. Seinfeld. *Fundamentals Of Air Pollution Engineering*. Prentice Hall, Englewood Cliffs, NJ, 1998.
- [40] N. Fuchs. *Mechanics Of Aerosols*. Pergamon Press, New York, NY, 1964.
- [41] T. Fujimoto, Y. Kuga, S. Pratsinis, and K. Okuyama. Unipolar Ion Charging And

Coagulation During Aerosol Formation By Chemical Reaction. *Powder Technology*, 135:321–335, 2003.

[42] M. Y. Gao, J. Q. Sun, E. Dulkeith, N. Gaponik, U. Lemmer, and J. Feldmann. Lateral Patterning Of CdTe Nanocrystal Films By The Electric Field Directed Layer-By-Layer Assembly Method. *Langmuir*, 18(10):4098–4102, 2002.

[43] C. Garcia, B. Garrido, P. Pellegrino, R. Ferre, J. A. Moreno, J. R. Morante, L. Pavesi, and M. Cazzanelli. Size Dependence Of Lifetime And Absorption Cross Section Of Si Nanocrystals Embedded In SiO<sub>2</sub>. *Applied Physics Letters*, 82(10):1595–1597, 2003.

[44] S. L. Girshick and C. P. Chiu. Kinetic Nucleation Theory—a New Expression for the Rate of Homogeneous Nucleation from an Ideal Supersaturated Vapor. *Journal of Chemical Physics*, 93(2):1273–1277, 1990.

[45] M. Glikin, I. Glikina, and E. Kauffeldt. Investigations And Applications Of Aerosol Nano-Catalysis In A Vibrofluidized (Vibrating) Bed. *Adsorption Science & Technology*, 23(2):135–143, 2005.

[46] M. Glikin, D. Kutakova, and E. Prin. Unsteady Processes And Aerosol Catalysis. *Chemical Engineering Science*, 54(20):4337–4342, 1999.

[47] M. A. Glikin. Aerosol Catalysis. *Theoretical Foundations of Chemical Engineering*, 30(4):390–394, 1996.

[48] M. A. Glikin, D. A. Kutakova, I. M. Glikina, and A. I. Volga. A New Way To Increase Catalyst Activity. *Adsorption Science & Technology*, 19(2):101–115, 2001.

[49] S. L. Goren. Thermophoresis of Aerosol-Particles in Laminar Boundary-Layer on a Flat-Plate. *Journal of Colloid and Interface Science*, 61(1):77–85, 1977.

- [50] O. Guillois, N. Herlin-Boime, C. Reynaud, G. Ledoux, and F. Huisken. Photoluminescence Decay Dynamics Of Noninteracting Silicon Nanocrystals. *Journal of Applied Physics*, 95(7):3677–3682, 2004.
- [51] V. Haas, R. Birringer, H. Gleiter, and S. Pratsinis. Synthesis Of Nanostructured Powders In An Aerosol Flow Condenser. *Journal Of Aerosol Science*, 28(8):1443–1453, 1997.
- [52] J. Haggerty. Powder Preparation By Laser-Induced Gas-Phase Reactions. *American Ceramic Society Bulletin*, 62(8):855–855, 1983.
- [53] M. Y. Han, X. H. Gao, J. Z. Su, and S. Nie. Quantum-dot-tagged microbeads for multiplexed optical coding of biomolecules. *Nature Biotechnology*, 19(7):631–635, 2001.
- [54] J. Heitmann, F. Muller, M. Zacharias, and U. Gosele. Silicon Nanocrystals: Size Matters. *Advanced Materials*, 17(7):795–803, 2005.
- [55] S. Hering and M. Stolzenburg. Online Determination Of Particle-Size And Density In The Nanometer-Size Range. *Aerosol Science And Technology*, 23(2):155–173, 1995.
- [56] N. Hill and K. Whaley. Size Dependence Of Excitons In Silicon Nanocrystals. *Physical Review Letters*, 75(6):1130–1133, 1995.
- [57] M. Hirasawa, T. Seto, and N. Aya. Morphological Control Of Laser-Synthesized Silicon Nanoparticles. *Journal Of Nanoscience And Nanotechnology*, 1(4):381–383, 2001.
- [58] H. Hofmeister, F. Huisken, and B. Kohn. Lattice Contraction In Nanosized Silicon

Particles Produced By Laser Pyrolysis Of Silane. *European Physical Journal D*, 9(1-4):137–140, 1999. Sp. Iss. SI.

[59] J. D. Holmes, K. J. Ziegler, R. C. Doty, L. E. Pell, K. P. Johnston, and B. A. Korgel. Highly Luminescent Silicon Nanocrystals With Discrete Optical Transitions. *Journal of the American Chemical Society*, 123(16):3743–3748, 2001.

[60] D. Holunga, R. Flagan, and H. Atwater. A Scalable Turbulent Mixing Aerosol Reactor for Oxide-Coated Silicon Nanoparticles. *Ind. Eng. Chem. Res.*, 2005.

[61] W. Hoppel and G. Frick. Ion Aerosol Attachment Coefficients and the Steady-State Charge-Distribution on Aerosols in a Bipolar Ion Environment. *Aerosol Science and Technology*, 5(1):1–21, 1986.

[62] R. Houriet, R. Vacassy, and H. Hofmann. Synthesis Of Powders And Films Using A New Laser Ablation Technique. *Nanostructured Materials*, 11(8):1155–1163, 1999.

[63] S. A. Husain and R. S. Anderssen. Modelling The Relaxation Modulus Of Linear Viscoelasticity Using Kohlrausch Functions. *Journal of Non-Newtonian Fluid Mechanics*, 125(2-3):159–170, 2005.

[64] D. K. Hutchins and J. Holm. Aerosol Charger Using Sinusoidally Driven Ion Current from a Corona Discharge. *Aerosol Science and Technology*, 11(3):244–253, 1989.

[65] L. Q. Jing, B. Q. Wang, B. F. Xin, S. D. Li, K. Y. Shi, W. M. Cai, and H. G. Fu. Investigations On The Surface Modification Of ZnO Nanoparticle Photocatalyst By Depositing Pd. *Journal of Solid State Chemistry*, 177(11):4221–4227, 2004.

[66] T. Johannessen, J. R. Jenson, M. Mosleh, J. Johansen, U. Quaade, and H. Livbjerg.

Flame Synthesis Of Nanoparticles—Applications In Catalysis And Product/Process Engineering. *Chemical Engineering Research & Design*, 82(A11):1444–1452, 2004.

[67] M. Kapoor, K. Singh, and R. K. Pandey. Dependence Of Photoluminescence Efficiency On Size In Silicon Nanostructures: Phenomenological Investigations. *Physica E-Low-Dimensional Systems & Nanostructures*, 23(1-2):183–187, 2004.

[68] M. N. A. Karlsson, K. Deppert, L. S. Karlsson, M. H. Magnusson, J. O. Malm, and N. S. Srinivasan. Size- And Composition- Controlled Au-Ga Aerosol Nanoparticles. *Aerosol Science And Technology*, 9(38):948–954, 2004.

[69] S. V. Kershaw, M. Harrison, A. L. Rogach, and A. Kornowski. Development of IR-Emitting Colloidal II-VI Quantum-Dot Materials. *IEEE Journal of Selected Topics in Quantum Electronics*, 6(3):534–543, 2000.

[70] A. Kilian and T. Morse. A Novel Aerosol Combustion Process For The High Rate Formation Of Nanoscale Oxide Particles. *Aerosol Science And Technology*, 34(2):227–235, 2001.

[71] E. Klarreich. Biologists Join The Dots. *Nature*, 413(6855):450–452, 2001.

[72] D. L. Klein, R. Roth, A. K. L. Lim, A. P. Alivisatos, and P. L. McEuen. A Single-Electron Transistor Made From A Cadmium Selenide Nanocrystal. *Nature*, 389(6652):699–701, 1997.

[73] W. Koch and S. Friedlander. The Effect Of Particle Coalescence On The Surface Area Of A Coagulating Aerosol. *Journal Of Aerosol Science*, 20(8):891–894, 1989.

[74] Y. Kogan and Z. Burnasheva. Growth And Measurement Of Condensation Nuclei In A Continuous Stream. *Rus. J. Phys. Chem.*, 34(12):1240–1243, 1960.

[75] U. R. Kortshagen, U. V. Bhandarkar, M. T. Swihart, and S. L. Girshick. Generation And Growth Of Nanoparticles In Low-Pressure Plasmas. *Pure and Applied Chemistry*, 71(10):1871–1877, 1999.

[76] Y. Kousaka, T. Niida, K. Okuyama, and H. Tanaka. Development of a Mixing Type Condensation Nucleus Counter. *Journal of Aerosol Science*, 13(3):231–240, 1982.

[77] Y. Kousaka, K. Okuyama, M. Adachi, and K. Ebie. Measurement of Electric Charge of Aerosol Particles Generated by Various Methods. *Journal of Chemical Engineering of Japan*, 14(1):54–58, 1981.

[78] F. Kruis, H. Fissan, and A. Peled. Synthesis Of Nanoparticles In The Gas Phase For Electronic, Optical And Magnetic Applications—A Review. *Journal of Aerosol Science*, 29(5-6):511–535, 1998.

[79] F. Kruis, K. Kusters, S. Pratsinis, and B. Scarlett. A Simple-Model For The Evolution Of The Characteristics Of Aggregate Particles Undergoing Coagulation And Sintering. *Aerosol Science And Technology*, 19(4):514–526, 1993.

[80] F. E. Kruis and H. Fissan. Nanoparticle Charging In A Twin Hewitt Charger. *Journal of Nanoparticle Research*, 3(1):39–50, 2001.

[81] F. Lai, G. Hidy, S. Friedlander, and J. Pich. Self-Preserving Particle-Size Distribution For Brownian Coagulation In Free-Molecule Regime. *Journal Of Colloid And Interface Science*, 39(2):395–398, 1972.

[82] G. Ledoux, J. Gong, F. Huisken, O. Guillois, and C. Reynaud. Photoluminescence Of Size-Separated Silicon Nanocrystals: Confirmation Of Quantum Confinement. *Applied Physics Letters*, 80(25):4834–4836, 2002.

[83] G. Ledoux, O. Guillois, D. Porterat, C. Reynaud, F. Huisken, B. Kohn, and V. Paillard. Photoluminescence Properties Of Silicon Nanocrystals As A Function Of Their Size. *Physical Review B*, 62(23):15942–15951, 2000.

[84] B. Lee and S. Kim. New Type Of Impactor With A Cooled Impaction Plate For Capturing PM2.5 And Other Aerosols. *Journal of Aerosol Science*, 34(7):957–962, 2003.

[85] P. Lee, D. Chen, and D. Pui. Experimental Study Of A Nanoparticle Virtual Impactor. *Journal of Nanoparticle Research*, 5(3-4):269–280, 2003.

[86] A. V. Malko, A. A. Mikhailovsky, M. A. Petruska, J. A. Hollingsworth, H. Htoon, M. G. Bawendi, and V. I. Klimov. From Amplified Spontaneous Emission To Microring Lasing Using Nanocrystal Quantum Dot Solids. *Applied Physics Letters*, 81(7):1303–1305, 2002.

[87] H. Z. Massoud. Thermal Oxidation Of Silicon In The Ultrathin Regime. *Solid-State Electronics*, 41(7):929–934, 1997.

[88] A. Maynard. The Application Of Electron-Energy-Loss Spectroscopy To The Analysis Of Ultrafine Aerosol- Particles. *Journal Of Aerosol Science*, 26(5):757–777, 1995.

[89] A. Maynard, Y. Ito, I. Arslan, N. Zimmer, A. T Browning, and A. Nicholls. Examining Elemental Surface Enrichment In Ultrafine Aerosol Particles Using Analytical Scanning Transmission Electron Microscopy. *Aerosol Science And Technology*, 38(4):365–381, 2004.

[90] W. McDermott, R. Ockovic, and M. Stolzenburg. Counting Efficiency Of An

Improved 30-A Condensation Nucleus Counter. *Aerosol Science And Technology*, 14(2):278–287, 1991.

[91] X. Michalet, F. Pinaud, T. Lacoste, M. Dahan, M. Bruchez, A. Alivisatos, and S. Weiss. Properties Of Fluorescent Semiconductor Nanocrystals And Their Application To Biological Labeling. *Single Molecules*, 2(4):261–276, 2001.

[92] K. S. Min, K. V. Shcheglov, C. M. Yang, H. A. Atwater, M. L. Brongersma, and A. Polman. Defect-Related Versus Excitonic Visible Light Emission From Ion Beam Synthesized Si Nanocrystals In SiO<sub>2</sub>. *Applied Physics Letters*, 69(14):2033–2035, 1996.

[93] P. F. Miquel and J. L. Katz. Formation and Characterization of Nanostructured V-P-O Particles in Flames–A New Route for the Formation of Catalysts. *Journal of Materials Research*, 9(3):746–754, 1994.

[94] M. Mohr and H. Burtscher. Photoelectric Aerosol Charging At High Particle Concentrations. *Journal of Aerosol Science*, 28(4):613–621, 1997.

[95] R. Mueller, L. Madler, and S. Pratsinis. Nanoparticle Synthesis At High Production Rates By Flame Spray Pyrolysis. *Chemical Engineering Science*, 58(10):1969–1976, 2003.

[96] D. Mukherjee, C. Sonwane, and M. Zachariah. Kinetic Monte Carlo Simulation Of The Effect Of Coalescence Energy Release On The Size And Shape Evolution Of Nanoparticles Grown As An Aerosol. *Journal Of Chemical Physics*, 119(6):3391–3404, 2003.

[97] H. Nguyen and R. Flagan. Particle Formation And Growth In Single-Stage Aerosol Reactors. *Langmuir*, 7(8):1807–1814, 1991.

[98] H. V. Nguyen, K. Okuyama, T. Mimura, Y. Kousaka, R. C. Flagan, and J. H. Seinfeld. Homogeneous and Heterogeneous Nucleation in a Laminar-Flow Aerosol Generator. *Journal of Colloid and Interface Science*, 119(2):491–504, 1987.

[99] K. Okuyama, R. Ushio, Y. Kousaka, R. Flagan, and J. Seinfeld. Particle Generation In A Chemical Vapor-Deposition Process With Seed Particles. *AICHE Journal*, 36(3):409–419, 1990.

[100] M. Ostraat, H. Atwater, and R. Flagan. The Feasibility Of Inert Colloidal Processing Of Silicon Nanoparticles. *Journal of Colloid and Interface Science*, 283(2):414–421, 2005.

[101] M. Ostraat, J. De Blauwe, M. Green, L. Bell, H. Atwater, and R. Flagan. Ultraclean Two-Stage Aerosol Reactor For Production Of Oxide-Passivated Silicon Nanoparticles For Novel Memory Devices. *Journal Of The Electrochemical Society*, 148(5):G265–G270, 2001.

[102] M. Ostraat, J. De Blauwe, M. Green, L. Bell, M. Brongersma, J. Casperson, R. Flagan, and H. Atwater. Synthesis And Characterization Of Aerosol Silicon Nanocrystal Nonvolatile Floating-Gate Memory Devices. *Applied Physics Letters*, 79(3):433–435, 2001.

[103] L. Pavesi and M. Ceschini. Stretched-Exponential Decay of the Luminescence in Porous Silicon. *Physical Review B*, 48(23):17625–17628, 1993.

[104] L. E. Pell, A. D. Schricker, F. V. Mikulec, and B. A. Korgel. Synthesis Of Amorphous Silicon Colloids By Trisilane Thermolysis In High Temperature Supercritical Solvents. *Langmuir*, 20(16):6546–6548, 2004.

[105] D. J. Phares, G. T. Smedley, and R. C. Flagan. Effect Of Particle Size And Material Properties On Aerodynamic Resuspension From Surfaces. *Journal of Aerosol Science*, 31(11):1335–1353, 2000.

[106] S. Pratsinis. Flame Aerosol Synthesis Of Ceramic Powders. *Progress In Energy And Combustion Science*, 24(3):197–219, 1998.

[107] J. P. Proot, C. Delerue, and G. Allan. Electronic-Structure and Optical-Properties of Silicon Crystallites—Application to Porous Silicon. *Applied Physics Letters*, 61(16):1948–1950, 1992.

[108] J. Pyykonen and J. Jokiniemi. Computational Fluid Dynamics Based Sectional Aerosol Modeling Schemes. *Journal Of Aerosol Science*, 31(5):531–550, 2000.

[109] N. Rao, S. Girshick, J. Heberlein, P. McMurry, S. Jones, D. Hansen, and B. Micheel. Nanoparticle Formation Using a Plasma Expansion Process. *Plasma Chemistry and Plasma Processing*, 15(4):581–606, 1995.

[110] D. Ravenhall, L. Forney, and A. Hubbard. Theory and Observation of a Two-Dimensional Virtual Impactor. *Journal of Colloid and Interface Science*, 85(2):508–520, 1982.

[111] H. Rumpf, K. Sommer, and K. Steier. Mechanisms of Enhancing Adhesive Forces on Adhesion of Particles by Plastic-Deformation, Sintering, and Viscoelastic Flow. *Chemie Ingenieur Technik*, 48(4):300–307, 1976.

[112] H. Rumpf, K. Sommer, and K. Steier. Effect of Plastic Deformation, Sintering, and Viscoelastic Flow on Particle Adhesion. *International Chemical Engineering*, 18(4):558–565, 1978.

[113] R. Sankaran, D. Holunga, R. Flagan, and K. Giapis. Synthesis Of Blue Luminescent Si Nanoparticles Using Atmospheric-Pressure Microdischarges. *Nano Letters*, 5(3):537–541, 2005.

[114] R. M. Sankaran and K. P. Giapis. Hollow Cathode Sustained Plasma Microjets: Characterization And Application To Diamond Deposition. *Journal of Applied Physics*, 92(5):2406–2411, 2002.

[115] H. Schlichting. *Boundary Layer Theory*. McGraw-Hill, New York, NY, 6th edition, 1968.

[116] T. Seto, A. Hirota, T. Fujimoto, M. Shimada, and K. Okuyama. Sintering Of Polydisperse Nanometer-Sized Agglomerates. *Aerosol Science And Technology*, 27(3):422–438, 1997.

[117] T. Seto, Y. Kawakami, N. Suzuki, M. Hirasawa, and N. Aya. Laser Synthesis Of Uniform Silicon Single Nanodots. *Nano Letters*, 1(6):315–318, 2001.

[118] T. Seto, T. Orii, M. Hirasawa, N. Aya, and H. Shimura. Ion Beam Charging Of Silicon Nanoparticles In Helium Background Gas: Design Of The Ion Beam Aerosol Charger. *Review of Scientific Instruments*, 74(6):3027–3030, 2003.

[119] T. Seto, T. Orii, H. Sakurai, M. Hirasawa, and S. B. Kwon. Ion Beam Charging Of Aerosol Nanoparticles. *Aerosol Science and Technology*, 39(8):750–759, 2005.

[120] P. S. Shah, T. Hanrath, K. P. Johnston, and B. A. Korgel. Nanocrystal And Nanowire Synthesis And Dispersibility In Supercritical Fluids. *Journal of Physical Chemistry B*, 108(28):9574–9587, 2004.

[121] F. G. Shi. Direct Measurement of Free-Energy Barrier to Nucleation of Crystallites in Amorphous-Silicon Thin-Films. *Journal of Applied Physics*, 76(9):5149–5153, 1994.

[122] D. Sinclair and V. Lamer. Light Scattering As A Measure Of Particle Size In Aerosols—The Production Of Monodisperse Aerosols. *Chemical Reviews*, 44(2):245–267, 1949.

[123] G. T. Smedley, D. J. Phares, and R. C. Flagan. Entrainment Of Fine Particles From Surfaces By Gas Jets Impinging At Normal Incidence. *Experiments in Fluids*, 26(4):324–334, 1999.

[124] G. T. Smedley, D. J. Phares, and R. C. Flagan. Entrainment Of Fine Particles From Surfaces By Impinging Shock Waves. *Experiments in Fluids*, 26(1-2):116–125, 1999.

[125] W. Stark and S. Pratsinis. Aerosol Flame Reactors For Manufacture Of Nanoparticles. *Powder Technology*, 126(2):103–108, 2002.

[126] M. Stolzenburg and P. McMurry. An Ultrafine Aerosol Condensation Nucleus Counter. *Aerosol Science And Technology*, 14(1):48–65, 1991.

[127] L. Talbot, R. K. Cheng, R. W. Schefer, and D. R. Willis. Thermophoresis of Particles in a Heated Boundary-Layer. *Journal of Fluid Mechanics*, 101(DEC):737–758, 1980.

[128] S. S. Talukdar and M. T. Swihart. Aerosol Dynamics Modeling Of Silicon Nanoparticle Formation During Silane Pyrolysis: A Comparison Of Three Solution Methods. *Journal of Aerosol Science*, 35(7):889–908, 2004.

[129] W. Teoh, L. Madler, D. Beydoun, S. Pratsinis, and R. Amal. Direct (One-Step) Synthesis Of TiO<sub>2</sub> And Pt/TiO<sub>2</sub> Nanoparticles For Photocatalytic Mineralisation Of Sucrose. *Chemical Engineering Science*, 60(21):5852–5861, 2005.

[130] S. Tiwari, F. Rana, H. Hanafi, A. Hartstein, E. F. Crabbe, and K. Chan. A Silicon Nanocrystals Based Memory. *Applied Physics Letters*, 68(10):1377–1379, 1996.

[131] C. Tsai and T. Lin. Particle Collection Efficiency Of Different Impactor Designs. *Separation Science and Technology*, 35(16):2639–2650, 2000.

[132] S. Turns. *An Introduction To Combustion*. McGraw-Hill, New York, NY, 2nd edition, 1996.

[133] G. Ulrich. Flame Synthesis Of Fine Particles. *Chemical And Engineering News*, 62(32):22–29, 1984.

[134] J. Valenta, R. Juhasz, and J. Linnros. Photoluminescence Spectroscopy Of Single Silicon Quantum Dots. *Applied Physics Letters*, 80(6):1070–1072, 2002.

[135] D. Vollath, D. Szabo, and J. Hausselt. Synthesis And Properties Of Ceramic Nanoparticles And Nanocomposites. *Journal Of The European Ceramic Society*, 17(11):1317–1324, 1997.

[136] R. Walters and H. Atwater. Silicon Optical Nanocrystal Memory. *Applied Physics Letters*, 85(13):2622–2, 2004.

[137] R. J. Walters, G. I. Bourianoff, and H. A. Atwater. Field-Effect Electroluminescence In Silicon Nanocrystals. *Nature Materials*, 4(2):143–146, 2005.

[138] R. J. Walters, P. G. Kik, J. D. Casperson, H. A. Atwater, R. Lindstedt, M. Giorgi, and G. Bourianoff. Silicon Optical Nanocrystal Memory. *Applied Physics Letters*, 85(13):2622–2624, 2004.

[139] J. Wang, V. McNeill, D. Collins, and R. Flagan. Fast Mixing Condensation Nucleus

Counter: Application To Rapid Scanning Differential Mobility Analyzer Measurements. *Aerosol Science And Technology*, 36(6):678–689, 2002.

[140] S. Wang and R. Flagan. Scanning Electrical Mobility Spectrometer. *Aerosol Science And Technology*, 13(2):230–240, 1990.

[141] P. J. Whitmore. Thermophoresis and Diffusiophoresis for Small Aerosol-Particles. *Journal of Aerosol Science*, 12(1):1–9, 1981.

[142] A. Wiedensohler. An Approximation Of The Bipolar Charge-Distribution For Particles In The Sub-Micron Size Range. *Journal Of Aerosol Science*, 19(3):387–389, 1988.

[143] A. Wiedensohler and H. Fissan. Bipolar Ion And Electron-Diffusion Charging Of Aerosol-Particles In High-Purity Argon And Nitrogen. *Particle & Particle Systems Characterization*, 7(4):250–255, 1990.

[144] M. Wilck and F. Stratmann. A 2-D Multicomponent Modal Aerosol Model And Its Application To Laminar Flow Reactors. *Journal of Aerosol Science*, 28(6):959–972, 1997.

[145] J. Wu and R. Flagan. Onset Of Runaway Nucleation In Aerosol Reactors. *Journal Of Applied Physics*, 61(4):1365–1371, 1987.

[146] J. Wu, H. Nguyen, R. Flagan, K. Okuyama, and Y. Kousaka. Evaluation And Control Of Particle Properties In Aerosol Reactors. *AICHE Journal*, 34(8):1249–1256, 1988.

[147] M. Wu, R. Windeler, C. Steiner, T. Bors, and S. Friedlander. Controlled Synthesis Of Nanosized Particles By Aerosol Processes. *Aerosol Science And Technology*, 19(4):527–548, 1993.

[148] T. Yoshida, Y. Kousaka, and K. Okuyama. Growth Of Aerosol-Particles By Condensation. *Industrial & Engineering Chemistry Fundamentals*, 15(1):37–41, 1976.

[149] T. Yoshida, S. Takeyama, Y. Yamada, and K. Mutoh. Nanometer-Sized Silicon Crystallites Prepared By Excimer Laser Ablation In Constant Pressure Inert Gas. *Applied Physics Letters*, 68(13):1772–1774, 1996.

[150] S. Zhang, Y. Akutsu, L. Russell, R. Flagan, and J. Seinfeld. Radial Differential Mobility Analyzer. *Aerosol Science And Technology*, 23(3):357–372, 1995.

[151] S. Zhang and R. Flagan. Resolution Of The Radial Differential Mobility Analyzer For Ultrafine Particles. *Journal Of Aerosol Science*, 27(8):1179–1200, 1996.